



HAL
open science

Topics in mathematical morphology for multivariate images

Santiago Velasco-Forero

► **To cite this version:**

Santiago Velasco-Forero. Topics in mathematical morphology for multivariate images. General Mathematics [math.GM]. Ecole Nationale Supérieure des Mines de Paris, 2012. English. NNT : 2012ENMP0086 . pastel-00820581

HAL Id: pastel-00820581

<https://pastel.hal.science/pastel-00820581v1>

Submitted on 6 May 2013

HAL is a multi-disciplinary open access archive for the deposit and dissemination of scientific research documents, whether they are published or not. The documents may come from teaching and research institutions in France or abroad, or from public or private research centers.

L'archive ouverte pluridisciplinaire **HAL**, est destinée au dépôt et à la diffusion de documents scientifiques de niveau recherche, publiés ou non, émanant des établissements d'enseignement et de recherche français ou étrangers, des laboratoires publics ou privés.

École doctorale n°432 : Sciences des Métiers de l'Ingénieur

Doctorat ParisTech

T H È S E

pour obtenir le grade de docteur délivré par

l'École nationale supérieure des mines de Paris

Spécialité « Morphologie Mathématique »

présentée et soutenue publiquement par

Santiago Velasco-Forero

le 14 juin 2012

**Contributions en morphologie mathématique pour l'analyse
d'images multivariées**

Directeur de thèse : **Jesús ANGULO**

Jury

M. Dominique JEULIN, Professeur, CMM-MS, Mines ParisTech

M. Jos B.T.M. ROERDINK, Professeur, University of Groningen

M. Pierre SOILLE, Directeur de recherche, Joint Research Centre of the European Commission

M. Jón Atli BENEDIKTSSON, Professeur, University of Iceland

M. Fernand MEYER, Directeur de recherche, CMM, Mines ParisTech

M. Jean SERRA, Professeur émérite, ESIEE, Université Paris-Est

M. Jesús ANGULO, Chargé de recherche, CMM, Mines ParisTech

Président
Rapporteur
Rapporteur
Examineur
Examineur
Examineur
Examineur

MINES ParisTech

Centre de Morphologie Mathématique, Mathématiques et Systèmes

35, rue Saint-Honoré, 77305 Fontainebleau, France

**T
H
È
S
E**

Acknowledgements

I would like to express my deepest gratitude to my advisor, Dr. Jesús Angulo, for his guidance, motivation and the research freedom he gave me during my Ph.D. studies. It was indeed a huge privilege to be his student.

I am grateful to Dr. Fernand Meyer, director of the Centre for Mathematical Morphology (CMM) at the Ecole des Mines de Paris, for his continuous support. My research activities were also partially supported by the IHMO Project (ANR-TecSan'07), funded by the French National Research Agency.

I would also like to thank my thesis reporters (Dr. Jos Roerdink and Dr. Pierre Soille) for their valuable suggestions and contributions that helped me to improve the quality of this document with their objective and pertinent comments. I am highly grateful to Dr. Jón Benediktsson, Dr. Dominique Jeulin, Dr. Fernand Meyer and Dr. Jean Serra, who have served in my committee and have contributed many useful comments before and during my dissertation.

Much of the inspiration for this work came during a three months visit to the Joint Research Center of the European Commission. I am very grateful to the members of the Institute to the Protection and Security of the Citizen (IPSC), particularly to Dr. Pierre Soille for our several enlightening conversations.

At Fontainebleau, I could not have asked for a more fun and interesting group of people to work with: Andres, Bea, Bruno, Catherine, Charles, Christoph, Dominique, El Hadji, Estelle, Etienne, Fernand, François, Guillaume, Hellen, Joana, Jorge, Jean, John, Julie, Louise, Luc, Matthieu, Michel, Petr, Serge, Torben, Vincent, Xiwei, and many others. Thank you all for making CMM a place where I truly enjoyed coming to work. Also, I would like to thank Julie who has been a great source of "bio-energy". She has supported me in hundreds of ways throughout the development and writing of this dissertation.

I also take this opportunity to mention my "boricuas" friends: Angel, Ana, Andrea, Catalina, Diana, Karen, Leidy, Marggie, Maider, Oscar, Pedro Alejo, Victor and Yolanda, for encourage me to cross the Atlantic few years ago.

At last, but not least, I would like to dedicate this thesis to my family: Esta tesis es para ustedes.... familia! Carlitos, Foreman, Lola, Papi, Mami, Carloncho, Bubita, Violeta, Paula Victoria y Carolina. Gracias por el constante apoyo, eterno amor y el ejemplo de superación que me han dado, día tras día.

Résumé

Cette thèse contribue au domaine de la morphologie mathématique et illustre comment les statistiques multivariées et les techniques d'apprentissage numérique peuvent être exploitées pour concevoir un ordre dans l'espace des vecteurs et pour inclure les résultats d'opérateurs morphologiques au processus d'analyse d'images multivariées. En particulier, nous utilisons l'apprentissage supervisé, les projections aléatoires, les représentations tensorielles et les transformations conditionnelles pour concevoir de nouveaux types d'ordres multivariés et de nouveaux filtres morphologiques pour les images multi/hyperspectrales. Nos contributions clés incluent les points suivants :

- Exploration et analyse d'ordres supervisés, basés sur les méthodes à noyaux.
- Proposition d'un ordre non supervisé, basé sur la fonction de profondeur statistique calculée par projections aléatoires. Nous commençons par explorer les propriétés nécessaires à une image pour assurer que l'ordre ainsi que les opérateurs morphologiques associés, puissent être interprétés de manière similaire au cas d'images en niveaux de gris. Cela nous amènera à la notion de décomposition en arrière plan / premier plan. De plus, les propriétés d'invariance sont analysées et la convergence théorique est démontrée.
- Analyse de l'ordre supervisé dans les problèmes d'appariement par forme de référence, qui correspond à l'extension de l'opérateur tout-ou-rien aux images multivariées grâce à l'utilisation de l'ordre supervisé.
- Discussion sur différentes stratégies pour la décomposition morphologique d'images. Notamment, la décomposition morphologique additive est introduite comme alternative pour l'analyse d'images de télédétection, en particulier pour les tâches de réduction de dimension et de classification supervisée d'images hyperspectrales.
- Proposition d'un cadre unifié basé sur des opérateurs morphologiques, pour l'amélioration de contraste et pour le filtrage du bruit poivre-et-sel.
- Introduction d'un nouveau cadre de modèles Booléens multivariés par l'utilisation d'une formulation en treillis complets. Cette contribution théorique est utile pour la caractérisation et la simulation de textures multivariées.

Abstract

This thesis contributes to the field of mathematical morphology and illustrates how multivariate statistics and machine learning techniques can be exploited to design vector ordering and to include results of morphological operators in the pipeline of multivariate image analysis. In particular, we make use of supervised learning, random projections, tensor representations and conditional transformations to design new kinds of multivariate ordering, and morphological filters for color and multi/hyperspectral images. Our key contributions include the following points:

- Exploration and analysis of supervised ordering based on kernel methods.
- Proposition of an unsupervised ordering based on statistical depth function computed by random projections. We begin by exploring the properties that an image requires to ensure that the ordering and the associated morphological operators can be interpreted in a similar way than in the case of grey scale images. This will lead us to the notion of background/foreground decomposition. Additionally, invariance properties are analyzed and theoretical convergence is showed.
- Analysis of supervised ordering in morphological template matching problems, which corresponds to the extension of hit-or-miss operator to multivariate image by using supervised ordering.
- Discussion of various strategies for morphological image decomposition, specifically, the additive morphological decomposition is introduced as an alternative for the analysis of remote sensing multivariate images, in particular for the task of dimensionality reduction and supervised classification of hyperspectral remote sensing images.
- Proposition of an unified framework based on morphological operators for contrast enhancement and salt-and-pepper denoising.
- Introduces a new framework of multivariate Boolean models using a complete lattice formulation. This theoretical contribution is useful for characterizing and simulation of multivariate textures.

Contents

Contents	9
List of Figures	13
1 Introduction	17
1.1 Motivation	17
1.2 Order and Mathematical morphology	20
1.3 Why do we need order?	22
1.4 Multivariate Ordering	23
1.5 Thesis overview and main contributions	25
I Learning Ordering for Multivariate Mathematical Morphology	29
2 Short review on morphological operators	31
2.1 Introduction	31
2.2 Scalar images	31
2.3 Morphological transformations	32
2.3.1 Dilation and erosion	32
2.3.2 Opening and closing	33
2.3.3 Contrast mappings	36
2.3.4 Morphological center	36
2.3.5 Geodesic reconstruction, derived operators, leveling	36
2.3.6 Residue-based operators	39
2.4 Morphological Segmentation	43
3 Preliminary Notions	47
3.1 Introduction	47
3.2 Notation and representation	48
3.2.1 Notation	48
3.2.2 Spectral representations	48
3.3 Mathematical morphology in multivariate images	50
3.4 Ordering in vector spaces	50
3.4.1 Complete lattices and mathematical morphology	51
3.4.2 Preorder by h -function	53
4 Supervised Ordering	55
4.1 Introduction	55
4.2 Complete lattices in \mathbb{R}^d	56
4.2.1 Basic Definitions	56
4.2.2 Reduced Ordering	56
4.2.3 h -supervised ordering	57
4.3 Learning the h -supervised ordering	58
4.3.1 Kriging	58
4.3.2 Support Vector Machines	60

4.3.3	Kriging vs. SVM	62
4.4	Morphological operators and h -supervised ordering	63
4.5	Applications to hyperspectral image processing	64
4.5.1	Influence of training set in h -ordering	64
4.5.2	Extracting spatial/spectral structures	65
4.5.3	Duality between background and foreground	65
4.5.4	Multi-target morphological-driven classification	66
4.6	Conclusions on supervised ordering	67
5	Hit-or-miss transform in multivariate images	81
5.1	Introduction	81
5.2	Hit-or-Miss Transform in Multivariate Images	82
5.2.1	Hit-or-Miss Transform in Binary Images	82
5.2.2	Hit-or-miss Transform in supervised h -orderings	83
5.3	Applications to Multivariate Images	84
5.3.1	Geometric Pattern Problem	84
5.3.2	Ship Detection in high-resolution RGB images.	86
5.4	Conclusions on supervised multivariate hit-or-miss	86
6	Unsupervised morphology	89
6.1	Introduction	89
6.2	Statistical depth functions	90
6.2.1	Definition	90
6.2.2	Projection depth function	91
6.2.3	Equivalence in Elliptically Symmetric Distribution	92
6.3	MM using projection depth functions	94
6.3.1	Morphological operators and depth h -mapping	98
6.3.2	Properties	99
6.4	Applications to multivariate image processing	101
6.4.1	Image enhancement	102
6.4.2	Image Simplification	103
6.4.3	Image segmentation	103
6.5	Conclusions	104
II	Contributions to morphological modeling	107
7	Additive morphological decomposition	109
7.1	Introduction	109
7.1.1	Main contributions and chapter organisation	111
7.2	Additive Morphological Decomposition	112
7.2.1	Notation	112
7.2.2	Basic Morphological Transformation	112
7.2.3	Morphological Reconstruction	114
7.2.4	Additive Morphological Decomposition	115
7.3	Tensor Modeling	117
7.3.1	Introduction	117
7.3.2	Tensor Decomposition	117
7.3.3	Tensor Principal Component Analysis (TPCA)	118
7.3.4	Equivalence with PCA	119
7.3.5	Modeling additive morphological decomposition with TPCA	119
7.4	Experiments	121
7.4.1	Data Description and Experimental Setup	121
7.4.2	Classification	128

7.4.3	Results and discussion	128
7.5	Conclusions of the chapter	130
8	Conditional Mathematical Morphology	131
8.1	Introduction	131
8.2	Brief review	133
8.3	Conditional toggle mapping	136
8.4	Experiments	143
8.4.1	Salt & pepper noise reduction	143
8.4.2	Comparison with the state of the art	145
8.4.3	Image enhancement	145
8.5	Conclusions and Perspectives of this chapter	152
9	Multivariate Chain-Boolean models	155
9.1	Introduction	155
9.2	Chain compact capacity	156
9.3	From Boolean Random Model to Chain Boolean Random Models	158
9.3.1	Notation	158
9.3.2	Binary Boolean Random Model	158
9.3.3	Chain Boolean Random Model	159
9.3.4	Properties	160
9.3.5	h -ordering and h -adjunctions	160
9.4	Experiments	161
9.5	Conclusions of this chapter	162
10	Conclusion and Perspectives	165
10.1	Conclusion	165
10.2	Suggestions for Future Works	166
	List of Symbols	170
	Bibliography	171

List of Figures

1.1	Scheme hyperspectral image acquisition. Each pixel of the image contains spectral information in d -bands. It is denoted as a pixel $\mathbf{x} \in \mathbb{R}^d$	18
1.2	Comparison of different spatial resolutions. The spatial resolution indicates the smallest distance between two objects that can be distinguished by the sensor. Note that when the size of the objects is close to the spatial resolution, the object is represented in the image as a single pixel.	19
1.3	Increasing in the spatial resolution for different satellites through time.	19
1.4	Traditional work-flow for supervised classification or segmentation of hyperspectral images.	20
1.5	Pixelwise and spatial-spectral classification. The aim of spatial-spectral approaches is integrating contextual spatial information with spectral information to produces more "real" results in the classification stage.	21
1.6	Notation for a binary image, $\mathbf{I} : \mathbf{E} \rightarrow \{0, 1\}$	22
1.7	Structuring element $\mathbf{SE} \subset \mathbf{E}$. Blue and red pixels correspond to $\{x \mathbf{SE}(x) = 1\}$ illustrating the spatial neighbourhood induced by the structuring element \mathbf{SE} centred at x (red pixel).	23
1.8	From binary erosion/dilation to multivariate counterparts	24
1.9	Notation for a d -variate image, $\mathbf{I} : \mathbf{E} \rightarrow \mathbb{F}$. Note that the image \mathbf{I} maps each spatial point x to a vector \mathbf{x} in \mathbb{R}^d (represented as a curve).	25
1.10	Different ordering strategies which are discussed in the Part I of this thesis: (c) Referenced Ordering (d) Supervised Ordering (e) Supervised Ordering and (f) Unsupervised ordering.	26
1.11	Representation of colour values of natural images as vector points in \mathbb{R}^3	26
1.12	Example of proposed unsupervised ordering	27
2.1	Basic morphological transformations: dilation (b) and erosion (c). The structuring element \mathbf{SE} is a disk of diameter three pixels.	34
2.2	Opening (a) and closing (b) transformations. The structuring element \mathbf{SE} is a disk of diameter 3 pixels.	35
2.3	Results of toggle mapping and morphological center.	37
2.4	Opening and closing by reconstructions	38
2.5	Leveling transformation.	40
2.6	Leveling transformation (b) with a marker given by a Gaussian Filter (a).	41
2.7	Morphological gradients	42
2.8	Watershed transform for a given image \mathbf{I} with markers point \mathbf{M}	44
2.9	Contrast-driven watershed transforms.	46
3.1	Scheme of different representation for the spectral information of a multivariate image	49
3.2	Spectral information is associated with vector spaces.	50
3.3	Some vector ordering strategies proposed in the literature. The associated ordering is also illustrated.	52
3.4	The h -ordering (preorder) produces a complete lattice for a given set.	54
4.1	Scheme of h -supervised function producing a partial ordering on a given original set.	58
4.2	Comparison of h -mappings and their corresponding h -ordering \leq_h in \mathbb{R}^2	59

4.3	Unitary background and foreground sets: $F = \mathbf{f}$ and $B = \mathbf{b}$	60
4.4	Training spectral for Pavia University HSI.	62
4.5	Some morphological transformation for Pavia University	68
4.6	Training spectral for Yellowstone Scene.	69
4.7	Morphological transformations for Yellowstone scene.	70
4.8	Toy example in supervised ordering.	71
4.9	Training size effect in the supervised ordering for the toy example.	71
4.10	Supervised dilation, erosion and gradient for two sets of background/foreground pixels.	72
4.11	Supervised transformation for Yellowstone for the first group of training sets.	73
4.12	Supervised transformation for Yellowstone for the second set of training sets.	74
4.13	Extraction of specific objects can be performed by using geodesic reconstruction in the supervised ordering.	75
4.14	Supervised Leveling for sets of background/foreground pixels.	76
4.15	HSI Moffett Field sub-scene using bands $\{115,70,30\}$. Reference pixels (background \mathbf{b} and foreground \mathbf{f}) used in the experiments. Curves are plots of the spectral values in the different frequency bands for the reference pixels.	77
4.16	Comparison of different supervised morphological operators	78
4.17	Comparison of supervised top-hats.	79
4.18	Illustrative example of multiclass supervised ordering.	79
4.19	A false colour of the original image is shown using bands number $[80,70,30]$. Morphological driven-classification using leveling operator with unitary structuring element hexagonal SE. $h_{\{\mathbf{T}_{-i}, \mathbf{T}_i\}}$ is obtained using SVM, with polynomial kernel of degree two.	80
5.1	Illustrative example of Hit-or-Miss transform for the set I: $HMT(\mathbf{I}; \mathbf{SE}_1, \mathbf{SE}_2)$	82
5.2	From the binary HMT to the extension for multiband images in the supervised ordering	83
5.3	Example of colour template matching using the proposed multivariate hit-or-miss transform.	85
5.4	ROC-curves in the geometric pattern recognition problem	86
5.5	SEs considered in the Bahrain Image. In both scenarios, the sets of pixels background (B_1) and foreground (B_2) are the same.	87
5.6	Ship detection in High-Resolution Samaheej Image using HMT_ϵ	87
6.1	Intrinsic ordering based on dichotomy background and foreground.	90
6.2	Toy example of the computation of (6.1). Projection depth function for a vector \mathbf{x} given \mathbf{X} is basically the maxima normalised eccentricity for all the possible projection $\mathbf{u}^T \mathbf{X}$ given a couple of centrality and variability univariate measures (μ, σ)	92
6.3	"White bird" colour image example.	95
6.4	"Canoe" colour image example.	96
6.5	"Cuenca map" colour image example.	97
6.6	Example of openings and associated top-hat transformation in the ordering induced by the projection depth function.	100
6.7	Projection depth function is invariant to affine transformation in \mathbb{R}^d	101
6.8	Edge enhancement of \mathbf{I} using toggle mapping $\tau_h(\mathbf{I})$ in the proposed ordering. Source: http://www.cellimagelibrary.org/	102
6.9	Original (\mathbf{I}), marker (\mathbf{M}) and simplification by h -depth vector leveling $\Lambda_{h_I}(\mathbf{I}, \mathbf{M})$. The marker \mathbf{M} is the product of a h -depth closing followed by an h -depth opening with the SE is a disk of radius 10.	103
6.10	h -depth gradient and segmentation by using watershed transformation (in red), where markers are calculated by selecting the minima of strong dynamics in h -depth gradient, with $t = .5$	105
6.11	Original multispectral images is the size 200 by 500 pixels in 31 channels. Segmentation for watershed transformation with different parameters of dynamics minima of h -depth gradient.	105

6.12	Original hyperspectral image is 610 by 340 pixels on 103-bands. Segmentation by h -depth watershed transformation with different parameters of dynamics minima of h -depth gradient.	106
7.1	Mathematical notation for a 2D multivariate image, $\mathbf{I} : \mathbf{E} \rightarrow \mathbb{F}$	110
7.2	Structuring element $\mathbf{SE} \subset \mathbf{E}$ at $x = (i, j) \in \mathbf{E}$. MM operators are non-linear neighbourhood-image transforms associated with the structuring element \mathbf{SE}	112
7.3	Morphological transformations of a scalar (grey level) image. Original image (a) is a 342×342 pixels in 70-cm-resolution satellite image from the panchromatic band of Quickbird.	113
7.4	Example of AMD and ADL for the remote sensing example.	116
7.5	Experiment shows clearly that TPCA is equivalent to PCA.	120
7.6	Illustration of dimensional reduction stage using additive morphological decomposition.	120
7.7	False colour composition of the HSI considered in the experiments.	121
7.8	Analysis of AMD in ROSIS Pavia University	122
7.9	First scenario of classification using Indian Pines. Only five pixels per class are selected for the training set. The results show the average and standard deviation in 25 repetitions.	124
7.10	Classification maps for the Indian Pines HSI using different approaches. Only five training pixels in nine classes are considered. The classification map is the best result in 25 random repetitions.	125
7.11	Behaviour of the overall accuracy in the Pavia University dataset for different morphological decompositions and dimensional reduction approach.	125
7.12	Classification maps obtained by the different tested methods for Pavia University data set (Overall accuracies are reported in parentheses)	129
8.1	Illustration of gradients and local extrema detectors.	134
8.2	Bi-dimensional representation of the evolution in the classical shock filter (8.4) for the Cameraman grey-scale image in (d).	135
8.3	Iteration number versus residual between two consecutive iterations of classical and conditional toggle mapping.	136
8.4	Conditional vs Classical Dilation.	137
8.5	Example showing that the pair conditional operators are not an adjunction in algebraic sense.	138
8.6	The proposed conditional toggle contrast sharpens the signal as well as classical enhancement method.	141
8.7	The proposed conditional toggle contrast does not produce halos as classical filters in ramp signals.	143
8.8	Comparison in free-noisy scenario.	144
8.9	Experimental results in PSNR for grey and colour images.	146
8.10	Example of noise removal by proposed method in grey scale images.	147
8.11	Example of noise removal by proposed method in Lena	148
8.12	Example of noise removal by proposed method in colour Birds.	149
8.13	Example of noise removal by proposed method in Baboon.	150
8.14	Example of noise removal by proposed method in Boat.	151
8.15	Conditional toggle mapping and segmentation by α -connected component in a WorldView-2 satellite image.	153
8.16	PSNR of restored image by using mean per α -connected component in original, toggle mapping and conditional toggle mapping.	154
9.1	Example of Binary Boolean Random image and Chain Boolean Random multivariate image. For illustration, the same $\Xi(M)$ is used in both simulations. We notice that \mathcal{L} is a color lattice from blue ($\top_{\mathcal{L}}$) to yellow ($\perp_{\mathcal{L}}$).	159

9.2	The Chain representation of a multivariate image allows the applications of non-linear filtering and random Boolean model theory.	161
9.3	Example of simulation for a hyperspectral image	162
9.4	Summary of proposed steps to generate random realization of a Boolean model in the lattice induced by the random projection depth function.	163
9.5	Realisations of the proposed algorithm of Multivariate Boolean model in the lattice induced for the projection depth function	163

1

Introduction

The world is continuous, but the mind is discrete. *David Mumford*

Résumé

Dans ce chapitre est présentée la motivation générale de l'analyse d'images numériques multivariées et de leur traitement basé sur la morphologie mathématique. Cette technique est fondée sur la théorie des treillis, théorie pour laquelle une relation d'ordre entre les pixels de l'image est nécessaire. La difficulté principale, d'une part, est due au fait qu'il n'existe pas de définition «naturelle» d'ordre entre vecteurs, ceux-ci correspondant aux pixels des images multivariées. D'autre part, une image représente un arrangement spatial de l'information et cette dimension est fondamentale pour les différentes analyses effectuées sur celle-ci. En tenant compte de ces deux points, une introduction générale à cette thèse est présentée dans ce chapitre, et les contributions principales sont listées et illustrées au moyen d'exemples simples.

1.1 Motivation

In modern society, huge amounts of images are collected and stored in computers so that useful information can be later extracted. In a concrete example, the online image hosting Flickr reported in August 2011, that it was hosting more than 6 billion images and 80 million unique visitors ¹. The growing complexity and volume of digitised sensor measurements, the requirements for their sophisticated real time exploitation, the limitations of human attention, and increasing reliance on automated adaptive systems all drive a trend towards heavily automated computational processing in order to refine out essential information and permit effective exploitation. Additionally, vast quantities of sophisticated sensor data is readily obtained and often available on the internet: large quantities of imagery from webcams, surveillance cameras, hyperspectral sensors, synthetic aperture radars (SAR), and X-ray astronomical data, to name only a few types, are basically colour or multi-bands images.

The science of extracting useful information from images is usually referred to as *image processing*. From the mathematical point of view, image processing is any form of signal processing for which the input is an image and the output may be either an image or a set of characteristics or

¹Source: <http://en.wikipedia.org/wiki/Flickr>

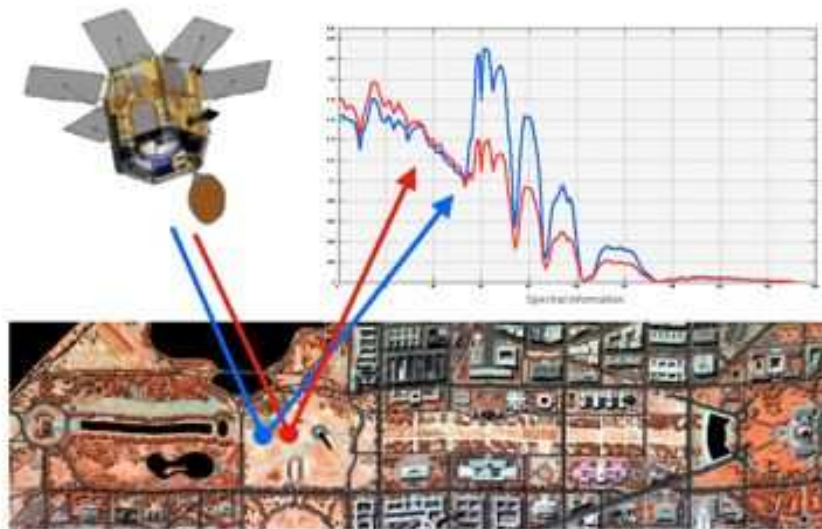


Figure 1.1: Scheme hyperspectral image acquisition. Each pixel of the image contains spectral information in d -bands. It is denoted as a pixel $\mathbf{x} \in \mathbb{R}^d$.

features related to the input image. In essence, image processing is concerned with efficient algorithms for acquiring and extracting information from images. In order to design such algorithms for a particular problem, we must have realistic *models* for the images of interest. In general, models are useful for incorporating *a priori* knowledge to help to distinguish interesting images, from uninteresting, which can help us to improve the methods for acquisition, analysis, and transmission.

Modern sensors technology have both high spatial and high spectral resolution covering up to several hundred bands. One of these modern sensors are the hyperspectral remote sensors. They collect image data simultaneously in dozens or hundreds of narrow, adjacent spectral bands. These measurements make it possible to derive an “almost” continuous spectrum for each image cell, as shown in the Fig. 1.1. The data consists of a large number of two dimensional images with each different image corresponding to radiation received by the sensor at a particular wavelength. These images are often referred as *band images* or simply *bands* or *channels* since they corresponds to reflected energy in a particular frequency band.

Hyperspectral data gives very fine spectral resolution, but this is not always an advantage. Obviously hyperspectral data is very high-dimensional compared to colour imagery, which is similar in concept but comprised only three spectral bands (red, green and blue channel). One of the problems dealing with hyperspectral images is the *curse of dimensionality* [Clarksona \(1994\)](#). Curse of dimensionality concerns the effect of increasing dimensionality on distance or similarity. The term was introduced by [Bellman \(1957\)](#) to describe the extraordinarily rapid growth in the difficulty of problems as the number of dimension (or variables) increases. The curse of dimensionality is explained with several artificial data problems in [Koppen \(2000\)](#). Additionally, the large data sets produced by hyperspectral imagers can also lead to significant computational and communication challenges, particularly for time-critical applications. In addition, an acquired image has a *spatial resolution*. It is a measure of the smallest object that can be resolved by the sensor, or the linear dimension on the ground represented by each pixel or grid cell in the image. Fig. 1.2 illustrates different spatial resolutions on the same scene. The tendency in the spatial resolution for the main remote sensing captors in the last 40 years shows that image quality is going to be better in the sense of spatial resolution, as it is illustrated in Fig. 1.3. It should be noted, however, that most of available hyperspectral data processing techniques focused on analysing the data without incorporating information on the spatially adjacent data, i.e., hyperspectral data are usually not treated as images,

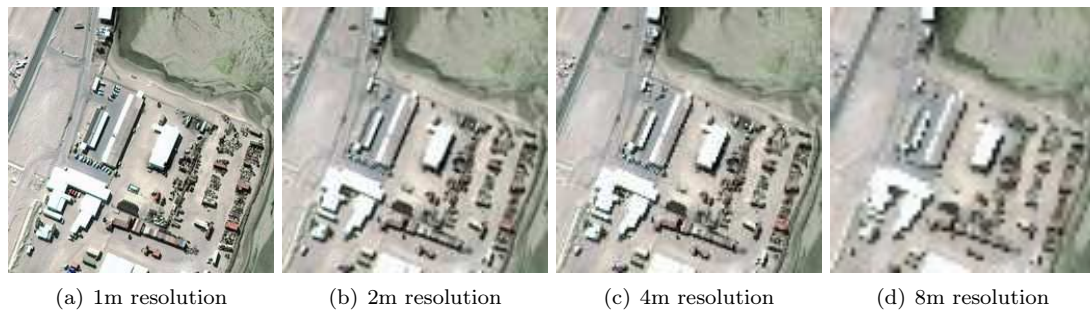


Figure 1.2: Comparison of different spatial resolutions. The spatial resolution indicates the smallest distance between two objects that can be distinguished by the sensor. Note that when the size of the objects is close to the spatial resolution, the object is represented in the image as a single pixel.

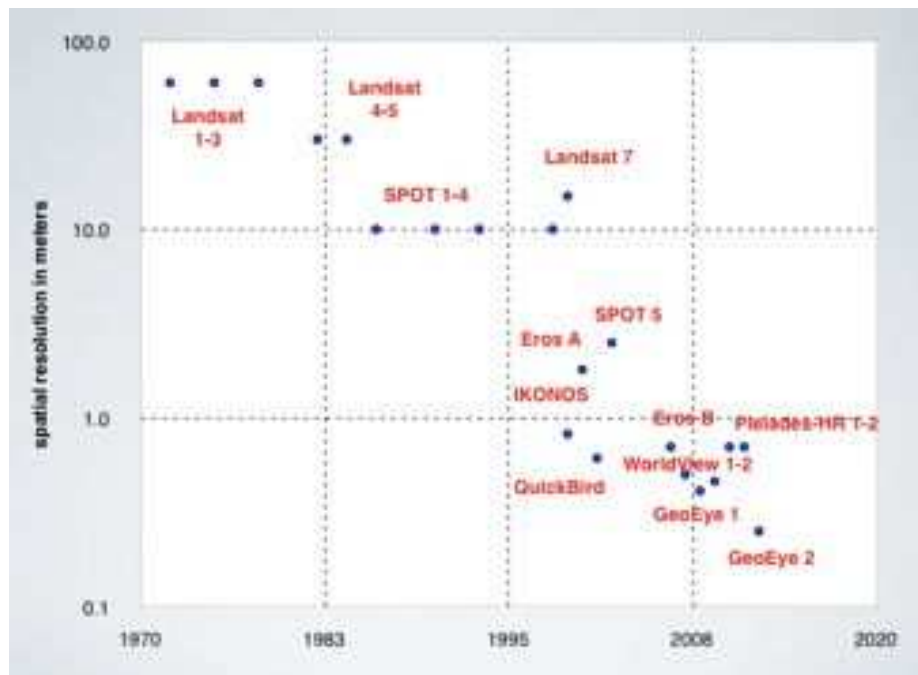


Figure 1.3: Increasing in the spatial resolution for different satellites through time.

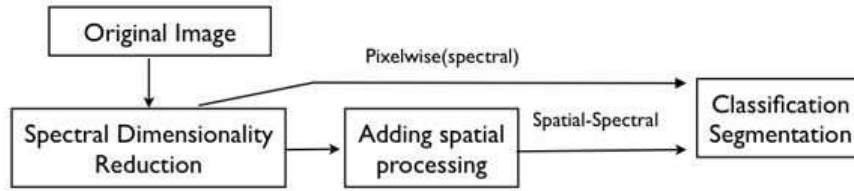


Figure 1.4: Traditional work-flow for supervised classification or segmentation of hyperspectral images.

but as unordered listings of spectral measurements with no particular spatial arrangement [Tadjudin and Landgrebe \(1998\)](#). An illustrative typical work-flow for classification is shown in Fig. 1.4. For a given hyperspectral image of n_1 rows and n_2 columns in d bands, the first stage is to reduce the dimension without loss of information [Landgrebe \(2003\)](#). Most of the techniques are based on linear algebra and signal processing. They analyse the image as a matrix of size $(n_1 \times n_2)$ rows and d columns. Some examples of these approaches are principal component analysis, orthogonal subspace projections [Harsanyi et al. \(1994\)](#), Maximum Noise Fraction [Green et al. \(1988\)](#) are some of these kernel dimensional reduction approaches. Secondly, in the reduced space, spatial features are calculated and included in the classification procedure by using PDEs [Duarte-Carvajalino et al. \(2008\)](#), [Velasco-Forero and Manian \(2009\)](#), Kernels [Camps-Valls and Bruzzone \(2005\)](#), and so on. The need of working on spatial-spectral pattern for analyzing multivariate images has been identified as an important goal by many scientists devoted to hyperspectral data analysis [Chanussot et al. \(2010\)](#). In [Plaza et al. \(2009\)](#), authors present three main challenges for the analysis of hyperspectral images:

- Robust analysis techniques to manage images which the spatial correlation between spectral responses of neighbouring pixels can be potentially high;
- Processing algorithms need to become more knowledge-based, i.e., a priori knowledge about shape, texture, spatial relationships and pattern may be used to improve the characterisation of scenes;
- Algorithms should deal with small number of training samples in high number of features available in remote sensing applications.

Spatial preprocessing methods are often applied to denoise and regularise images. These methods also enhance spatial texture information resulting in features that improve the performance of classification techniques. For illustrative purposes, Fig. 1.5 shows a comparison of spectral pixel-wise and spectral-spatial supervised classification in a real hyperspectral image. In this thesis, we study different aspects of spatial-spectral analysis of hyperspectral images, where the spatial information is incorporated by using non-linear filters. There are two general families of nonlinear filters: the polynomial filters, and morphological filters. The polynomial filters are based on traditional nonlinear system theory based mainly in Volterra series [Schetzen \(1980\)](#). In the set of non-linear image processing disciplines, mathematical morphology involves the concept of image transformations based on geometrical-spatial concepts related to size/shape relationship as prior information. This dissertation investigates the use of morphological based nonlinear filters for processing multivariate images.

1.2 Order and Mathematical morphology

Mathematical morphology was originally developed in the end of 1960's by Georges Matheron and Jean Serra at the Ecole des Mines in Paris. It has a solid mathematical theory leaning on concepts from algebra, topology, integral geometry, and stochastic geometry [Matheron \(1975\)](#). The basic idea of mathematical morphology, as described by [Heijmans \(1995\)](#), is “to examine the geometric structure of an image by matching it with small patterns at various locations in the image. By



Figure 1.5: Pixelwise and spatial-spectral classification. The aim of spatial-spectral approaches is integrating contextual spatial information with spectral information to produce more "real" results in the classification stage.

varying the size and shape of the matching patterns, called *structuring elements*, one can extract useful information about the shape of the different parts of the image and their interactions." Thus, structuring elements play the role of a priori knowledge. Originally, mathematical morphology was developed for binary images; these can be represented mathematically as sets. Serra (1982) were the first to observe that a general theory on morphological image analysis should include the assumption that the underlying objects of analysis have to be a partially *order set structure* in which all subsets have both a supremum and an infimum, i.e., a complete lattice. It should be noted that the term "order" is commonly used in two senses. First, "order" denotes an *ordering principle*: a pattern by which the elements of a given set may be arranged. For instance, the alphabetical order, marginal ordering, and so forth. Second, "order" denotes the condition of a given set, its *conformity* to the ordering principle. Lorand (2000) give us a concrete example for this dichotomy. Two libraries that arrange their books according to the same principle, for instance, by authors surnames, thereby follow an identical order. This is order in the first sense. Yet these libraries may differ in respect to "order" in the second sense: books may be shelved more carelessly in one library than in the other. In this second usage, "order" denotes the degree of conformity of the set to its ordering principle. In the case of multidimensional images, the objects of interest are vectors in high-dimensional spaces. In this thesis, we study the ordering problem (in the first sense) for elements laying in vector spaces, as well as other related problems that occur frequently when dealing with mathematical morphology in multivariate images. This thesis is motivated for the demand for a detailed analysis of this problem and the development of algorithms useful for the analysis of real-life images in suitable running time. Many of the techniques used for colour noise reduction are direct implementations of the methods used for grayscale imaging. The independent processing of colour image channels is however inappropriate and leads to strong artefacts. To overcome this problem, this thesis extends techniques developed for monochrome images in a way which exploits the vector structure of spectra and correlation among the image channels.

1.3 Why do we need order?

In the simplest case, the object of interest is a binary image (denoted by \mathbf{I}) which maps the spatial support \mathbf{E} onto a bi-valued set $\{0, 1\}$.

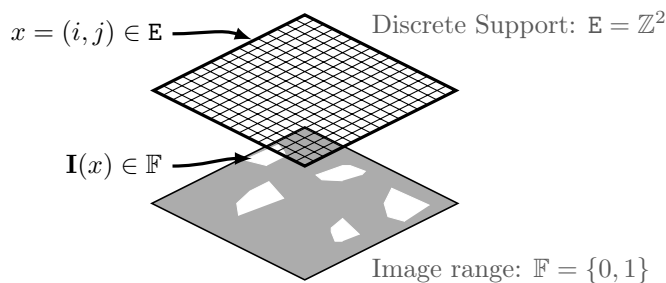


Figure 1.6: Notation for a binary image, $\mathbf{I} : \mathbf{E} \rightarrow \{0, 1\}$

Morphological operators aim at extracting relevant structures of the image. This is achieved by carrying out an inquest into the image through a set of known shape called *structuring element* (SE). Fig. 1.7 shows the neighbourhood induced by two structuring elements. The two basic words in the mathematical morphology language are *erosion* and *dilation*. They are based on the notion of infimum and supremum. For the case of symmetric structuring element (SE), the *erosion* and *dilation* operators are defined as follow,

$$\varepsilon_{\text{SE}}(\mathbf{I})(x) = \bigwedge_{y \in \text{SE}(x)} \mathbf{I}(y) \quad (1.1)$$

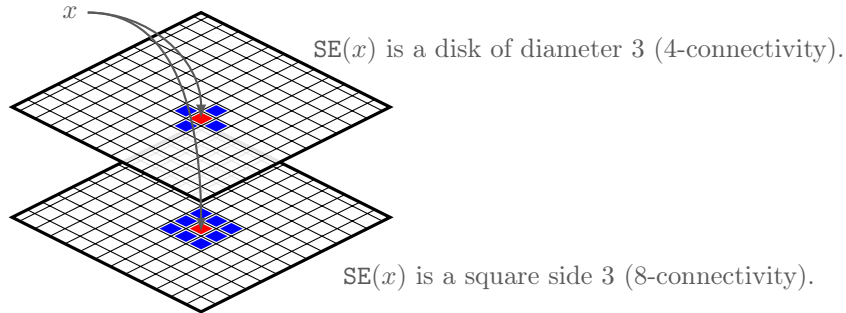


Figure 1.7: Structuring element $\mathbf{SE} \subset \mathbf{E}$. Blue and red pixels correspond to $\{x | \mathbf{SE}(x) = 1\}$ illustrating the spatial neighbourhood induced by the structuring element \mathbf{SE} centred at x (red pixel).

and

$$\delta_{\mathbf{SE}}(\mathbf{I})(x) = \bigvee_{y \in \mathbf{SE}(x)} \mathbf{I}(y) \quad (1.2)$$

where $\mathbf{SE}(x) \in \mathbf{E}$ denote the spatial neighbourhood induced by the structuring element \mathbf{SE} centred at x , and \mathbf{SE} is the transpose structuring element.

For binary images, they are simple in the sense that they usually have an intuitive interpretation. Erosion $\varepsilon_{\mathbf{SE}}(\mathbf{I})$ shrinks bright objects, whereas dilation $\delta_{\mathbf{SE}}(\mathbf{I})$ expands bright object from their boundaries. The size and shape effect is controlled by the structuring element \mathbf{SE} . Fig. 1.8 shows these two basic operators in a binary image. This pair of transformations are not inverses, however, they constitute an algebraic-adjunction (Heijmans (1994)), namely

$$\delta_{\mathbf{SE}}(\mathbf{J}) \leq \mathbf{I} \iff \mathbf{J} \leq \varepsilon_{\mathbf{SE}}(\mathbf{I}) \quad (1.3)$$

for every pair of images \mathbf{I}, \mathbf{J} . This is called the *adjunction relation* (Heijmans (1994)). The same definitions can be directly applied to grey scale image, preserving the interpretation of these operators. Image analysis tasks that can be tackled by morphological operators include the following ones (Soille and Pesaresi (2002)): Image filtering, image segmentation and image measurement. In spite of the simplicity of the definition of erosion and dilation, based only on local minimum/maximum operators, composition and more elaborated combination of these operators allow to extract object, noise filtering and characterisation of important objects in the image (Soille (2003)). A natural question arises: "Can we define a total order for vectors to have useful morphological operators to analysis real-life multivariate images?"

1.4 Multivariate Ordering

The extension of mathematical morphology to vector spaces, for instance to colour, multispectral or hyperspectral images, is neither direct nor trivial due, on one hand, to the eventual high dimensional nature of the data and, on the other hand, because there is no notion of natural ordering in a vector space, as opposed to one-dimensional (scalar) case (Barnett (1976)). Let us introduce the notation for a multivariate image, as it is illustrated in Fig. 1.9, where the object of interest is a d -dimensional image (denoted by \mathbf{I}) which maps the spatial support \mathbf{E} to the vector support \mathbb{F} , i.e.,

$$\begin{aligned} \mathbf{I}: \quad \mathbf{E} &\rightarrow \mathbb{F} = \mathbb{R}^d \\ x &\rightarrow \mathbf{x} \end{aligned}$$

Given a multivariate image \mathbf{I} , there are two general methods for morphological processing: component-wise (marginal) and vector. Marginal approach consists in processing separately each band or channel of the image. The correlation among bands is totally ignored as well as the vector nature of pixel values. However, it allows to employ directly all methods available for grey-scale images with

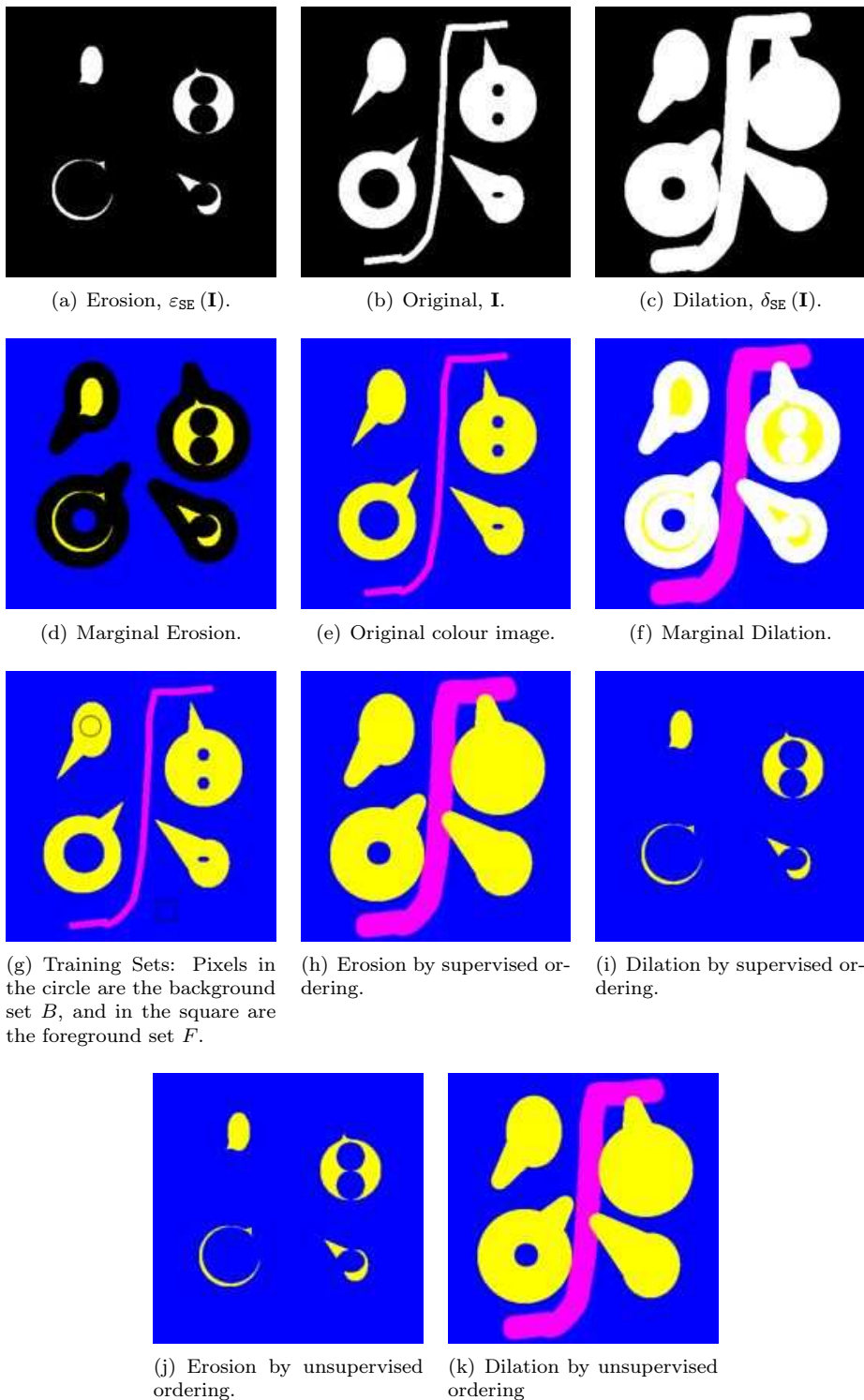


Figure 1.8: From binary erosion/dilation to multivariate counterparts: Original image is a binary image of size 350×350 . SE is a disk of radius 11. Supervised ordering (Chapter 4) is designed to learn an ordering based on the couple of training sets (B, F) . Morphological transformation results are adaptive to the spectral information from (B, F) . Unsupervised ordering based on random projections (Chapter 6) is fully automatic approach to learn a chain that produces mathematical morphology transformations interpretable in the physical meaning of erosion and dilation as in the case of binary images, on the contrary to the marginal extensions. Needless to say, multivariate image have to fit some assumption to get this sort of interpretation.

complexity increased by a constant value d , the number of bands. Despite the intense focus of mathematical morphology community on the problem of generalisation to multivariate images as colour and multispectral images it is not actually clear how to proceed in general manner (Aptoula and Lefèvre (2007)). The bottleneck is the definition of a total ordering for vector pixel laying in $\mathbb{F} = \mathbb{R}^d$, i.e., an reflexive, anti-symmetric, transitive and total binary relation. In response to this challenge, there has been a surge of interest in recent years across many fields in a variety of *multivariate ordering* (Angulo (2007), Aptoula and Lefèvre (2007)). In this thesis, we provide for instance, a multivariate ordering for capturing the fact that in many cases high-dimensional images contain an intrinsic ordering of their objects. To motivate this important point, a dummy example is illustrated in Fig. 1.10. Additionally, we remark that vector space representation for natural colour images involves a structured cloud as it is illustrated in Fig. 1.11.

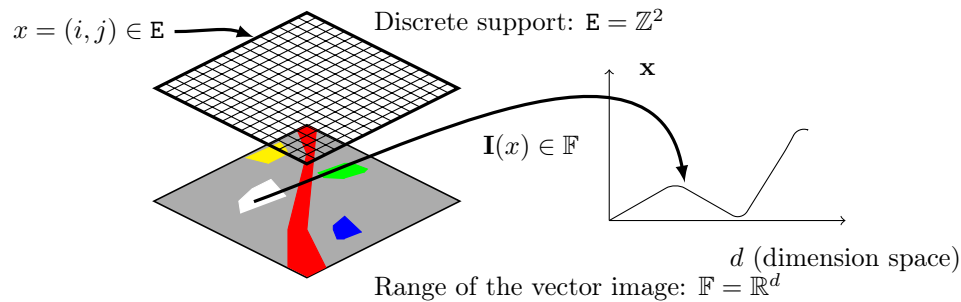


Figure 1.9: Notation for a d -variate image, $\mathbf{I} : E \rightarrow \mathbb{F}$. Note that the image \mathbf{I} maps each spatial point x to a vector \mathbf{x} in \mathbb{R}^d (represented as a curve).

1.5 Thesis overview and main contributions

This thesis contributes to the field of mathematical morphology and illustrates how multivariate statistics and machine learning techniques can be exploited to design vector ordering and to include results of morphological operators in the pipeline of hyperspectral image analysis (see Fig. 1.4), with a particular focus on the manner in which supervised learning, random projections, tensor representations and conditional transformations can be exploited to design new kinds of multivariate ordering, and morphological filters for colour and multi/hyperspectral images. Our key contributions include the following points:

- Exploration and analysis of supervised ordering based on kernel based methods,
- Insight into unsupervised ordering based on random projections,
- Formulation of additive morphological based decomposition and analysis by using tensor modelling,
- Proposition and analysis of a morphological based unified framework for contrast enhancement and salt-and-pepper noise denoising,
- Formulation of multivariate Boolean models using lattice notions.

For the sake of clarity, these contributions are organised into two main parts. In Part I the concept of supervised and unsupervised ordering for mathematical morphology is introduced.

- A description of preliminary subject is included in Chapter 3.
- Chapter 4 introduces the notion of supervised ordering based on learning algorithms. Additionally, applications in real hyperspectral images are included.

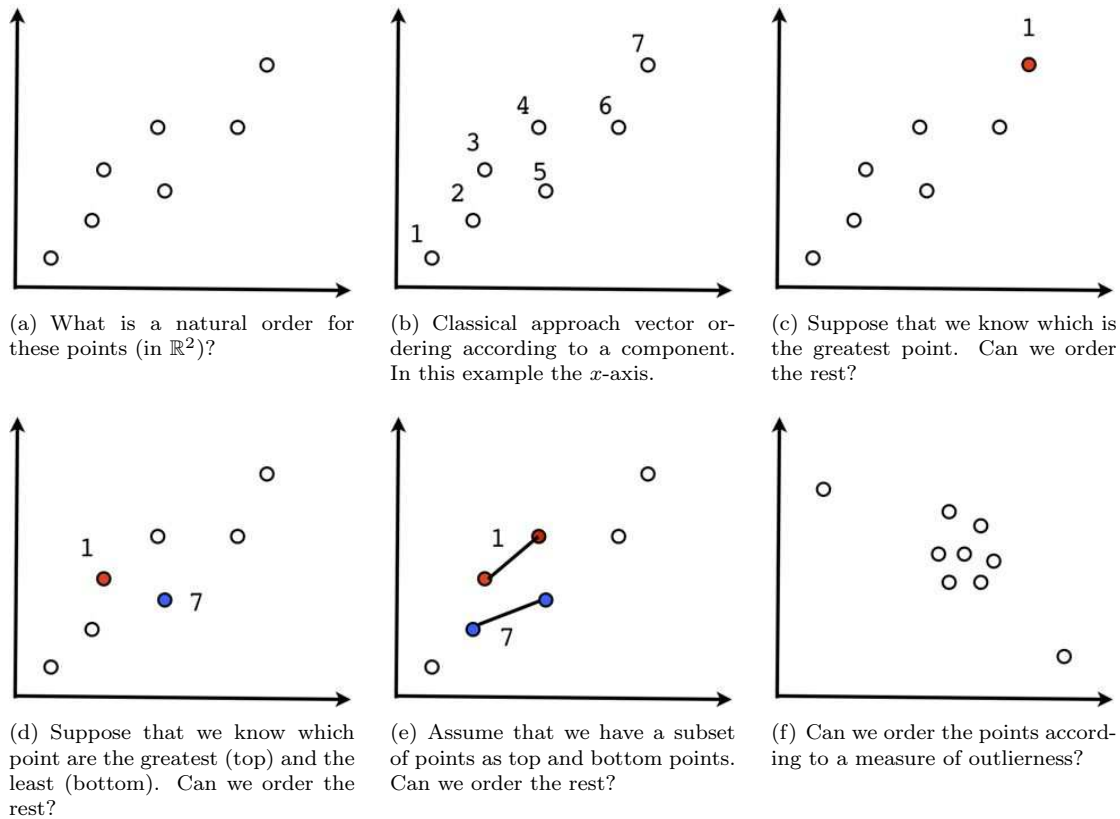
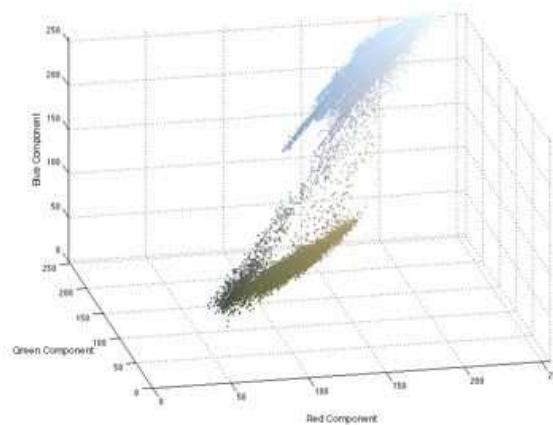


Figure 1.10: Different ordering strategies which are discussed in the Part I of this thesis: (c) Referenced Ordering (d) Supervised Ordering (e) Supervised Ordering and (f) Unsupervised ordering.



(a) \mathbf{I}



(b) Scatterplot of \mathbf{X} is illustrated.

Figure 1.11: Representation of colour values of natural images as vector points in \mathbb{R}^3 . \mathbf{X} represents pixel values of the image \mathbf{I} . Color information are included in the scatterplot to aid the comprehension.

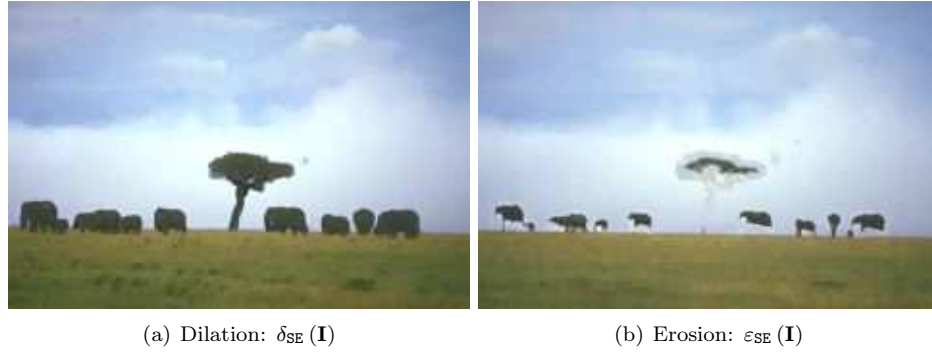


Figure 1.12: Basic Morphological Transformation obtained by proposed unsupervised ordering (Chapter 6).

- Chapter 5 analyses the potential of supervised ordering in morphological template matching problems, which corresponds to the extension of hit-or-miss operator to multivariate image by using supervised ordering.
- Chapter 6 proposes methods for unsupervised ordering based on statistical depth function computed by random projections. We begin by exploring the properties that we will require our image to ensure that the ordering and the associated morphological operators can be interpreted in a similar way to grey scale images. This will lead us to the notion of background/foreground decomposition. Additionally, invariance properties are analysed and theoretical convergence is showed.

Part II we present other contributions on mathematical morphology for the analysis of multivariate images.

- Chapter 7 discusses various strategies for morphological image decomposition, specifically, the additive morphological decomposition is introduced as an alternative for the analysis of remote sensing multivariate images, in particular for the task of supervised/unsupervised classification of hyperspectral remote sensing images.
- That includes also Tensor modelling as an alternative to dimensional reduction approach in multivariate images, by including this step in the traditional pipeline to analysis a hyperspectral image.
- Chapter 8 shifts the focus of our research to conditional morphology as an unified low complexity framework for enhancement and impulse noise removal. Theoretical properties of conditional morphology are discussed and applications are widely studied.
- Chapter 9 introduces a new framework of multivariate Boolean models using a complete lattice formulation. This theoretical contribution is useful for characterising and simulation of multivariate textures.

We conclude with a summary of our findings, discussion of ongoing work, and directions for future research in Chapter 10. This thesis is the culmination of a variety of intensive collaborations. Most of results have been already published, the first page of each chapter provides the associated references.

Part I

Learning Ordering for Multivariate Mathematical Morphology

2

Short review on morphological operators for scalar images

As morphology deals with forms and relations of position, it demands a careful selection of terms, and a methodized nomenclature.

The Anatomical Memoirs of *John Goodsir*
(Volume 2) Chapter V (pp. 83D84)
Edinburgh, Scotland. 1868

Résumé

Ce chapitre donne un compendium des principaux opérateurs de morphologie mathématique utilisés au cours de la thèse. Les résultats sont illustrés au travers d'exemples d'images en niveaux de gris provenant de la télédétection.

2.1 Introduction

Mathematical morphology is a mathematical theory of image processing which facilitates the quantitative analysis and description of the geometric structures of image. Mathematical morphology discusses nonlinear image transformations such as erosion, dilation, opening, closing, leveling and watershed transformations. In more general scenarios, morphological operators need a complete lattice structure, i.e., the possibility of defining an ordering relationship between the points to be processed [Ronse \(1990b\)](#), [Goutsias and Heijmans \(2000\)](#). This key point has been introduced by Jean Serra in [Serra \(1982\)](#) is analysed in Chapter 3. The aim of this chapter is to provide a background on the basic morphological operators for scalar images (grey scale images). This short review is necessary to fix the notation and to make easier the definition of the operators for images valued on \mathbb{R}^d .

2.2 Scalar images

Let E be a subset of the Euclidean \mathbb{R}^n or the discrete space \mathbb{Z}^n , considered as the *support space* of the image, and let \mathcal{T} be a set of grey-levels, corresponding to the *space of values* of the image. It is

assumed that $\mathcal{T} = \overline{\mathbb{R}} = \mathbb{R} \cup \{-\infty, +\infty\}$. A grey-level image is represented by a function,

$$\mathbf{I}: \begin{cases} \mathbf{E} & \rightarrow \mathcal{T} \\ x & \mapsto t \end{cases} \quad (2.1)$$

i.e., $\mathbf{I} \in \mathcal{F}(\mathbf{E}, \mathcal{T})$, where $\mathcal{F}(\mathbf{E}, \mathcal{T})$ denotes the functions from the discrete support \mathbf{E} onto the space of values of the image \mathcal{T} . Thus, \mathbf{I} maps each pixel $x \in \mathbf{E}$ into a grey-level value $t \in \mathcal{T}$: $t = \mathbf{I}(x)$. Note that \mathcal{T} with the natural order relation \leq is a complete lattice. It is important to remark that if the \mathcal{T} is a complete lattice, then $\mathcal{F}(\mathbf{E}, \mathcal{T})$ is a complete lattice too (Serra (1988)).

2.3 Morphological transformations

2.3.1 Dilation and erosion

The two basic morphological mappings $\mathcal{F}(\mathbf{E}, \mathcal{T}) \rightarrow \mathcal{F}(\mathbf{E}, \mathcal{T})$ are the *grey-level dilation* and the *grey-level erosion* given respectively by

$$\delta_{\mathbf{b}}(\mathbf{I})(x) = \sup_{h \in \mathbf{E}} (\mathbf{I}(x - h) + \mathbf{b}(h)) \quad (2.2)$$

and

$$\varepsilon_{\mathbf{b}}(\mathbf{I})(x) = \inf_{h \in \mathbf{E}} (\mathbf{I}(x + h) - \mathbf{b}(h)), \quad (2.3)$$

where $\mathbf{I} \in \mathcal{F}(\mathbf{E}, \mathcal{T})$ is the original grey-level image and $\mathbf{b} \in \mathcal{F}(\mathbf{E}, \mathcal{T})$ is the fixed *structuring function*. The further convention to avoid ambiguous expression is considered: $\mathbf{I}(x - h) + \mathbf{b}(h) = -\infty$ when $\mathbf{I}(x - h) = -\infty$ or $\mathbf{b}(h) = -\infty$, and that $\mathbf{I}(x + h) - \mathbf{b}(h) = +\infty$ when $\mathbf{I}(x + h) = +\infty$ or $\mathbf{b}(h) = -\infty$. Particularly interesting in theory and in practical applications, the flat grey-level dilation and erosion is obtained when the structuring function is flat and becomes a *structuring element* (Soille (2003)). More precisely, a *flat* structuring function of the set \mathbf{SE} is defined as

$$\mathbf{b}(x) = \begin{cases} 0 & x \in \mathbf{SE} \\ -\infty & x \in \mathbf{SE}^c \end{cases},$$

where \mathbf{SE} is a set which indicator function as a Boolean set, *i.e.*, $\mathbf{SE} \subseteq \mathbf{E}$ or $\mathbf{SE} \in \mathcal{P}(\mathbf{E})$, which defines the “shape” of the structuring element. We notice that \mathbf{SE}^c denotes the complement set of \mathbf{SE} (*i.e.*, $\mathbf{SE} \cap \mathbf{SE}^c = \emptyset$ and $\mathbf{SE} \cup \mathbf{SE}^c = \mathbf{E}$). The structuring element is defined at the origin $y \in \mathbf{E}$, then to each point z of \mathbf{E} corresponds the translation mapping y to z , and this translation maps \mathbf{SE} onto \mathbf{SE}_z , *i.e.*, $\mathbf{SE}_z = \{y + z : y \in \mathbf{SE}\}$. Therefore, the *flat grey-level image dilated* $\mathbf{I}(x)$ with respect to the structuring element \mathbf{SE} is

$$\begin{aligned} \delta_{\mathbf{SE}}(\mathbf{I})(x) &= \sup_{h \in \mathbf{SE}} (\mathbf{I}(x - h)) \\ &= \{\mathbf{I}(y) \mid \mathbf{I}(y) = \sup[\mathbf{I}(z)], z \in \mathbf{SE}_x\} \end{aligned} \quad (2.4)$$

and respectively the *flat grey-level erosion* of a image

$$\begin{aligned} \varepsilon_{\mathbf{SE}}(\mathbf{I})(x) &= \inf_{h \in \mathbf{SE}} (\mathbf{I}(x + h)) \\ &= \{\mathbf{I}(y) \mid \mathbf{I}(y) = \inf[\mathbf{I}(z)], z \in \check{\mathbf{S}}\mathbf{E}_x\}, \end{aligned} \quad (2.5)$$

where $\check{\mathbf{S}}\mathbf{E}$ is the *reflection* of \mathbf{SE} with respect to the origin, *i.e.*, $\check{\mathbf{S}}\mathbf{E} = \{-\mathbf{b} \mid \mathbf{b} \in \mathbf{SE}\}$. Dilation and erosion are dual operators with respect to the image complement (negative), *i.e.*,

$$\delta_{\mathbf{SE}}(\mathbf{I}) = (\varepsilon_{\check{\mathbf{S}}\mathbf{E}}(\mathbf{I}^c))^c$$

where $\mathbf{I}^c(x) = -\mathbf{I}(x)$. Dilation and erosion are increasing operators: if $\mathbf{I}(x) \leq \mathbf{J}(x)$, $\forall x \in \mathbf{E}$, then $\delta_{\mathbf{SE}}(\mathbf{I}) \leq \delta_{\mathbf{SE}}(\mathbf{J})$ and $\varepsilon_{\mathbf{SE}}(\mathbf{I}) \leq \varepsilon_{\mathbf{SE}}(\mathbf{J})$, $\forall x \in \mathbf{E}$. Dilation (erosion) is an extensive (anti-extensive) operator, *i.e.*, $\mathbf{I} \leq \delta_{\mathbf{SE}}(\mathbf{I})$ ($\varepsilon_{\mathbf{SE}}(\mathbf{I}) \leq \mathbf{I}$), $\forall x \in \mathbf{E}$, when the structuring element \mathbf{SE} contains the origin.

Dilation and erosion are also negative operators in the following sense:

$$(\delta_{\mathbf{SE}}(\mathbf{I}))^c = \varepsilon_{\mathbf{SE}}(\mathbf{I}^c)$$

This means that dilation of the image foreground has the same effect as erosion of the background (with the reflected structuring element). However, the heart of the construction of the morphological operators is the duality in the adjunction sense, namely

$$\delta_{\mathbf{SE}}(\mathbf{J}) \leq \mathbf{I} \iff \mathbf{J} \leq \varepsilon_{\mathbf{SE}}(\mathbf{I}) \quad (2.6)$$

for every pair of images $\mathbf{I}, \mathbf{J} \in \mathcal{F}(\mathbf{E}, \mathcal{T})$. This is called the *adjunction relation* forms the basis of the extension of mathematical morphology to complete lattice Serra (1982), Heijmans (1995). An important point is that given an adjunction $(\varepsilon_{\mathbf{SE}}(\cdot), \delta_{\mathbf{SE}}(\cdot))$, then $\varepsilon_{\mathbf{SE}}(\cdot)$ is an erosion (it distributes over infimum) and $\delta_{\mathbf{SE}}(\cdot)$ is a dilation (it distributes over supremum). Additionally, the two following properties also hold:

- Distributivity:

$$\begin{aligned} \delta_{\mathbf{SE}}(\mathbf{I} \vee \mathbf{J})(x) &= \delta_{\mathbf{SE}}(\mathbf{J})(x) \vee \delta_{\mathbf{SE}}(\mathbf{I})(x) \\ \varepsilon_{\mathbf{SE}}(\mathbf{I} \wedge \mathbf{J})(x) &= \varepsilon_{\mathbf{SE}}(\mathbf{I})(x) \wedge \varepsilon_{\mathbf{SE}}(\mathbf{J})(x) \end{aligned}$$

- Associativity:

$$\delta_{\mathbf{SE}_1 \oplus \mathbf{SE}_2}(\delta_{\mathbf{SE}_3}(\mathbf{I}))(x) = \delta_{\mathbf{SE}_1}(\delta_{\mathbf{SE}_2 \oplus \mathbf{SE}_3}(\mathbf{I}))(x)$$

where $\mathbf{SE}_1 \oplus \mathbf{SE}_2$ is the Minkowski addition of the structuring elements. Fig. 2.1 shows the effect of these operators for a real high-resolution remote sensing image. These two elementary operators can be viewed as building blocks of more advanced morphological operators.

2.3.2 Opening and closing

The two elementary operations of grey-level erosion and dilation can be composed together to yield a new set of grey-level operators having desirable feature extractor properties which are the opening and the closing. More precisely, starting from the adjunction pair $\{\varepsilon_b(\cdot), \delta_b(\cdot)\}$, the *opening and closing of a grey-level image* \mathbf{I} according to the structuring function b are the mappings $\mathcal{F}(\mathbf{E}, \mathcal{T}) \rightarrow \mathcal{F}(\mathbf{E}, \mathcal{T})$ given respectively by

$$\gamma_b(\mathbf{I})(x) = \delta_b(\varepsilon_b(\mathbf{I}))(x), \quad (2.7)$$

and

$$\varphi_b(\mathbf{I})(x) = \varepsilon_b(\delta_b(\mathbf{I}))(x). \quad (2.8)$$

The flat counterparts are obtained by using the flat erosion and flat dilation by the structuring element \mathbf{SE} . The opening and closing are dual operators, i.e.,

$$\gamma_{\mathbf{SE}}(\mathbf{I}) = (\varphi_{\mathbf{SE}}(\mathbf{I}^c))^c$$

Opening (closing) removes positive (negative) structures according to the predefined size and shape criterion of the structuring element \mathbf{SE} : they smooth in a nonlinear way the image.

The pair $(\gamma_{\mathbf{SE}}(\cdot), \varphi_{\mathbf{SE}}(\cdot))$ is called adjunction opening and adjunction closing. Let $\mathbf{I}, \mathbf{J} \in \mathcal{F}(\mathbf{E}, \mathcal{T})$ be two grey-level images. The opening $\gamma_{\mathbf{SE}}(\cdot)$ and closing $\varphi_{\mathbf{SE}}(\cdot)$ verify the following properties.

- Increasingness (ordering preservation): $\gamma_{\mathbf{SE}}(\cdot)$ and $\varphi_{\mathbf{SE}}(\cdot)$ are increasing as products of increasing operators, i.e., $\mathbf{I}(x) \leq \mathbf{J}(x) \Rightarrow \gamma_{\mathbf{SE}}(\mathbf{I})(x) \leq \gamma_{\mathbf{SE}}(\mathbf{J})(x)$, $\varphi_{\mathbf{SE}}(\mathbf{I})(x) \leq \varphi_{\mathbf{SE}}(\mathbf{J})(x)$.
- Idempotence (invariance with respect to the transformation itself): $\gamma_{\mathbf{SE}}(\cdot)$ and $\varphi_{\mathbf{SE}}(\cdot)$ are idempotent, i.e., $\gamma_{\mathbf{SE}}(\gamma_{\mathbf{SE}}(\mathbf{I})) = \gamma_{\mathbf{SE}}(\mathbf{I})$, $\varphi_{\mathbf{SE}}(\varphi_{\mathbf{SE}}(\mathbf{I})) = \varphi_{\mathbf{SE}}(\mathbf{I})$.
- Extensivity and anti-extensivity: $\gamma_{\mathbf{SE}}(\cdot)$ is anti-extensive, i.e., $\gamma_{\mathbf{SE}}(\mathbf{I})(x) \leq \mathbf{I}(x)$; and $\varphi_{\mathbf{SE}}(\cdot)$ is extensive, i.e., $\mathbf{I}(x) \leq \varphi_{\mathbf{SE}}(\mathbf{I})(x)$.

Examples of opening/closing in a high-resolution remote sensing image are illustrated in Fig. 2.2. The other morphological operators are obtained as products of openings/closings or by residues between erosion/dilation and opening/closing.

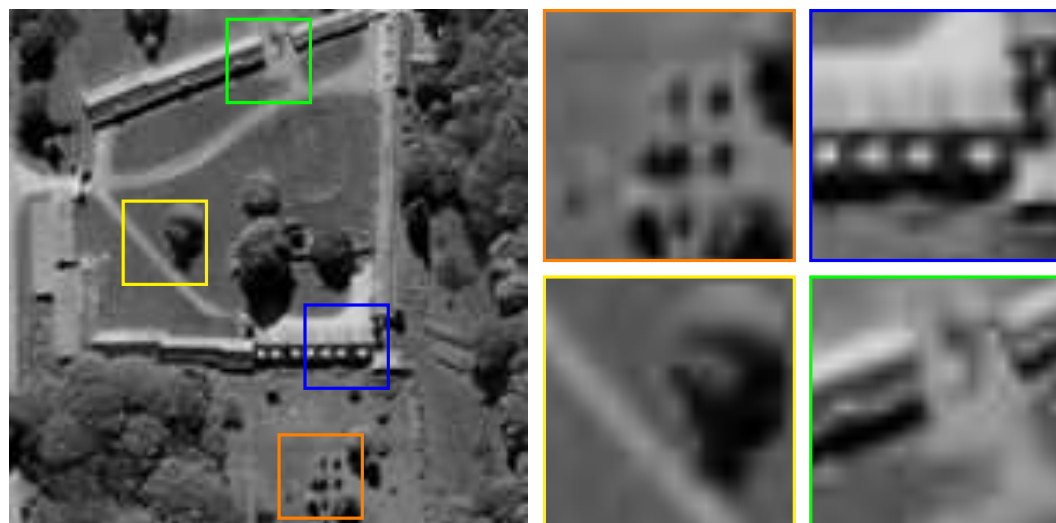
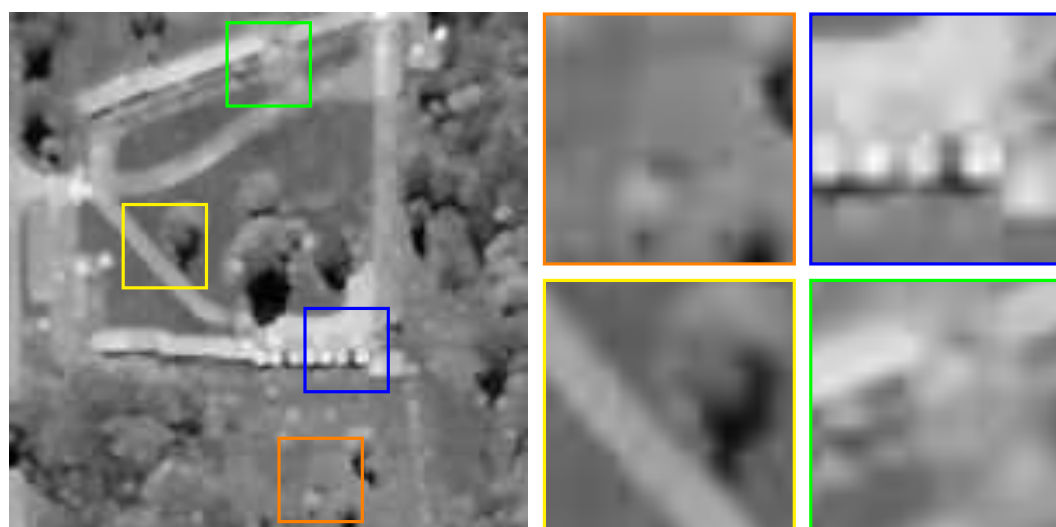
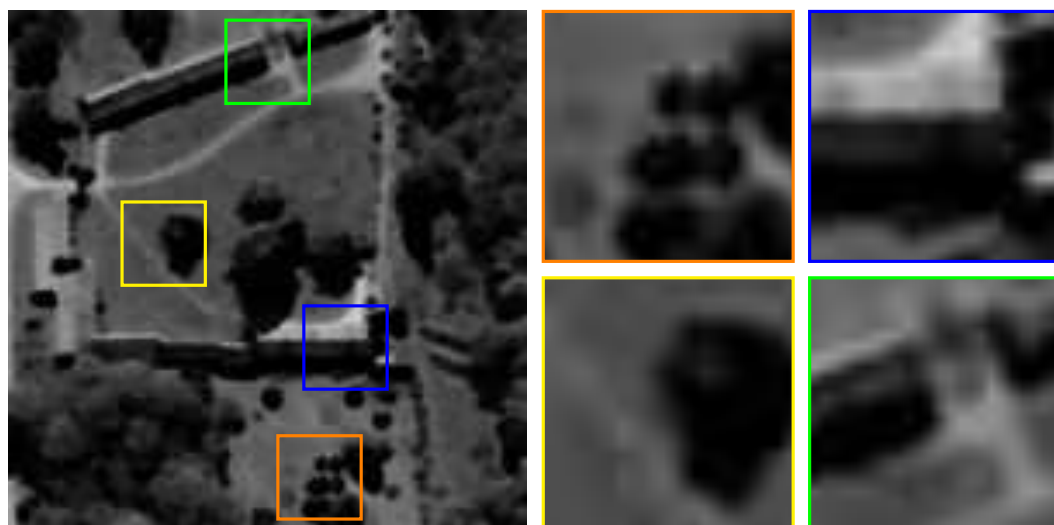
(a) \mathbf{I} (b) $\delta_{SE}(\mathbf{I})$ (c) $\varepsilon_{SE}(\mathbf{I})$

Figure 2.1: Basic morphological transformations: dilation (b) and erosion (c). The structuring element SE is a disk of diameter three pixels.

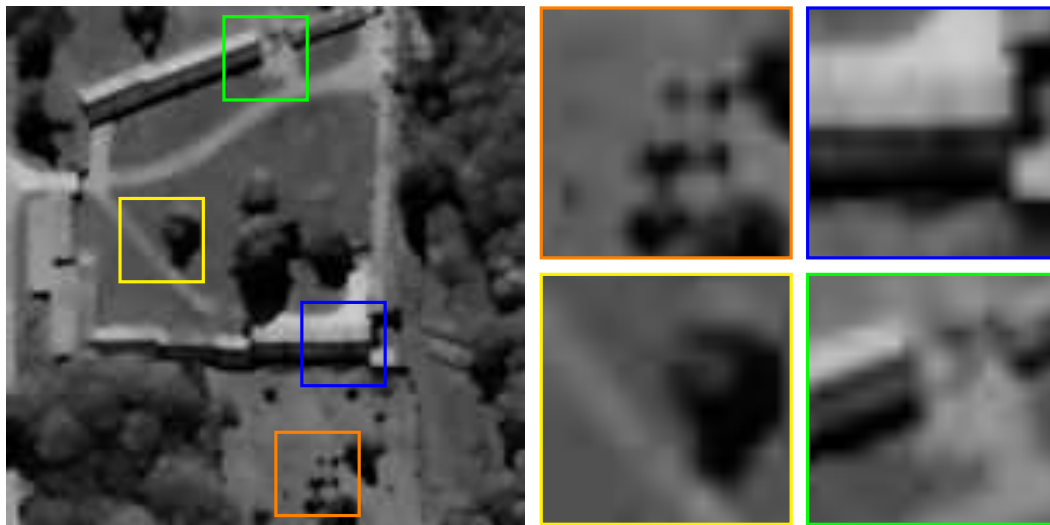
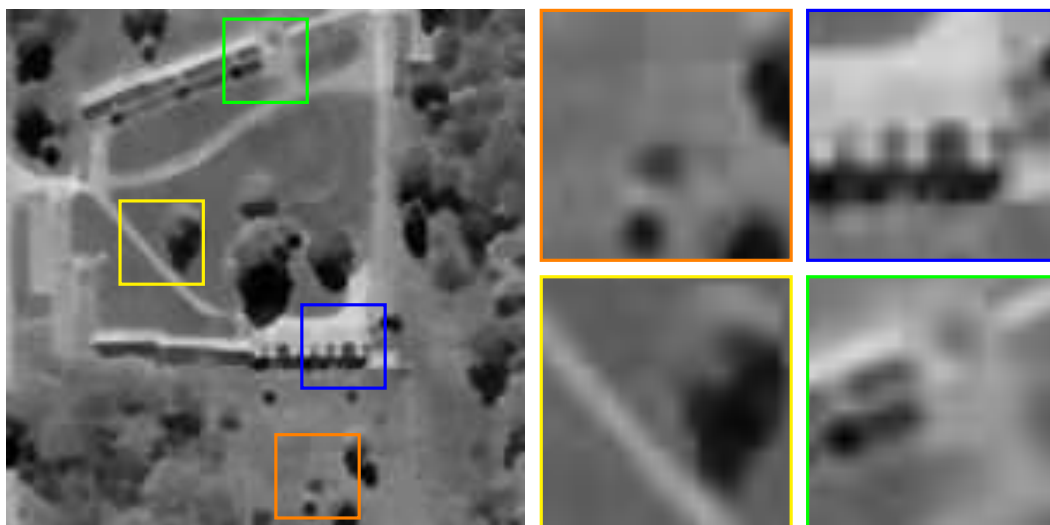
(a) $\gamma_{SE}(\mathbf{I})$ (b) $\varphi_{SE}(\mathbf{I})$

Figure 2.2: Opening (a) and closing (b) transformations. The structuring element SE is a disk of diameter 3 pixels.

2.3.3 Contrast mappings

The contrast mapping is a particular operator from a more general class of transformations called toggle mappings [Serra \(1989b\)](#). A contrast mapping is defined, on the one hand, by two primitives Φ_1 and Φ_2 applied to the initial function, and on the other hand, by a decision rule which makes, at each point x the output of this mapping toggles between the value of Φ_1 at x and the value of Φ_2 , according to which is closer to the input value of the function at x .

$$\tau_{(\Phi_1, \Phi_2)}(\mathbf{I})(x) = \begin{cases} \Phi_2(\mathbf{I})(x) & \text{if } \|\mathbf{I}(x) - \Phi_2(\mathbf{I})(x)\| \leq \|\mathbf{I}(x) - \Phi_1(\mathbf{I})(x)\| \\ \Phi_1(\mathbf{I})(x) & \text{if } \|\mathbf{I}(x) - \Phi_2(\mathbf{I})(x)\| > \|\mathbf{I}(x) - \Phi_1(\mathbf{I})(x)\| \end{cases} \quad (2.9)$$

If the pair of primitives $(\Phi_1(\mathbf{I}), \Phi_2(\mathbf{I}))$ are an erosion $\varepsilon_{\text{SE}}(\mathbf{I})$ and the adjunction dilation $\delta_{\text{SE}}(\mathbf{I})$, the *toggle mapping* for an image \mathbf{I} is given by [Kramer and Bruckner \(1975\)](#):

$$\tau_{(\varepsilon_{\text{SE}}(\cdot), \delta_{\text{SE}}(\cdot))} := \tau(\mathbf{I})(x) = \begin{cases} \delta_{\text{SE}}(\mathbf{I})(x) & \text{if } \|\mathbf{I}(x) - \delta_{\text{SE}}(\mathbf{I})(x)\| \leq \|\mathbf{I}(x) - \varepsilon_{\text{SE}}(\mathbf{I})(x)\| \\ \varepsilon_{\text{SE}}(\mathbf{I})(x) & \text{if } \|\mathbf{I}(x) - \delta_{\text{SE}}(\mathbf{I})(x)\| > \|\mathbf{I}(x) - \varepsilon_{\text{SE}}(\mathbf{I})(x)\| \end{cases} \quad (2.10)$$

where $\delta_{\text{SE}}(\mathbf{I})$ and $\varepsilon_{\text{SE}}(\mathbf{I})$ are dilation and erosion transformations and the norm are differences in grey scale values. This morphological transformation enhances the local contrast of \mathbf{I} by sharpening its edges. It is usually applied more than once, being iterated, and the iterations converge to a limit reached after a finite number of iterations, because we only consider the case of images with finite support. An example is shown in [Fig. 2.3](#). Another interesting contrast mapping is defined by changing the previous expression for the pair of opening $\gamma_{\text{SE}}(\mathbf{I})$ and its dual closing $\varphi_{\text{SE}}(\mathbf{I})$ [Meyer and Serra \(1989\)](#).

2.3.4 Morphological center

The opening/closing are nonlinear smoothing filters, and classically an opening followed by a closing (or a closing followed by an opening) can be used to suppress impulse noise, i.e., suppressing positive spikes via the opening and negative spikes via the closing and without blurring the contours. A more interesting operator to suppress noise is the morphological center, also known as automedian filter [Serra \(1982, 1989b\)](#). Given an opening $\gamma_{\text{SE}}(\mathbf{I})$ and the dual closing $\varphi_{\text{SE}}(\mathbf{I})$ with a small structuring element (typically a discrete disk of diameter equal to the “noise scale”), the *morphological center* associated to these primitives for an image \mathbf{I} is given by the algorithm:

$$\zeta(\mathbf{I}) = [\mathbf{I} \vee (\gamma_{\text{SE}}(\varphi_{\text{SE}}(\gamma_{\text{SE}}(\mathbf{I}))) \wedge \varphi_{\text{SE}}(\gamma_{\text{SE}}(\varphi_{\text{SE}}(\mathbf{I}))))] \wedge (\gamma_{\text{SE}}(\varphi_{\text{SE}}(\gamma_{\text{SE}}(\mathbf{I}))) \vee \varphi_{\text{SE}}(\gamma_{\text{SE}}(\varphi_{\text{SE}}(\mathbf{I}))). \quad (2.11)$$

This is an increasing and autodual operator, not idempotent, but the iteration of $\zeta(\cdot)$ presents a point monotonicity and converges to the idempotence, i.e. $\widehat{\zeta(\mathbf{I})} = [\zeta(\mathbf{I})]^i$, such that $[\zeta(\cdot)]^i = [\zeta(\cdot)]^{i+1}$. An example of this filter is illustrated in [Fig. 2.3](#).

2.3.5 Geodesic reconstruction, derived operators, leveling

The *geodesic dilation* is based on restricting the iterative unitary dilation of an image $\mathbf{M} \in \mathcal{F}(\mathbf{E}, \mathcal{T})$ called *function marker* by an isotropic structuring element associated with the smallest connectivity (a disk of diameter three for *4-connectivity* or a square of side three for *8-connectivity*, see [Fig. 1.7](#)), denoted by \mathbf{B} , to a function reference \mathbf{I} [Vincent \(1993\)](#), i.e.,

$$\delta_{\mathbf{B}}^i(\mathbf{I}, \mathbf{M}) = \delta_{\mathbf{B}}^1(\delta_{\mathbf{B}}^{i-1}(\mathbf{I}, \mathbf{M})), \quad (2.12)$$

where the unitary dilation controlled by \mathbf{I} is given by $\delta_{\mathbf{B}}^1(\mathbf{I}, \mathbf{M}) = \delta_{\mathbf{B}}(\mathbf{M}) \wedge \mathbf{I}$. The *reconstruction* by dilation is then defined by

$$\delta_{\mathbf{B}}^\infty(\mathbf{I}, \mathbf{M}) = \delta_{\mathbf{B}}^i(\mathbf{I}, \mathbf{M}), \quad (2.13)$$

such that $\delta_{\mathbf{B}}^i(\mathbf{I}, \mathbf{M}) = \delta_{\mathbf{B}}^{i+1}(\mathbf{I}, \mathbf{M})$ (idempotence).

Equivalently, *geodesic erosion* is defined as follows

$$\varepsilon_{\mathbf{B}}^i(\mathbf{I}, \mathbf{M}) = \varepsilon_{\mathbf{B}}^1(\varepsilon_{\mathbf{B}}^{i+1}(\mathbf{I}, \mathbf{M})), \quad (2.14)$$

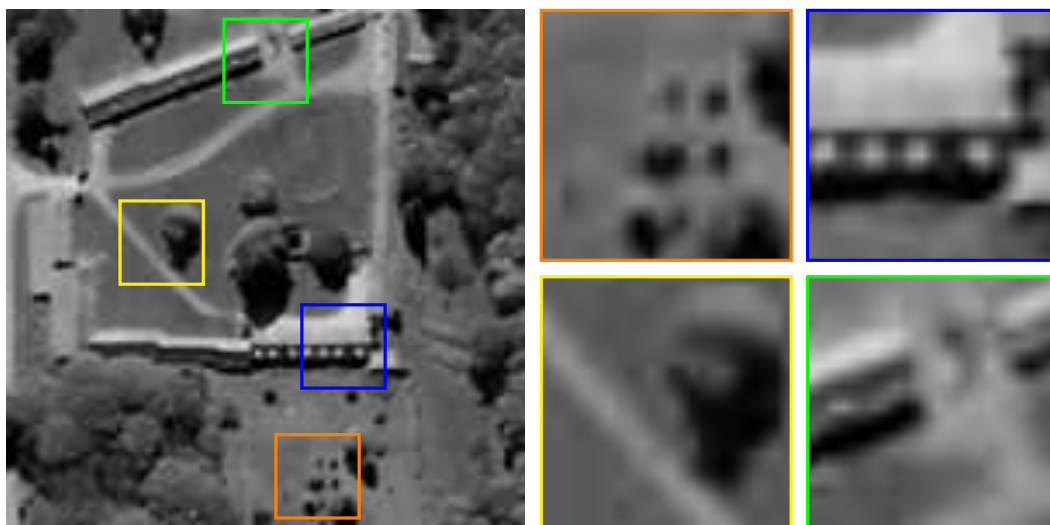
(a) $\tau(\mathbf{I})$ (b) $\zeta(\mathbf{I})$

Figure 2.3: Results of toggle mapping and morphological center. In both cases, the structuring element SE is a digital disk of diameter three pixels.

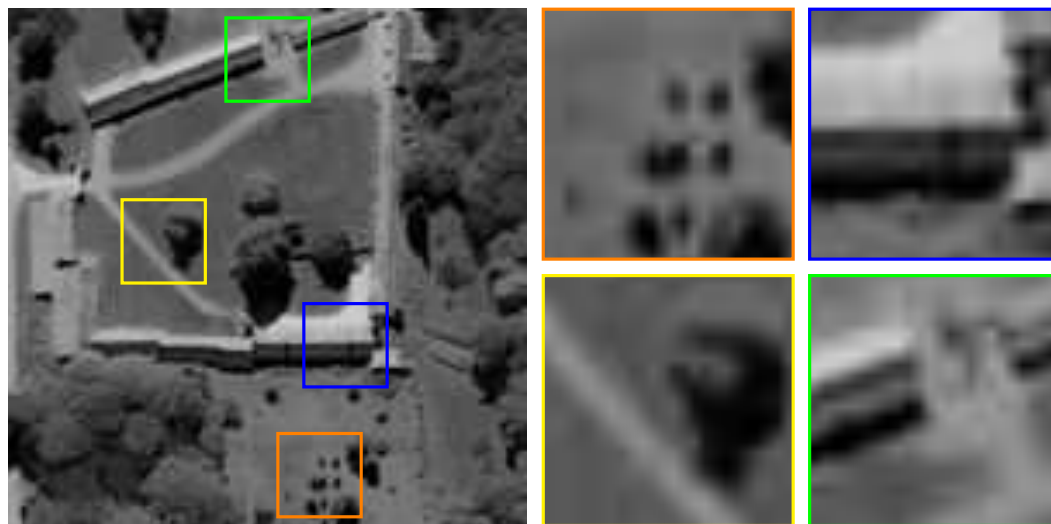
(a) $\gamma_{SE}^{REC}(\mathbf{I})$ (b) $\phi_{SE}^{REC}(\mathbf{I})$

Figure 2.4: Opening (a) and closing (b) by reconstructions, where the markers are respectively the opening and closing adjunction of Fig. 2.2.

where the unitary dilation controlled by \mathbf{I} is given by $\varepsilon_{\mathbf{B}}^1(\mathbf{I}, \mathbf{M}) = \varepsilon_{\mathbf{B}}(\mathbf{M}) \vee \mathbf{I}$. The *reconstruction* by erosion is then defined by

$$\varepsilon_{\mathbf{B}}^{\infty}(\mathbf{I}, \mathbf{M}) = \varepsilon_{\mathbf{B}}^i(\mathbf{I}, \mathbf{M}), \quad (2.15)$$

such that $\varepsilon_{\mathbf{B}}^i(\mathbf{I}, \mathbf{M}) = \varepsilon_{\mathbf{B}}^{i+1}(\mathbf{I}, \mathbf{M})$ (idempotence). The important issue at this point is how to select an adequate image marker \mathbf{M} .

Opening/Closing by reconstruction

The opening by reconstruction is a geodesic reconstruction by using an opening as marker, i.e.,

$$\gamma_{\mathbf{SE}}^{\text{REC}}(\mathbf{I}) := \gamma_{\mathbf{SE}}^{\text{REC}}(\mathbf{I}, \gamma_{\mathbf{SE}}(\mathbf{I})) = \delta_{\mathbf{B}}^{\infty}(\mathbf{I}, \gamma_{\mathbf{SE}}(\mathbf{I})) \quad (2.16)$$

$\gamma_{\mathbf{SE}}(\mathbf{I})$ (from an erosion/dilation) modifies the contours, the opening by reconstruction $\gamma_{\mathbf{SE}}^{\text{REC}}(\mathbf{I})$ is aimed at efficiently and precisely reconstructing the contours of the objects which have not been totally removed by the marker filtering process. Accordingly the closing by reconstruction $\varphi_{\mathbf{SE}}^{\text{REC}}(\mathbf{I})$ is a erosion by reconstruction by using a closing as marker. Comparison of both morphological transformations is shown in Fig. 2.4.

Leveling

In a similar way, the *leveling* $\Lambda(\mathbf{I}, \mathbf{M})$ of a reference function \mathbf{I} and a marker function \mathbf{M} is a symmetric geodesic operator computed by means of an iterative algorithm with geodesic dilations and geodesic erosions until idempotence Meyer (1998), i.e.

$$\Lambda^i(\mathbf{I}, \mathbf{M}) = [\mathbf{I} \wedge \delta_{\mathbf{B}}^i(\mathbf{M})] \vee \varepsilon_{\mathbf{B}}^i(\mathbf{M}), \quad (2.17)$$

until $\Lambda^i(\mathbf{I}, \mathbf{M}) = \Lambda^{i+1}(\mathbf{I}, \mathbf{M})$. The leveling simplifies the image, removing the objects and textures smaller than the structuring element and preserving the contours of the remaining objects. Moreover, it acts simultaneously on the “bright” and “dark” objects. The usefulness of this transformation is related to the role of the marker image \mathbf{M} . Different types of markers have been considered in the literature, for instance, Alternate Sequential Filter, Isotropic Gaussian Function or Anisotropy diffusion filtering. Figs. 2.5 and 2.6 illustrate two different markers and the correspondent leveling operator.

2.3.6 Residue-based operators

From definition of basic morphological operators is easy to define the *morphological gradient*

$$\Delta_{\mathbf{SE}}(\mathbf{I}) := \delta_{\mathbf{SE}}(\mathbf{I}) - \varepsilon_{\mathbf{SE}}(\mathbf{I}) \quad (2.18)$$

The structuring element \mathbf{SE} for the gradient is generally the unitary ball \mathbf{B} . This function gives the contours of the image, attributing more importance to the transitions between regions close/far to the background/foreground. Similarly, the *positive(white) top-hat transformation* is the residue of an opening, i.e.,

$$\rho_{\mathbf{SE}}^+(\mathbf{I}) = \mathbf{I} - \gamma_{\mathbf{SE}}(\mathbf{I}). \quad (2.19)$$

Dually, *negative(black) top-hat transformation* is given by

$$\rho_{\mathbf{SE}}^-(\mathbf{I}) = \varphi_{\mathbf{SE}}(\mathbf{I}) - \mathbf{I}. \quad (2.20)$$

The top-hat transformation yields grey level images and is used to extract contrasted components. Moreover, top-hats remove the slow trends, and thus enhancing the contrast of objects smaller than the structuring element \mathbf{SE} used for the opening/closing.

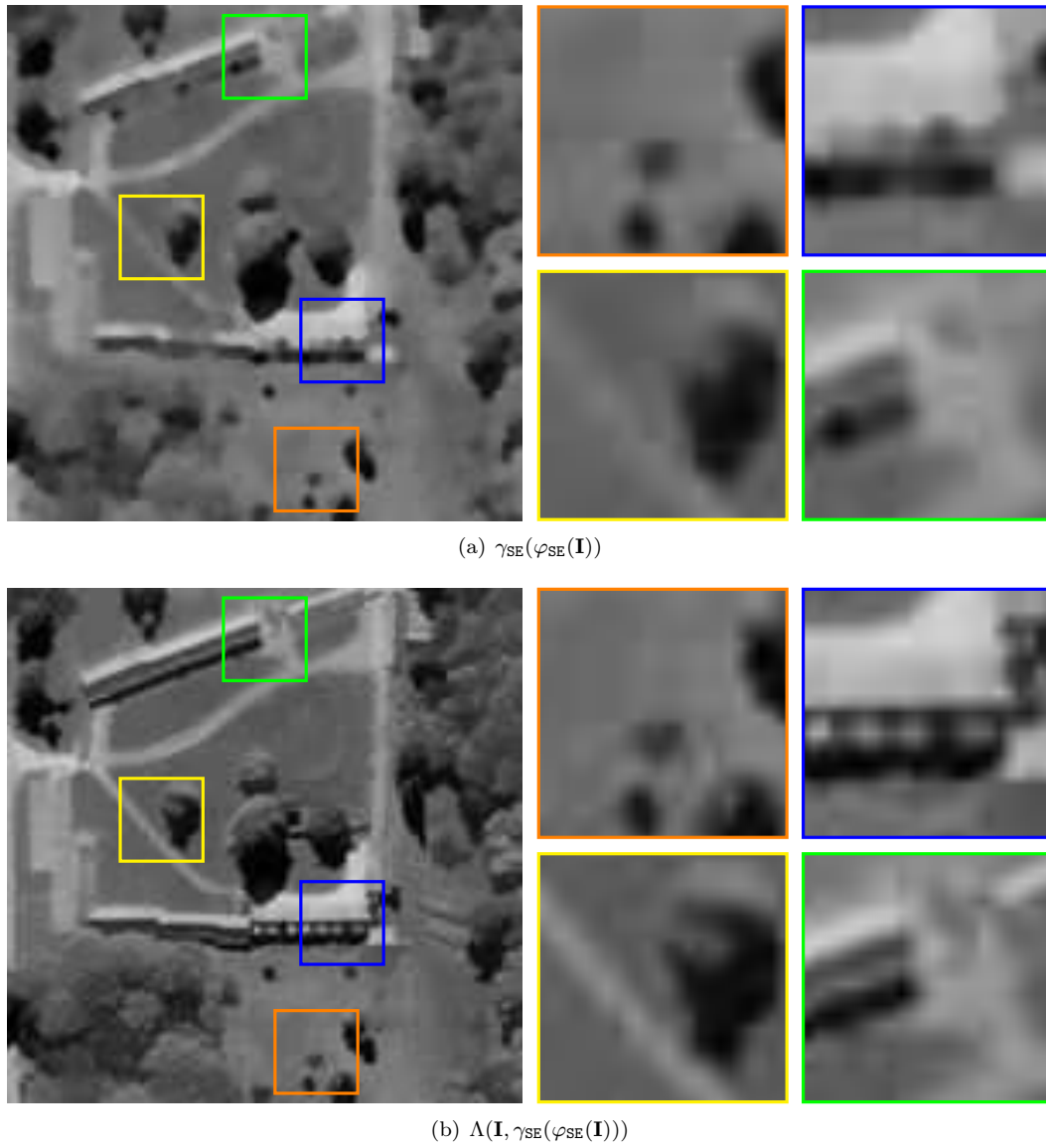


Figure 2.5: Leveling transformation (b) with a morphological marker (a).

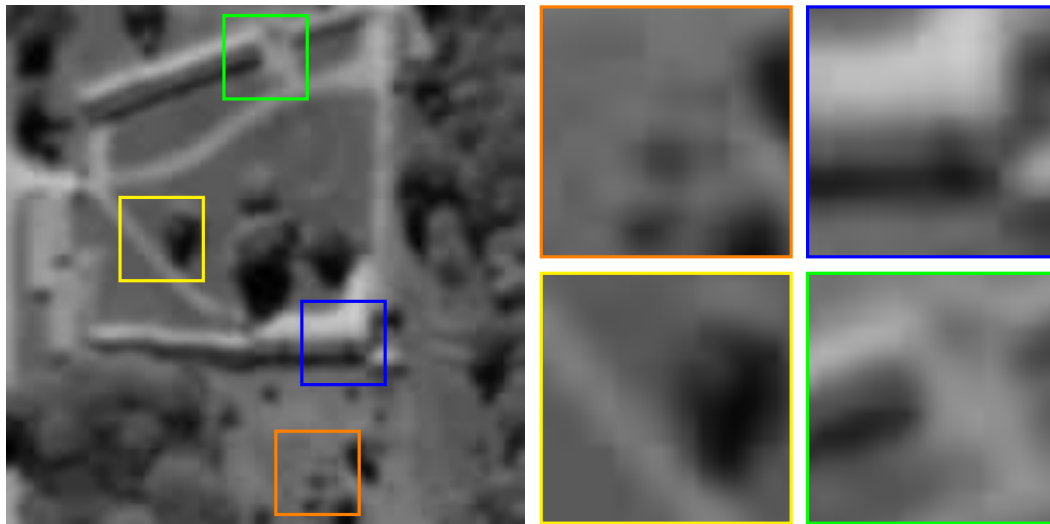
(a) $\sigma * \mathbf{I}$ (b) $\Lambda(\mathbf{I}, \sigma * \mathbf{I})$

Figure 2.6: Leveling transformation (b) with a marker given by a Gaussian Filter (a).

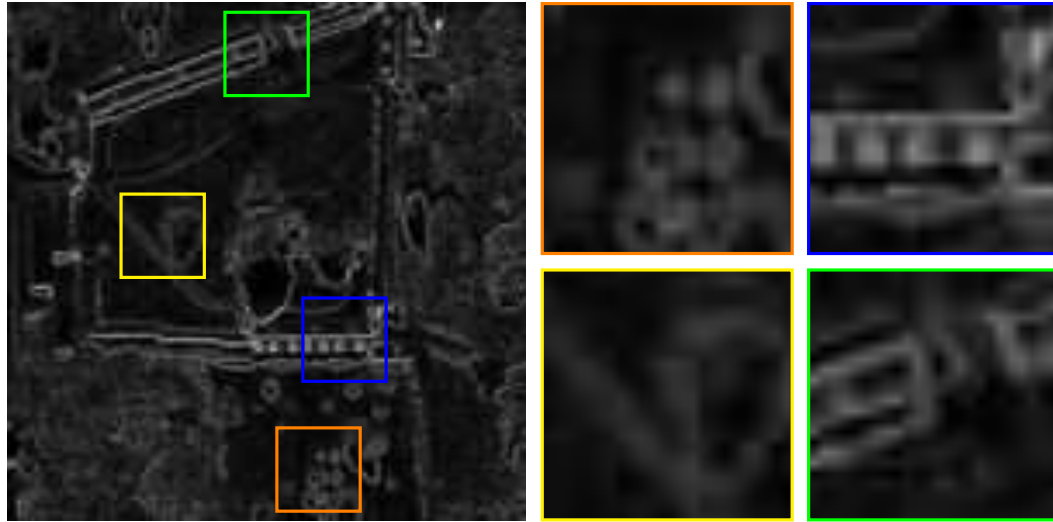
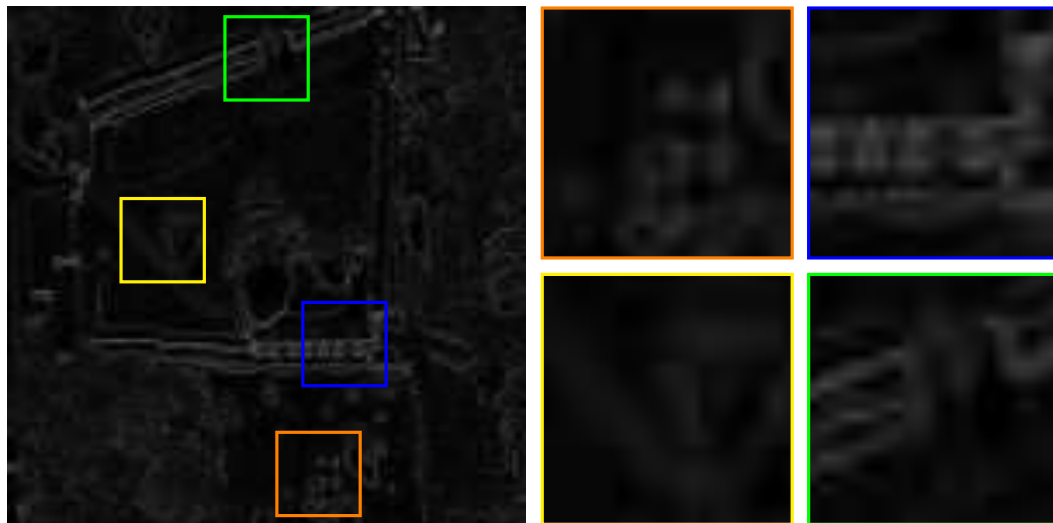
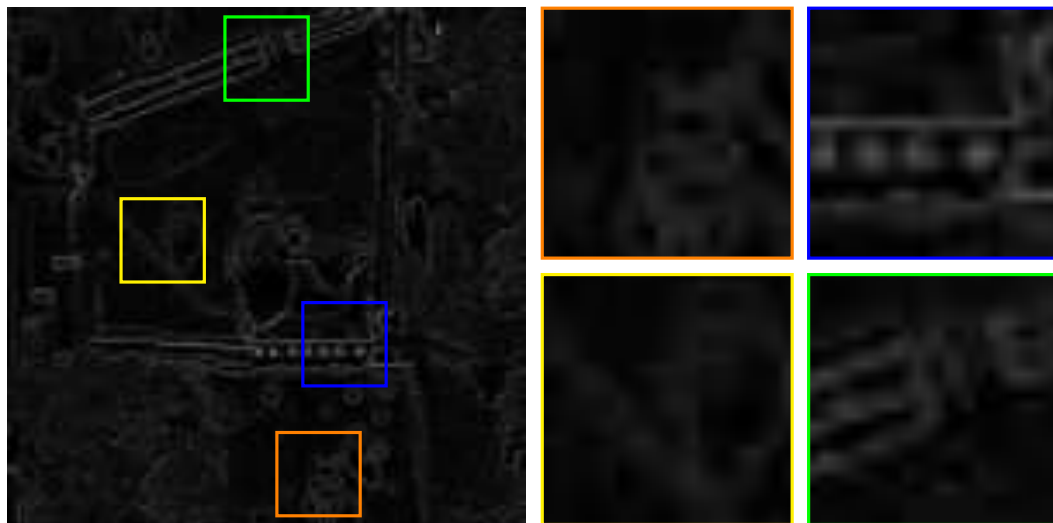
(a) $\Delta_{SE}(\mathbf{I})$ (b) $\Delta_{SE}^{\delta}(\mathbf{I})$ (c) $\Delta_{SE}^{\varepsilon}(\mathbf{I})$

Figure 2.7: Morphological gradients: (a) symmetric gradient, (b) gradient by dilation ($\Delta_{SE}^{\delta}(\mathbf{I}) = \delta_{SE}(\mathbf{I}) - \mathbf{I}$) and (c) gradient by erosion ($\Delta_{SE}^{\varepsilon}(\mathbf{I}) = \mathbf{I} - \varepsilon_{SE}(\mathbf{I})$).

2.4 Morphological Segmentation

For grey scale images, the watershed transform, originally proposed by [Lantuéjoul \(1978\)](#) and later improved by [Beucher and Lantuejoul \(1979\)](#), is a region based image segmentation [Beucher and Meyer \(1993\)](#). Works on watersheds began over a hundred years ago when Cayley and Maxwell ([Cayley \(1859\)](#), [Maxwell \(1870\)](#)), described how smooth surfaces could be decomposed into hills and dales by studying the critical points and slope lines of a surface. The intuitive idea underlying this method comes from geography: it is that of a landscape or topographic relief which is flooded by water, watersheds being the divide lines of the domains of attraction of rain falling over the region. The watershed algorithm [Vincent and Soille \(1991\)](#) is a flooding process: water, starting from specified markers, "floods" the image, from the smallest to highest grey values. When two catchment basins meet, a dam is created, called "watershed plane". This presentation is called the "flooding paradigm". However, there exist many possible way to defining a watershed [Najman and Schmitt \(1994\)](#), [Roerdink and Meijster \(2000\)](#), [Bertrand \(2005\)](#), [Cousty et al. \(2009\)](#), [Meyer \(2012\)](#). Additionally, random marker process have been introduced in [Angulo and Jeulin \(2007\)](#) to yield a stochastic watershed that can be interpreted as to give an edge probability for a given image. Recently, links between watershed algorithm as a Maximum a Posteriori estimation of a Markov Random Field have been introduced in [Couprie et al. \(2011\)](#).

In this document, we denote the watershed transformation of an image \mathbf{I} , by using a set the markers \mathbf{M} (seeds in the flooding process) as $\text{WS}(\mathbf{I}, \mathbf{M})$. Watershed transformation is typically applied on the gradient magnitude image, i.e., the morphological gradient. A simple example of the watershed with two markers is illustrated in [Fig. 2.8](#). We can observe that watershed is relatively sensitive to noise. Over-segmentation is a well-known difficulty with this approach, which has led to a number of approaches for merging watershed regions to obtain larger regions corresponding to objects of interest [Beucher and Meyer \(1993\)](#), [Gauch \(1999\)](#), [Cousty et al. \(2010\)](#), [Najman \(2011\)](#). A simple approach to deal with the over-segmentation problem consists in determine markers for each region of interest, for instance, the dynamics or contrast based transform applied to the minima of the gradient image. The parameter t in the contrast based transform, is normalized to $(0, 1)$ with respect to the minimum and maximum of the original image. We denote this approach as $\text{WS}(\mathbf{I}, t)$ for some parameter $t \in (0, 1)$. Note that $\text{WS}(\mathbf{I}, 0) = \text{WS}(\mathbf{I})$. Watershed regions associated with different value of t are illustrated for the same original image (see [Fig. 2.9](#)). From this example, we observe that different levels of segmentation with respect to t constitute a hierarchical (pyramid) of regions. Watershed transform have been applied in multidimensional remote sensing application, where the important selection of an adequate multivariate gradient is still an open problem [Noyel et al. \(2007\)](#), [Tarabalka et al. \(2010b\)](#).

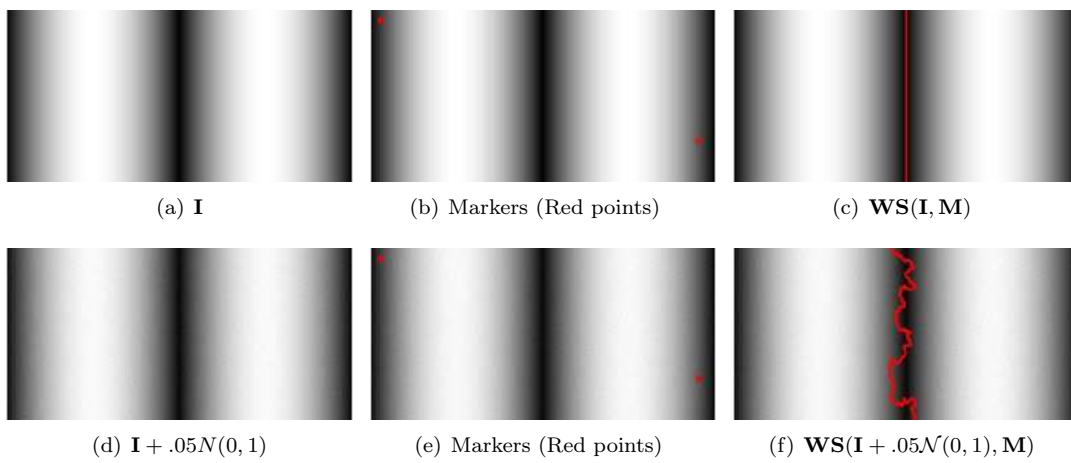
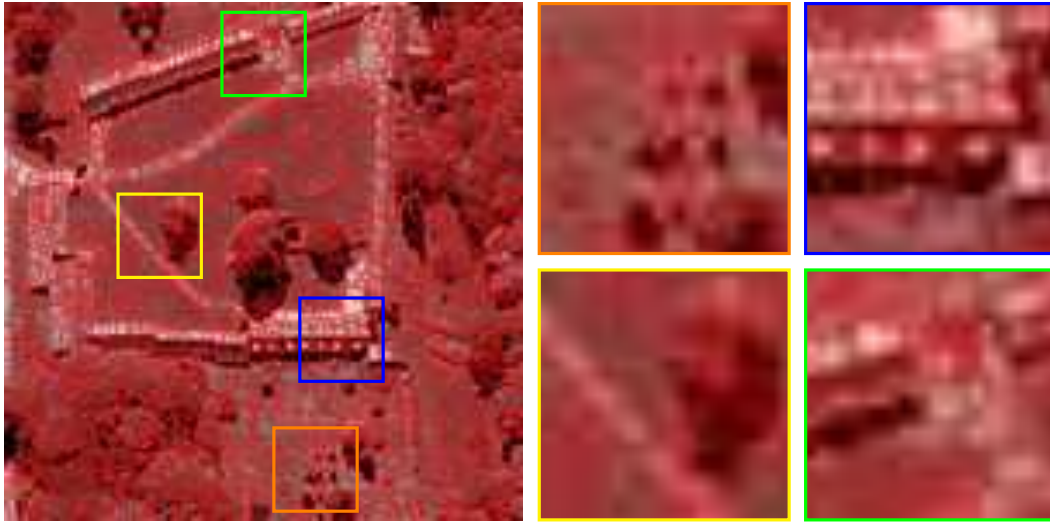
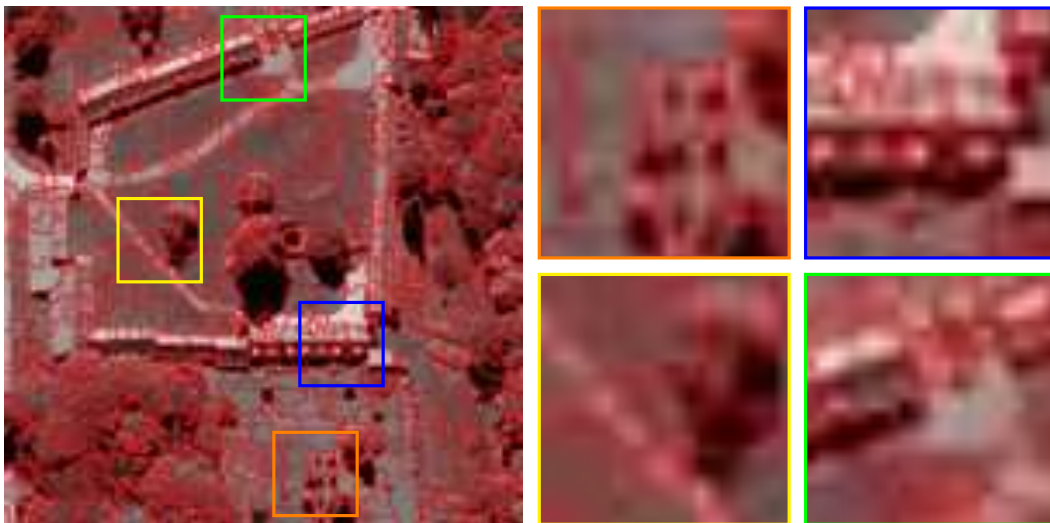
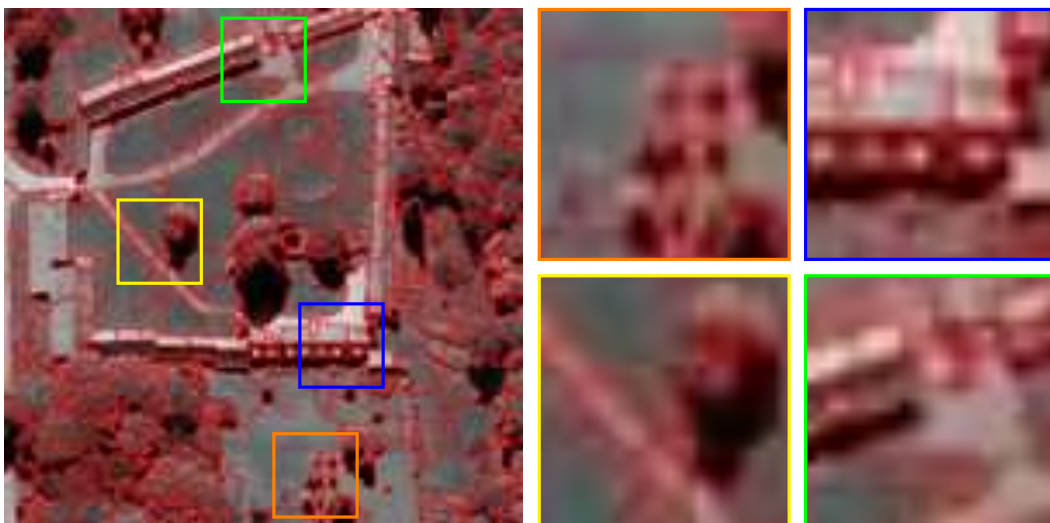


Figure 2.8: Watershed transform for a given image \mathbf{I} , with markers point \mathbf{M} are the red points in (b) and (e). (Watershed Transform is applied in $\Delta_{SE}(\mathbf{I})$).

(a) $WS(I, .01)$ (b) $WS(I, .06)$ (c) $WS(I, .11)$

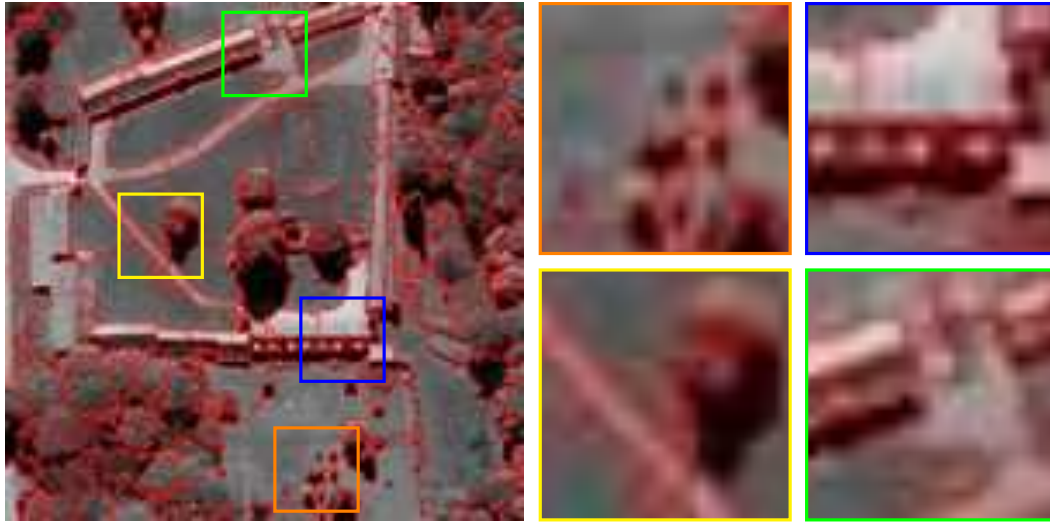
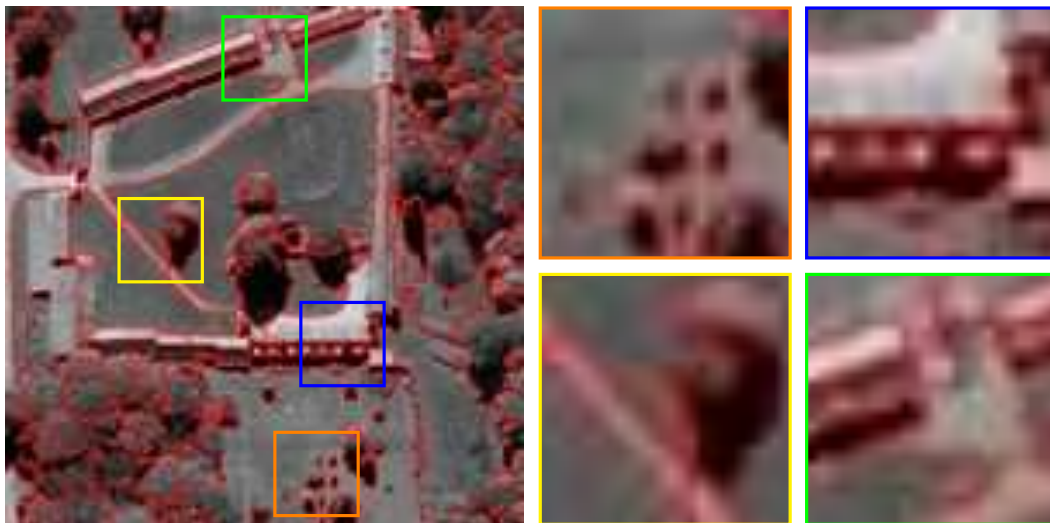
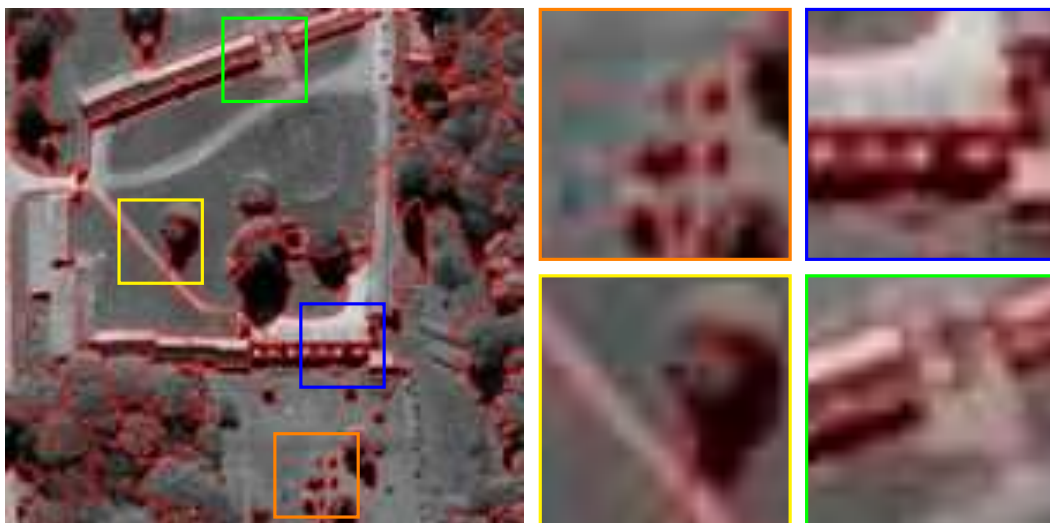
(d) $WS(I, .16)$ (e) $WS(I, .21)$ (f) $WS(I, .26)$

Figure 2.9: Contrast-driven watershed transforms with markers calculated as % of the maximum value in I .

3

Preliminary Notions

By a tranquil mind I mean nothing else than a mind well ordered. *Marcus Aurelius*

Résumé

Ce chapitre donne une présentation générale de la représentation spectrale d'une image multivariée. Pour le cas particulier de la représentation basée sur un ordre total, l'ordre-h est utilisé pour appréhender le caractère vectoriel des images multidimensionnelles. Les aspects les plus importants de la théorie des treillis liés à cette thèse sont présentés en détail.

3.1 Introduction

Digital image processing is an expanding and dynamic area with applications reaching out into our everyday life as surveillance, medicine, authentication, automated industrial quality control and many more areas. An important research topic is to design parameter-free algorithms or at least approaches where the parameter model can be interpreted in the context of the problem. However, on the one hand, a parameter-free algorithm would limit our ability to impose our prejudices, expectations, presumptions, or any a priori information on the problem setting. On the other hand, an incorrect setting in a non-parameter free approach may cause that an algorithm to fail in finding the true patterns. A useful approach to tackle this kind of problems for image processing is mathematical morphology. It consists of a set of operators that transform image according to geometric characteristics as size, shape, connectivity, etc. [Serra \(1982\)](#). In this chapter we review some results related to mathematical morphology for multivariate images, i.e., in each pixel of the image a vector information is available. We include several results of flat operator for images $\mathbf{I} : \mathbf{E} \rightarrow \mathcal{L}$, where \mathcal{L} is a lattice of values. Details about lattice formulation and mathematical morphology can be found in e.g. [Ronse \(2006\)](#) and Chapter 2 (J. Serra and C. Ronse) in [Najman and Talbot \(2010\)](#). Most morphological operators used for processing and filtering are *flat operators*. This means that they are grey-level extensions of the operators for binary images, and they can be obtained by [Serra \(1982\)](#):

1. thresholding the grey-level image for all values of the image,
2. applying the binary operator to each thresholded image set,
3. superposing the resulting set.

Flat operators have been also studied under the name of *stack filters* [Wendt et al. \(1986\)](#), *threshold decomposition filters* [Shih and Mitchell \(1989\)](#), *rank filters* [Soille \(2002\)](#) and *order-configuration filters* [Ronse \(1990a\)](#).

In the case of grey scale images, two types of lattices \mathcal{L} have been considered. First, in a “continuous” scenario the values of the image belong to a $\mathbb{R} \cup \{-\infty, \infty\}$. Second, in a “discrete” setting, the grey levels be in $[a, b] \cap \mathbb{Z}$, i.e. the set of integer values from a to b by step of one. An important issue to remark is that some properties like commutation with thresholding hold unconditionally in the discrete grey-levels, and only for upper semicontinuous operators in the case of continuous grey-levels [Ronse \(1990a\)](#). A general theory of flat morphology for real grey-levels is made in [Guichard and Morel \(2002\)](#), where it is shown in particular that the commutation with thresholding holds “almost everywhere”. In this thesis, we limit our analysis to the “discrete” setting, i.e., the \mathcal{L} is finite. In this case, if \mathcal{L} is modular, distributive, infinitely supremum or infimum distributive, or complete distributive, then the lattice of functions $\mathcal{F}(\mathbf{E}, \mathcal{L})$ will share that property. That lattice is denoted by $\mathcal{L}^{\mathbf{E}}$. $\mathcal{L}^{\mathbf{E}}$ is fundamental in mathematical morphology due to a morphological transformation (called operator) is a map $\mathcal{L}^{\mathbf{E}} \rightarrow \mathcal{L}^{\mathbf{E}}$. To make easier the presentation of the concept, we analysis the simplest case where the lattice \mathcal{L} is a chain. In this particular case, $\mathcal{L}^{\mathbf{E}}$ will be completely distributive.

3.2 Notation and representation

3.2.1 Notation

Let us make precise the terms and notation to be used in the rest of the thesis. Let \mathbf{E} be a subset of the discrete space \mathbb{Z}^2 , considered as the support space of the 2D image, and $\mathbb{F} \subseteq \mathbb{R}^d$ be a set of pixels values in dimension d , corresponding to the space of values of the multivariate image with d channels. A *vector-value image* is represented by the mapping,

$$\mathbf{I} : \begin{cases} \mathbf{E} & \rightarrow \mathbb{F} \\ x = (i, j) & \rightarrow \mathbf{x} \end{cases} \quad (3.1)$$

i.e., $\mathbf{I} \in \mathcal{F}(\mathbf{E}, \mathbb{F})$ the set of maps from a point x at the discrete spatial coordinates $(i, j) \in \mathbf{E}$ into a vector value $\mathbf{x} \in \mathbb{F} \subseteq \mathbb{R}^d$. Let us assume that the pixel x is represented by a d -dimensional vector $\mathbf{x}(i, j) = [x_1(i, j), x_2(i, j), \dots, x_d(i, j)] \in \mathbb{R}^d$, where \mathbb{R} denotes the set of real numbers in which the pixel’s spectral response $x_l(i, j)$ at sensor channels $l = 1, \dots, d$. Additionally, let the data matrix $\mathbf{X}_{\mathbf{I}}$ be an $n \times d$ matrix representing d spectral bands for each n pixels in the vector-value image \mathbf{I} . In fact, $\mathbf{X}_{\mathbf{I}}$ is a matrix, with a slight abuse of notation we denote it as \mathbf{X} to make easier the presentation. A representation of this notation is illustrated in [Fig. 1.9](#).

3.2.2 Spectral representations

In this thesis we focus on multivariate image, but to illustrate the performance of our algorithms we analyse colour and hyperspectral images. Hyperspectral images provide both spatial and spectral representations of scenes, materials, and sources of illumination. They differ from images obtained with a conventional RGB colour camera, which divides the light spectrum into broad overlapping red, green, and blue image slices that when combined seem realistic to the eye. By contrast, a hyperspectral camera effectively divides the spectrum into very many thin image slices, the actual number depending on the camera and application. To understand its structure, a hyperspectral image may be represented as an image containing two spatial dimensions (pixels) and one spectral dimension (wavelength), as illustrated in [Fig. 1.9](#). Usually, at each sample wavelength, there is an intensity (grey-level) representation of the reflectance or radiance in the scene. From a mathematical point of view, spectral information corresponds to points in a vector space of dimension d equal to the number of channels of the image. However, in the vector space, the spectral information can be represented by different mathematical structures, for instance:

- Probability density models. It is the classical assumption of the statistical modelling for a multivariate image. The classical assumption is a Multivariate Gaussian Distribution, i.e., the

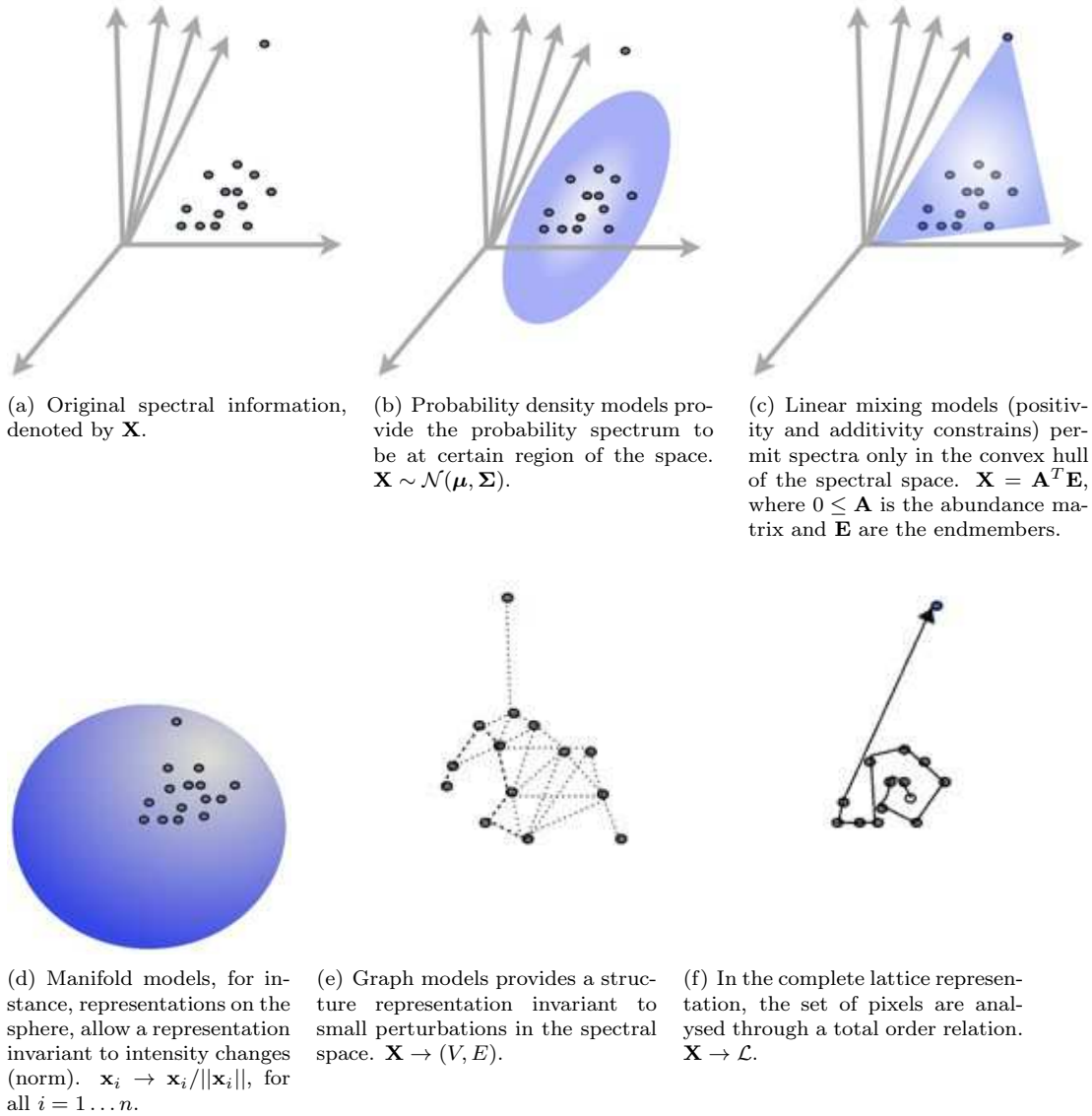


Figure 3.1: Scheme of different representation for the spectral information of a multivariate image. This thesis deals with spectral representation based on complete lattice representation as in (f).

probability of a spectrum to be at certain region of the space follows $\mathcal{N}(\boldsymbol{\mu}, \boldsymbol{\Sigma})$ for some mean vector $\boldsymbol{\mu}$ and covariance matrix $\boldsymbol{\Sigma}$.

- Linear mixing models: In such a way that each pixel in a scene may be decomposed into a sum of finite number of constituent endmembers, which represent the purest pixels in the scene. The abundances (weights in the sum) are subject to non-negativity constraint and, in some cases, sum-to-one constraint.
- Manifold models: The idea of capturing the complex geometry in the spectral representation of an image is the core of a (non-Euclidean) manifold representation [Peyré \(2009\)](#). Manifold learning methods are commonly becoming a standard to embedding data onto their new transformed spaces. For instance, on the $d - 1$ hypersphere by normalising by the norm per pixel, or in supervised projections on the sphere as in [Lunga and Ersoy \(2011\)](#). Another manifold structure in a local-graph. It is denoted by the graph $G = (E, \mathbf{W})$, where $E = \mathbf{X}$ is the set

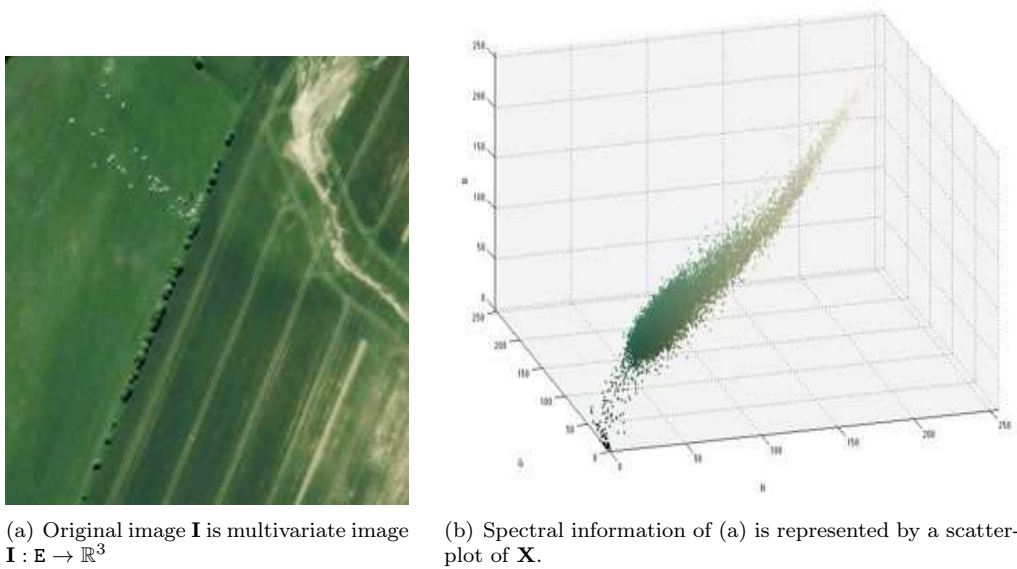


Figure 3.2: Spectral information is associated with vector spaces.

of vertices and $\mathbf{V} = [v_{ij}] \in \mathbb{R}^n \times \mathbb{R}^n$ the edge weight matrix. The graph is constructed in an unsupervised manner, with a goal of automatically determining the neighborhood structure as well as the corresponding connection weight for each datum. Examples of this type of representation are k -graph, ϵ -graph and \mathcal{L}_1 -graph [Wright et al. \(2010\)](#). Clustering, dimensionality reduction, image segmentation and analysis can be performed in this representation space.

- Complete lattice model: A total ordering definition for a cloud of points. The relation $x \leq y$ have to be know for all pair of pixels x and y of the multivariate image. That is the main goal of this thesis. Mathematical morphology requires this kind of representation to ensure the appropriate application of lattice based transformations.

[Fig. 3.1](#) shows a scheme of the different representation for the spectral information of a given multivariate image.

3.3 Mathematical morphology in multivariate images

Mathematical morphology operators in modern image analysis are a set of powerful, robust and computationally efficient tools with multiple applications including image filtering, segmentation and visualization [Najman and Talbot \(2010\)](#). It requires the definition of a complete lattice structure, i.e., an ordering among the pixels to be analysed. However, there is not difficult to see that the idea of order is entirely absent from multivariate scene, i.e., there is no unambiguous means of defining the minimum and maximum values between two vectors of more than one dimension. Accordingly, the extension of mathematical morphology to vector spaces, for instance, colour/multi/hyper/ultraspectral images, is neither direct nor trivial because the pixels in the images are vectors. We refer keen readers to [Angulo \(2007\)](#) [Aptoula and Lefèvre \(2007\)](#) for a comprehensive review of vector morphology.

3.4 Ordering in vector spaces

In his seminal paper about multivariate ordering, [Barnett \(1976\)](#) identified four families of ordering for vectors:

- The *marginal ordering* (M-ordering), is a trivial approach consisting in applying grayscale morphology techniques to each channel separately, that has been called marginal morphology in the literature [Soille \(2003\)](#). However, the marginal approach is often unacceptable in several applications because, when morphological techniques are applied independently to each image channel, analysis techniques are subject to the well-known problem of *false colours* [Serra \(2009\)](#); that is, it is very likely that new spectral constituents (not present in the original image) may be created as a result of processing the channels separately.
- To strictly preserve input vectors, the *conditional ordering* (C-ordering) approach, also known as lexicographic ordering, is frequently used. The C-ordering is based on the ordering of the components selected sequentially according to different conditions or priorities. When all the components are used, the C-ordering is a total ordering [Aptoula and Lefèvre \(2008\)](#).
- The *reduced ordering* (R-ordering) which performs the ordering of vectors in some scalar space, computed from a mapping of the vector onto a different representation where the ordering is naturally defined, typically distances or projections onto a dimensionality reduced space (using for instance the principal component analysis). For instance, Mahalanobis distance has been employed in several works on multivariate morphology including the information from a reference set [Al-Otum \(2003\)](#). Chapter 4 introduces a reduced supervised ordering has shown be useful in the analysis of high dimensional images.
- The *P-ordering*, is based on the partition of the vectors into groups, such that the groups can be distinguished with respect to rank or extremeness. Recently, approaches using combinatorial techniques and median/anti-median filters have been also used to construct ordering [Lezoray et al. \(2007\)](#), [Plaza et al. \(2004\)](#). There is however a problem of these latter approaches: the ordering is locally depending on the values of the spatial window, consequently it is not a partial ordering for the set of vectors in an image, i.e., dilation (erosion) obtained does not commute with the supremum (infimum) and the distributive property is not valid. Chapter 6 introduces a reduced supervised ordering has shown be useful in the analysis of high dimensional images

Different reported approaches are illustrated in Fig. 3.3. Figs. 3.3(a-c) presents three different schemes to order the vector space, but they are not taking into consideration the information contained in the data. These orderings share the same minimum and maximum in the induced lattice, the vectors $\mathbf{0} = \perp$ and $\mathbf{1} = \top$, i.e., the vector with the minimum(maximum) value in each marginal ordering. Another approach is to use a dimensional reduction algorithm, for example, principal component analysis (PCA) [Jolliffe \(1986\)](#) or some non-linear projections approach [Lezoray et al. \(2009\)](#). It considers the first projection to induce the ordering. The minimum and maximum induced for that ordering are a priori unknown. An example is illustrated in Fig. 3.3(d). In this case, the minimum or maximum can change including a new element in the set. In [Angulo \(2007\)](#), the ordering is based on a reference spectrum exhibiting lattice where the minimum has been fixed. However, that maximum is associated with the “farthest” vector but that does not have a real interpretation. In Chapter 4, the supervised ordering is introduced. It brings forth an interesting observation, the lattice exploits the information carried directly by the vectors in $\{F, B\}$. Figs. 3.3(e-f) show these two referenced ordering, but in advantage the supervised ordering induces a lattice with predefined minimum/maximum. The basic idea is to deduce a prediction function from training data $\{B, F\}$ to induce the ordering.

The theoretical framework of the proposed morphological operators roots in the notions of h -ordering and h -adjunction introduced in [Goutsias et al. \(1995\)](#). So let us start by a reminder of the main results from [Heijmans and Ronse \(1990\)](#) and [Goutsias et al. \(1995\)](#) useful for our approach. Additionally, an excellent presentation of mathematical morphology and lattice theory can be found in [Ronse \(2006\)](#).

3.4.1 Complete lattices and mathematical morphology

Theoretical formulation of mathematical morphology is nowadays phrased in terms of complete lattices and operators defined on them. For a detailed exposition on complete lattice theory in

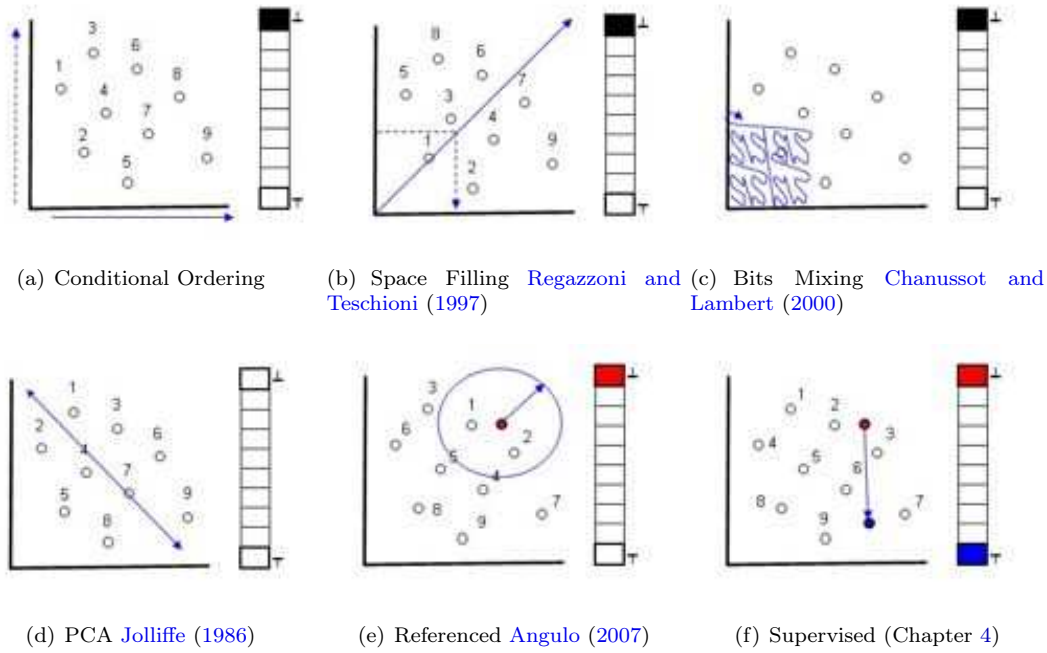


Figure 3.3: Some vector ordering strategies proposed in the literature. The associated ordering is also illustrated.

mathematical morphology, we refer to Chapter 2 (J. Serra and C. Ronse) in [Najman and Talbot \(2010\)](#).

Definition 1. A space \mathcal{L} endowed with a partial order \leq is called a complete lattice, denoted (\mathcal{L}, \leq) if every subset $\mathcal{M} \subseteq \mathcal{L}$ has both supremum (join) $\bigvee \mathcal{M}$ and infimum (meet) $\bigwedge \mathcal{M}$.

A minimum (or least) $\perp \in \mathcal{M}$ is an element which is least than or equal to any other element of \mathcal{M} , that is, $r \in \mathcal{M} \Rightarrow \perp \leq r$. We denote the minimum of \mathcal{L} by \perp . Equivalently, a maximum (largest) \top in \mathcal{M} is the greatest element of \mathcal{M} , that is, $r \in \mathcal{M} \Rightarrow r \leq \top$. We denote the maximum of \mathcal{L} by \top .

Definition 2. A mapping $f : \mathcal{L}_1 \rightarrow \mathcal{L}_2$ of a complete lattice \mathcal{L}_1 into a complete lattice \mathcal{L}_2 is said to be a dilation if $f(\bigvee_{j \in J} r_j) = \bigvee_{j \in J} f(r_j)$ for all families $(r_j)_{j \in J}$ of elements in \mathcal{L}_1 . A mapping is said to be an erosion if $f(\bigwedge_{j \in J} r_j) = \bigwedge_{j \in J} f(r_j)$ for all families $(r_j)_{j \in J}$ of elements in \mathcal{L}_1 .

The important relationship between dilation and erosion is that they are dual concepts from the lattice point of view. [Heijmans and Ronse \(1990\)](#) showed that for any complete lattice \mathcal{L} , we always have a dual isomorphism between the complete lattice of dilation on \mathcal{L} and the complete lattice of erosions on \mathcal{L} . This dual isomorphism is called by Serra [[Serra \(1988\)](#), Chapter 1] the *morphological duality*. In fact it is linked to what one calls *Galois connections* in lattice theory, as we will see at the end of this section.

Definition 3. Let $\delta, \varepsilon \in \mathcal{L}^{\mathcal{L}}$. Then we say that (ε, δ) is an adjunction of every $r, s \in \mathcal{L}$, we have

$$\delta(r) \leq s \iff r \leq \varepsilon(r) \quad (3.2)$$

In an adjunction (ε, δ) , ε is called the *upper adjoint* and δ the *lower adjoint*.

Proposition 1 ([Heijmans and Ronse \(1990\)](#) p. 264). Let $\delta, \varepsilon \in \mathcal{L}^{\mathcal{L}}$. If (ε, δ) is an adjunction, then δ is a dilation and ε is an erosion.

Definition 4. Let \mathcal{L}_1 and \mathcal{L}_2 be lattices and let $\alpha : \mathcal{L}_1 \rightarrow \mathcal{L}_2$ and $\beta : \mathcal{L}_2 \rightarrow \mathcal{L}_1$ satisfy the following conditions.

1. For $r, s \in \mathcal{L}_1$, if $r \leq s$, then $\alpha(s) \leq \alpha(r)$.
2. For $r, s \in \mathcal{L}_1$, if $r \leq s$, then $\beta(s) \leq \beta(r)$.
3. For $r \in \mathcal{L}_1$, $\beta\alpha(r) \leq r$.
4. For $r \in \mathcal{L}_2$, $\alpha\beta(r) \leq r$.

Then (α, β) is a Galois connection between \mathcal{L}_1 and \mathcal{L}_2 .

Proposition 2. Let the lattices \mathcal{L}_1 and \mathcal{L}_2 , maps $\alpha : \mathcal{L}_1 \rightarrow \mathcal{L}_2$ and $\beta : \mathcal{L}_2 \rightarrow \mathcal{L}_1$ a Galois connection. Then the following condition holds for all $r \in \mathcal{L}_1$ and $s \in \mathcal{L}_2$:

$$s \leq \alpha(r) \iff r \leq \beta(s) \quad (3.3)$$

Clearly an adjunction in \mathcal{L} is a Galois connection between (\mathcal{L}, \leq) and its dual (\mathcal{L}, \geq) (indeed, compare definition 3 and proposition 2).

3.4.2 Preorder by h -function

Let \mathbf{E} be a nonempty set and assume that \mathcal{L} is a complete lattice. Let $h : \mathbf{E} \rightarrow \mathcal{L}$ be a surjective mapping. Define an equivalence relation $=_h$ on \mathbf{E} as follows: $x =_h y \iff h(x) = h(y) \quad \forall x, y \in \mathbf{E}$. As it was defined in Goutsias et al. (1995), we refer by \leq_h the h -ordering given by the following relation on \mathbf{E}

$$\forall x, y \in \mathbf{E}, \quad x \leq_h y \iff h(x) \leq h(y)$$

Note that \leq_h preserves reflexivity ($x \leq_h x$) and transitivity ($x_1 \leq_h x_2$ and $x_2 \leq_h x_3 \Rightarrow x_1 \leq_h x_3$). However, \leq_h is not a partial ordering because $x \leq_h y$ and $y \leq_h x$ implies only that $x =_h y$ but not $x = y$. Note that h -ordering is a preorder in \mathbf{E} .

An operator $\psi : \mathbf{E} \rightarrow \mathbf{E}$ is h -increasing if $x \leq_h y$ implies that $\psi(x) \leq_h \psi(y)$. Additionally, since h is surjective, an equivalence class is defined by $\mathcal{L}[r] = \{y \in \mathbf{E} | h(y) = r\}$. The Axiom of Choice Goutsias et al. (1995) implies that there exist mappings $h^\leftarrow : \mathcal{L} \rightarrow \mathbf{E}$ such that $hh^\leftarrow(r) = r$, for $r \in \mathcal{L}$. Unless h is injective, there exist more than one such h^\leftarrow mappings: h^\leftarrow is called the semi-inverse of h . Note that $h^\leftarrow h$ is not the identity mapping in general (but $h^\leftarrow h =_h \text{id}$). However, we have that for any h -increasing $\psi : \mathbf{E} \rightarrow \mathbf{E}$ the result $\psi h^\leftarrow h =_h \psi$ and hence $h\psi h^\leftarrow h = h\psi$. Let us introduce $\tilde{\psi}$ the operator associated to ψ in the lattice \mathcal{L} . A mapping $\psi : \mathbf{E} \rightarrow \mathbf{E}$ is h -increasing if and only there exists an increasing mapping $\tilde{\psi} : \mathcal{L} \rightarrow \mathcal{L}$ such that $\tilde{\psi}h = h\psi$. The mapping $\tilde{\psi}$ is uniquely determined by ψ and can be computed from

$$\tilde{\psi} = h\psi h^\leftarrow$$

We can now define the h -erosion and h -dilation. Let $\varepsilon, \delta : \mathbf{E} \rightarrow \mathbf{E}$ be two mappings with the property

$$\delta(x) \leq_h y \iff x \leq_h \varepsilon(y), \quad \forall x, y \in \mathbf{E}$$

then the pair (ε, δ) is called an h -adjunction. Moreover, let (ε, δ) be h -increasing mappings on \mathbf{E} , and let $\varepsilon \mapsto^h \tilde{\varepsilon}$, $\delta \mapsto^h \tilde{\delta}$. Then (ε, δ) is an h -adjunction on \mathbf{E} if and only if $(\tilde{\varepsilon}, \tilde{\delta})$ is an adjunction on the lattice \mathcal{L} . Therefore a mapping δ (resp. ε) on \mathbf{E} is called h -dilation (resp. h -erosion) if $\tilde{\delta}$ (resp. $\tilde{\varepsilon}$) is a dilation (resp. erosion) on \mathcal{L} . h -adjunctions inherit a large number of properties from ordinary adjunctions between complete lattices. Assume that (ε, δ) is an h -adjunction then

$$\gamma = \delta\varepsilon \leq_h \text{id} \leq_h \varphi = \varepsilon\delta.$$

Hence, γ is h -anti-extensive and ϕ is h -extensive. The operator γ on \mathbf{E} is called h -opening if the operator $\tilde{\gamma}$ on \mathcal{L} determined by $\gamma \mapsto^h \tilde{\gamma}$ is an opening. The operator γ is also h -increasing and satisfies $\gamma\gamma =_h \gamma$ (h -idempotency). The h -closing is similarly defined.

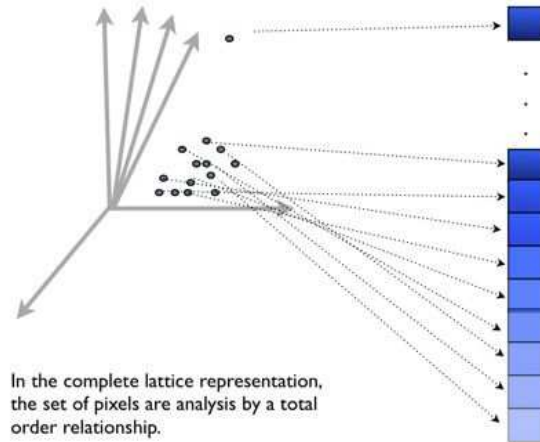


Figure 3.4: The h -ordering (preorder) produces a complete lattice for a given set. In this thesis a “tie-break rule” is applied in each equivalence class of h to yield a chain.

In this thesis, we assume that \mathcal{L} is a complete totally ordering lattice, i.e. a chain. A “tie-break rule” is applied in each equivalence class of h as it is illustrate in Fig. 3.4. Summarising, in simple words this thesis deals with the idea of analyse multivariate images taking advantage of the lattice representation via h -orderings. Thus, spatial components can be studied by the constituent “shape/size” that characterise most of the mathematical morphology transformations.

4

Supervised ordering and multivariate mathematical morphology

Order and complexity are antagonistic, in that order tends to reduce complexity while complexity tends to reduce order. To create order requires not only rearrangement but in most cases also the elimination of what does not fit the principles determining the order. On the other hand, when one increases the complexity of an object, order will be harder to achieve. *Rudolf Arnheim*(1966)

Résumé

Une approche originale d'ordre sur l'espace des vecteurs est introduite dans ce chapitre. Le cadre générique est basé sur une formulation de type apprentissage supervisé qui mène à des ordres réduits. Un ensemble d'apprentissage pour l'arrière-plan (ou le fond) de l'image, et un ensemble d'apprentissage pour le premier plan (ou les objets), sont nécessaires, ainsi qu'une méthode supervisée pour construire l'ordre-h. Deux cas particuliers de techniques d'apprentissage numérique sont considérés en détail: 1) ordre vectoriel basé sur le krigeage et 2) ordre vectoriel basé les SVM. Ces ordres supervisés peuvent être utilisés pour l'extension dans un cadre supervisé de la morphologie mathématique aux images vectorielles¹.

4.1 Introduction

This chapter introduces a supervised learning formulation which leads to reduced orderings for vector spaces. In our model, a training set for the background and another training set for the foreground as well as a supervised method, are needed to construct the h-ordering mapping. According to the

¹The content of this chapter is mainly based on the following published papers:

- [Velasco-Forero and Angulo \(2010b\)](#), *Morphological Processing of Hyperspectral images using kriging-based supervised ordering*. In IEEE - International Conference of Image Processing.
- [Velasco-Forero and Angulo \(2011c\)](#), *Supervised Ordering in \mathbb{R}^P : Application to Morphological Processing of Hyperspectral Images*. IEEE Transaction on Image Process. 20(11):3301-3308.
- [Velasco-Forero and Angulo \(2011b\)](#), *Multiclass ordering for filtering and classification of hyperspectral images*, 3rd Workshop on Hyperspectral Image and Signal Processing: Evolution in Remote Sensing (WHISPERS), 1-4 (2011).

learning technique considered, two particular cases are studied in detail in Section 4.3. On the one hand, the Kriging-based vector ordering and on the other hand, the support vector machines-based vector ordering. Some analytical results and pedagogical examples allow us to understand how the corresponding orderings are constructed. These supervised orderings may then be used for the extension of mathematical morphology to vector images. In Section 4.4, the general definitions of morphological operators in vector spaces are briefly revised. Then, we focus, in Section 4.5, on their application to hyperspectral image processing. The performance of the morphological operators is illustrated with some examples. Conclusions close the chapter in Section 4.6.

4.2 Complete lattices in \mathbb{R}^d

In this section, fundamentals of complete lattices for \mathbb{R}^d is reviewed and a new supervised ordering is introduced. For a detailed exposition see Chapter 3.

4.2.1 Basic Definitions

A space \mathcal{L} endowed with a partial order \leq is called a *complete lattice*, denoted (\mathcal{L}, \leq) if every subset $\mathcal{M} \subseteq \mathcal{L}$ has both supremum (join) $\bigvee \mathcal{M}$ and infimum (meet) $\bigwedge \mathcal{M}$. The *smallest* $\perp \in \mathcal{M}$ is an element smaller or equal than all other elements of \mathcal{M} , that is, $r \in \mathcal{M} \Rightarrow \perp \leq r$. We denote the smallest element (bottom) of \mathcal{L} by \perp . Equivalently, the *largest* \top in \mathcal{M} is an element that is larger than every element of \mathcal{M} , that is, $r \in \mathcal{M} \Rightarrow r \leq \top$. We denote the largest element (top) of \mathcal{L} by \top . Let R be a nonempty set and \mathcal{L} a complete lattice. Furthermore, let $h : R \rightarrow \mathcal{L}$ be a surjective mapping. As it was defined in Goutsias et al. (1995), we refer by \leq_h as the *h-ordering* given by:

$$r \leq_h r' \Leftrightarrow h(r) \leq h(r'), \quad \forall r, r' \in R$$

Note that \leq_h preserves reflexivity ($r \leq_h r$) and transitivity ($r_1 \leq_h r_2$ and $r_2 \leq_h r_3 \Rightarrow r_1 \leq_h r_3$) but is not necessarily a total ordering. Additionally, an equivalence class is defined by $\mathcal{L}[r] = \{r \in R | h(r) = r\}$. We remark that in practical application, the *h-ordering* has to be completed in each equivalence class to lead to a *h-injective*, therefore a complete total ordering.

4.2.2 Reduced Ordering

For multi-band imagery, as colour or hyperspectral images, pixel values are vectors defined in $\mathbb{F} = \mathbb{R}^d$. Consequently the main challenge to build complete lattice structures is to define a mapping $h : \mathbb{R}^d \rightarrow \mathcal{L}$, where \mathcal{L} can be the lattice of the extended real line $(\overline{\mathbb{R}}, \leq)$ using $\overline{\mathbb{R}} = \mathbb{R} \cup \{-\infty, +\infty\}$ and \leq as the "less than or equal to" relation (the natural partial ordering). Once an ordering is defined for a set, the application of mathematical morphology operators is direct, and these operators are useful for denoising, object extraction and other tasks. Many authors have already worked in this idea. As it was noted in Barnett (1976), two main families of mappings h for a given $\mathbf{x} = (x_1, x_2, \dots, x_d) \in \mathbb{R}^d$ can be defined as follow:

- Based on projections (unsupervised), i.e.;

$$h(\mathbf{x}) = \sum_{i=1}^d \lambda^i x_i \quad (4.1)$$

That can be obtained by using the more representative projection in a statistical dimensional reduction technique, for example a linear approach as PCA Jolliffe (1986).

- Based on distances (supervised): Given a subset $T \subset \mathbb{F}$, $T = \{\mathbf{t}_1, \dots, \mathbf{t}_{|T|}\}$, with $\mathbf{t}_i \in \mathbb{R}^d, \forall i$; the mapping $h(\mathbf{x})$ can be written as:

$$h(\mathbf{x}) = \sum_{i=1}^{|T|} \lambda^i \phi(\mathbf{t}_i, \mathbf{x}) \quad (4.2)$$

where $\phi : \mathbb{R}^d \times \mathbb{R}^d \rightarrow \mathbb{R}^+$ is a kernel-induced distance. Different authors have utilised this approach using mainly the Mahalanobis distance as [Goutsias et al. \(1995\)](#), [Al-Otum \(2003\)](#), [Garcia et al. \(2008\)](#). Nonlinear approaches as Kernel PCA [Scholkopf et al. \(1998\)](#), or ISOMAP [Tenenbaum et al. \(2000\)](#) are also example of this category. An interesting example had been introduced in [Lezoray et al. \(2009\)](#) using Laplacian eigenmaps [Belkin and Niyogi \(2002\)](#).

Additionally, projections can take in consideration local structures in \mathbb{R}^d , mainly under so-called “cluster assumption” (the data is “structured” into groups of points, in such a way that a local coordinate system for each group is more efficient than a global one), namely, expressions (4.1) and (4.2) can be generalised to:

- Based on local projections: The different projections are obtained per cluster, i.e.;

$$h(\mathbf{x}) = \sum_{i=1}^d \lambda_{\mathbf{x}}^i x_i \quad (4.3)$$

Examples of techniques useful for that are Local-PCA [Kambhatla and Leen \(1997\)](#) and mixtures of factor analysis as in [Ghahramani and Hinton \(1997\)](#). The clusters are usually determined using unsupervised algorithms such as Expectation-Maximization (EM) algorithm or k-means, which usually require at least the number of clusters.

- Based on local adaptive distances: Given a reference set $T \subset \mathbb{F}$, $T = \{\mathbf{t}_1, \dots, \mathbf{t}_{|T|}\}$, with $\mathbf{t}_i \in \mathbb{R}^d, \forall i$, as in (4.2) but including a contribution which depends on \mathbf{x} . Thus, $h(\mathbf{x})$ can be written as:

$$h(\mathbf{x}) = \sum_{i=1}^{|T|} \lambda_{\mathbf{x}}^i \phi(\mathbf{t}_i, \mathbf{x}) \quad (4.4)$$

where ϕ is a kernel-induced distance and weights $\lambda_{\mathbf{x}}^i$ are fitted for each vector \mathbf{x} in \mathbb{R}^d . As it will be presented in section 3.1., if $\phi(\mathbf{t}_i, \mathbf{x}) = \phi(\mathbf{t}_i, \mathbf{t}_i)$ we obtain the local linear combination based on Kriging [Matheron \(1969\)](#).

4.2.3 h -supervised ordering

Let us focus on the case of h -ordering based on distances. We define a *h -supervised ordering* for a nonempty set \mathbb{R} based on the subsets $B, F \subset \mathbb{R}$, such that $B \cap F = \emptyset$, as a h -ordering that satisfies the conditions: $h(\mathbf{b}) = \perp$, if $\mathbf{b} \in B$, and $h(\mathbf{f}) = \top$ if $\mathbf{f} \in F$. Note that \perp, \top are the smallest and largest element in the lattice \mathcal{L} . Such an *h -supervised ordering* is denoted by $h_{\{B, F\}}$. Fig. (4.1) illustrates the main idea for a h -supervised ordering function. Note the important conditions $B \subseteq \mathcal{L}(\perp)$ and $F \subseteq \mathcal{L}(\top)$. Once this additional supervised restriction is imposed, an adequate vector ranking scheme can be formulated based on $T = B \cup F$. The main motivation of defining this new supervised ordering schema is to obtain maximum and minimum in the lattice \mathcal{L} interpretable with respect to sets B and F . It is important to remind that max and min are the basic words in the construction of all mathematical morphology operators. At this point, the problem is how to define an adequate supervised ordering for a given vector space \mathbb{F} and two pixel sets B, F . Our approach takes advantage of algorithms to solve a supervised classification problem to define the function $h(\mathbf{x})$ as in (4.4), but based on B and $F \subset \mathbb{R}^d$ as follows:

$$h(\mathbf{x}) = \sum_{i=1}^{|T|} \lambda_{\mathbf{x}}^i \phi(\mathbf{t}_i, \mathbf{x}) = \sum_{k=1}^{|B|} \lambda_{\mathbf{x}}^k \phi(\mathbf{b}_k, \mathbf{x}) + \sum_{j=1}^{|F|} \lambda_{\mathbf{x}}^j \phi(\mathbf{f}_j, \mathbf{x}) \quad (4.5)$$

Different h -mappings and induced ordering \leq_h are illustrated in the Fig. (4.2) for some vectors in \mathbb{R}^2 .

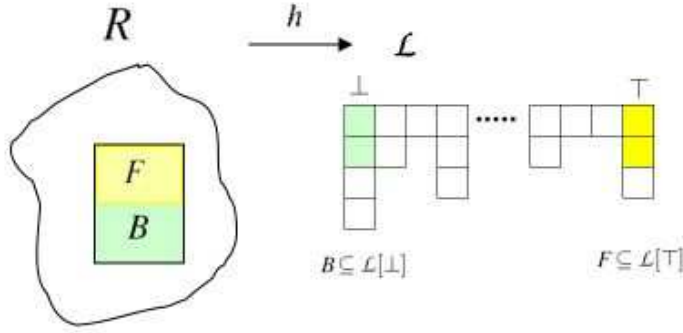


Figure 4.1: Scheme of h -supervised function producing a partial ordering on the original set R based on the subsets B and F . h -supervised function requires that $h(b)$ belong to the equivalence class $\mathcal{L}[\perp]$, for all $b \in B$ and equivalently $h(f)$ belong to $\mathcal{L}[\top]$, for all $f \in F$. \mathcal{L} is the lattice (\mathbb{R}, \leq) using \leq as the “less than or equal to” relation.

4.3 Learning the h -supervised ordering

In this section, we introduce how to calculate h -supervised ordering using well-known supervised learning algorithms. The two approaches presented in this chapter are selected to illustrate the design of h -supervised ordering, but other supervised or semi-supervised approaches can be also explored. However, due to $h(\cdot)$ is not necessary injective, the complete ordering have to be completed in practical examples.

4.3.1 Kriging

A Kriging model gives an interpolating predictor, which can be used to approximate a function based on a finite number of evaluations. Kriging was originated in geostatistics by [Matheron \(1969\)](#). Kriging is also referred to as the Gaussian process predictor in the machine learning domain [Rasmussen and Williams \(2006\)](#). The kriging model postulates estimate an unknown function of interest in the value \mathbf{x} as a linear combination of known realisations of the form $\hat{h}(\mathbf{x}) = \sum \lambda_{\mathbf{x}}^i h(\mathbf{t}_i)$. The most commonly used variant is called *ordinary kriging*, which is often referred to as a Best Linear Unbiased Estimator (BLUE) [Matheron \(1969\)](#). It is considered to be best because it minimises the variance of the estimation error. It is “linear” because estimates are a weighted linear combination of available data, and is “unbiased” since it aims to have the mean error equal to zero. A more complete introduction to kriging can be found in [Matheron \(1969\)](#). Denoting by e the estimation error, i.e., $h(\mathbf{x}) - \hat{h}(\mathbf{x})$, we would like to find an unbiased estimator as follows

$$E(e) = E[h(\mathbf{x}) - \hat{h}(\mathbf{x})] = E[h(\mathbf{x}) - \sum_i^{|T|} \lambda_{\mathbf{x}}^i h(\mathbf{t}_i)] = 0 \Rightarrow \sum_i^{|T|} \lambda_{\mathbf{x}}^i = 1.$$

where $E(\cdot)$ is the expected value. Additionally, the variance of the estimation error, with the assumption of weak-stationarity, is given by:

$$\begin{aligned} \text{Var}(e) &= E[(h(\mathbf{x}) - \hat{h}(\mathbf{x}))^2] \\ &= E[h(\mathbf{x})^2] - 2E[h(\mathbf{x})\hat{h}(\mathbf{x})] + E[\hat{h}(\mathbf{x})^2] \\ &= E[h(\mathbf{x})^2] - 2 \sum_{i=1}^{|T|} \lambda_{\mathbf{x}}^i \mathbf{K}(\mathbf{t}_i, \mathbf{x}) + \sum_i^{|T|} \sum_j^{|T|} \lambda_{\mathbf{x}}^i \lambda_{\mathbf{x}}^j \mathbf{K}(\mathbf{t}_i, \mathbf{t}_j) \end{aligned}$$

where \mathbf{K} is the matrix $|T| \times |T|$ of points pairwise covariances. Minimising the variance of the estimation error forms the objective function of an optimisation problem. Ensuring unbiasedness

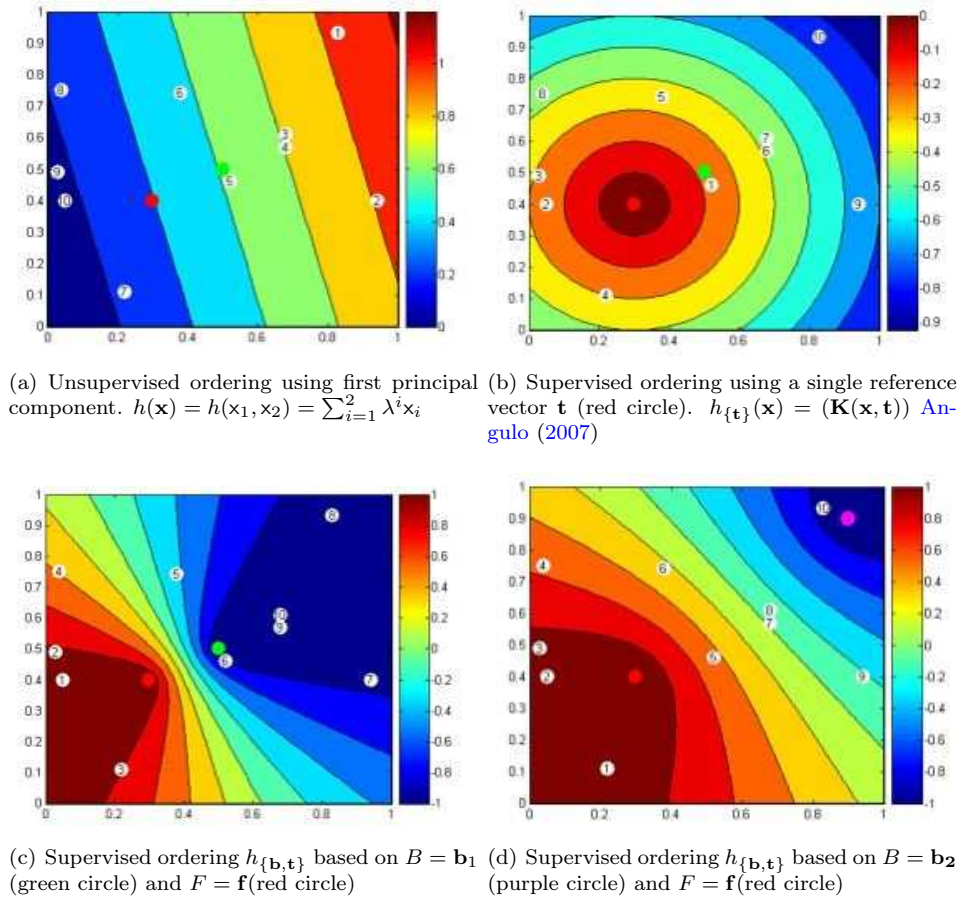


Figure 4.2: Comparison of h -mappings and their corresponding h -ordering \leq_h in \mathbb{R}^2 . Circles in white represent the pixels that we would like to order and colored circles are the information about background and foreground. Vector with the same value in h -function (value in the level set) are in the same equivalence class produced by the h -supervised ordering. Proposed supervised ordering is adaptive to the training set $T = \{B, F\}$. A Gaussian kernel is used as \mathbf{K} in the examples.

of the error imposes a constraint on this function. Formalising this objective function with its constraint results in the following system Matheron (1969):

$$\varphi(\lambda_{\mathbf{x}}^1, \dots, \lambda_{\mathbf{x}}^{|T|}, \mu) = \text{Var}(e) - 2\mu \left(\sum_i^{|T|} \lambda_{\mathbf{x}}^i - 1 \right) \quad (4.6)$$

where μ is a Lagrangian multiplier. Setting the partial first derivatives of (4.6) to zero with respect to μ and λ 's. After $|T| + 1$ differentiations, the set of weight that minimise the error variance can be expressed in matrix form as:

$$\begin{pmatrix} \mathbf{K} & \mathbf{1} \\ \mathbf{1}^t & 0 \end{pmatrix} \begin{pmatrix} \lambda_{\mathbf{x}} \\ \mu \end{pmatrix} = \begin{pmatrix} \mathbf{K}_{\mathbf{x}} \\ 1 \end{pmatrix} \quad (4.7)$$

where \mathbf{K} is the matrix $|T| \times |T|$ of points pairwise covariances and $\mathbf{K}_{\mathbf{x}}$ is a column vector containing $\mathbf{K}(\mathbf{x}, \mathbf{t}_i)$ for all $i = 1, \dots, |T|$. Pairwise covariances are often modelled as a function of points separation. The flexibility in kriging is achieved through a variety of spatial correlation functions Matheron (1969). Finally, to obtain a h -supervised ordering based on B, F , we set $h(\mathbf{b}) = \perp = -1$

and $h(\mathbf{f}) = \top = 1$ to interpret $\widehat{h}(\mathbf{x})$ as a kriging interpolation using \mathbf{K} . Thus, the h -supervised ordering using ordinary kriging is given by

$$\widehat{h}(\mathbf{x}) = \sum_i^{|T|} \lambda_{\mathbf{x}}^i h(\mathbf{t}_i) = \sum_i^{|F|} \lambda_{\mathbf{x}}^i h(\mathbf{f}) - \sum_j^{|B|} \lambda_{\mathbf{x}}^j h(\mathbf{b}) = \sum_i^{|F|} \lambda_{\mathbf{x}}^i - \sum_j^{|B|} \lambda_{\mathbf{x}}^j \quad (4.8)$$

where the $\lambda_{\mathbf{x}}$'s are found using expression (4.7), that is, by solving the corresponding linear system (4.7). Note that (4.8) is defined in the sense of expression (4.5), and it can be used to obtain a supervised ordering. As an illustrative example, we propose to solve the expression (4.7) when both

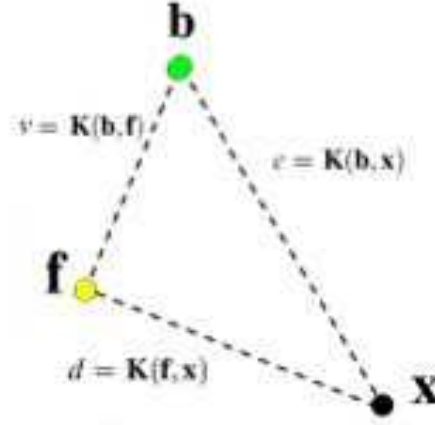


Figure 4.3: Unitary background and foreground sets: $F = \mathbf{f}$ and $B = \mathbf{b}$

background and foreground sets are singletons, that is to say, $B = \{\mathbf{b}\}$ and $F = \{\mathbf{f}\}$. In this case, the kernels are negative exponential of euclidean distances between pairs of vectors are denoted as is illustrated in figure 4.3, i.e., $u = \mathbf{K}(\mathbf{x}, \mathbf{x})$, $v = \mathbf{K}(\mathbf{f}, \mathbf{b})$, $c = \mathbf{K}(\mathbf{b}, \mathbf{x})$ and $d = \mathbf{K}(\mathbf{f}, \mathbf{x})$. From (4.7), we obtain using the notation $u = \mathbf{K}(\mathbf{x}, \mathbf{x})$, $v = \mathbf{K}(\mathbf{f}, \mathbf{b})$, $c = \mathbf{K}(\mathbf{b}, \mathbf{x})$ and $d = \mathbf{K}(\mathbf{f}, \mathbf{x})$,

$$\begin{pmatrix} u & v & 1 \\ v & u & 1 \\ 1 & 1 & 0 \end{pmatrix} \begin{pmatrix} \lambda_{\mathbf{x}}^1 \\ \lambda_{\mathbf{x}}^2 \\ \mu \end{pmatrix} = \begin{pmatrix} c \\ d \\ 1 \end{pmatrix} \Rightarrow$$

$$\lambda_{\mathbf{x}}^1 = \frac{u - v + (c - d)}{2(u - v)}, \lambda_{\mathbf{x}}^2 = \frac{u - v - (c - d)}{2(u - v)}$$

Clearly, $\lambda_{\mathbf{x}}^i$ depends on \mathbf{x} because of values $c = \mathbf{K}(\mathbf{b}, \mathbf{x})$ and $d = \mathbf{K}(\mathbf{f}, \mathbf{x})$. Finally, to obtain a h -supervised ordering, using expression (4.8),

$$\widehat{h}(\mathbf{x}) = \lambda_{\mathbf{x}}^2 - \lambda_{\mathbf{x}}^1 = \frac{d - c}{u - v} = \frac{\mathbf{K}(\mathbf{f}, \mathbf{x}) - \mathbf{K}(\mathbf{b}, \mathbf{x})}{\mathbf{K}(\mathbf{x}, \mathbf{x}) - \mathbf{K}(\mathbf{f}, \mathbf{b})} \quad (4.9)$$

Thus, the supervised reduced ordering is basically the difference between kernelized distances. Note that as $u > v$ then if $\mathbf{x} \rightarrow \mathbf{f} \Rightarrow h(\mathbf{x}) \rightarrow 1$ and if $\mathbf{x} \rightarrow \mathbf{b} \Rightarrow h(\mathbf{x}) \rightarrow -1$, where “ \rightarrow ” means “tends to”.

4.3.2 Support Vector Machines

Let us focus now on linearly separable problems, because they are the simplest for Support Vector Machines (SVM) [Cristianini and Shawe-Taylor \(2000\)](#). Given a labeled training set

$$\{(\mathbf{t}_1, y_1), (\mathbf{t}_2, y_2), \dots, (\mathbf{t}_i, y_i), \dots, (\mathbf{t}_{|T|}, y_{|T|})\},$$

where $\mathbf{t} \in \mathbb{R}^d$ and a class label $y_i = \pm 1$, it is said to be linearly separable if there exists a linear discriminant function whose sign matches the class of all training examples. In this case, the discrimination function is modelled by $\hat{y}(\mathbf{x}) = \mathbf{u}^T \mathbf{x} + \beta_0$ and it is used to separate the two classes. However, there usually exist infinite separating hyperplanes which can separate the training set perfectly. [Vapnik and Lerner \(1963\)](#) proposes to choose the separating hyperplane that maximises the margin, i.e., the largest distance to the nearest training vector (\mathbf{t}) of any class. This new additional requirement, at the basis of the SVM framework, is the main difference, with respect to classical classifiers as Fisher's linear discriminant or logistic regression. As it is pointed out by several authors [Cristianini and Shawe-Taylor \(2000\)](#), the signed distance from a point \mathbf{x} to a given hyperplane is $\frac{1}{y_i} \|\mathbf{u}\| (\mathbf{u}^T \mathbf{x} + \beta_0)$. Hence, the aim is to obtain the biggest positive C which makes all examples satisfy $\frac{1}{\|\mathbf{u}\|} (\mathbf{u}^T \mathbf{t}_i + \beta_0) \geq C, \forall i$. Since the length of \mathbf{u} is insignificant, SVM assumes $\frac{1}{\|\mathbf{u}\|} = C$. Thus, the constrained optimisation problem can be written as,

$$\begin{cases} \max_{\mathbf{u}, \beta_0}, & \frac{1}{2} \|\mathbf{u}\|^2 \\ \text{subject to,} & \frac{1}{\|\mathbf{u}\|} y_i (\mathbf{u}^T \mathbf{t}_i + \beta_0) \geq 1, \forall i \end{cases} \quad (4.10)$$

One method for solving optimisation problems involves introducing Lagrange multipliers [Boyd and Vandenberghe \(2004\)](#), $\lambda_i, i = 1, \dots, |T|$, one for each of the inequality constraints in (4.10). In such case, the so-called Lagrangian function is given by

$$\phi(\mathbf{u}, \beta_0, \lambda)_P = \frac{1}{2} \|\mathbf{u}\|^2 - \sum_{i=1}^{|T|} \lambda_i y_i (\mathbf{u}^T \mathbf{t}_i + \beta_0) + \sum_{i=1}^{|T|} \lambda_i \quad (4.11)$$

Taking the partial derivatives in \mathbf{u} and β_0 gives

$$\mathbf{u} = \sum_{i=1}^{|T|} \lambda_i y_i \mathbf{t}_i, \quad \sum_{i=1}^{|T|} \lambda_i y_i = 0 \quad (4.12)$$

The solution is usually obtained using a dual formulation for the primal problem (4.11) [Vapnik and Lerner \(1963\)](#). Hence substituting (4.12) in (4.11) we obtain the so-called Wolfe dual [Cristianini and Shawe-Taylor \(2000\)](#):

$$\phi(\lambda)_D = \sum_{i=1}^{|T|} \lambda_i - \frac{1}{2} \sum_{i=1}^{|T|} \sum_{k=1}^{|T|} \lambda_i \lambda_k y_i y_k \mathbf{t}_i^T \mathbf{t}_k \quad (4.13)$$

Due to dual formulation of the primal problem and the equation involved in this formulation [Boyd and Vandenberghe \(2004\)](#), [Vapnik and Lerner \(1963\)](#), [Cristianini and Shawe-Taylor \(2000\)](#), we can express the original linear model as:

$$\hat{y}(\mathbf{x}) = \mathbf{u}^T \mathbf{x} + \beta_0 = \sum_{i=1}^{|T|} \lambda_i y_i \mathbf{t}_i^T \mathbf{x} + \beta_0 \quad (4.14)$$

where λ 's are the Lagrangian coefficients. Additionally, this formulation can be extended to construct non-linear classifiers in the original space. Notice that in (4.14) the training points are included only via their inner products. Thus, we obtain using nonlinear functions a "kernel trick" [Cristianini and Shawe-Taylor \(2000\)](#),

$$\hat{y}(\mathbf{x}) = \sum_{i=1}^{|T|} \lambda_i y_i \mathbf{K}(\mathbf{x}, \mathbf{t}_i) + \beta_0.$$

The evaluation function is discriminating between labels as background and foreground, then to obtain a h -supervised ordering, we set $y_i = h(\mathbf{b}) = \perp = -1$ and $y_i = h(\mathbf{f}) = \top = 1$. Thus, omitting β_0 because is constant for all \mathbf{x} our h -ordering based on SVM is obtained by:

$$\hat{h}(\mathbf{x}) = \sum_{i=1}^{|F|} \lambda_i \mathbf{K}(\mathbf{x}, \mathbf{f}_i) - \sum_{j=1}^{|B|} \lambda_j \mathbf{K}(\mathbf{x}, \mathbf{b}_j) \quad (4.15)$$

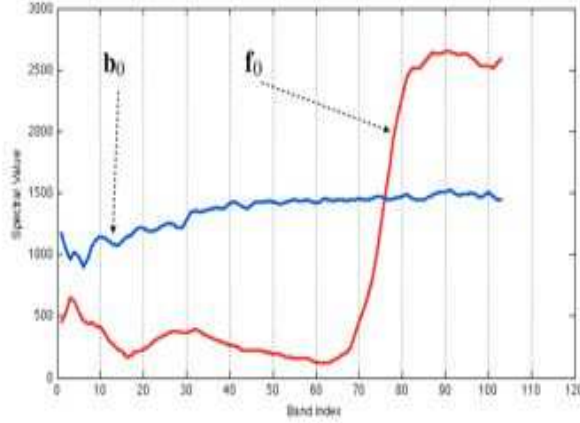


Figure 4.4: Training spectra for Pavia University: \mathbf{b}_0 (tree) and \mathbf{f}_0 (gravel). Morphological operators are calculated using the h -supervised ordering induced by $B = \{\mathbf{b}_0\}$ and $F = \{\mathbf{f}_0\}$. Curves are plots of the spectral values in the different wavelength for these two pixels.

where λ 's are the Lagrangian solution in (4.10). Note that (4.15) can be used to obtain a supervised ordering because it is defined in the sense of expression (4.5). For the example presented in the section 4.3.1, the corresponding function of h -ordering based on SVM can be calculated. Thus, we obtain $\lambda_1 = \lambda_2$, substituting this in a kernelized dual formulation, and finding the value where the derivative is equal to zero, we can say that $\phi_D = 2\lambda_1 - \lambda_1^2(u - v) \Rightarrow \lambda_1 = \lambda_2 = \frac{1}{u-v}$. Thus, from (4.15), the h -ordering using SVM in the unitary background and foreground example is:

$$\hat{h}(\mathbf{x}) = \lambda_1 \mathbf{K}(\mathbf{x}, \mathbf{f}_i) - \lambda_2 \mathbf{K}(\mathbf{x}, \mathbf{b}_j) = \frac{d - c}{u - v} = \frac{\mathbf{K}(\mathbf{f}, \mathbf{x}) - \mathbf{K}(\mathbf{b}, \mathbf{x})}{\mathbf{K}(\mathbf{x}, \mathbf{x}) - \mathbf{K}(\mathbf{f}, \mathbf{b})}$$

We must remark that is the same h -ordering found in (4.9) using ordinary kriging. In Fig. 4.2, we provide a comparison among different ordering schemes in \mathbb{R}^2 . Fig. 4.2(a) shows non-supervised ordering using the first principal component, 4.2(b) an ordering based on a unique reference vector Angulo (2007), and 4.2(c), 4.2(d) two examples of h -ordering using the proposed supervised ordering.

4.3.3 Kriging vs. SVM

As we have shown, the same function $h(\mathbf{x})$ is obtained for both methods in the simplest case, when the training set is composed of a vector for the background and a vector for the foreground. However, in general, the results are different. Let us compare in detail Kriging and SVM ordering approaches. First of all, we notice that the ordering in Kriging is formulated as an interpolation problem, whereas in SVM as an optimisation one. In both cases, the choice of the kernelized distance introduces a great flexibility and the possibility to extend the approach to non vector spaces. From a computational viewpoint, Kriging requires a global computation of the Gram matrix for the training set and the vector of distances for each vector: the value is obtained by the product of the inverse matrix and the vector. Hence, it is a linear algorithm, without any parameter, and quite efficient for a low number of training vectors. The optimisation algorithms used for SVM requires basically a few penalisation parameters. After the learning procedure, only a subset of the training vectors (the support vectors) are used to compute the value of the ordering function at each vector. It has been proven that SVM are particularly robust in the case of high dimension spaces and SVM are also very efficient in large training sets.

4.4 Morphological operators and h -supervised ordering

Once the family of orderings has been established, the morphological vector operators are defined in the standard way. To illustrate the design of morphological operator by h -supervised ordering, we limited our example to the ordering by SVM in (4.15). However, an equivalent analysis can be done in the case of ordering by Kriging in (4.8). The evaluation function of the SVM in (4.15) requires a training set T with two classes. We denote these classes as B (background) and F (foreground) and the correspondent h -supervised ordering by $h_{\{B,F\}}$. Additionally, all morphological operators based on this $h_{\{B,F\}}$ will be referred to as supervised. We limit here our developments to the flat operators, i.e., the structuring elements are planar shapes. The *supervised erosion* of an image $\mathbf{I} \in \mathcal{F}(\mathbf{E}, \mathcal{L})$ at pixel $x \in \mathbf{E}$ by the structuring element $\mathbf{SE} \subset \mathbf{E}$ based on the set of pixels B, F is given by

$$\varepsilon_{\mathbf{SE}, h_{\{B,F\}}}(\mathbf{I}(x)) = \{\mathbf{I}(y) = \wedge_{h_{\{B,F\}}}[\mathbf{I}(z)], z \in \mathbf{SE}(x)\}, \quad (4.16)$$

where $\wedge_{h_{\{B,F\}}}$ is the minimum according to the total ordering $h_{\{B,F\}}$ and $\mathbf{SE}(x)$ is the neighbourhood region centred on the considered pixel x .

The corresponding adjunct *supervised dilation* $\delta_{\mathbf{SE}, h_{\{B,F\}}}(\cdot)$ is obtained by replacing the $\wedge_{h_{\{B,F\}}}$ by the $\vee_{h_{\{B,F\}}}$, i.e.,

$$\delta_{\mathbf{SE}, h_{\{B,F\}}}(\mathbf{I}(x)) = \{\mathbf{I}(y) = \vee_{h_{\{B,F\}}}[\mathbf{I}(z)], z \in \check{\mathbf{SE}}(x)\}, \quad (4.17)$$

where $\check{\mathbf{SE}}$ is the reflected structuring element Soille (2003). The erosion and the dilation are increasing operators. Moreover, the erosion is anti-extensive and the dilation is extensive if \mathbf{SE} contains the origin. In practice, the supervised erosion shrinks the structures which have a spectrum close to the foreground; “peaks of spectra” thinner than the structuring element disappear by taking the spectrum of neighbouring structures with a spectrum values close to the background. As well, it expands the structures which have a vector value close to background. Dilation produces the dual effects, enlarging the regions having a spectrum close to the foreground and contracting the background. One of the most interesting properties of grey-level morphological operators is the duality by the complementation. The *complement image* f^c is defined as the negative of f ($f(x)^c = -f(x) = f^c(x)$). Let the pair of erosion/dilation (ε, δ) be an adjunction, the property of *duality* holds that $\varepsilon(f^c) = (\delta(f))^c \Rightarrow \varepsilon(f) = (\delta(f^c))^c$; and this is verified for any other pair of dual operators, such as the opening/closing. In practice, this property allows us to implement exclusively the dilation, and using the complement, to be able to obtain the corresponding erosion. In our case, it is easy to see that we have the following equivalent properties of duality:

1. $\varepsilon_{\mathbf{SE}, h_{\{B,F\}}}(\mathbf{I}) = \delta_{\mathbf{SE}, h_{\{F,B\}}}(\mathbf{I})$,
2. $\varepsilon_{\mathbf{SE}, h_{\{B,F\}}}(\mathbf{I}) = \delta_{\mathbf{SE}, -h_{\{B,F\}}}(\mathbf{I})$.

Dilation and erosion allow us to define morphological filters Serra (1988), Soille (2003). A morphological filter is defined as an increasing operator that is also idempotent (the erosion/dilation are not idempotent) Serra (1988). A *supervised opening* is an erosion followed by a dilation, i.e.,

$$\gamma_{\mathbf{SE}, h_{\{B,F\}}}(\mathbf{I}) = \delta_{\mathbf{SE}, h_{\{B,F\}}}(\varepsilon_{\mathbf{SE}, h_{\{B,F\}}}(\mathbf{I})) \quad (4.18)$$

and a *supervised closing* is a dilation followed by an erosion. The opening (closing) is an anti-extensive (extensive) morphological filter. More precisely, the opening removes spectra peaks that are thinner than the structuring element, having a vector value close to the foreground; the closing remove vector values peaks that are thinner than the structuring element, having a spectrum close to background.

It is important to remark that the residue-based operator for multivariate are defined in h -units, i.e., the *supervised morphological gradient*

$$\Delta_{\mathbf{SE}, h_{\{B,F\}}}(\mathbf{I}) = h_{\{B,F\}}(\delta_{\mathbf{SE}, h_{\{B,F\}}}(\mathbf{I})) - h_{\{B,F\}}(\varepsilon_{\mathbf{SE}, h_{\{B,F\}}}(\mathbf{I})), \quad (4.19)$$

and accordingly the supervised top-hat as follows

$$\rho_{\mathbf{SE}, h_{\{B,F\}}}^+(\mathbf{I}) = h_{\{B,F\}}(\mathbf{I}) - h_{\{B,F\}}(\gamma_{\mathbf{SE}, h_{\{B,F\}}}(\mathbf{I})) \quad (4.20)$$

for the *positive supervised top-hat transformation* and

$$\rho_{\text{SE},h_{\{B,F\}}}^-(\mathbf{I}) = h_{\{B,F\}}(\varphi_{\text{SE},h_{\{B,F\}}}(\mathbf{I})) - h_{\{B,F\}}(\mathbf{I}) \quad (4.21)$$

for the *negative supervised top-hat transformation*. Their interpretation are similar than in grey scale image, but under the consideration of the h -ordering. For instance, the positive top-hat transformation yields grey level images and it is used to extract contrasted components with respect to the background B .

4.5 Applications to hyperspectral image processing

In practice, the construction of a total order is required to avoid arbitrary decisions among pixels that belong to the same equivalence class. In the sequel, the total ordering is induced including a lexicographic order in $\mathcal{L}[r]$, for all r , in cases with equal value in the h -supervised ordering and hence a *chain* is obtained for the pixels from a given hyperspectral image. We must notice however that using h -mapping for \mathbb{R}^d ($d \gg 2$) the possibility of having two different spectra with equal value in h is quite rare in practice.

We present our examples over three images:

- *Pavia University hyperspectral image* is an urban area that was recorded by the ROSIS-03 optical sensor with spatial resolution of 1.3 meters per pixel. The number of bands is 115 with a spectral coverage ranging from 0.43 to 0.86 μm . The 12 most noisy channels have been removed, and the experiments are conducted on the 103-band image. Fig. 4.5(a) is the false-colour preview for an image of 340 columns, 610 rows in 103 bands.
- *Yellowstone calibrated scene 3* is an AVIRIS image which has been provided in [Kiely and Klimesh \(2009\)](#). The spatial resolution is 20 meter-pixels. Fig. 4.7(a) is the false-color preview for the 512 columns, 677 rows in 224 bands.
- *Moffett Field* is a Airborne Visible/Infrared Imaging Spectrometer (AVIRIS) image developed at the Jet Propulsion Laboratory of NASA. This sensor operates in the Visible to Near Infrared (VNIR) and Short-Wave Infrared (SWIR) range to achieve 224 spectral bands. To test the ability to detect targets with *a priori* the number of spectral bands is initially reduced to 203 by removing extremely noisy bands, i.e., we include the information contained in bands [1:106,114:153,168:224]. False colour is illustrated in Fig. 4.15.

In the studied scenarios, only *two* pixels for foreground and background had been selected as it is shown in Fig. 4.4 for the experiments in Pavia University and Fig. 4.6 for Yellowstone HSI. Erosion and dilation operators (Figs. 4.7(c), 4.5(c) and 4.7(b), 4.5(b)) do not introduce false spectra. By computing the morphological gradient Figs. 4.7(d), 4.5(d), as difference in h between the erosion and the dilation, we obtain contours which correspond here to the spatial transition but it gives priority to changes according with the training set, i.e. water-land or trees-gravel.

4.5.1 Influence of training set in h -ordering

Obviously, the results obtained can be improved including a higher number of training pixels in F and B . Examples illustrate that even using a limited number of training set size, our approach produces operators that can be interpreted as grey-scale mathematical morphological operators according with the spatial size of the structuring element SE, but it takes into consideration the inherent dependence of our approach to the sets B and F . However, the selection of reference spectra have to be done according with practical needs.

In the present study, we considered only one set of a single pixel for B and as well as for F . Our motivation is to show the worst case of the supervised-ordering. However, a "toy-example" has been designed to illustrate the behaviour of the h -function, induced ordering and its respective morphological operator. The performance of the proposed approach is presented using a the well-known Indiana's Indian Pines hyperspectral image. The number of bands is initially reduced to

200 by removing bands covering water absorption and noisy bands. A spatial section is selected (40 : 60, 122 : 140). A square 8×8 is generated by using random spectrum from class 11 at it shows Fig. 4.8. The cardinality of B and F take different values $\{1, 5, 30\}$. The corresponding h -supervised an associated morphological gradient are presented in Fig. 4.9. The experiment shows as the gradient is higher when the training size increases. It follows the intuition of the performance of supervised morphological transformation improves when the number of training pixels increases.

4.5.2 Extracting spatial/spectral structures

Morphological opening and closing are appropriate operators for structure extraction according to their spatial/spectral properties. More precisely, the top-hats or residues between the original image and the opened/closed image give the structures selectively removed by the opening/closing. Examples of positive supervised top-hat are shown in Figs. 4.11(c), 4.5(e) and 4.5(f), which allow us to extract regions with size smaller than the corresponding structuring element and whose spectra are close to the F . By modifying the size of the structuring element, a scale-space spectral extraction is obtained. In Figs. 4.10(b) and 4.10(a) are also given the counterpart operators but using as another foreground (vegetation) and another background (water) and as we can observe, particularly for the gradient (Fig. 4.10(c)), the obtained results are totally different.

Examples of supervised positive top-hat transformations are presented in Figs. (4.11(c)) and (4.11(g)), which allow to extract regions with spectrum is close to the foreground (water) and whose size is smaller than the correspondent structuring element. Dually, supervised negative top-hat transformations (Figs. (4.11(d)) and (4.11(h))) emphasise information according background/size. By modifying the size of the structuring element, an scale-space spectral extraction is obtained. In Figs. (4.12(c)), (4.12(g)), (4.12(d)) and (4.12(h)) are compared again the importance of the role played by the choice in the training set for the background and foreground.

As it has been mentioned above, the morphological openings/closings extract the object according to the size/shape of the structuring element. However, after applying these operators, all the image contours are “modified”. Opening/closing by reconstruction can be used in order to selectively extract the objects “marked” by the marker image, and which are spectrally near to the foreground and far from the background, but preserving the objects contours.

The marker image can be for instance defined interactively, by choosing a pixel of the image. In Fig. (4.13(b)) is given an example of this method, where the used marker is given in Fig. (4.13(a)): the marker is a point touching one of the lakes, and after reconstruction only the marked lake is totally preserved; the other structures having a spectral value close to the foreground are removed (we observe in the image that the river is not connected to the lake). Then, by computing the difference in h between the original image and the reconstructed image, all the image structures (independently of their size/shape) associated with the foreground and do not marked are perfectly extracted, see Fig. (4.13(c)). We must notice that to obtain an appropriate result the choice of the foreground set must be coherent with the spectrum of the marked structure.

Nevertheless the power of the operators by reconstruction are not limited to “interactive” filtering. The marker image can also be defined as a rough image simplifications. A typical size-selective maker is an alternate sequential filter of size n . The corresponding leveling operator, a product of an opening and a closing by reconstruction, allows to simplify the image, removing the objects and textures smaller than the size n and preserving the contours of the remaining objects. Moreover, it acts simultaneously on the “foreground objects” and “background objects”. Figs. (4.14(a)) and (4.14(b)) and their corresponding residues (4.14(c)), (4.14(d)) illustrate the fundamental advantage of these operators. We can also observe once more the role of background/foreground comparing with their equivalents for the second set of reference spectra, i.e., Figs. (4.14(e)), (4.14(f)), (4.14(g)), (4.14(h)).

4.5.3 Duality between background and foreground

Let us now compare in another example how the idea of using a framework where the notion of a prior foreground F and background B are used for the ordering performs with respect to the most

classical framework which only uses the notion of foreground F (as for instance in works [Angulo \(2007\)](#) [Goutsias et al. \(1995\)](#) [Garcia et al. \(2008\)](#)). Conceptually, in the classical case, the dilation tends to approach the pixels towards the F , and by duality, the erosion tends to move further away F , but without defining to which “image background” the spectrum must be addressed. This *asymmetric* situation is one the problems which motivate this chapter. The case with a single spectrum of reference for the foreground \mathbf{f} ([Angulo \(2007\)](#)) is equivalent to the h -ordering by $h_{\{\mathbf{f}\}}(\mathbf{x}) := \mathbf{K}(\mathbf{f}, \mathbf{x})$. A comparative experiment was performed using Moffett Field data set. Single target signatures were inserted at known locations in a lake and another over a building. A set of two pixels are selected for foreground (water) and background (building) as it is shown in Fig. 4.15. In our experiments, the unitary structuring element \mathbf{SE} is the hexagon. Supervised erosion and dilation are given respectively in Fig. 4.16(a), 4.16(b), (4.16(c)) and (4.16(d)). The supervised morphological gradient based on $h_{\{\mathbf{f}\}}$ in Fig. 4.16(e) favours structures with high differences among pixels close or far from \mathbf{f} . The supervised morphological gradient based on $h_{\{\mathbf{b}, \mathbf{f}\}}$ in Fig. 4.16(f) highlights spatial patterns favouring structures containing the reference pixels \mathbf{b} or \mathbf{f} .

Similarly, supervised positive/negative top-hat transformations are presented in Fig. 4.17(b) which allows to extract regions with spectrum close to foreground (water) contrasted with respect to the background and whose size is smaller than the corresponding structuring element, as well as regions close to the background and contrasted with respect to the foreground. We remark that in the case of $h_{\{\mathbf{f}\}}$, the interpretation of the positive/negative top-hat Fig. 4.17(a), is not clear due to a lack of duality in ordering induced by the asymmetric training set, i.e., we can say that dilation “takes” the spectral information from pixels close to \mathbf{f} but we do not have a dual interpretation for the erosion. Note that in the proposed $h_{\{\mathbf{b}, \mathbf{f}\}}$ both interpretations are available.

4.5.4 Multi-target morphological-driven classification

In real hyperspectral applications, it is often necessary to analyse the image with multiple set of targets (i.e., multiple foregrounds using our terminology) and that task is classically tackled in the context of multi-class supervised classification [Cristianini and Shawe-Taylor \(2000\)](#). Inspired by this same rationale, we propose a version of one-versus-all classification based in supervised morphological processing for a set of multi-targets. For a morphological operator $\Upsilon_{\{B, F\}} : \mathcal{F}(E, \mathcal{L}) \rightarrow \mathcal{F}(E, \mathcal{L})$ induced by the supervised order $h_{\{B, F\}}$ in the complete lattice (\mathcal{L}, \leq_h) , we define the *morphological-driven classification* $\Upsilon_{\{\mathbf{T}\}}$, for each pixel \mathbf{x} , based on the multi-target set $\mathbf{T} = \{\bigcup_i \mathbf{T}_i \mid \mathbf{T}_i \cap \mathbf{T}_j = \emptyset \ \forall \ i \neq j\}$, as

$$\Upsilon_{\{\mathbf{T}\}}(\mathbf{x}) = \operatorname{argmax}_i \Upsilon_{\{\mathbf{T}_{-i}, \mathbf{T}_i\}}(\mathbf{x}) \quad (4.22)$$

where argmax is calculated using the associated order \leq_h in the complete lattice \mathcal{L} and $\{\mathbf{T}_{-i}, \mathbf{T}_i\}$ denotes one-versus-all decomposition of the multi-target set. For instance, if $\mathbf{T} = \{\mathbf{T}_1, \mathbf{T}_2, \mathbf{T}_3\}$ then $\{\mathbf{T}_{-2}, \mathbf{T}_2\}$ denotes the background/foreground set $\{B = \{\mathbf{T}_1 \cup \mathbf{T}_3\}, F = \mathbf{T}_2\}$. Accordingly, the usual one-versus-all classification, associated to $h_{\{\mathbf{T}_{-i}, \mathbf{T}_i\}}$, is obtained when the operator Υ is the identity. For this problem of classification, the mapping $h_{\{\mathbf{T}_{-i}, \mathbf{T}_i\}}$ which induces the ordering is constructed using SVM framework. The intuition of the multi-class ordering is given in Fig. 4.18. Additionally, we proposed to use as $\Upsilon_{\{B, F\}}$, which regularise the classification, the leveling $\lambda_{\{B, F\}, \mathbf{SE}}$, where the marker is an alternate sequential filter. To illustrate the performance of our approach, we use the University of Pavia hyperspectral image. That image is an urban area that was recorded by the ROSIS-03 optical sensor. Nine classes of interest are considered, with the number of test and training samples detailed for each class in Table (4.1). The accuracies in terms of classification are listed in Table (4.2). The overall accuracy (OA) is the percentage of correctly classified pixels whereas the average accuracy (AA) represents the average of class classification accuracies. Kappa coefficient is another criterion used in remote sensing classification to measure the degree of agreement and takes into account the correct classification that may have been obtained “by chance” by weighting the measured accuracies. Per class classification accuracy has been also reported in Table (4.1). Classification map using leveling operator (using as a marker a hexagonal alternate sequential filter) in a multi-target approach is depicted in Fig. (4.19) for different sizes of the structuring element. The parameters of the SVMs were fixed to $(C = 10^3, \gamma = 0.0001)$. As we can observe, the spectral-

Table 4.1: Performance comparison per class for Pavia University Hyperspectral Image. Note that $Id_{\{\mathbf{T}\}}$ is equivalent to standard one-vs-all SVM. The best score for each class is highlighted in bold face font.

i -Class	$ \mathbf{T}_i $	Test samples	$Id_{\{\mathbf{T}\}}(\cdot)$	$\Lambda_{\{\mathbf{T}\},SE}(\cdot)$	$\Lambda_{\{\mathbf{T}\},2SE}(\cdot)$	$\Lambda_{\{\mathbf{T}\},3SE}(\cdot)$
1-asphalt	548	6304	0.7914	0.9246	0.9624	0.9774
2-meadows	540	18146	0.6949	0.7138	0.7177	0.7256
3-gravel	392	1815	0.7365	0.7770	0.7842	0.6951
4-tress	524	2912	0.8688	0.8913	0.8456	0.7771
5-metal sheets	265	1113	0.9926	0.9993	0.9993	1
6-bare soil	532	4572	0.9572	0.9998	1	1
7-bitumen	375	981	0.8917	0.9398	0.9519	0.9662
8-bricks	514	3364	0.8764	0.9772	0.9940	0.9978
9-shadows	231	795	0.9747	1	0.9984	0.6684

Table 4.2: Performance comparison for Pavia University Hyperspectral Image. Note that $Id_{\{\mathbf{T}\}}$ is equivalent to standard one-vs-all SVM. OA is the overall accuracy, AA the average accuracy and κ is the kappa statistic.

Method	(OA)	(AA)	κ
$Id_{\{\mathbf{T}\}}(\cdot)$	0.7925	0.8649	0.7394
$\Lambda_{\{\mathbf{T}\},SE}(\cdot)$	0.8409	0.9136	0.8002
$\Lambda_{\{\mathbf{T}\},2SE}(\cdot)$	0.8472	0.9159	0.8081
$\Lambda_{\{\mathbf{T}\},3SE}(\cdot)$	0.8373	0.8675	0.7957

spatial processing by means of morphological operators improves notably the classification results. But obviously, the spatial regularisation effect involves that small regions can disappear and for large structuring elements the performance of classification for classes associated to small regions can be deteriorated.

4.6 Conclusions on supervised ordering

Hyperspectral imaging is an active field of image analysis which is usually considered under the supervised paradigm [Melgani and Bruzzone \(2004\)](#): both the complexity of the data and the typical real-life applications require the construction of training sets of spectra which drive the algorithms of classification, feature extraction, segmentation, etc. Hence, from our viewpoint, the construction of hyperspectral mathematical morphology operators should be also coherent with this idea of supervised processing. In previous works, some of the introduced ideas were useful but their formulation was not correct in the theoretical framework of mathematical morphology. Other works, following direct extensions of the works on colour morphology, were basically based on the notion of colour of reference (for the supervised ones) or on the projection on main directions (for the unsupervised ones). We consider that the present methodology generalises most of the precedent works on vector mathematical morphology. In particular, we have shown how mathematically sound machine learning techniques can be also used to define supervised partial orderings in vector spaces. In fact, using for instance the kernel-trick and SVM algorithms, the framework is valid to define supervised ordering in any space providing that a kernel between the points is defined. Additionally, this formulation based on both a background and a foreground training set allows an adequate interpretation of dual morphological operations. The examples given in the chapter illustrate the potential interest of the algorithms for real applications in hyperspectral images processing.

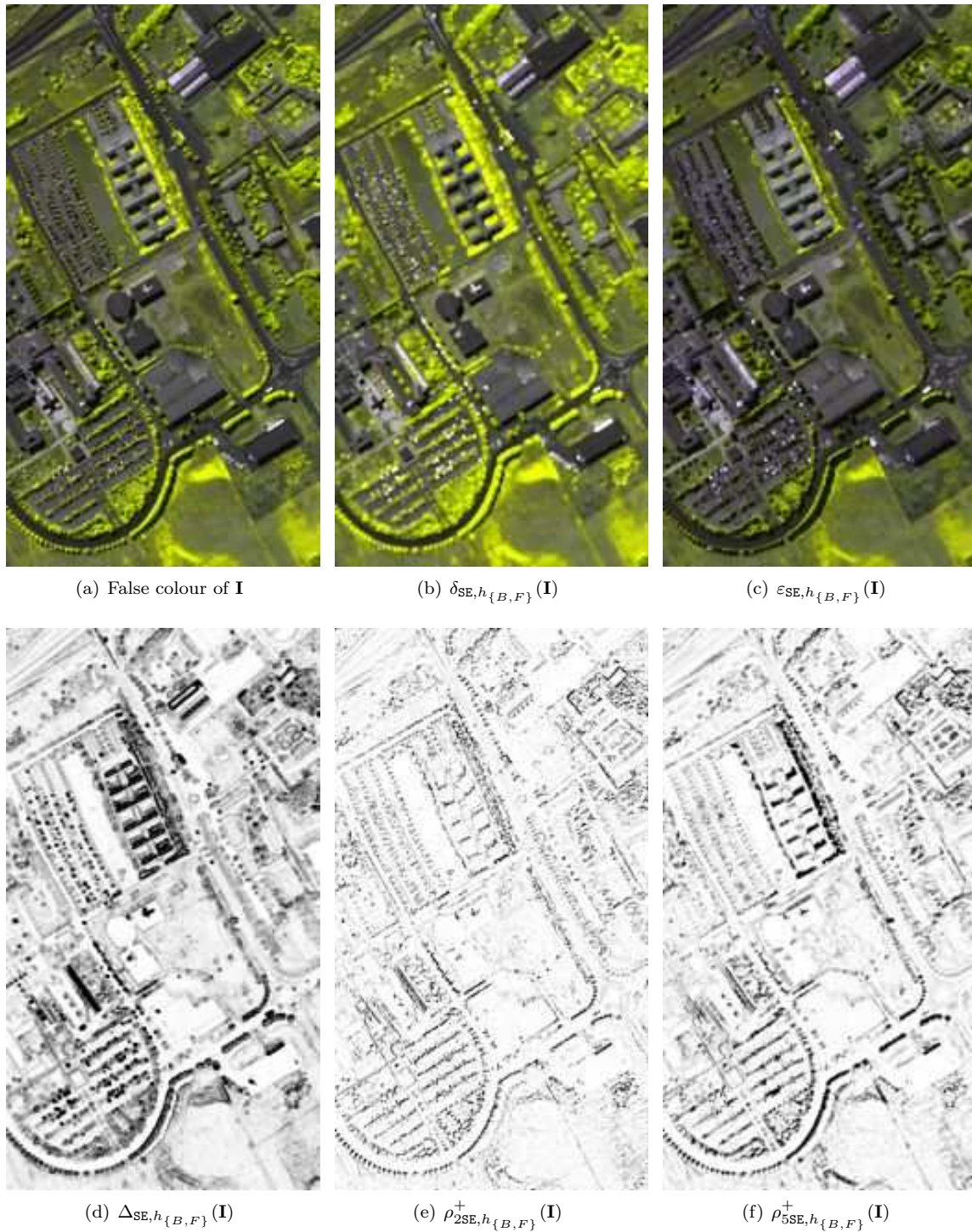


Figure 4.5: *Pavia University* with 340×610 pixels in 103 bands. Supervised dilation, erosion, gradient, and positive top-hats for a set of background/foreground pixels $B = \{\mathbf{b}_0\}$ and $F = \{\mathbf{f}_0\}$ illustrated in Fig. 4.4. Unitary structuring element SE is a square of side three pixels. Spectra are shown using bands $\{80, 90, 70\}$. h -ordering calculated using SVM as (4.9) with a polynomial kernel of order 2.

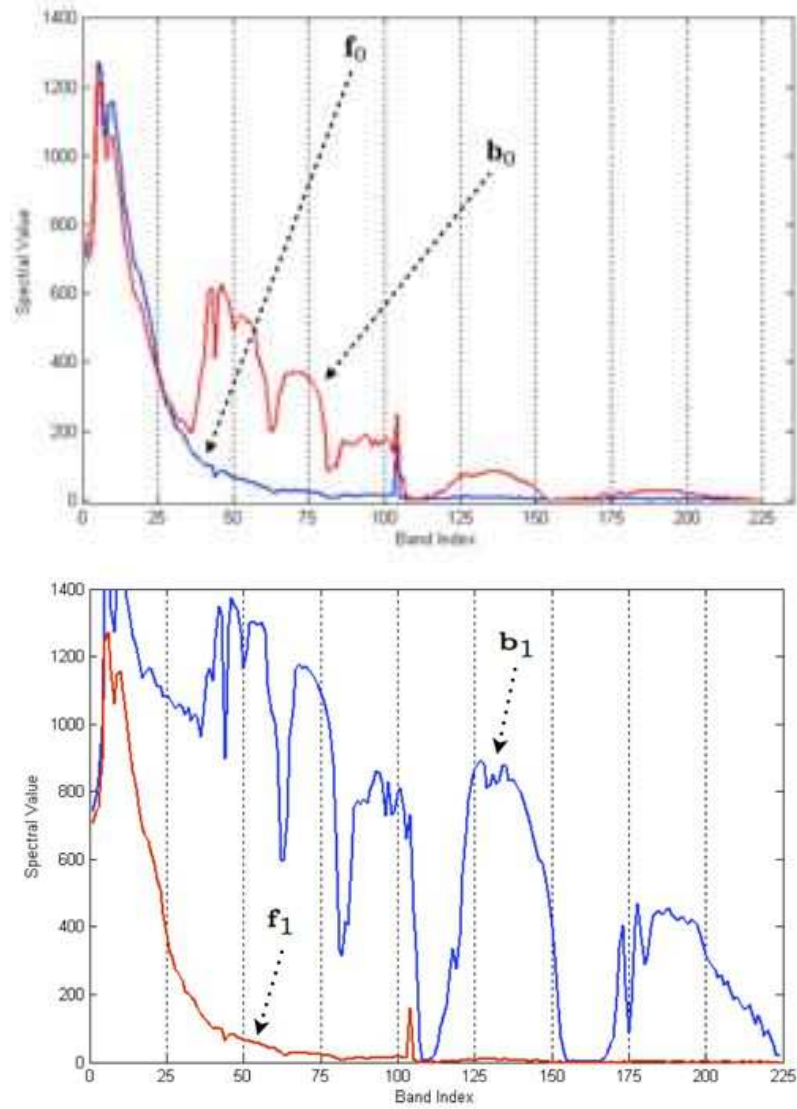


Figure 4.6: Training spectral for Yellowstone Scene. **Left:** First example (\mathbf{b}_0 (land) and \mathbf{f}_0 (water)). **Right:** Second example of the Yellowstone Scene: (\mathbf{b}_0 (water) and \mathbf{f}_0 (unknown material)). Curves are plots of the spectral values in the different frequency bands for these pixels.

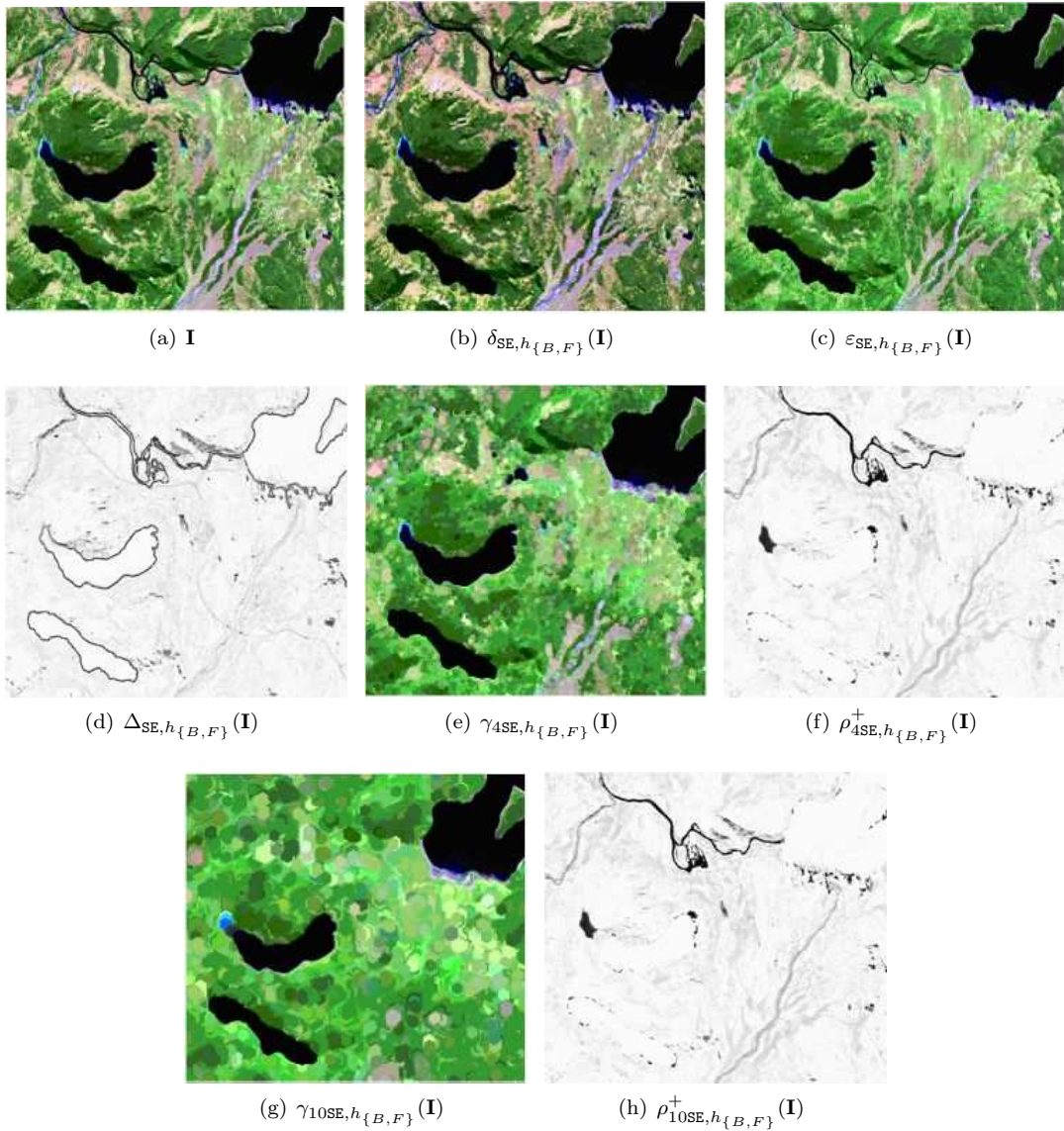


Figure 4.7: *Yellowstone scene* with 512×677 pixels in 224 bands. Supervised dilation, erosion, opening, and their positive top-hats for a set of background/foreground pixels $B = \{\mathbf{b}_0\}$, $F = \{\mathbf{f}_0\}$ illustrated in Fig. 4.6. Unitary structuring element SE is an hexagon. Spectra are shown using bands $\{125, 70, 30\}$. h -ordering calculated using (4.9) with a polynomial kernel of order 2.

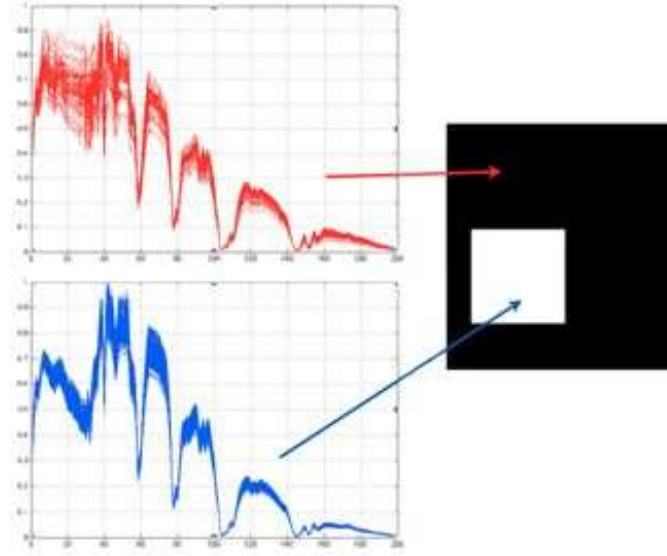


Figure 4.8: Toy example: A square 8×8 is generated by using random selection of spectra from class 11 of well-know Indian Pines hyperspectral image. The background is the image subset between $[40:60,122:140]$ from the same hyperspectral image.

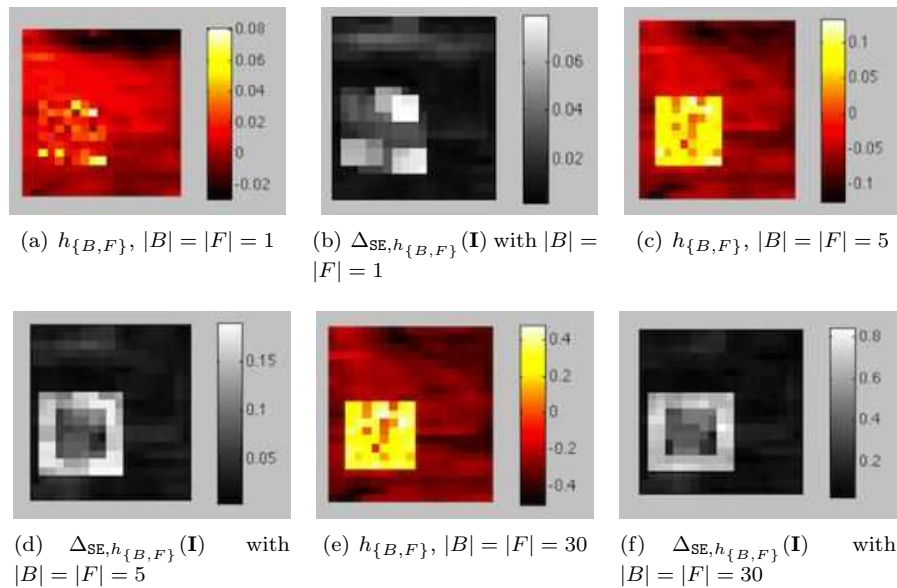


Figure 4.9: Comparison of h function, ordering and morphological gradient using different size of training set in the Toy example of Fig. 4.8. The experiment shows as the gradient is higher when the training size increases. We remark that the scale gradient in (f) is larger than (d) and (b).

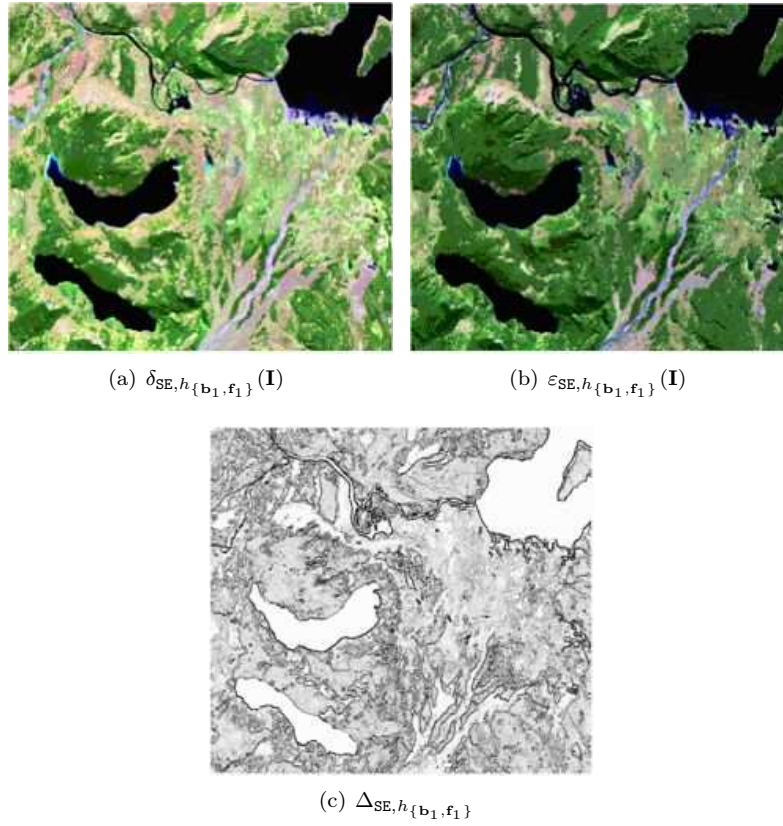


Figure 4.10: Supervised dilation (4.17), erosion (4.16) and gradient (4.19) for two sets of background/foreground pixels. Unitary structuring element SE is an hexagon. Spectra are showed using bands $\{125,70,30\}$. h -ordering calculated using (4.9) with a polynomial kernel of order 2.

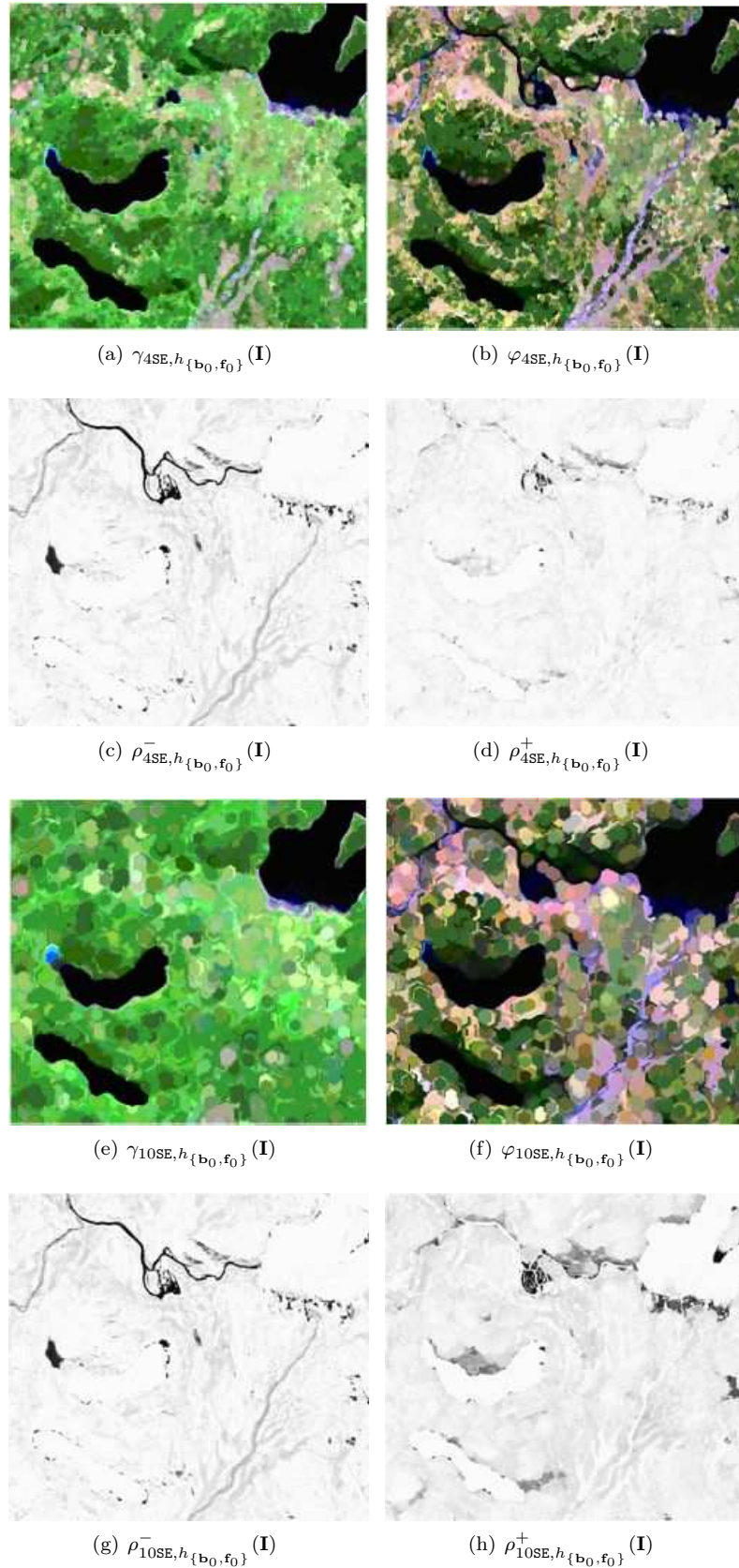


Figure 4.11: Supervised opening (4.4), closing (and their positive and negative top-hats for a set of background/foreground pixels $B = \{\mathbf{b}_0\}$, $F = \{\mathbf{f}_0\}$). Spectra are showed using bands $\{125, 70, 30\}$. h -ordering calculated using (4.9) with a polynomial kernel of order 2.

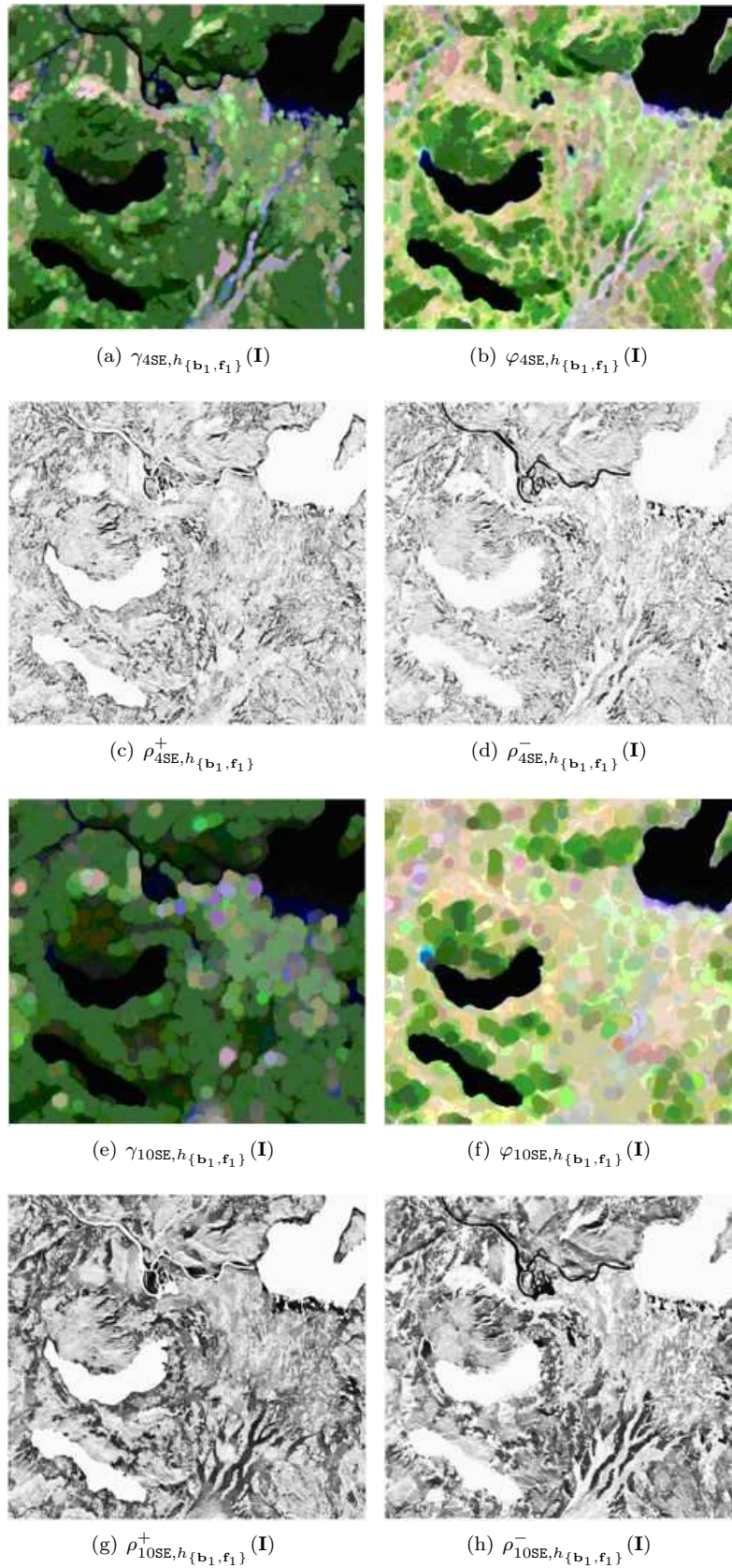
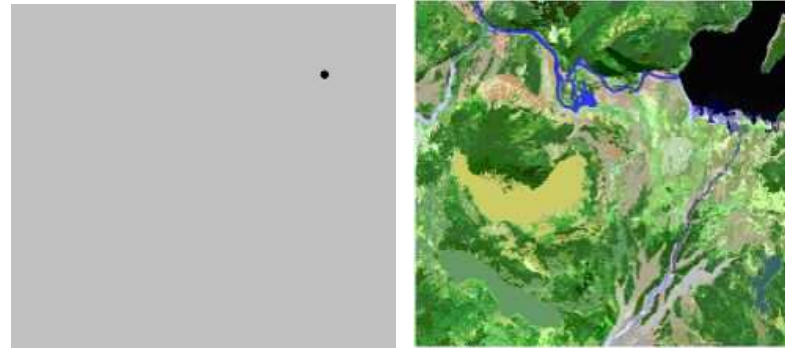
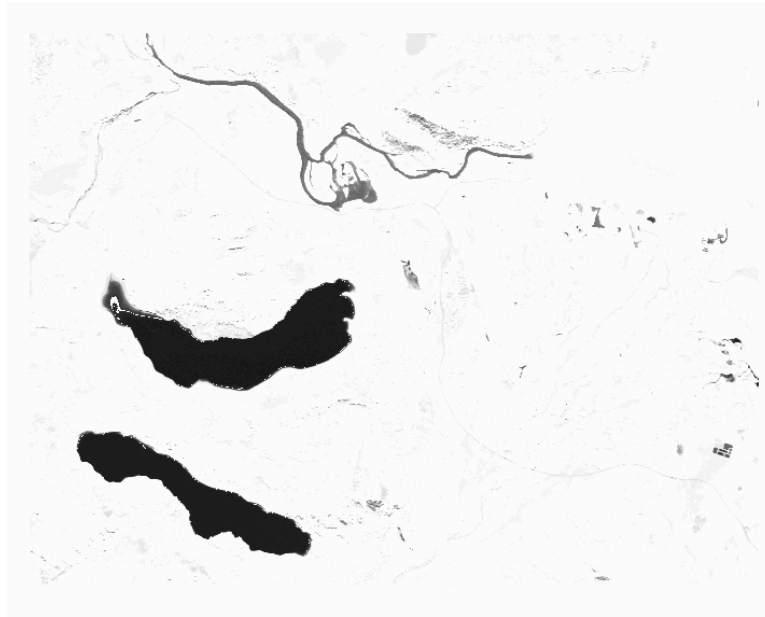


Figure 4.12: Supervised opening (4.4), closing and their positive and negative supervised top-hats for a set of background/foreground pixels $\{b_1, f_1\}$. Spectra are shown using bands $\{125, 70, 30\}$. h -ordering calculated using (4.9) with a polynomial kernel of order 2.



(a) Marker contains the spectral values correspondent to the pixel in the original image in the dark spot and \mathbf{b}_0 in the rest of the image (illustrated as grey color). That multivariate image is denote as \mathbf{M} .

(b) $\delta_{\{\mathbf{b}_0, \mathbf{f}_0\}}^\infty(\mathbf{M}, \mathbf{I})$



(c) $h_{\{\mathbf{b}_0, \mathbf{f}_0\}}(\mathbf{I}) - h_{\{\mathbf{b}_0, \mathbf{f}_0\}}(\delta_{\{\mathbf{b}_0, \mathbf{f}_0\}}^\infty(\mathbf{M}, \mathbf{I}))$

Figure 4.13: Extraction of specific objects can be performed by using geodesic reconstruction in the supervised ordering. Unitary structuring element SE is an hexagon. Spectra are showed using bands $\{125,70,30\}$. h -ordering calculated using (4.9) with a polynomial kernel of order 2. The image c) has been resized to make details visible.

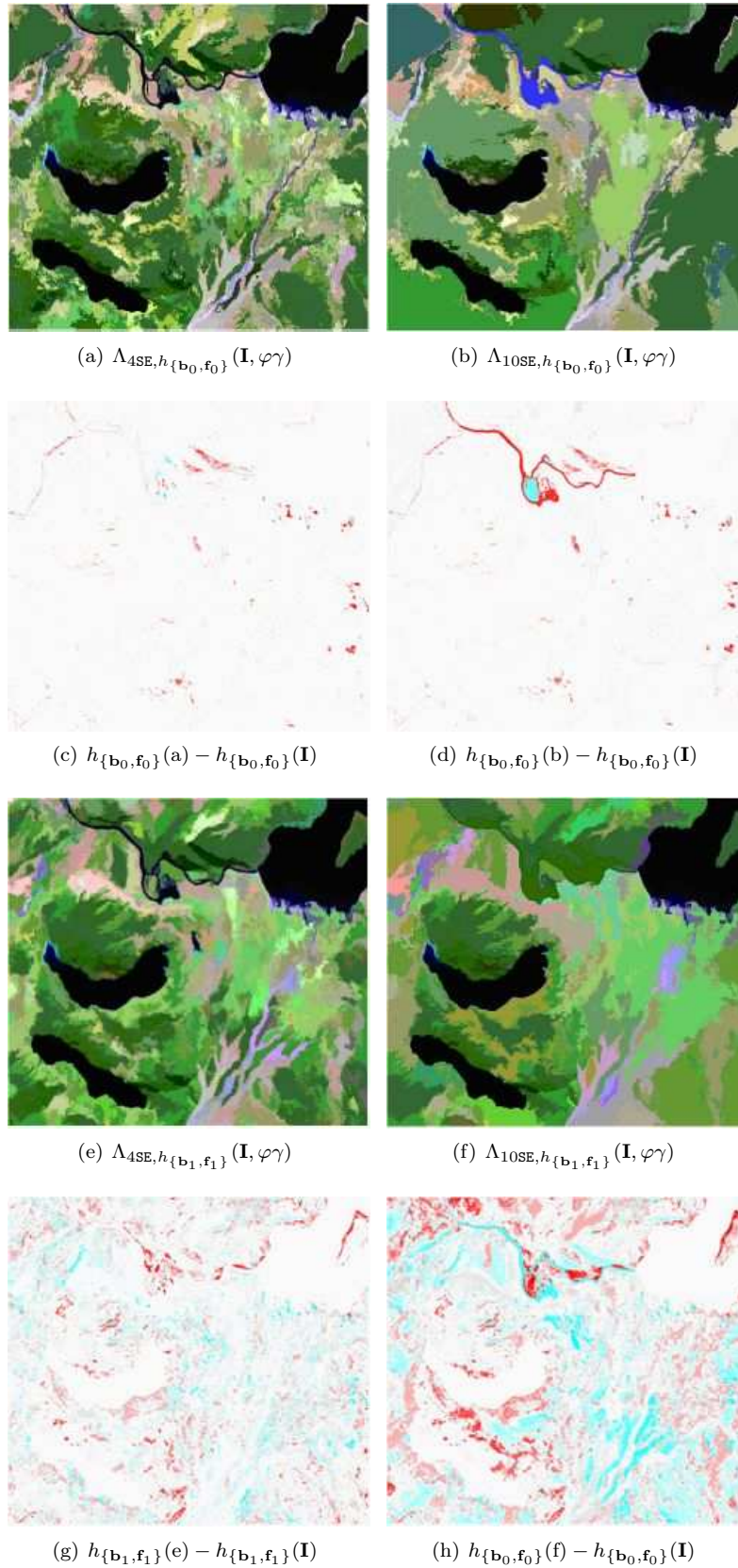


Figure 4.14: Supervised leveling for sets of background/foreground pixels. Unitary structuring element SE is a hexagon. False colour image are showed using bands $\{125,70,30\}$. h -ordering calculated using (4.9) with a polynomial kernel of order 2. Red and blue colors are incorporate to illustrate positive or negative values in the difference.

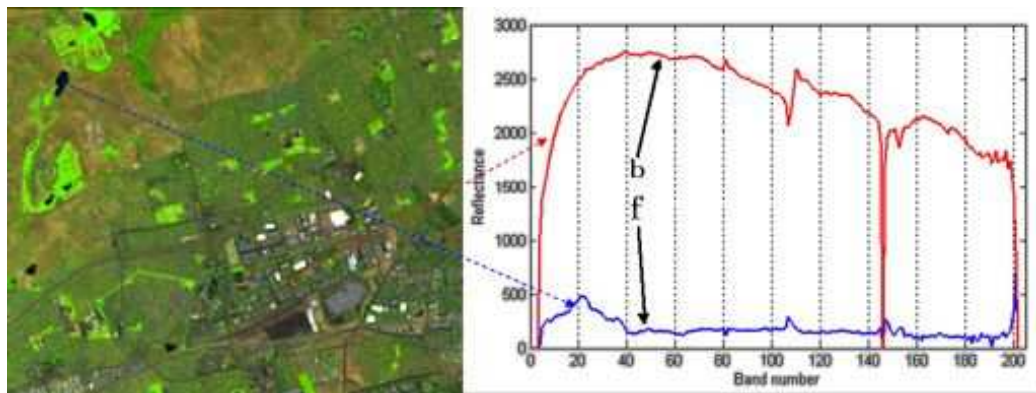


Figure 4.15: HSI Moffett Field sub-scene using bands $\{115,70,30\}$. Reference pixels (background **b** and foreground **f**) used in the experiments. Curves are plots of the spectral values in the different frequency bands for the reference pixels.

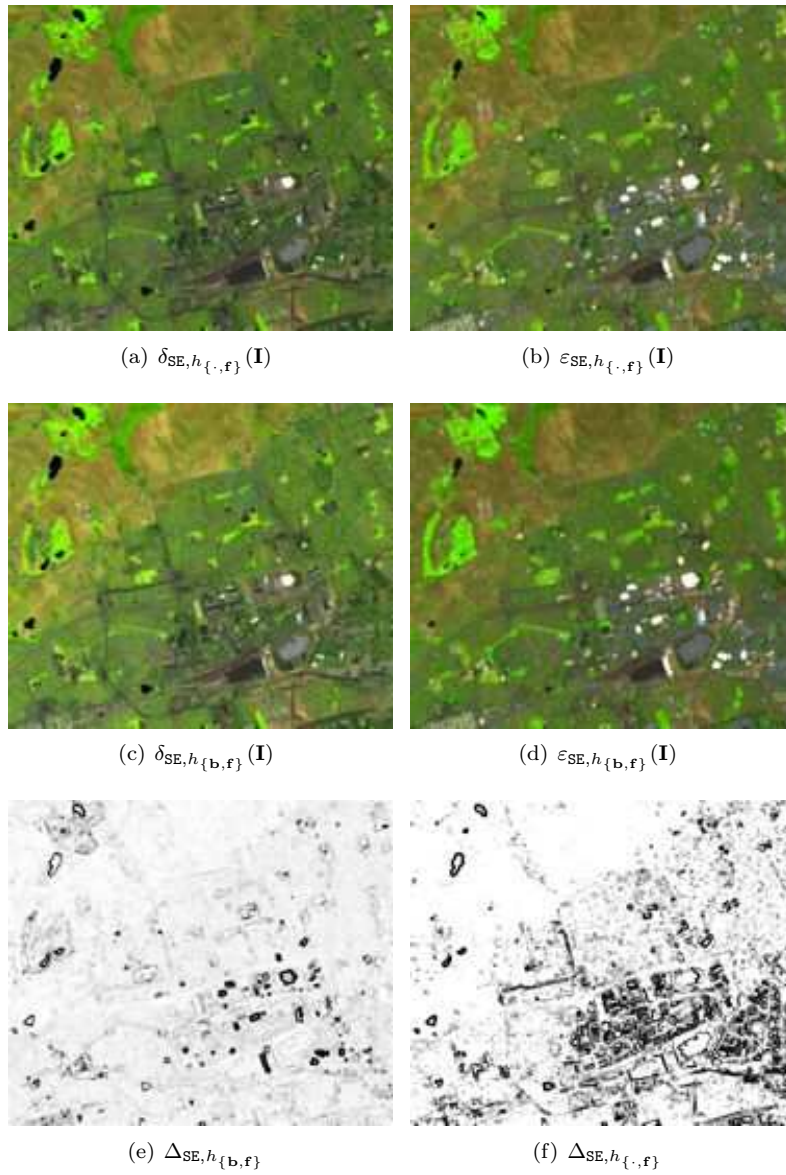


Figure 4.16: Comparison of different supervised morphological operators for $h_{\{\cdot, f\}}$ and $h_{\{\mathbf{b}, f\}}$. Spectra are showed using bands $\{115, 70, 30\}$. Both h -orderings are calculated using (4.9) with a polynomial kernel of degree two.

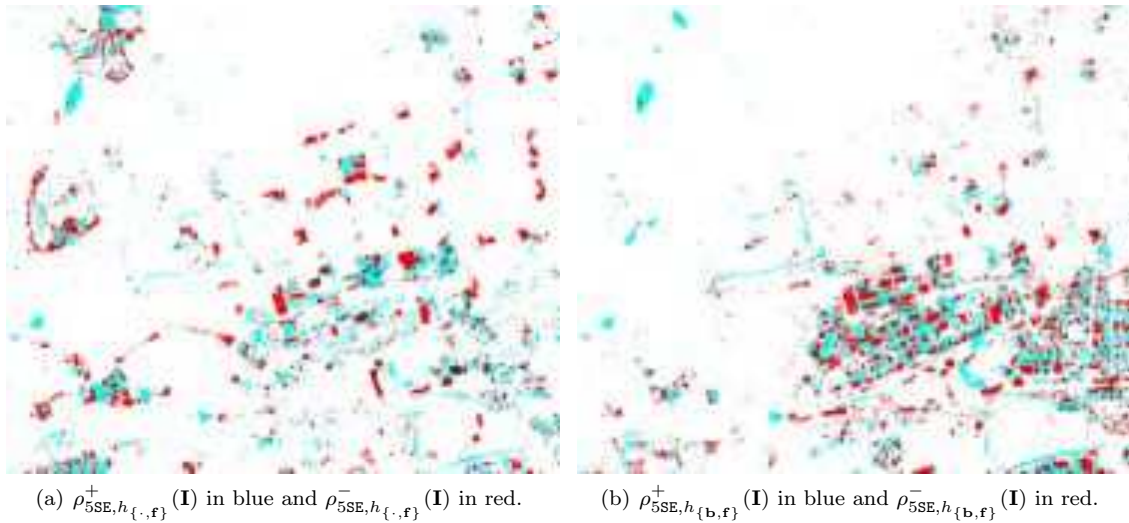


Figure 4.17: Comparison of supervised top-hats. In the single reference ordering ($h_{\{f\}}$) [Angulo \(2007\)](#) positive top-hat detects the spatial component with spectral information close to the water (\mathbf{f}) in blue. However interpretation of the negative top-hat is not easy to perceive. For the proposed $h_{\{b,f\}}$ positive top-hat has similar interpretation than $h_{\{f\}}$ and negative top-hat can be explicated with respect to the spectral data included in **b**.

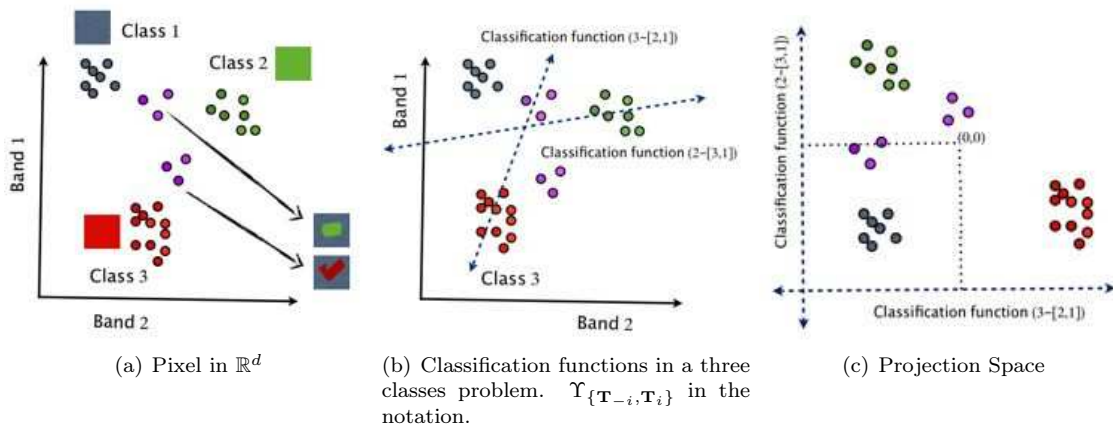


Figure 4.18: Given a training set of three classes, the pixels in the original image $\mathbf{I} \in \mathbb{R}^d$ are projected to \mathbb{R}^J , where J is the number of classes by using supervised evaluation functions.

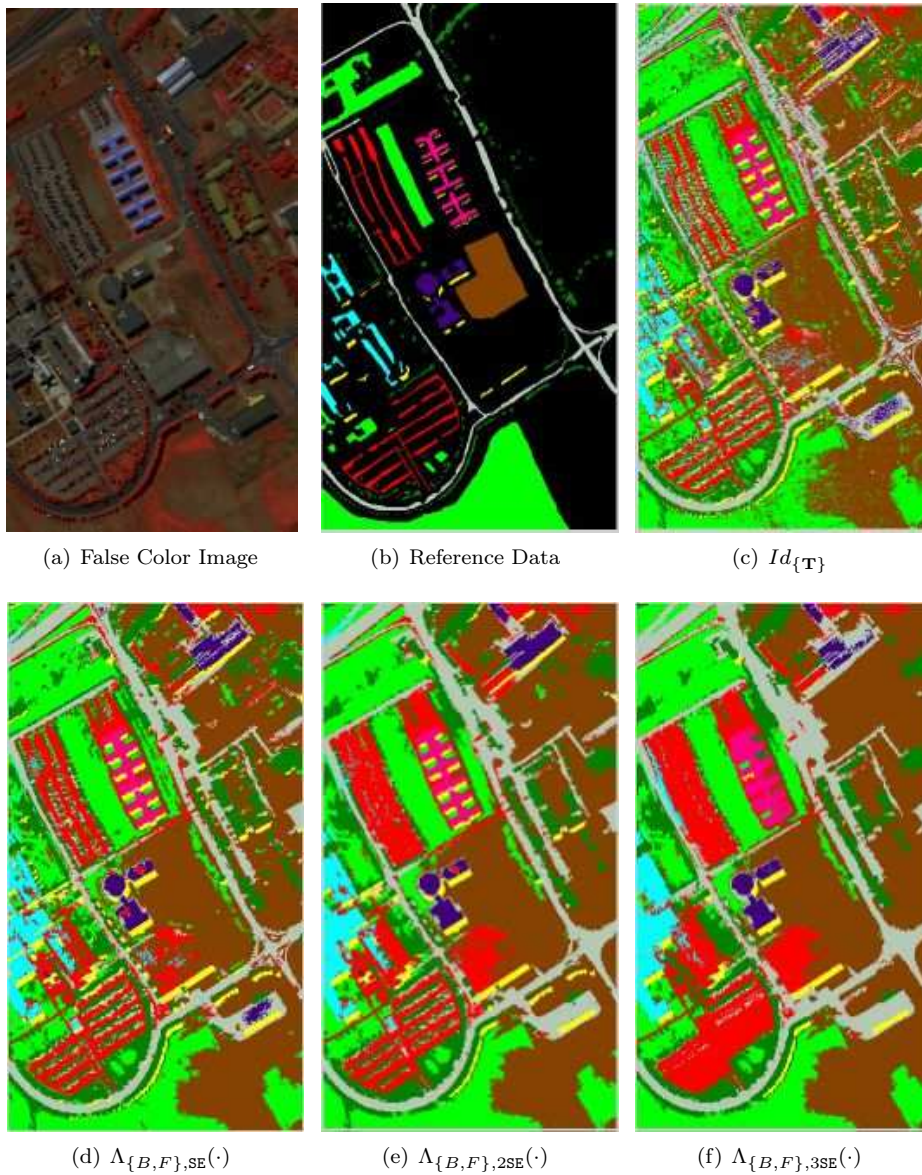


Figure 4.19: A false colour of the original image is shown using bands number [80,70,30]. Morphological driven-classification using leveling operator with unitary structuring element hexagonal SE. $h_{\{\mathbf{T}_i, \mathbf{T}_i\}}$ is obtained using SVM, with polynomial kernel of degree two.

5

Hit-or-miss transform in multivariate images

Yes, I've learnt from my mistakes and I think I'm now able to repeat them almost exactly.
Peter Cook

Résumé

La transformation en Tout-Ou-Rien est un opérateur morphologique classique pour l'appariement par forme de référence sur des images binaires. Une approche originale pour les images multivariées est introduite dans ce chapitre. Le cadre proposé est une généralisation du cas binaire en utilisant l'ordre-h supervisé introduit au chapitre 4. En particulier, nous nous concentrons sur l'application de la transformation en Tout-Ou-Rien multivariée à la détection de cibles sur des images à haute résolution spatiale. Les résultats ainsi obtenus montrent la performance de l'approche proposée¹.

5.1 Introduction

Since the first Landsat satellite was launched by the NASA in 1972, satellite remote sensing has become an important source of data for better understanding the earth's natural resources, and to increase the number of researchers in image processing with applications from international security system to archaeology. Depending on the sensor systems, civil and commercial satellites can produce several types of imagery data, including high-resolution RGB, panchromatic, multispectral, hyperspectral and radar, each of which have particular advantages and withdraws, depending on the specific requirements of the user. An efficient template matching operator to deal with automatic processing of these huge collections of images to extract spatial/spectral structures matching with a prototype or target is required in many applications. In the literature, template matching as hypothesis test under Gaussian distribution assumptions, feature template matching in low-dimensional representation, matching points using Hausdorff Distance [Sim et al. \(1999\)](#), [Zhu et al. \(2004\)](#) and normalised cross-correlation, are the most frequently alternatives to solve this problem. However, the extension to vector images is not evident or it requires strong theoretical assumptions. On the other hand, mathematical morphology (MM) offers several tools for image processing, including a template matching operator called the Hit-or-Miss Transform (HMT). This operation was devised in [Serra \(1982\)](#) in the mid-sixties, but unfortunately, there are not an unique extension to grey-level

¹The content of this chapter is mainly based on the published paper, [Velasco-Forero and Angulo \(2010a\)](#), "*Hit-or-miss Transform in Multivariate Images*" in *Advanced Concepts for Intelligent Vision Systems*, vol. 6474 of *Lecture Notes in Computer Science*, pp. 452–462. Springer-Verlag.

images Soille (2002, 2003), Naegel et al. (2007), Ronse (1996), or multivariate images Aptoula and Lefèvre (2009), Weber and Lefevre (2008). Our approach, it is inspired by ideas presented in chapter 4, see also Velasco-Forero and Angulo (2010b), using supervised ordering to formulate a HMT for multiband images as a natural extension of the binary case to complete lattices. In this chapter, we use the Support Vector Machines (SVMs) to calculate the supervised ordering Cristianini and Shawe-Taylor (2000). SVMs constructs a set of hyperplanes in a high dimensional space, to separate in two classes, the vectors emanate from $\{F\}$ and $\{B\}$. Thus, the distance to that maximum-margin hyperplane can be employed as a supervised ordering. See details in previous chapter.

5.2 Hit-or-Miss Transform in Multivariate Images

We briefly recall in this section the definition of the Hit-or-Miss Transform, then we explain how these notion can be extended to colour and multivariate images.

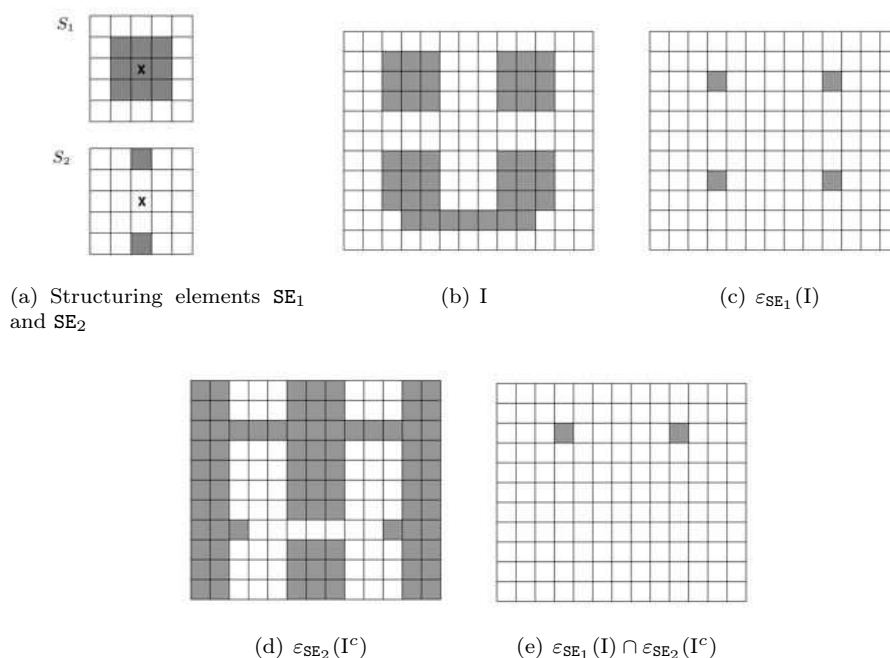


Figure 5.1: Illustrative example of Hit-or-Miss transform for the set I : $HMT(I; SE_1, SE_2)$

5.2.1 Hit-or-Miss Transform in Binary Images

A pattern probe SE called *structuring element* (SE) is involved in most of the morphological operators. In binary case, at it was presented in Soille (2003): “the first question that may arise when we probe a set with a structuring element is: Does the structuring element fit the set? The eroded set is the locus of points where the answer to this question is affirmative.” Thus the erosion of a set I by a structuring element SE is denoted by $\varepsilon_{SE}(I)$ and it is defined by:

$$\varepsilon_{SE}(I) = \bigcap_{x \in SE} I_{-x} \quad (5.1)$$

The hit-or-miss transform (HMT) is a fundamental operation on binary images. In fact, historically it is one of the first operators introduced in mathematical morphology (Serra (1982)). In such images, this operator uses two disjoint structuring elements: the first has to match the foreground

while the second has to match the background. Both matches are necessary in order the operator to give a positive matching response. HMT uses a pair $(\text{SE}_1, \text{SE}_2)$ of SEs, and looks for all positions where SE_1 can be fitted within a set I , and SE_2 within the background I^c , in other words, it is defined by:

$$HMT(I; \text{SE}_1, \text{SE}_2) = \varepsilon_{\text{SE}_1}(I) \cap \varepsilon_{\text{SE}_2}(I^c) \quad (5.2)$$

One assumes that $\text{SE}_1 \cap \text{SE}_2 = \emptyset$, otherwise we always have $HMT(I; \text{SE}_1, \text{SE}_2) = \emptyset$. One calls SE_1 and SE_2 , respectively, the foreground and background SE. Fig. 5.1 presents the binary HMT for a pedagogical example. We remark that HMT is simultaneously finding templates for the both pattern contained in the SEs, for the set I and its complementary dual. Let us define the binary image I as the indicator function of the set I , i.e., $I(x) = 1$ if $x \in I \subseteq E$ and zero otherwise. Consequently, we can rewrite (5.2) as follows,

$$HMT(I; \text{SE}_1, \text{SE}_2) = \{x \in E \mid \varepsilon_{\text{SE}_1}(I(x)) = \varepsilon_{\text{SE}_2}(I^c(x)) = 1\} \quad (5.3)$$

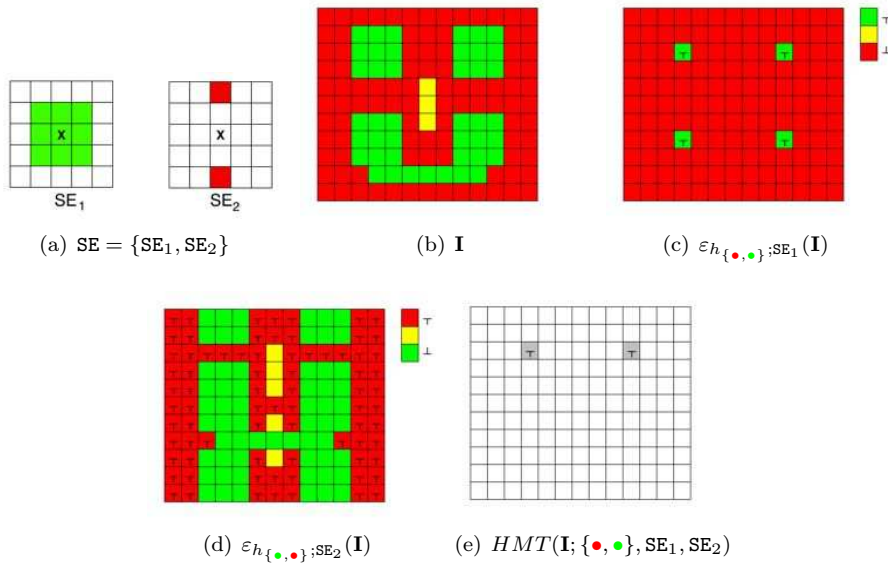


Figure 5.2: From the binary HMT 5.1 to the extension for multiband images in the supervised ordering. The proposed Hit-or-miss transform (e) finds pixels such that both erosions detect the corresponding spectrum associated to the SE, i.e., $\varepsilon_{h_{\{\bullet, \bullet\}}; \text{SE}_1}(I) = \bullet = \top_1$ and $\varepsilon_{h_{\{\bullet, \bullet\}}; \text{SE}_2}(I) = \bullet = \top_2$. The lattice induced by the h -supervised ordering is presented in each case, using \perp and \top for least and greatest values in the corresponding ordering.

5.2.2 Hit-or-miss Transform in supervised h -orderings

We introduce now an extension of hit-or-miss transformation for multivariate images in the framework of supervised h -orderings. The proposal can be used to find an exact template matching in the original multivariate image I with the structuring element $\text{SE} = \text{SE}_1 \cup \text{SE}_2$ with $\text{SE}_1 \cap \text{SE}_2 = \emptyset$ and $\text{SE}_1, \text{SE}_2 \in E$, where E is the support space of the image. Our approach defines HMT using the h -supervised ordering presented in Chapter 4, as a natural extension of the original HMT defined in the binary case. It is important to remark that expression 5.3 can be expressed in term of h -supervised ordering as follows,

$$HMT(I; \text{SE}_1, \text{SE}_2) = \{x \in E \mid h_{\{0,1\}}(\varepsilon_{\text{SE}_1, h_{\{0,1\}}}(I)) = \mathbf{1} \wedge h_{\{1,0\}}(\varepsilon_{\text{SE}_2, h_{\{1,0\}}}(I)) = \mathbf{0}\}$$

In the case that \mathbf{I} and \mathbf{SE} are sets, then the natural order is $\{\mathbf{0} = \perp, \mathbf{1} = \top\}$ and the complement inverses the order to $\{\mathbf{1} = \perp, \mathbf{0} = \top\}$. In the h -supervised ordering the inverse ordering, associated to complementation can be induced interchanging the referenced set $\{B, F\}$ by $\{F, B\}$. Thus the expression 5.3 can be generalised using the h -supervised ordering as follows,

$$HMT(\mathbf{I}; \{B, F\}, \mathbf{SE}_1, \mathbf{SE}_2) = \{x \in \mathbf{E} \mid \forall i \in \{1, 2\}, h_i(\varepsilon_{\mathbf{SE}_i, h_i}(\mathbf{I}(x))) = \top_i\} \quad (5.4)$$

where

$$h_i = \begin{cases} h_{\{B, F\}} \mid h(\mathbf{b}) = \perp, h(\mathbf{f}) = \top & \text{if } i=1, \\ h_{\{F, B\}} \mid h(\mathbf{f}) = \perp, h(\mathbf{b}) = \top & \text{if } i=2. \end{cases}$$

From 5.4, it easy to note that for each structuring element there are a set of vector value associated. Therefore, we introduce a *generalised* HMT based on the sets of couples $\{B_i, \mathbf{SE}_i\}_{i=1, \dots, k}$ such that $\mathbf{SE}_i \subset \mathbf{E}, \mathbf{SE}_i \cap \mathbf{SE}_j = \emptyset, \forall i \neq j$, and $B_i \subset \mathbb{F} = \mathbb{R}^d$, as follows,

$$HMT(\mathbf{I}; \{B_i, \mathbf{SE}_i\}) = \{x \in \mathbf{E} \mid \forall i \in \{1, 2, \dots, k\}, h_{\{B_i, B_{-i}\}}(\varepsilon_{\mathbf{SE}_i, h_{\{B_i, B_{-i}\}}}(\mathbf{I}(x))) = \top_i\} \quad (5.5)$$

where $B_{-i} = \bigcup_{j \neq i} B_j$, $\{\mathbf{SE}_i\}_{i=1 \dots k}$ is the family of structuring elements and $\{B_i\}_{i=1 \dots k}$ is the family of vector values associated with $\{\mathbf{SE}_i\}_{i=1 \dots k}$. The expression 5.4 is a particular case when $i = 2$, $B_1 = B$ and $B_{-1} = F$.

For practical applications, the generalised HMT can be useful as a template matching technique, but it requires to be robust to noise and easy to tune parameters. We refer keen readers to [Aptoula and Lefèvre \(2009\)](#) for a comprehensive review of robust HMT in grey scale images using a different framework. In our formulation, the robust against noise version can be naturally defined by including a threshold ϵ in equation 5.5 to allow a degree of noise in the “detection” of each \mathbf{SE}_i related to B_i . Thus, the HMT_ϵ is defined as follows,

$$HMT_\epsilon(\mathbf{I}; \{B_i, \mathbf{SE}_i\}) = \{x \in \mathbf{E} \mid \forall i, h_{\{B_i, B_{-i}\}}(\top_i) - h_{\{B_i, B_{-i}\}}(\varepsilon_{\mathbf{SE}_i, h_{\{B_i, B_{-i}\}}}(\mathbf{I}(x))) \leq \epsilon\} \quad (5.6)$$

Clearly 5.4 is a particular case of 5.6 with $\epsilon = 0$. The parameter ϵ can be interpreted as the allowed maximum difference between each theoretical value \top_i and the value detected for the operator HMT_ϵ .

5.3 Applications to Multivariate Images

In order to illustrate the interest of $HMT_\epsilon(\mathbf{I}; \{B_i, \mathbf{SE}_i\})$ for template matching, we consider two different problems and show the corresponding results

5.3.1 Geometric Pattern Problem

The proposed algorithm is tested using a colour image of size 448×322 with a “diamond pattern” of size 6×6 of different colours. In figure 5.3, the application of multivariate HMT to the original colour image (Figure 5.3(a)) is illustrated using two sets of template to match (Figure 5.3(b-c)). The intermediate steps (h-supervised erosions) are further exemplified in figure 5.3(d-e,g-h). The final detection maps are presented in figure 5.3(f,i). In this toy example, the detection is perfect, and it is according with the natural generalisation from the binary case.

To analyse the robustness of our proposal, the original image is normalised to the interval $[0, 1]$ and then corrupted with white Gaussian noise with variance, $\Sigma = 0.05$. The results were recorded and plotted as Receiver Operating Characteristic (ROC) curves. In that case, HMT_ϵ have to be more accurate to avoid the false positives caused by inadequate parameters. In this experiment, the supervised ordering is calculated using SVMs with Gaussian and polynomial kernels. Figure 5.4(a) shows that the low-degree polynomial kernel has a similar performance that a Gaussian kernel with a adequate parameter σ . Additionally, ROC-curves are presented in 5.4(b) for different noisy versions of the image, with various values of Gaussian noise of variance Σ using a polynomial kernel of degree one.

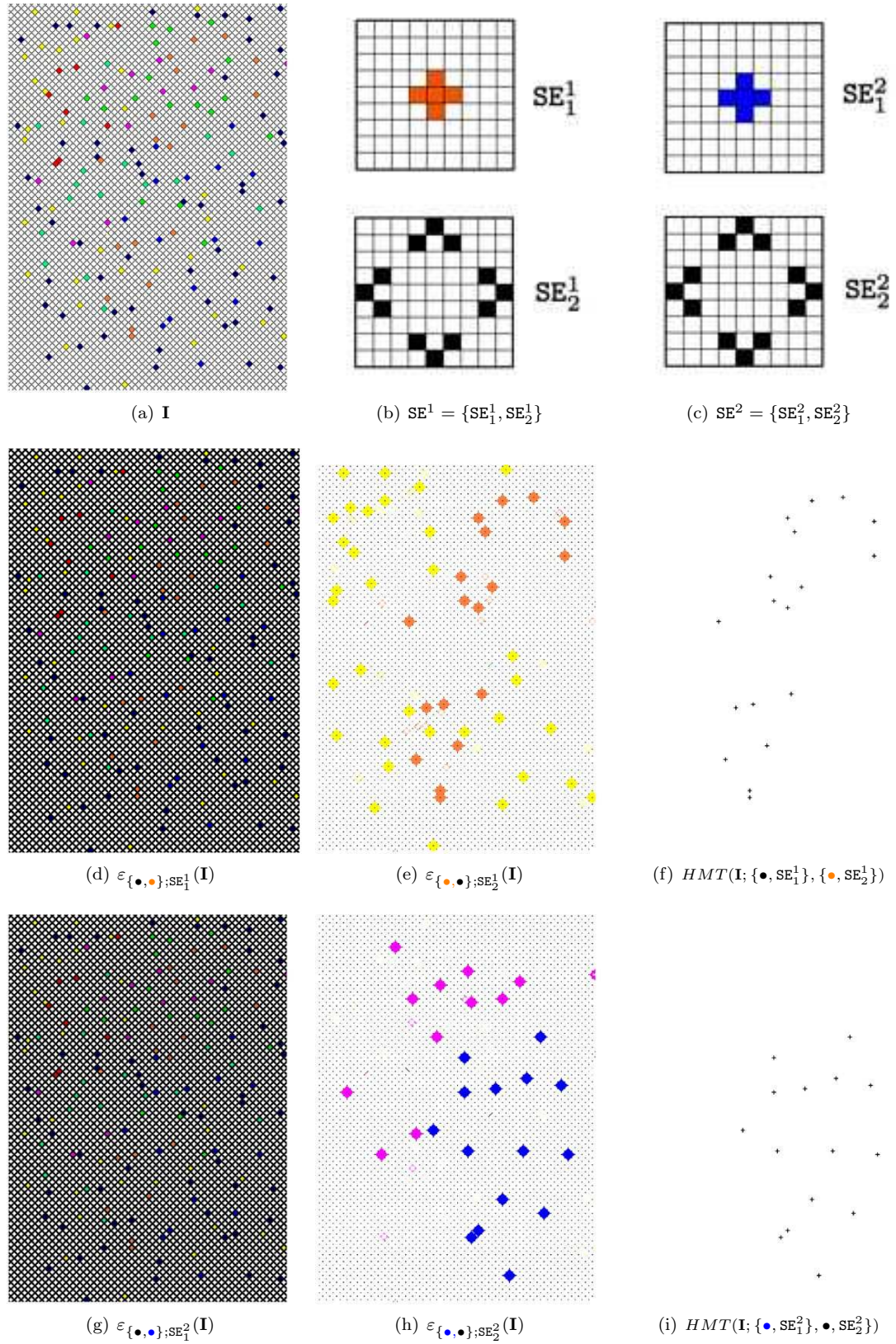
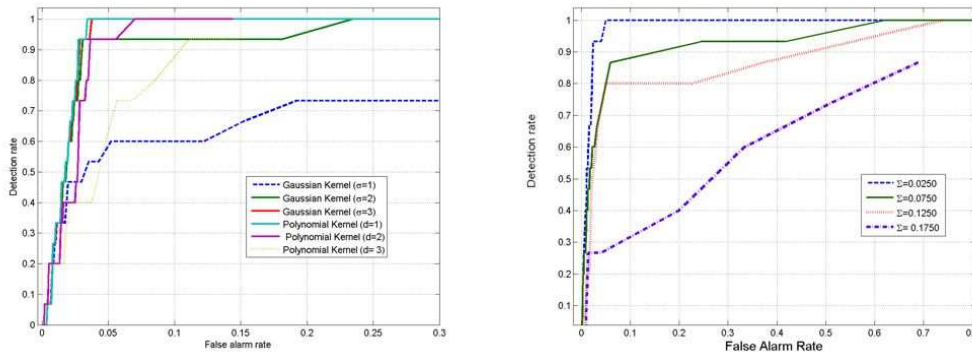


Figure 5.3: Example of colour template matching using the proposed multivariate hit-or-miss transform.



(a) HMT_ϵ using Gaussian and polynomial kernel with different parameters (b) HMT_ϵ using polynomial kernel with different value of noise variance Σ with additive Gaussian noise

Figure 5.4: ROC-curves in the geometric pattern recognition problem

5.3.2 Ship Detection in high-resolution RGB images.

To illustrate the performance of this operator in a real example, we compare the proposed $HMT_\epsilon(\mathbf{I}, \cdot)$ in the extraction of image objects characterised by spectrum and shape simultaneously. This is a natural RGB, 50 centimetre high-resolution, WorldView-2 satellite image featuring the village Samaheej, Bahrain in the Persian Gulf, collected at January 28, 2010, and available in www.digitalglobe.com. The original colour image is reduced to $[2326, 864, 3]$ pixels for improve the visualisation (5.6(a)). Our approach run over that test image for two sets of SEs. The main goal is the extraction of ships using the colour information in $\{B_1, B_2\}$ and the shape information in SE^1, SE^2 . In the first scenario we extract the bigger ships using as SE^1 a square of 47 pixels, such that $SE^1 = \{SE_1^1, SE_2^1\}$ as it is shown in figures 5.5(a) and 5.5(b). The set of pixels background B and foreground F are shown in figures 5.5(e)5.5(f), which roughly correspond to the distribution of colour for the ships and for the ocean. In the second scenario the small ships are extracted using SE^2 as a square of 28 pixels, such that $SE^2 = \{SE_1^2, SE_2^2\}$. SE_1^2 and SE_2^2 are presented in figures 5.5(c-d). The results are presented in figures 5.6 (b-c) for the two scenarios using the proposed robust HMT_ϵ . It is important to remark the sole large ship which is not detected correspond to one (bottom-right 5.6(d)) presenting an orientation which involves that the background shape template (i.e. SE_1^1) does no match in a suitable way. In the case of small ships, some false alarms are obtained, which correspond to objects on the sea and colour similar to the distribution B_1 in the shape SE_2^2 . Obviously, the results should be more robust using a more selective shape prototype of the ship shape as well as a better spectral resolution which would involve more selective values of B_1 and B_2 . The values in the h-ordering were normalised between $[0, 1]$ and the parameter ϵ was fixed to 0.4. An optimal parameter selection can be done, however that is beyond the scope of this illustrative example.

5.4 Conclusions on supervised multivariate hit-or-miss

We have introduced a genuine extension of the classical binary Hit-or-miss transform based on h-supervised ordering for multivariate images in \mathbb{R}^d . Standard HMT involves a pair of disjoint structuring elements, one for the foreground and the other el background. Hence, our formulation of supervised h-orderings which requires training sets for the foreground and background is appropriate for the definition of generalised HMT. In addition, the natural duality by inverting foreground and background solves the complementation required for the binary formulation of HMT. More practically, the interest of the HMT transform for combined spatial/spectral image detection has been illustrated for multivariate images. The combination of prior information given by the shape of the structuring elements as well as the spectral values for the foreground and background is compatible

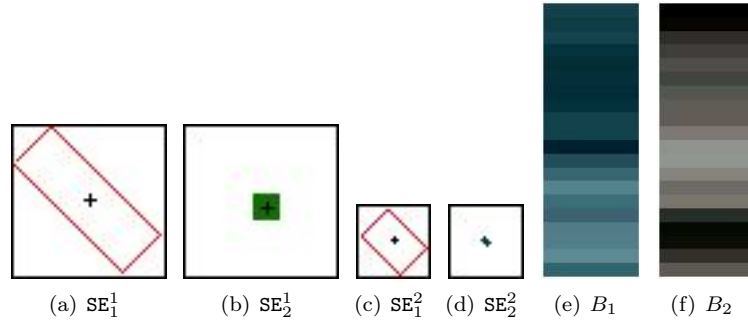


Figure 5.5: SEs considered in the Bahrain Image. In both scenarios, the sets of pixels background (B_1) and foreground (B_2) are the same.

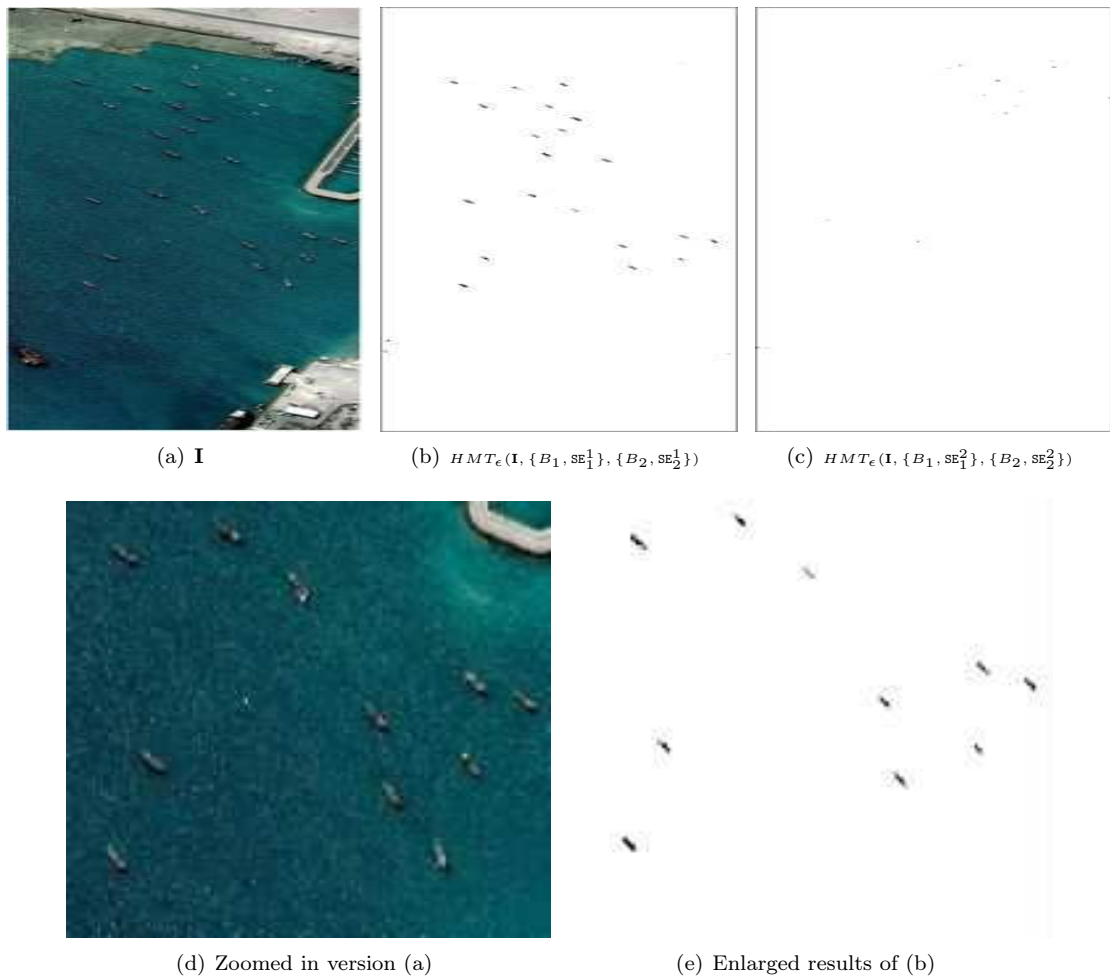


Figure 5.6: Ship detection in High-Resolution Samaheej Image using HMT_ϵ

with the current paradigm of structural target detection in remote sensing applications. We should remark also that our supervised morphological framework can simultaneously implementing HMT where templates have the same shape but different alternative values for the foreground/background.

We have also studied the influence of the learning method (i.e., kernel parameters of SVM), used in the construction of the h-ordering, in the results of the HMT. This robustness as well as the good properties against noise of HMT entail promising perspectives for its application in many real problems. In ongoing research two issues should be considered in depth. On the one hand, to evaluate the interest of non-flat erosions in the construction of HMT, which will allow to define more "fuzzy" structuring elements. On the other, to conceive different ways of parallelisation of the HMT for an efficient implementation of the generic case where a family of templates is associated to the target structure, e.g., group of rotations and scale transformation of the object shape.

6

Random projection depth for unsupervised multivariate mathematical morphology

Probability is a lot of logic at once: If you don't know which one to pick, take 'em all.
Tommaso Toffoli

Résumé

Le problème ouvert de la généralisation de la morphologie mathématique à des images vectorielles est géré dans ce chapitre par l'utilisation du paradigme des fonctions de profondeur statistique. Celles-ci fournissent, à partir du point «le plus profond», un «ordre centre-vers-extérieur» de la distribution de données multidimensionnelles et elles peuvent être alors utilisées pour construire des opérateurs morphologiques. L'hypothèse fondamentale de cette approche «adaptée aux données» est l'existence d'une représentation «arrière-plan/premier plan» de l'image. Des exemples sur des images réelles en couleurs et multivariées illustrent les résultats¹.

6.1 Introduction

In this chapter, a P-ordering for pixels in multivariate images is presented. To the best of our knowledge, this is the first approach which uses P-ordering to extend MM to multivariate image. Fig. 6.1 gives the intuition of the proposed ordering.

The chapter is organised as follows. Restricting ourselves to data in vector spaces, in Section 6.2 the statistical depth functions definition is reviewed. This is the basic ingredient for the construction of P-ordering. The case of projection depth function is analysed in detail and its convergence to classical Mahalanobis distance is presented for elliptically contoured distributions. Section 6.3 analyses the application of ordering based on projected depth function in the context of vector images and it presents some interesting properties for practical problems in image processing. Section 6.4 shows

¹The content of this chapter is mainly based on the following published papers:

- [Velasco-Forero and Angulo \(2011a\)](#), "Mathematical morphology for vector images using statistical depth". In *Mathematical Morphology and Its Applications to Image and Signal Processing*, vol. 6671 of *Lecture Notes in Computer Science*, pp. 355–366. Springer.
- [Velasco-Forero and Angulo \(2012\)](#), "Random projection depth for multivariate mathematical morphology". *IEEE-Journal of Selected Topics in Signal Processing*, accepted.

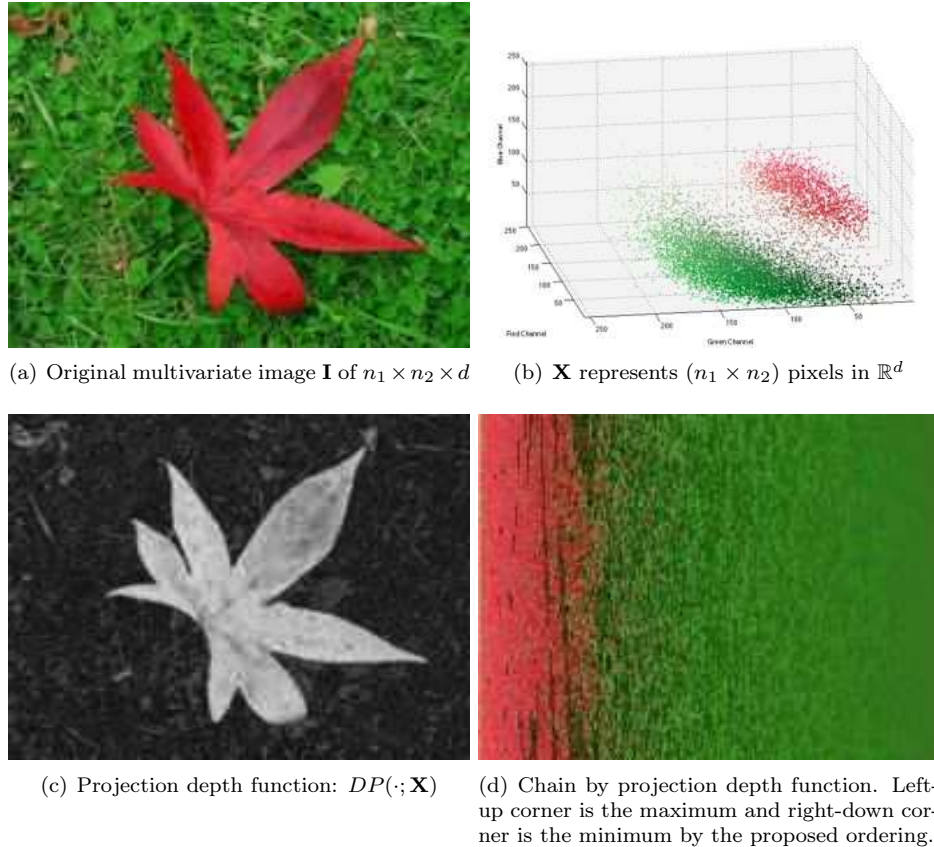


Figure 6.1: Intrinsic ordering based on dichotomy background and foreground. $\mathbf{x}_1 < \mathbf{x}_2 \Leftrightarrow DP(\mathbf{x}_1; \mathbf{I}) < DP(\mathbf{x}_2; \mathbf{I})$

the effectiveness of the proposed approach via practical examples and visual comparison in image enhancement, simplification and segmentation. Finally, Section 6.5 concludes the chapter.

6.2 Statistical depth functions

6.2.1 Definition

Depth functions for multivariate data have been pursued in nonparametric data analysis and robust inference [Zuo and Serfling \(2000\)](#). Depth functions assign to each point its degree of centrality with respect to a data cloud or a probability distribution. A depth function suitable for a distribution \mathfrak{F} in \mathbb{R}^d , denoted by $D(\mathbf{x}; \mathfrak{F})$, brings out the non-central ranking of the vector \mathbf{x} in \mathbb{R}^d with respect to \mathfrak{F} . A number of depth functions are available in the literature, for instance *halfspace depth* [Tukey \(1975\)](#), *simplicial depth* [Liu \(1990\)](#), *projection depth* [Donoho and Gasko \(1992\)](#), *spatial depth* [Vardi and Zhang \(2000\)](#), *Mahalanobis depth* [Zuo and Serfling \(2000\)](#), etc. Roughly speaking, for a distribution $\mathfrak{F} \in \mathbb{R}^d$, a corresponding depth function $D(\mathbf{x}; \mathfrak{F})$ provides an \mathfrak{F} -based center-outward ordering of point $\mathbf{x} \in \mathbb{R}^d$. Hence, $D(\mathbf{x}; \mathfrak{F})$ is a function $\mathbb{R}^d \rightarrow \mathbb{R}$. Depth-based methods are completely data-driven and avoid strong distributional assumption. Moreover, they provide intuitive visualisation of the data set via depth contours for a low dimensional input space. Analogous to linear order in one dimension, statistical depth functions provide an ordering of all points from the centre outward in a multivariate data set, where the median is the “deepest” point in the data set. This leads to centre-outward ordering to points and to a description in terms of nested contours. Let us start by

a formal definition of a depth function.

Definition 1. *Liu (1990), Zuo and Serfling (2000)* A statistical depth function is a bounded non-negative mapping $D(\cdot; \cdot) : \mathbb{R}^d \times \mathfrak{F} \rightarrow \mathbb{R}$ satisfying

1. $D(\mathbf{A}\mathbf{x} + \mathbf{b}; \mathfrak{F}_{\mathbf{A}\mathbf{x} + \mathbf{b}}) = D(\mathbf{x}; \mathfrak{F})$ holds for any random vector \mathbf{x} in \mathbb{R}^d , any $d \times d$ nonsingular matrix \mathbf{A} , and any $\mathbf{b} \in \mathbb{R}^d$, where $\mathfrak{F}_{\mathbf{A}\mathbf{x} + \mathbf{b}}$ denotes the distribution \mathfrak{F} after rotation by \mathbf{A} and translation by \mathbf{b} . That invariance to affine transformation means, the depth of a vector $\mathbf{x} \in \mathbb{R}^d$ should not depend on the underlying coordinate system or, in particular, on the scales of the underlying measurements.
2. $D(\theta; \mathfrak{F}) = \sup_{\mathbf{x} \in \mathbb{R}^d} D(\mathbf{x}; \mathfrak{F})$ holds for any \mathfrak{F} having center θ . That means, for any distribution having a unique ‘‘centre’’, the depth function should attain maximum value at this centre.
3. $D(\mathbf{x}; \mathfrak{F}) \leq D(\theta + \alpha(\mathbf{x} - \theta); \mathfrak{F})$ holds for any \mathfrak{F} having a deepest point θ and any $\alpha \in [0, 1]$, i.e., as a point $\mathbf{x} \in \mathbb{R}^d$ moves away from the ‘‘deepest point’’ along any fixed ray through the centre, the depth at \mathbf{x} should decrease monotonically.
4. $D(\mathbf{x}; \mathfrak{F}) \rightarrow 0$ as $\|\mathbf{x}\| \rightarrow \infty$, for each \mathfrak{F} , i.e., the depth of a point \mathbf{x} should approach to zero as its norm approaches infinity.

In the sequel, we focus on the *projection depth function* Donoho and Gasko (1992), and we describe some useful properties to support it as a clever option to produce P-order. Other statistical depth functions have considered in our preliminary work Velasco-Forero and Angulo (2011a) for vector morphology. However, projection depth function presents the best trade-off between robustness and computation time.

6.2.2 Projection depth function

The basic concept of a projection depth function was introduced by Donoho and Gasko (1992) and posteriorly developed by Zuo and Serfling (2000), Zuo (2003). It defines the measure of centrality for a vector \mathbf{x} with respect to a multivariate distribution or a multivariate data cloud (\mathbf{X}) as the worst case outlyingness with respect to the one-dimensional scale functional in any one-dimensional projection, that is,

Definition 2. *Donoho and Gasko (1992)* The projection depth function for a vector \mathbf{x} according with a data cloud $\mathbf{X} = [\mathbf{x}_1, \dots, \mathbf{x}_n]$ as follows,

$$DP(\mathbf{x}; \mathbf{X}) = \sup_{\mathbf{u} \in \mathbb{S}^{d-1}} \frac{|\mathbf{u}^T \mathbf{x} - \text{med}(\mathbf{u}^T \mathbf{X})|}{\text{mad}(\mathbf{u}^T \mathbf{X})} \quad (6.1)$$

where med is the median and mad is the median absolute deviation (MAD) and $\mathbb{S}^{d-1} = \{\mathbf{x} \in \mathbb{R}^d : \|\mathbf{x}\|_2 = 1\}$ is the d -dimensional hypersphere. Fig. 6.2 shows two random projections to compute (6.1) in a simple example. MAD is a robust estimator of variability attributed to Gauss in 1816 Hampel et al. (1986). The pair of robust estimators (med, mad) is included in (6.1) because they are not unduly affected by outliers Zuo (2003). Projection depth has been used to robust multivariate classification Cui et al. (2008) and classification of functional data Cuevas et al. (2007). Note that $DP(\mathbf{x}; \mathbf{X})$ is impossible to calculate in practice, because it requires the analysis for an infinite set of random projections. Our approach follows the suggestion of Zuo (2006): replacing the supremum in (6.1) by a maximum over a finite number of randomly chosen projection, obtaining a stochastic approximation to the random projection depth. The same argument have been used in Cuesta-Albertos and Nietos-Reyes (2008) for other type of statistical depth function. Thus, we can calculate an approximate value of $DP(\mathbf{x}; \mathbf{X})$ by using k random projections uniformly distributed in \mathbb{S}^{d-1} as follow

$$DP(\mathbf{x}; k, \mathbf{X}) = \max_{\mathbf{u} \in \mathbb{U}} \frac{|\mathbf{u}^T \mathbf{x} - \text{med}(\mathbf{u}^T \mathbf{X})|}{\text{mad}(\mathbf{u}^T \mathbf{X})} \quad (6.2)$$

where $\mathbb{U} = \{\mathbf{u}_1, \mathbf{u}_2, \dots, \mathbf{u}_k\}$ with $\mathbf{u}_i \in \mathbb{S}^{d-1}$. Clearly, if $k \rightarrow \infty$ then $DP(\mathbf{x}; k, \mathbf{X}) \rightarrow DP(\mathbf{x}; \mathbf{X})$.

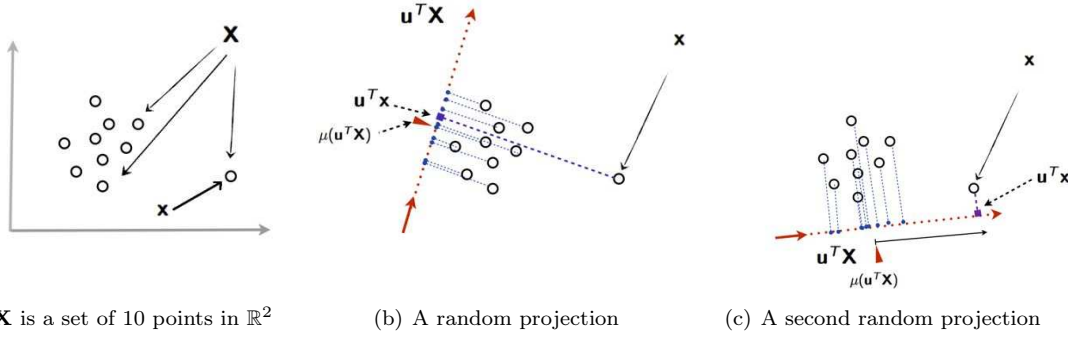


Figure 6.2: Toy example of the computation of (6.1). Projection depth function for a vector \mathbf{x} given \mathbf{X} is basically the maxima normalised eccentricity for all the possible projection $\mathbf{u}^T \mathbf{X}$ given a couple of centrality and variability univariate measures (μ, σ) .

6.2.3 Equivalence in Elliptically Symmetric Distribution

The depth function admits an analytical formulation when elliptically symmetric random variables are considered.

Definition 3. *Fang et al. (1990)* A $d \times 1$ random vector \mathbf{x} is said to have an elliptically symmetric distribution with parameters $\boldsymbol{\mu}_{(d \times 1)}$ and a semidefinite matrix $\boldsymbol{\Sigma}_{(d \times d)}$ if

$$\mathbf{x} \stackrel{\text{dist}}{=} \boldsymbol{\mu} + \mathbf{A}^T \mathbf{y} \quad (6.3)$$

where, $\mathbf{A}^T \mathbf{A} = \boldsymbol{\Sigma}$ with $\text{rank}(\boldsymbol{\Sigma}) = r$. Where $\mathbf{y} \stackrel{\text{dist}}{=} \alpha \mathbf{u}^{(r)}$, $\alpha \in \mathbb{R}$, $\mathbf{u}^{(r)}$ denote a random vector distributed uniformly on the unit sphere surface in \mathbb{R}^r and $\stackrel{\text{dist}}{=}$ means equality in distribution.

Proposition 1. *Fang et al. (1990)* The d -dimension random vector \mathbf{X} has a multivariate elliptical distribution, written as $\mathbf{X} \sim E_d(\boldsymbol{\mu}, \boldsymbol{\Sigma}, \psi)$, if its characteristic function can be expressed as:

$$\phi_{\mathbf{X}} = \exp(it^T \boldsymbol{\mu}) \psi \left(\frac{1}{2} \mathbf{t}^T \boldsymbol{\Sigma} \mathbf{t} \right) \quad (6.4)$$

for some vector $\boldsymbol{\mu}$, positive-definite matrix $\boldsymbol{\Sigma}$, and for some function ψ , which is called the characteristic generator.

From $\mathbf{X} \sim E_d(\boldsymbol{\mu}, \boldsymbol{\Sigma}, \psi)$, it does not generally follow that \mathbf{X} has a density $f_{\mathbf{X}}(\mathbf{x})$, but, if it exists, it has the following form:

$$f_{\mathbf{X}}(\mathbf{x}) = \frac{c_d}{\sqrt{|\boldsymbol{\Sigma}|}} g_d \left[\frac{1}{2} (\mathbf{x} - \boldsymbol{\mu})^T \boldsymbol{\Sigma}^{-1} (\mathbf{x} - \boldsymbol{\mu}) \right] \quad (6.5)$$

where c_d is the normalisation constant and g_d is some nonnegative function with $(\frac{d}{2} - 1)$ -moment finite. g_d is called density generator *Fang et al. (1990)*. In this case we shall use the notation $E_d(\boldsymbol{\mu}, \boldsymbol{\Sigma}, g_d)$ instead of $E_d(\boldsymbol{\mu}, \boldsymbol{\Sigma}, \psi)$.

Proposition 2. *If \mathbf{x} has a symmetric probability density function $\Phi(\cdot)$ that is continuous and positive on its support then*

$$\frac{\text{mad}^2(\mathbf{x})}{\text{var}(\mathbf{x})} = (\Phi^{-1}(3/4))^2 \quad (6.6)$$

The next result is very well known in linear algebra and it will be used to prove the equivalence of the projection depth function and the Mahalanobis distance; see, for example *Johnson and Wichern (2007)* p. 65.

Proposition 3. For \mathbf{A} a positive definite matrix, and \mathbf{b} a given vector, and \mathbf{u} a non zero arbitrary vector,

$$\sup_{\mathbf{u} \neq \mathbf{0}} \frac{(\mathbf{u}^T \mathbf{b})^2}{\mathbf{u}^T \mathbf{A} \mathbf{u}} = \mathbf{b}^T \mathbf{A}^{-1} \mathbf{b} \quad (6.7)$$

Proposition 4 (Fang et al. (1990) p.43). Assume that $\mathbf{X} \sim E_d(\boldsymbol{\mu}, \boldsymbol{\Sigma}, \psi)$ with $\text{rank}(\boldsymbol{\Sigma}) = r$, \mathbf{B} is a $d \times k$ matrix and \mathbf{v} is a $k \times 1$ vector, then

$$\mathbf{v} + \mathbf{B}^T \mathbf{X} \sim E_d(\mathbf{v} + \mathbf{B}^T \boldsymbol{\mu}, \mathbf{B}^T \boldsymbol{\Sigma} \mathbf{B}, \psi) \quad (6.8)$$

We now state our first proposition for the case of standardised random projections.

Proposition 5. Let $\mathbf{X}_{(d \times n)}$ be a i.i.d. random sample of size n , where $\mathbf{x}_i \sim E_d(\boldsymbol{\mu}, \boldsymbol{\Sigma}, g)$, then:

$$\sup_{\mathbf{u} \in \mathbb{S}^{d-1}} \frac{(\mathbf{u}^T \mathbf{x} - \text{mean}(\mathbf{u}^T \mathbf{X}))^2}{\text{var}(\mathbf{u}^T \mathbf{X})} = (\mathbf{x} - \boldsymbol{\mu})^T \boldsymbol{\Sigma}^{-1} (\mathbf{x} - \boldsymbol{\mu}) \quad (6.9)$$

where mean is the univariate mean and var is the univariate variance.

Proof. From Prop. 4, we have $\text{mean}(\mathbf{u}^T \mathbf{X}) = \mathbf{u}^T \boldsymbol{\mu}$ and $\text{var}(\mathbf{u}^T \mathbf{X}) = \mathbf{u}^T \boldsymbol{\Sigma} \mathbf{u}$. Therefore

$$\begin{aligned} \sup_{\mathbf{u} \in \mathbb{S}^{d-1}} \frac{(\mathbf{u}^T \mathbf{x} - \text{mean}(\mathbf{u}^T \mathbf{X}))^2}{\text{var}(\mathbf{u}^T \mathbf{X})} &= \sup_{\mathbf{u} \in \mathbb{S}^{d-1}} \frac{(\mathbf{u}^T \mathbf{x} - \mathbf{u}^T \boldsymbol{\mu})^2}{\mathbf{u}^T \boldsymbol{\Sigma} \mathbf{u}} \\ \sup_{\mathbf{u} \in \mathbb{S}^{d-1}} \frac{(\mathbf{u}^T (\mathbf{x} - \boldsymbol{\mu}))^2}{\mathbf{u}^T \boldsymbol{\Sigma} \mathbf{u}} &= \sup_{\mathbf{u} \neq \mathbf{0}} \frac{((\mathbf{u}/\|\mathbf{u}\|)^T (\mathbf{x} - \boldsymbol{\mu}))^2}{(\mathbf{u}/\|\mathbf{u}\|)^T \boldsymbol{\Sigma} (\mathbf{u}/\|\mathbf{u}\|)} \end{aligned}$$

by Prop. 3 the proof is complete. \square

Finally, we provide the corresponding particularised result to the case of projection depth function in elliptically *symmetric* random variables.

Proposition 6. Let $\mathbf{X}_{(d \times n)}$ be a i.i.d. random sample of size n , where $\mathbf{x}_i \sim E_d(\boldsymbol{\mu}, \boldsymbol{\Sigma}, g)$, then:

$$c_g DP(\mathbf{x}; \mathbf{X})^2 = (\mathbf{x} - \boldsymbol{\mu})^T \boldsymbol{\Sigma}^{-1} (\mathbf{x} - \boldsymbol{\mu}) \quad (6.10)$$

with $c_g = (\Phi^{-1}(3/4))^2$.

Proof.

$$\begin{aligned} DP(\mathbf{x}; \mathbf{X})^2 &= \sup_{\mathbf{u} \in \mathbb{S}^{d-1}} \left\{ \frac{|\mathbf{u}^T \mathbf{x} - \text{med}(\mathbf{u}^T \mathbf{X})|^2}{\text{mad}^2(\mathbf{u}^T \mathbf{X})} \right\} \\ &= \sup_{\mathbf{u} \in \mathbb{S}^{d-1}} \left\{ \frac{(\mathbf{u}^T (\mathbf{x} - \boldsymbol{\mu}))^2}{\mathbf{u}^T \boldsymbol{\Sigma} \mathbf{u}} \left(\frac{\text{var}(\mathbf{u}^T \mathbf{X})}{\text{mad}^2(\mathbf{u}^T \mathbf{X})} \right) \right\} \end{aligned}$$

and by using Propositions 2 and 5, we obtain:

$$DP(\mathbf{x}; \mathbf{X})^2 (\Phi^{-1}(3/4))^2 = (\mathbf{x} - \boldsymbol{\mu})^T \boldsymbol{\Sigma}^{-1} (\mathbf{x} - \boldsymbol{\mu}).$$

\square

Summarising our theoretical results, projection depth function provides an robust order from the ‘‘centre’’ of multidimensional data to ‘‘outlier’’ values. Theoretically, in the case of elliptically symmetric random variables, it approximates the Mahalanobis distance from the ‘‘vector mean’’ without any covariance matrix estimation. We end this section by providing an implementation of the proposed approach (see Algorithm 1).

Algorithm 1 Calculate $DP(\cdot; \mathbf{X})$ based on k projections

Require: $k \geq 1$ and the data matrix \mathbf{X} of (n) rows and d columns.

Ensure: $\mathbf{y} = DP(\cdot; \mathbf{X})$

```

1:  $\mathbf{y} = \mathbf{0}_{n_1 \times 1}$ 
2: for all  $i = 1$  to  $k$  do
3:    $\mathbf{r} = \text{RANDN}(d, 1)$  (Random Gaussian generation).
4:    $\mathbf{r} = \mathbf{r}/\|\mathbf{r}\|$  (Random value in  $\mathbb{S}^{d-1}$ ).
5:    $\mathbf{p} = \mathbf{X}\mathbf{r}$  (Random projection of the original data).
6:    $\text{medi} = \text{med}(\mathbf{p})$  (Median of the Random projection).
7:    $\mathbf{p} = |\mathbf{p} - \text{medi}|$ 
8:    $\text{madi} = \text{med}(\mathbf{p})$  (MAD of the Random projection).
9:   if  $\text{madi} \neq 0$  then
10:     $\mathbf{p} = \mathbf{p}/\text{madi}$ 
11:     $\mathbf{y} = \max(\mathbf{y}, \mathbf{p})$ 
12:   end if
13: end for

```

6.3 Multivariate vector morphology using projection depth functions

The rationale behind our formulation of MM for multivariate images is to use projection depth functions in the vector space to produce a vector ordering. As discussed above, statistical depth functions provide from the “deepest” point a “centre-outward” ordering of multidimensional data. According to the taxonomy of Barnett’s orderings [Barnett \(1976\)](#), it seems natural to say that statistical depth function involves a P-ordering. However, according to the result provided in the previous section, statistical depth function can be interpreted as a robust estimation, up to a multiplicative constant, of a distance from the centre of the image vector values and consequently it can be considered also as a R-ordering. In fact, from our viewpoint, any P-ordering based on extremeness is essentially a R-ordering according to a particular centrality measure.

Given a vector image $\mathbf{I} \in \mathcal{F}(\mathbb{E}, \mathbb{F})$, let $\mathbf{X}_{\mathbf{I}}$ be the set of vector values of the image, which can be viewed as a cloud of points in \mathbb{F} . [Fig. 6.1](#) shows an example of colour image \mathbf{I} , its representation as points $\mathbf{X}_{\mathbf{I}}$, and the image of the associated depth function $DP(\cdot; \mathbf{I})$. The ordering for two pixel vectors is given by $\mathbf{x}_1 < \mathbf{x}_2 \iff DP(\mathbf{x}_1; \mathbf{I}) < DP(\mathbf{x}_2; \mathbf{I})$. That is an ordering based on a data-adapted function and in such a way that the interpretation of supremum and infimum operations is known a priori, because max values can be associated with “outlier” pixels in the high-dimensional space and min are “central” pixels in \mathbb{R}^d space. Projection depth function can be computed for any image, but is the order associated to the statistical depth function appropriate for any image? Or in other terms, in which cases the notions of “outlier” pixels and “central” pixels make sense? We consider that for such images the assumption of existence of a background/foreground representation is required. Formally we could express the assumption of *background/foreground representation* in this way. Given a vector image $\mathbf{I} : \mathbb{E} \rightarrow \mathbb{F}$, the subset of vector values $\mathbf{X}_{\mathbf{I}}$ has a decomposition $\mathbf{X}_{\mathbf{I}} = \{\mathbf{X}_{B(\mathbf{I})}, \mathbf{X}_{F(\mathbf{I})}\}$ such that $\mathbf{X}_{B(\mathbf{I})} \cap \mathbf{X}_{F(\mathbf{I})} = \emptyset$ and $\text{card}\{\mathbf{X}_{B(\mathbf{I})}\} > \text{card}\{\mathbf{X}_{F(\mathbf{I})}\}$. Roughly speaking, the assumption means: (1) the image has two main components: the background and the foreground; (2) There are more pixels in the background than in the foreground. We notice that there is no hypothesis about the multivariate or spatial distribution of the background $\mathbf{X}_{B(\mathbf{I})}$ and the foreground $\mathbf{X}_{F(\mathbf{I})}$.

The theoretical framework of the proposed morphological operators roots in the notions of h -ordering and h -adjunction introduced in [Goutsias et al. \(1995\)](#). So let us start by a reminder of the main results from [Goutsias et al. \(1995\)](#) useful for our approach.



Figure 6.3: Example of different vector morphology operator in the “White-bird” colour image. Erosions by a disk of radius 10 in the family of orders proposed by [Barnett \(1976\)](#). C-ordering uses the priority red>green>blue. R-ordering is calculated by the saturation component of the colour image. Proposed P-ordering is illustrated in (e).

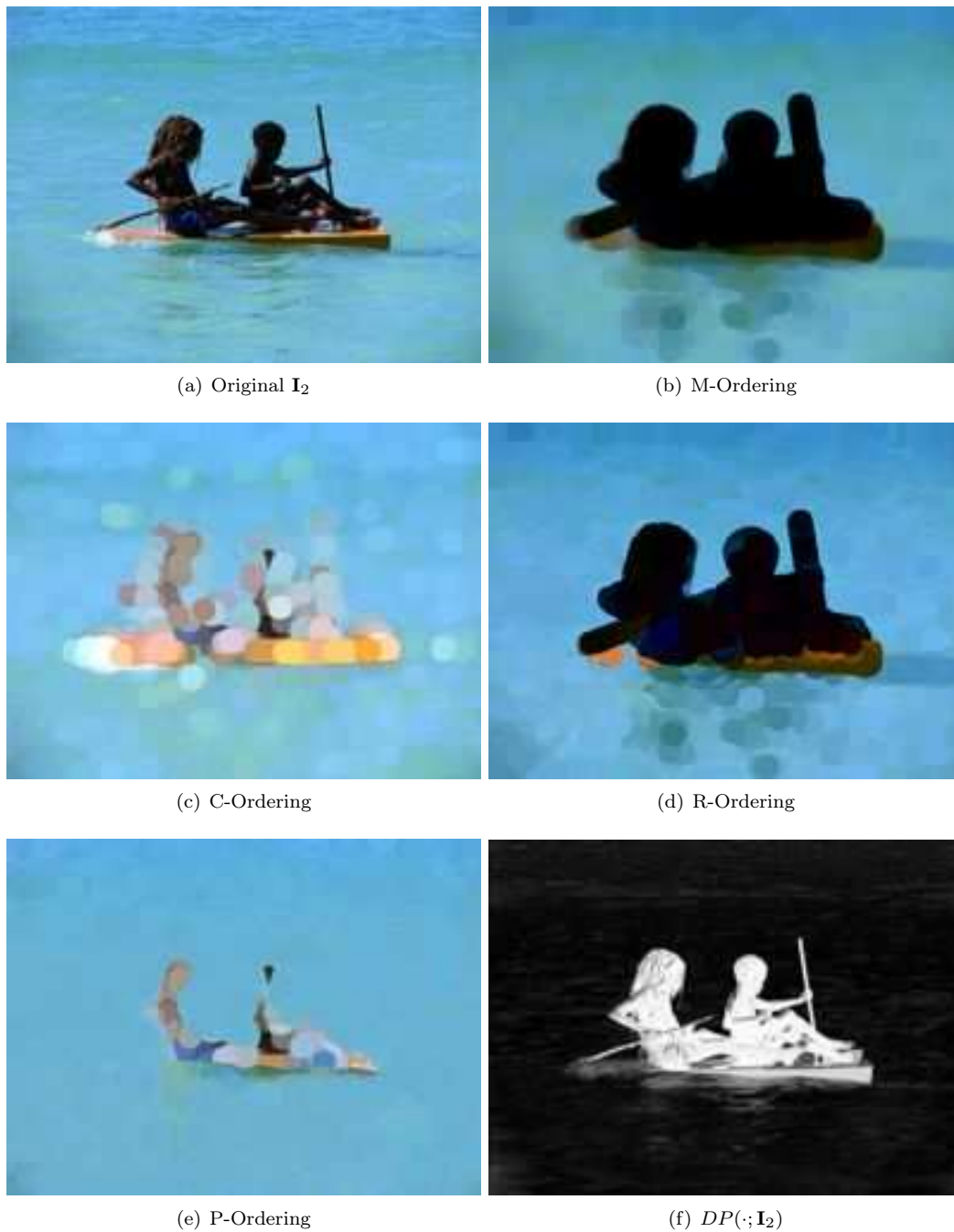


Figure 6.4: Example of different vector morphology operator in the "canoe" colour image. Erosions by a disk of radius 10 in the family of orders proposed by [Barnett \(1976\)](#). C-ordering uses the priority red>green>blue. R-ordering is calculated by the saturation component of the colour image. Proposed P-ordering is illustrated in (e).

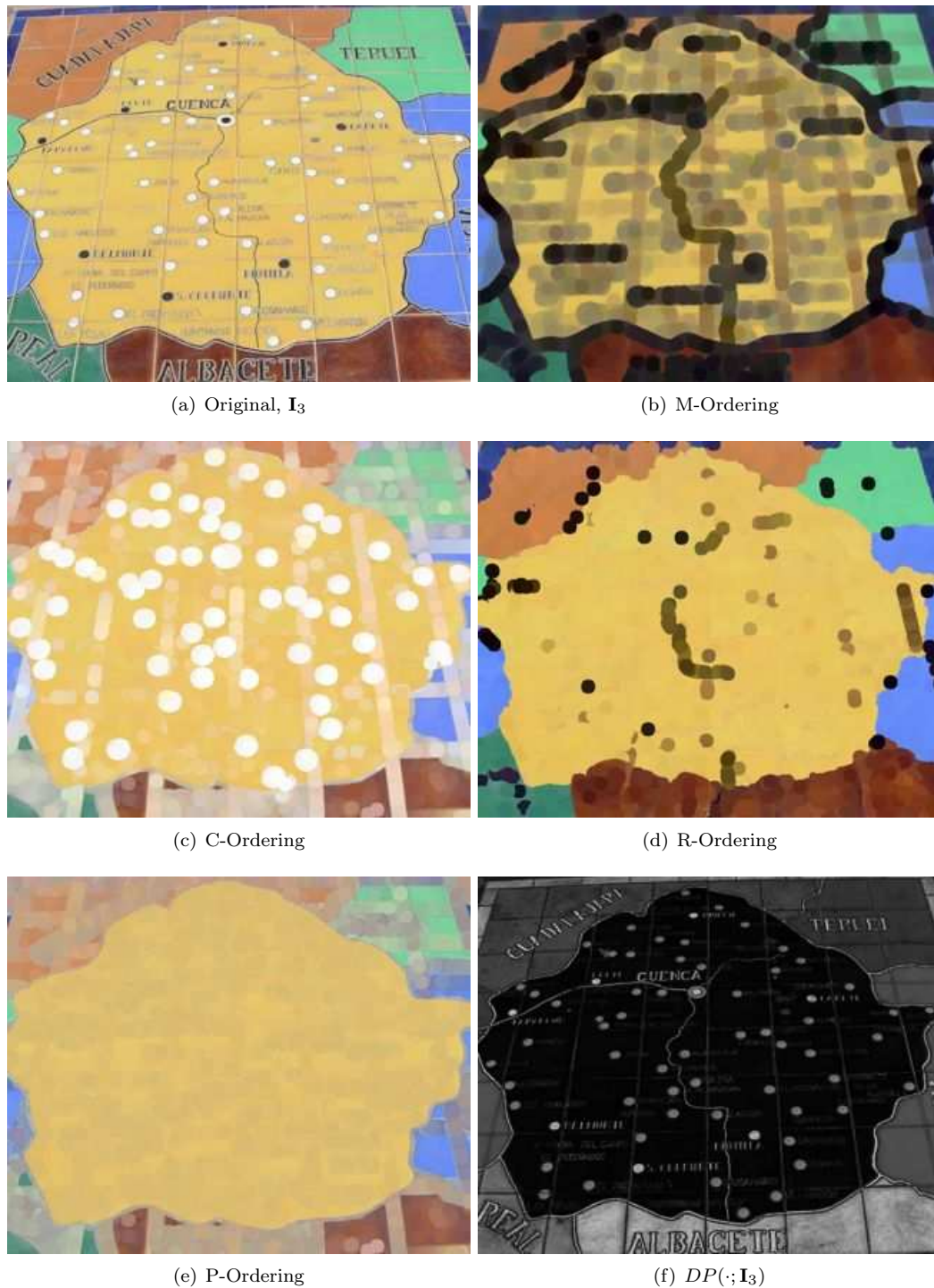


Figure 6.5: Example of different vector morphology operator in the “Cuenca map” colour image. Erosions by a disk of radius 10 in the family of orders proposed by Barnett (1976). C-ordering uses the priority red>green>blue. R-ordering is calculated by the saturation component of the colour image. Proposed P-ordering is illustrated in (e).

6.3.1 Morphological operators and depth h -mapping

The previous theoretical results can be particularised to the case of vector images using projection depth.

For multivariate images $\mathbf{I} : \mathbf{E} \rightarrow \mathbb{F}$, as colour or hyperspectral ones, pixel values are vectors defined in $\mathbb{F} = \mathbb{R}^d$. Consequently the main challenge to build complete lattice structures is to define a mapping

$$h : \mathbb{F} \rightarrow \mathcal{L},$$

where \mathcal{L} can be the lattice of the extended real line, i.e., $\mathcal{L} = (\overline{\mathbb{R}}, \leq)$, with $\overline{\mathbb{R}} = \mathbb{R} \cup \{-\infty, +\infty\}$ and \leq as the “less than or equal to” operation (the natural total ordering). Furthermore the composition of \mathbf{I} and h will be denoted by $h(\mathbf{I}) : \mathbf{E} \rightarrow \mathcal{L}$. According to the previous subsection, once the mapping h has been established, the morphological vector operators can be defined as h -adjunction.

Given a multivariate vector image $\mathbf{I} \in \mathcal{F}(\mathbf{E}, \mathbb{F})$, its h -depth mapping is defined as

$$h_{\mathbf{I}}(\mathbf{x}) = DP(\mathbf{x}; \mathbf{X}_{\mathbf{I}}) \quad (6.11)$$

Therefore, the ordering $\leq_{h_{\mathbf{I}}}$ generated by the projection depth function yields morphological operators which can be interpreted as follows: low values in \mathcal{L} induced by $h_{\mathbf{I}}(\mathbf{x})$ correspond to pixels close to the “background” (median vector) and high values in \mathcal{L} coincide with “foreground” (outlier vectors). That is coherent with binary and gray-level morphology, where high gray-levels are associated to the objects (foreground) and low gray-levels to the background.

We have now the ingredients to formulate the corresponding multivariate vector erosion and dilation. We limit here our developments to the flat operators, i.e., the structuring elements are planar shapes. The non-planar structuring functions are defined by weighting values on their support [Serra \(1982\)](#). The h -depth erosion $\varepsilon_{\mathbf{SE}, h_{\mathbf{I}}}(\mathbf{I})$ and h -depth dilation $\delta_{\mathbf{SE}, h_{\mathbf{I}}}(\mathbf{I})$ of an image \mathbf{I} at pixel $x \in \mathbf{E}$ by the structuring element $\mathbf{SE} \subset \mathbf{E}$ are the two mappings $\mathcal{F}(\mathbf{E}, \mathbb{F}) \rightarrow \mathcal{F}(\mathbf{E}, \mathbb{F})$ defined respectively by

$$h_{\mathbf{I}}(\varepsilon_{\mathbf{SE}, h_{\mathbf{I}}}(\mathbf{I})(x)) = \tilde{\varepsilon}_{\mathbf{SE}}(h_{\mathbf{I}}(\mathbf{I}))(x), \quad (6.12)$$

and

$$h_{\mathbf{I}}(\delta_{\mathbf{SE}, h_{\mathbf{I}}}(\mathbf{I})(x)) = \tilde{\delta}_{\mathbf{SE}}(h_{\mathbf{I}}(\mathbf{I}))(x), \quad (6.13)$$

where $\tilde{\varepsilon}_{\mathbf{SE}}(I)$ and $\tilde{\delta}_{\mathbf{SE}}(I)$ are the standard numerical flat erosion and dilation of image $I \in \mathcal{F}(\mathbf{E}, \mathcal{L})$:

$$\tilde{\varepsilon}_{\mathbf{SE}}(I)(x) = \left\{ I(y) : I(y) = \bigwedge_{z \in \mathbf{SE}_x} [I(z)] \right\} \quad (6.14)$$

$$\tilde{\delta}_{\mathbf{SE}}(I)(x) = \left\{ I(y) : I(y) = \bigvee_{z \in \check{\mathbf{S}}\mathbf{E}_x} [I(z)] \right\} \quad (6.15)$$

with \mathbf{SE}_x being the structuring element centred at point x and $\check{\mathbf{S}}\mathbf{E}$ is the reflected structuring element. If the inverse mapping $h_{\mathbf{I}}^{-1}$ is defined, the h -depth erosion and dilation can be explicitly written as:

$$\varepsilon_{\mathbf{SE}, h_{\mathbf{I}}}(\mathbf{I})(x) = h_{\mathbf{I}}^{-1}(\tilde{\varepsilon}_{\mathbf{SE}}(h_{\mathbf{I}}(\mathbf{I})))(x),$$

and

$$\delta_{\mathbf{SE}, h_{\mathbf{I}}}(\mathbf{I})(x) = h_{\mathbf{I}}^{-1}(\tilde{\delta}_{\mathbf{SE}}(h_{\mathbf{I}}(\mathbf{I})))(x).$$

Of course, the inverse h^{-1} only exists if h is injective. Theoretically, this is not guaranteed for $h_{\mathbf{I}}$ since two different vectors \mathbf{x}_1 and \mathbf{x}_2 can have the same projection depth; i.e., $\mathbf{x}_1 \neq \mathbf{x}_2$ but $DP(\mathbf{x}_1; \mathbf{X}_{\mathbf{I}}) = DP(\mathbf{x}_2; \mathbf{X}_{\mathbf{I}})$. We can impose in practice the invertibility of $h_{\mathbf{I}}$ by considering a lexicographic ordering for equivalence class $\mathcal{L}[\mathbf{x}]$. In fact, this solution involves a structure of total ordering which allows to compute directly the h -depth erosion and dilation without using the inverse mapping, i.e.,

$$\varepsilon_{\mathbf{SE}, h_{\mathbf{I}}}(\mathbf{I})(x) = \left\{ \mathbf{I}(y) : \mathbf{I}(y) = \bigwedge_{h_{\mathbf{I}}} [\mathbf{I}(z)], z \in \mathbf{SE}_x \right\}, \quad (6.16)$$

and

$$\delta_{\text{SE},h_{\mathbf{I}}}(x) = \left\{ \mathbf{I}(y) : \mathbf{I}(y) = \bigvee_{h_{\mathbf{I}}} [\mathbf{I}(z)], z \in \tilde{\text{SE}}_x \right\}, \quad (6.17)$$

where $\bigwedge_{h_{\mathbf{I}}}$ and $\bigvee_{h_{\mathbf{I}}}$ are respectively the infimum and supremum according to the ordering $\leq_{h_{\mathbf{I}}}$, induced for the projection depth function $DP(\mathbf{x}; \mathbf{X}_{\mathbf{I}})$ and completed with a lexicographic ordering in \mathbb{F} . Starting from the h -depth adjunction $(\varepsilon_{\text{SE},h_{\mathbf{I}}}(\mathbf{I}), \delta_{\text{SE},h_{\mathbf{I}}}(\mathbf{I}))$, all the morphological filters such as the opening and closing have their h -depth counterpart, e.g., the h -depth opening and closing are defined as

$$\gamma_{\text{SE},h_{\mathbf{I}}}(\mathbf{I}) = \delta_{\text{SE},h_{\mathbf{I}}}(\varepsilon_{\text{SE},h_{\mathbf{I}}}(\mathbf{I})), \quad \varphi_{\text{SE},h_{\mathbf{I}}}(\mathbf{I}) = \varepsilon_{\text{SE},h_{\mathbf{I}}}(\delta_{\text{SE},h_{\mathbf{I}}}(\mathbf{I})) \quad (6.18)$$

Similarly, geodesic operators as opening by reconstruction Soille (2003), $\gamma_{\text{SE}}^{\text{REC}}(\mathbf{I})$, can be also naturally extended to multivariate images.

6.3.2 Properties

h -depth vector erosion and dilation inherit the standard algebraic properties of morphological operators Serra (1982), Najman and Talbot (2010) since they fit into the theory of h -adjunctions. Nevertheless, some remarks about their particular behavior are useful for practical applications.

Filtering effects. Multivariate morphological operators defined using h -depth adjunction have the classical filtering properties Soille (2003). Namely, the erosion shrinks the structures which pixel values distant to the centre in the vector dimensional space; “spatial peaks” thinner than the structuring element disappear by taking the value of neighbouring pixels with a vector value close to the “background”. As well, it expands the structures which have a vector value close to “foreground”. Fig. 6.5 illustrates these effects in comparison with marginal, conditional and reduced order by saturation Angulo and Serra (2003). Dilation produces the dual effects, enlarging the regions having values close to the outliers and contracting the background. The other morphological operators are naturally interpreted as products of dilations and erosions. Concerning the product operators, opening (closing) is an idempotent and anti-extensive (extensive) operator, which removes foreground (background) objects that are smaller than the structuring element, leaving intact the structures invariant to the structuring element, for instance, see Fig. 6.6.

From the image analysis viewpoint, we can consider that the h -depth erosion/dilation, and all the associated operators, are *unsupervised transformations*, in the sense that ordering is intrinsically adapted to the image without giving any training set of vectors for the background and foreground.

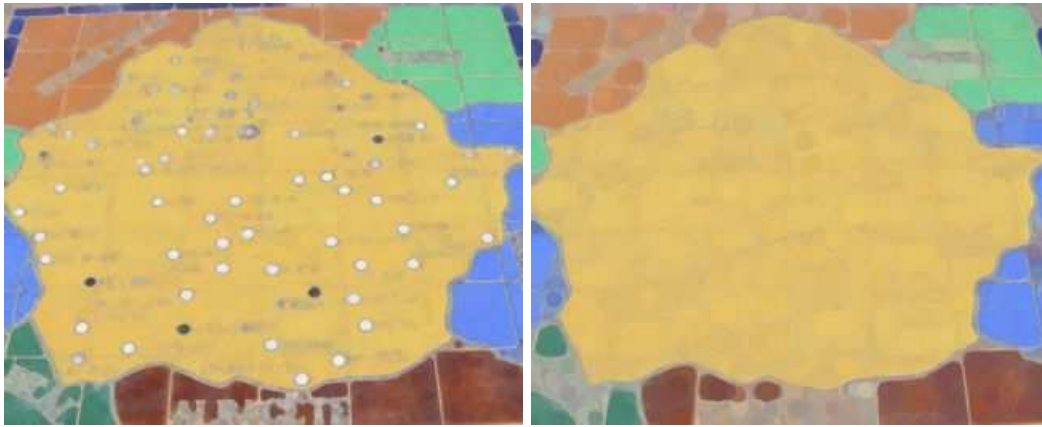
Duality. The notion of duality by complement in grey level images $I \in \mathcal{F}(\mathbb{E}, \mathcal{L})$ allows us to compute the dilation using the erosion operator, i.e., $\tilde{\delta}_{\text{SE}}(I) = \mathbb{C}_{\tilde{\varepsilon}_{\text{SE}}}(\mathbb{C}I)$, where $\mathbb{C}I = -I$. The ordering function $h_{\mathbf{I}}(\mathbf{x}) \leq h_{\mathbf{I}}(\mathbf{f})$ for all $\mathbf{x} \in \mathbb{F}$ and some $\mathbf{f} \in \mathbf{X}_{F(\mathbf{I})}$, and equivalently, $h_{\mathbf{I}}(\mathbf{x}) \geq h_{\mathbf{I}}(\mathbf{b})$ for all $\mathbf{x} \in \mathbb{F}$ and some $\mathbf{b} \in \mathbf{X}_{B(\mathbf{I})}$. Hence, the smallest element of the vector space belongs to the “background” and the largest to the “foreground”, i.e., $\perp_{\mathbb{F}} \in \mathbf{X}_{B(\mathbf{I})}$ and $\top_{\mathbb{F}} \in \mathbf{X}_{F(\mathbf{I})}$. We have therefore a qualitative dual role played by the background and foreground of the image. However, the quantitative duality does not involved an involution on \mathbb{F} : projection depth is invariant to the complement of the vector coordinates. The duality by complement appears in the h -depth mapping which involves:

$$h_{\mathbf{I}}(\delta_{\text{SE},h_{\mathbf{I}}}(\mathbf{I})(x)) = -\tilde{\varepsilon}_{\text{SE}}(-h_{\mathbf{I}}(\mathbf{I}))(x)$$

and consequently

$$\delta_{\text{SE},h_{\mathbf{I}}}(\mathbf{I})(x) = \varepsilon_{\text{SE},-h_{\mathbf{I}}}(\mathbf{I})(x). \quad (6.19)$$

Invariance. From its original formulation MM is contrast invariant due to its basic operators are based on rank filters Soille (2002). The representation of the image as a topographic map is a key point of the contrast invariance properties of MM in grey scale images Caselles and Morel (1999). Contrast invariance is an interesting property linked to the fact that image grey level is not an absolute data, since in many cases the pixel values depend of the acquisition circumstances. For instance, the contrast depends on the type of the camera and illuminations conditions of the scene.



(a) Proposed $\gamma_{SE, h_I}(\mathbf{I})$, with SE a disk of radius 4. (b) Proposed $\gamma_{SE, h_I}(\mathbf{I})$, with SE a disk of radius 10.



(c) $h_I(\mathbf{I}) - h_I(\gamma_{SE, h_I}(\mathbf{I}))$

(d) $h_I(\gamma_{SE, h_I}(\mathbf{I})) - h_I(\mathbf{I})$

Figure 6.6: Example of openings and associated top-hat transformation, in the ordering induced by the projection depth function. Note that the both white and dark small circles are considered as foreground.

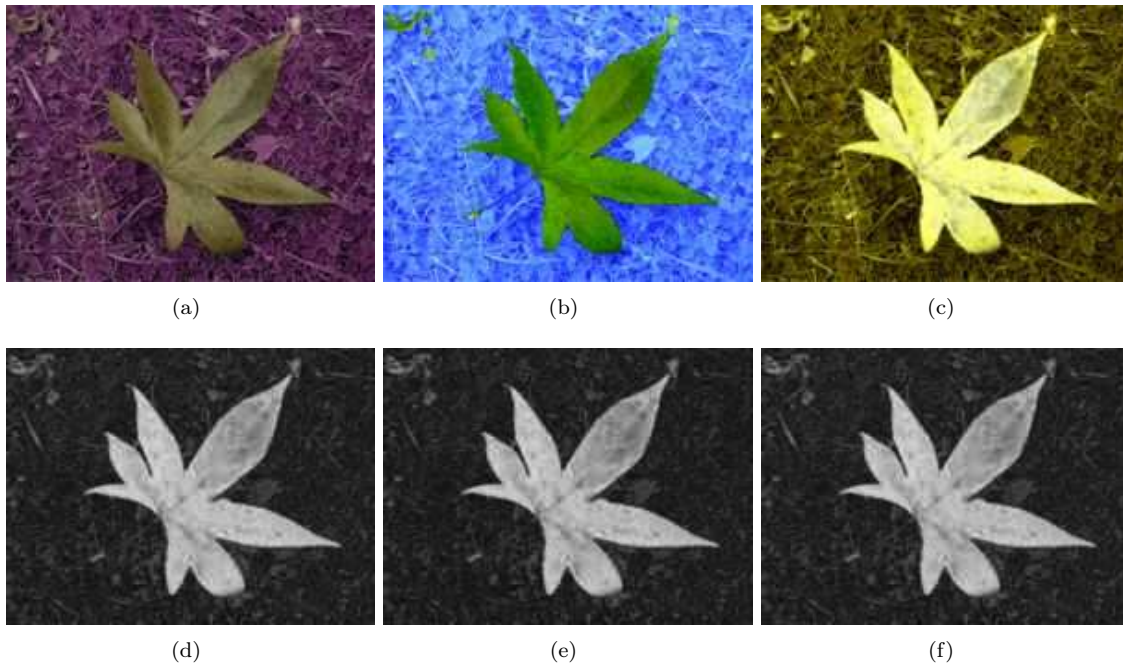


Figure 6.7: Projection depth function is invariant to affine transformation in \mathbb{R}^d . (a)-(c) are obtained by affine transformations in \mathbb{R}^3 of Fig. 6.1(a). (d)-(f) show approximated $DP(\cdot; k, \mathbf{I})$, with $k = 1000$ random projections.

Mathematically, we say that the h -ordering is contrast invariant if for every continuous contrast change $\mathbf{b} \in \mathbb{R}^d$, $\mathbf{x}_1 \leq_{h_{\mathbf{I}}} \mathbf{x}_2 \Rightarrow \mathbf{x}_1 \leq_{h_{\mathbf{I}+\mathbf{b}}} \mathbf{x}_2$, for all $\mathbf{x}_1, \mathbf{x}_2, \mathbf{b} \in \mathbb{R}^d$ and $\forall \mathbf{I} \in \mathcal{F}(\mathbf{E}, \mathbb{R}^d)$, where $h_{\mathbf{I}+\mathbf{b}}$ denotes the h -mapping calculated from $\mathbf{I} + \mathbf{b}$. From definition (6.1), it is easy to see $DP(\mathbf{x}; \mathbf{X}_{\mathbf{I}}) = DP(\mathbf{x}; \mathbf{X}_{\mathbf{I} + \mathbf{b}}), \forall \mathbf{x}, \mathbf{b} \in \mathbb{R}^d$, and its approximated version (6.2) is contrast invariance when the number of random projection k is large enough, i.e., $DP(\cdot; k, \mathbf{X}_{\mathbf{I}}) = DP(\cdot; k, \mathbf{X}_{\mathbf{I} + \mathbf{b}}), \forall \mathbf{x} \in \mathbb{R}^d$, when k tend to ∞ . Thus, the contrast invariance property is not automatic guaranteed, but it depends on the number of projections in the expression (6.2).

A more general suitable property is the invariance to affine transformation. An h -ordering is said to be invariant to affine transformation if, for every $\mathbf{A} \in \mathbb{R}^{d \times d}$ definite positive matrix and $\mathbf{b} \in \mathbb{R}^d$ a vector, h -ordering is invariant to the transformation defined by $\Gamma(\mathbf{I}) = \mathbf{A}\mathbf{X}_{\mathbf{I}} + \mathbf{b}$, i.e., $\mathbf{x}_1 \leq_{h_{\mathbf{I}}} \mathbf{x}_2 \Rightarrow \mathbf{x}_1 \leq_{h_{\Gamma(\mathbf{I})}} \mathbf{x}_2$, for all $\mathbf{x}_1, \mathbf{x}_2 \in \mathbb{R}^d$. Affine transformations includes rotation and scaling, but also shearing. From Zuo and Serfling (2000), (6.1) is affine invariant for \mathbf{X} in the family of symmetric distributions, i.e., $DP(\cdot; \mathbf{X}) = DP(\cdot; \mathbf{A}\mathbf{X} + \mathbf{b})$ for $\mathbf{A} \in \mathbb{R}^{d \times d}$ a definite positive matrix and $\mathbf{b} \in \mathbb{R}^d$. Nevertheless, there is not guarantee of an image \mathbf{I} with background/foreground representation has symmetric distribution. However, experimental results shows that proposed ordering is robust to affine transformation in the vector space \mathbb{R}^d . This situation is illustrated in Fig. 6.7.

Local knowledge. Given an image \mathbf{I} parameterized for its spatial support, $\mathbf{I}_{\mathbf{E}} : \mathbf{E} \rightarrow \mathbb{F}$, and a subset in its spatial support, $\mathbf{E}' \subset \mathbf{E}$, the depth functions associated of both images are not equivalent, i.e., $h_{\mathbf{I}_{\mathbf{E}}} \neq h_{\mathbf{I}_{\mathbf{E}'}}$. However, the *local knowledge* property Serra (1982) is preserved if and only if the depth function is calculated using the whole available image in \mathbf{E} .

6.4 Applications to multivariate image processing

This section presents three applicative examples that utilise MM operators in the induced ordering by random projection depth. The aim is to demonstrate the impact of this unsupervised ordering

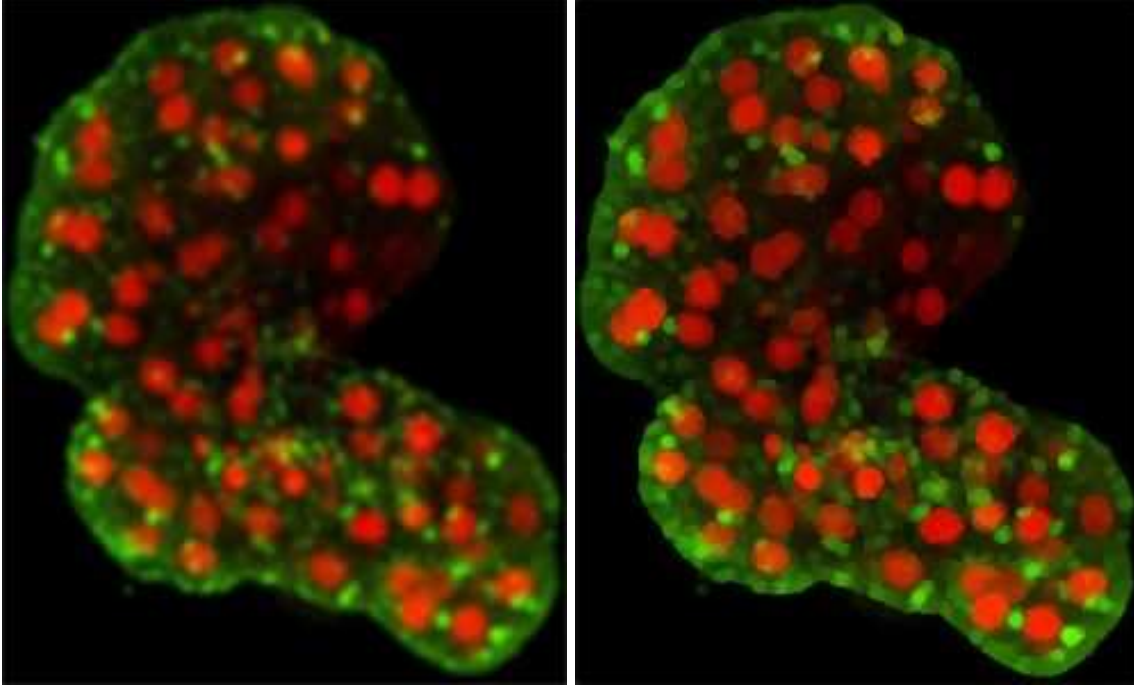


Figure 6.8: Edge enhancement of \mathbf{I} using toggle mapping $\tau_h(\mathbf{I})$ in the proposed ordering. Source: <http://www.cellimagelibrary.org/>

in standard morphological operators for object filtering and segmentation in vector images. The definition h -depth ordering can be applied to multivariate images, allowing to use “any” morphological operator for colour, multispectral and hyperspectral images. Theoretically, convergence of iterative algorithms is guaranteed if the h -depth ordering induced a total order, once completed with lexicographic order. The first application concerns edge enhancement in multivariate images and is based on shock filters [Serra \(1982\)](#), [Soille \(2003\)](#).

6.4.1 Image enhancement

Given an image \mathbf{I} , and two transformations $\Psi(\mathbf{I}) \leq_{h_{\mathbf{I}}} \mathbf{I} \leq_{h_{\mathbf{I}}} \Upsilon(\mathbf{I})$ the shock filter is defined as follows

$$\tau_{h_{\mathbf{I}}}(\mathbf{I}) = \begin{cases} \Psi_{h_{\mathbf{I}}}(\mathbf{I}) & \text{if } \Delta_{h_{\mathbf{I}}}(\mathbf{I}, \Psi, \Upsilon) < 0, \\ \Upsilon_{h_{\mathbf{I}}}(\mathbf{I}) & \text{if } \Delta_{h_{\mathbf{I}}}(\mathbf{I}, \Psi, \Upsilon) > 0, \\ \mathbf{I} & \text{otherwise.} \end{cases} \quad (6.20)$$

where $\Delta_{h_{\mathbf{I}}}(\mathbf{I}, \Psi, \Upsilon) = h_{\mathbf{I}}(\mathbf{I} - \Psi(\mathbf{I})) - h_{\mathbf{I}}(\Upsilon(\mathbf{I}) - \mathbf{I})$ is the morphological Laplacian of the original image, based on Ψ and Υ in the domain of h -depth function. For grey scale images, in the particular case of h as the identity function, $\Psi_{h_{\mathbf{I}}}(\mathbf{I}) = \varepsilon_{\text{SE}, h_{\mathbf{I}}}(\mathbf{I})$, $\Upsilon_{h_{\mathbf{I}}}(\mathbf{I}) = \delta_{\text{SE}, h_{\mathbf{I}}}(\mathbf{I})$, and SE as the unitary ball, we have the classical shock filter introduced by [Kramer and Bruckner \(1975\)](#). It is based on the idea of using a dilation process near a local maximum and an erosion process around a local minimum. The toggle mapping $\tau_{h_{\mathbf{I}}}$ enhances images edges detected by differences in the projection depth function, i.e., background/foreground transitions. The enhanced image tends to be piecewise constant due to morphological operators and preserves the original information in pixels where the edge detector is ambiguous (otherwise case in (8.4)). Additionally, the vector formulation allows to perform edge enhancement without include false colours during the procedure. Fig. 6.8 presents an illustrative example to show how the toggle mapping works for a vector image.

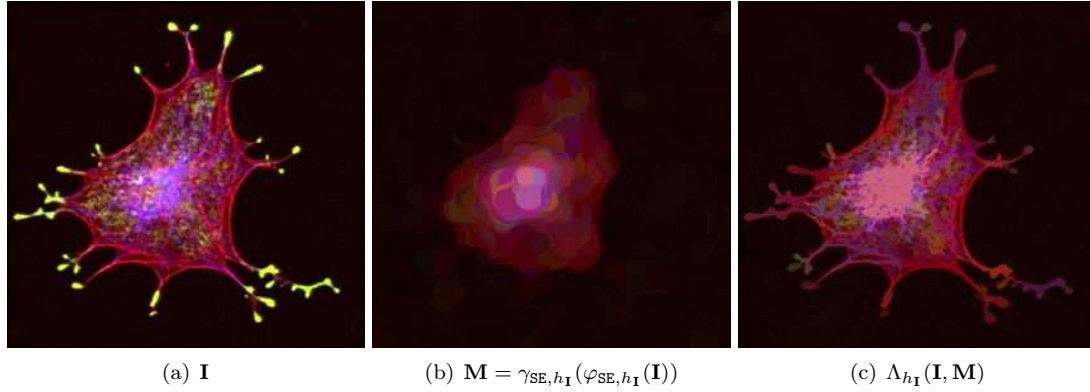


Figure 6.9: Original (\mathbf{I}), marker (\mathbf{M}) and simplification by h -depth vector leveling $\Lambda_{h_{\mathbf{I}}}(\mathbf{I}, \mathbf{M})$. The marker \mathbf{M} is the product of a h -depth closing followed by an h -depth opening with the SE is a disk of radius 10.

6.4.2 Image Simplification

The task of image simplification is the subject of various approaches and applications [Soille \(2008\)](#) [Pizarro et al. \(2010\)](#). The aim is to produce from an initial image, an approximated version with is simpler in some sense. In the list of MM operators, the morphological leveling attempts to produce flat zones for an original image \mathbf{I} from a given marker image \mathbf{M} , consequently, simpler according to the norm of the gradient, but preserving the main object according to the marker \mathbf{M} . The idea of such a filter goes back to [Matheron \(1997\)](#) and [Meyer \(1998\)](#). In the induced order produced by a h -depth function, an image \mathbf{J} is a leveling of the image \mathbf{I} , denoted by $\mathbf{J} \in \Lambda(\mathbf{I})$, iff $\forall (p, q) \in \mathbf{E} \times \mathbf{E}$ neighbours:

$$\mathbf{J}(p) >_{h_{\mathbf{I}}} \mathbf{J}(q) \Rightarrow \mathbf{I}(p) \leq_{h_{\mathbf{I}}} \mathbf{J}(p) \text{ and } \mathbf{J}(q) \geq_{h_{\mathbf{I}}} \mathbf{I}(q).$$

The criterion also gives the clue to the algorithm for constructing a leveling. The function \mathbf{J} is modified until the criterion is satisfied, on $K^+ = \{x \text{ s.t. } \mathbf{J}(x) <_{h_{\mathbf{I}}} \mathbf{I}(x)\}$, \mathbf{J} is replaced by $\mathbf{I} \wedge_{h_{\mathbf{I}}} \delta_{\text{SE}, h_{\mathbf{I}}}(\mathbf{J})$ and on $K^- = \{x \text{ s.t. } \mathbf{J}(x) >_{h_{\mathbf{I}}} \mathbf{I}(x)\}$, \mathbf{J} , by $\mathbf{I} \vee_{h_{\mathbf{I}}} \varepsilon_{\text{SE}, h_{\mathbf{I}}}(\mathbf{J})$ until the criterion is satisfied everywhere. The leveling $\Lambda_{h_{\mathbf{I}}}(\mathbf{I}, \mathbf{M})$ can be obtained by the following iterative algorithm:

$$\Lambda_{h_{\mathbf{I}}}(\mathbf{I}, \mathbf{M}) = \Lambda^i(\mathbf{I}, \mathbf{M}) = [\mathbf{I} \wedge_{h_{\mathbf{I}}} \delta_{\mathbf{I}, h_{\mathbf{I}}}^i(\mathbf{M})] \vee_{h_{\mathbf{I}}} \varepsilon_{\mathbf{I}, h_{\mathbf{I}}}^i(\mathbf{M}),$$

such that $\Lambda^i(\mathbf{I}, \mathbf{M}) = \Lambda_{h_{\mathbf{I}}}^{i+1}(\mathbf{I}, \mathbf{M})$ (convergence until idempotency), where the geodesic dilation (erosion) of size i denotes $\delta_{\mathbf{I}, h_{\mathbf{I}}}^i(\mathbf{M})$ ($\varepsilon_{\mathbf{I}, h_{\mathbf{I}}}^i(\mathbf{M})$). Fig. 6.9 gives a real example of our method. The leveling is a simplified version of the original image, and it contains less transitions. Naturally, the simplification level is controlled by the marker image \mathbf{M} . In the example illustrated in Fig. 6.9, \mathbf{M} is an opening followed by a closing with a disk of radius 10 as structuring element (SE). Clearly, objects smaller than SE have been eliminated in \mathbf{M} and they are not recovered by $\Lambda_{h_{\mathbf{I}}}(\mathbf{I}, \mathbf{M})$. Thus, Fig. 6.9(c) is a simplified version of Fig. 6.9(a) where small structures have been removed but contours of larger components are preserved.

6.4.3 Image segmentation

Multivariate image segmentation has been widely considered from different approaches [Qin and Clausi \(2010\)](#), [Grana et al. \(2009\)](#), [Nguyen and Wu \(2011\)](#). Although theoretically feasible to extend many univariate segmentation techniques to their multivariate analogs, practical behaviour is influenced by the multivariate nature of the image. Intra-class variation increases at the same time that the dimension in vector images, reducing class distinguishability and degrading segmentation performance. Multivariate imagery is specially sensitive to large intra-class variation since every component image is a variation contributor. Additionally, computational cost of segmentation

algorithms increases while algorithmic robustness tends to decrease with increasing feature space sparseness and solution space complexity. We proposed to use the proposed random projection depth in combination with classical watershed transform Meyer and Beucher (1990) to yield a segmentation in multivariate images. The same idea can be applied to a larger family of segmentation techniques Couprie et al. (2011). A watershed transform, denoted by $\text{WS}(\mathbf{I})$ associate a catch basin to each minimum of the image \mathbf{I} Meyer and Beucher (1990). We note in passing that in practice one often does not apply the watershed transform to the original image, but to its (morphological) gradient Soille (2003). Watershed transform have been applied in multivariate image, where the important issue is the selection of an adequate multivariate gradient Noyel et al. (2007), Tarabalka et al. (2010b). Basically, we apply the watershed transformation in the gradient induced by the h -ordering calculated by the projection depth function (6.2), i.e., $h_{\mathbf{I}}(\delta_{\text{SE}, h_{\mathbf{I}}}(\mathbf{I}) - \varepsilon_{\text{SE}, h_{\mathbf{I}}}(\mathbf{I}))$.

However, even in the case of grey scale images, the watershed transformation without any preprocessing leads to a over-segmentation. There are two possibilities to throw out the over-segmentation. The first one involves hierarchical approaches based on merging of catchment basins or based on the selection of the most significant minima according to different criteria Meyer (2001). The second one consists in determining markers for each interest region, for instance, the dynamics or contrast based transform applied to the minima of the gradient Soille (2003). In the framework of h -depth morphology, the dynamics-based selection of minima is able to suppress minima whose depth is smaller than a given threshold t Soille (2003). We denote $\text{WS}(\mathbf{I}, t)$ the watershed transform where the seeds are the local minima, calculated from a dynamics-based minima transform of parameter t (The dynamic is normalise between 0 and 1 in the experiments). Experimental results of the segmentation strategy are shown in Figs. 6.10, 6.11 and 6.12. The first set of examples are colour images, where the watershed segmentation produces sharp borders. The main advantage of the formulation is it is directly applicable to multidimensional images. Thus, we perform experiment in multispectral images from Chakrabarti and Zickler (2011). The hyperspectral images were captured with a time-multiplexed 31-channel camera. We can observe that, our approach performs well and produce shrewd segmentation in the sense that only anomalous regions are segmented, for instance, fruits in Fig. 6.11. Fig. 6.12 also shows an example on a well-known hyperspectral image from the remote sensing community acquired by the ROSIS-03 optical sensor. The original image is a 610 by 340 pixels on 103-bands. Our approach can produce a very selective foreground segmentation guided by the value of the projection depth function, i.e., buildings and some isolated pixels in the image.

6.5 Conclusions on random projections depth-based mathematical morphology

The chapter proposes the statistical depth function as a powerful approach to induce a vector ordering for multivariate images and consequently a framework for unsupervised multivariate mathematical morphology. Indeed, it reaches a good compromise between simplicity and effectiveness in cases where no prior information is available for a supervised approach. Multivariate segmentation based on projection depth function is a sort of anomaly segmentation algorithm. That is understandable because the proposed method is a measure of eccentricity (outlandishness) from a cloud point representation, where the spatial representation is not considered. In the future, we are planning to further speed up the proposed ordering and sharpness enhancement algorithm, then extend the proposed method to video segmentation and enhancement.

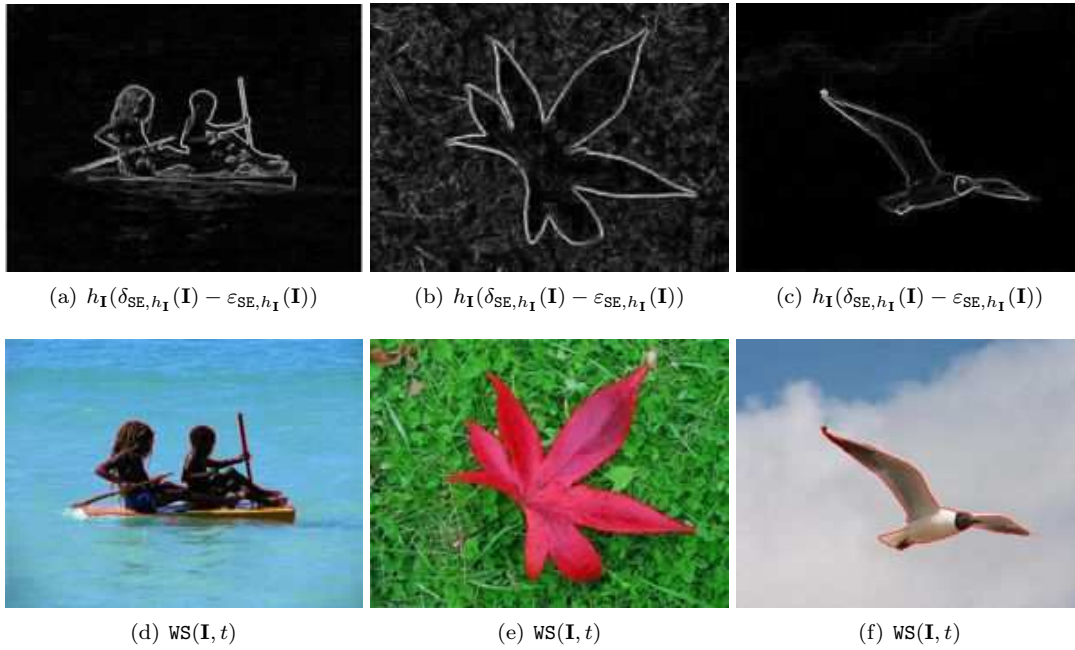


Figure 6.10: h -depth gradient and segmentation by using watershed transformation (in red), where markers are calculated by selecting the minima of strong dynamics in h -depth gradient, with $t = .5$.

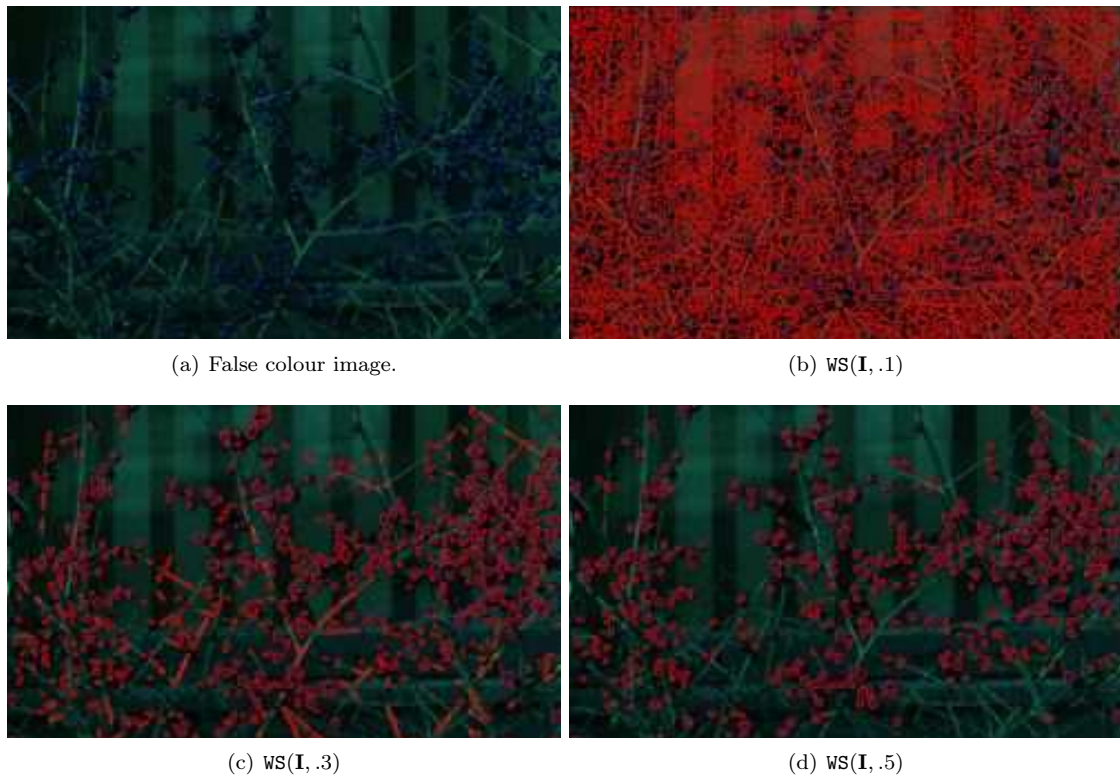


Figure 6.11: Original multispectral images is the size 200 by 500 pixels in 31 channels. Segmentation for watershed transformation with different parameters of dynamics minima of h -depth gradient.

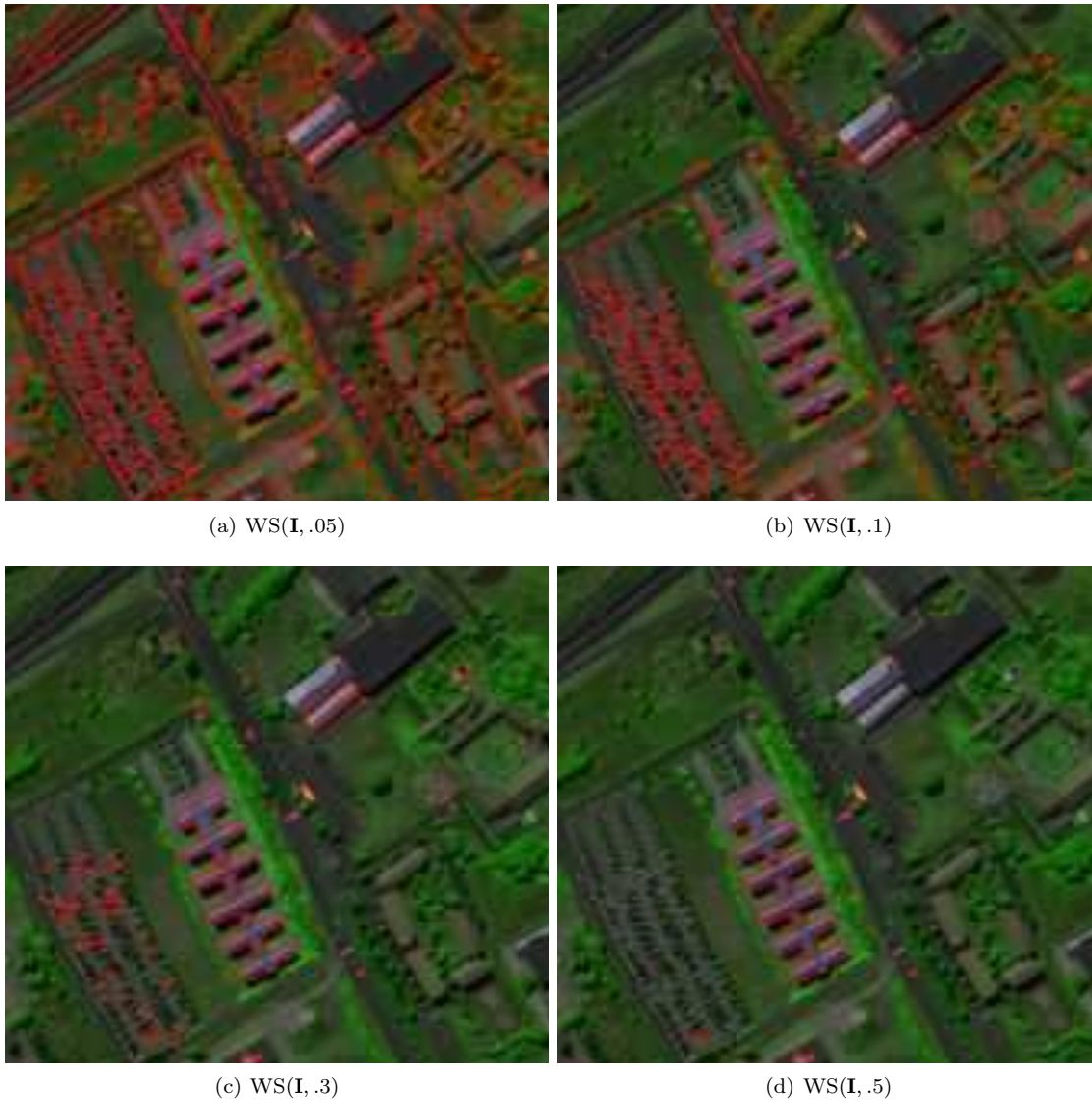


Figure 6.12: Original hyperspectral image is 610 by 340 pixels on 103-bands. Segmentation by h -depth watershed transformation with different parameters of dynamics minima of h -depth gradient.

Part II

Contributions to morphological modeling

7

Additive morphological decomposition and tensor modeling of multivariate images

No question is so difficult to answer as that to which the answer is obvious.
George Bernard Shaw

Résumé

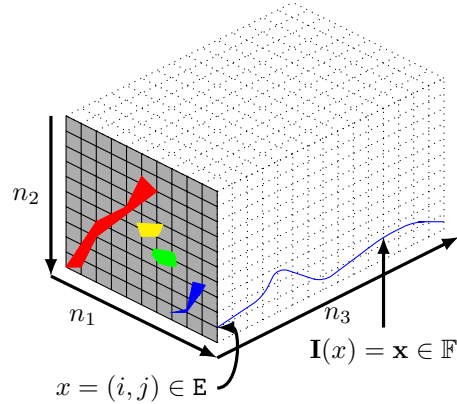
La classification pixel-à-pixel d'images multivariées de haute dimension est étudiée dans ce chapitre. La méthode proposée est basée sur l'analyse conjointe de l'information spectrale et spatiale de l'image hyperspectrale. Une décomposition additive morphologique (DAM) basée sur les opérateurs morphologiques est proposée. Elle définit une décomposition espace/échelle pour les images multivariées, sans perte d'information. La DAM est modélisée par une structure tensorielle et la version tensorielle de l'analyse en composantes principales est comparée, en tant qu'algorithme de réduction de dimension, à la version matricielle. La comparaison expérimentale montre que l'algorithme proposé peut donner une meilleure performance pour la classification pixel-à-pixel des images hyperspectrales que de nombreuses autres techniques classiques¹.

7.1 Introduction

Hyperspectral imaging (HSI) is a remote sensing technique that acquires two dimension spatial images in typically hundreds of contiguous bands of high spectral resolution covering the visible, near-infrared, and shortwave infrared bands. This technique has been applied for planetary exploitation [Gendrin et al. \(2005\)](#), environmental monitoring [Brekke and Solberg \(2005\)](#), agriculture [Haboudane \(2004\)](#), forestry [Clark et al. \(2005\)](#), geology [Kruse et al. \(2003\)](#), food safety [Sun \(2010\)](#), [Barbin et al.](#)

¹The content of this chapter is mainly based on the following published papers:

- [Velasco-Forero and Angulo \(2009\)](#), "*Morphological scale-space for hyperspectral images and dimensionality exploration using tensor modeling*". First IEEE Workshop on Hyperspectral Image and Signal Processing: Emerging Remote Sensing (WHISPERS 2009).
- [Velasco-Forero and Angulo \(2010c\)](#), "*Parameters selection of morphological scale-space decomposition for hyperspectral images using tensor modeling*". In *Proceeding of the SPIE*, vol. 7695, p. 76951B (12pp).
- [Velasco-Forero and Angulo \(2013\)](#), "*Classification of hyperspectral images by tensor modeling and additive morphological decomposition*". accepted to *Pattern Recognition*, (2012).



(a) Multivariate image as a tensor \mathcal{I} of size $n_1 \times n_2 \times n_3$

Figure 7.1: Mathematical notation for a 2D multivariate image, $\mathbf{I} : \mathbf{E} \rightarrow \mathbb{F}$

(2011), counterfeit drugs detection [Rodionova et al. \(2005\)](#), urban geography [Chen et al. \(2003\)](#), detection of military target activities [Manolakis et al. \(2003\)](#), and biology [Schultz et al. \(2001\)](#). That technology produces a signature for each pixel in the image in many highly correlated bands presenting considerable amounts of spectral redundancy. On the one hand, *dimension reduction* of multivariate images is one of the main subject of interest for the hyperspectral community. Target detection, image segmentation, pixel classification and spectral unmixing in HSI have the additional difficulty that pixels are located in a high dimension space increasing computational complexity and degrading accuracy [Landgrebe \(2002\)](#), [Keshava and Mustard \(2002\)](#), [Manolakis et al. \(2001\)](#), [Jiménez et al. \(2007\)](#). Due to its simplicity, principal component analysis (PCA) is the most popular approach to dimensionality reduction in HSI using singular value decomposition over zero mean covariance matrix. Unfortunately, PCA requires a preliminary step to vectorize the images retaining spectral information and neglecting the spatial information presented in the original array.

On the other hand, identification of relatively small objects incorporates issues because spatial resolution is necessary for accurate classification. Accordingly, if the spatial contents of the image is not used, the resulting thematic map sometimes looks noisy (salt and pepper classification noise). In the particular case of supervised classification, that topic is called *spatial/spectral classification*. The aim is to assign each image pixel to one class using a feature vector based on its own spectral value (the spectral information) and information extracted from its neighbourhood (referred to as the spatial information). The pioneer work in introducing spatial context into a multivariate image classification is ECHO (Extraction and Classification of Homogeneous Objects) classifier [Landgrebe \(2003\)](#). Since then, many studies have been led to propose new algorithms to perform spectral-spatial classification. Recent works in HSI have seen a surge of research toward developing approaches that exploit various features specific to the spatial/spectral classification. The approaches due to ([Jackson and Landgrebe \(2002\)](#), [Camps-Valls and Bruzzone \(2005\)](#), [Bruzzone and Carlin \(2006\)](#), [Martin-Herrero \(2007\)](#), [Fauvel et al. \(2008\)](#), [Duarte-Carvajalino et al. \(2008\)](#), [Zhang et al. \(2008\)](#), [Velasco-Forero and Manian \(2009\)](#), [Tarabalka et al. \(2010b\)](#), [Bolton and Gader \(2009\)](#), [Bourennane et al. \(2010\)](#), [Wang et al. \(2010\)](#), [Li et al. \(2011, 2012\)](#), [Dalla-Mura et al. \(2011\)](#)) show some degree of success. Pixel-wise classification incorporating spatial information in HSI can be roughly divided according to their mathematical formulation as follows.

- Smoothing by partial differential equation [Duarte-Carvajalino et al. \(2008\)](#), [Velasco-Forero and Manian \(2009\)](#), [Wang et al. \(2010\)](#), [Martin-Herrero \(2007\)](#): anisotropic diffusion from classic grey-scale image processing [Perona and Malik \(1990\)](#) is extended to multivariate scenarios, by using a general definition of vector gradient.
- Markov random field, which takes into account the spatial dependence between the pixels

based on the observed intensity field [Jackson and Landgrebe \(2002\)](#), [Li et al. \(2011\)](#).

- Mathematical morphology [Palmason et al. \(2005\)](#), [Fauvel et al. \(2008\)](#), [Dalla-Mura et al. \(2011\)](#), [Pesaresi and Benediktsson \(2001\)](#): Incorporate the results of morphological operators over features calculated by some dimensionality reduction technique as Principal (or Independent) Component Analysis.
- Classifiers with spatial information [Camps-Valls and Bruzzone \(2005\)](#), [Dundar et al. \(2006\)](#): pairwise classification based on kernel formulation where the spatial information is incorporated as an operation among spatial, spectral and spatial-spectral kernels.
- Segmentation and post-processing [Tarabalka et al. \(2010b,a\)](#), [Li et al. \(2012\)](#): approaches start with a preliminary spatial/spectral clustering/segmentation followed by a fusion-area stage based on supervised criterium.
- Tensor modeling [Renard and Bourennane \(2008\)](#), [Zhang et al. \(2008\)](#), [Bourennane et al. \(2010\)](#): three dimension array or third-order tensor preserves the usual image representation and band continuity is represented as the third tensor dimension. Spatial information is included as row-column correspondence in the mathematical structure.
- Context-based classification [Bolton and Gader \(2009\)](#), [Bruzzone and Carlin \(2006\)](#) attempts to identify relevant models to a test sample through context estimation in the feature space, using random set framework [Bolton and Gader \(2009\)](#) or hierarchical multilevel segmentation [Bruzzone and Carlin \(2006\)](#).

7.1.1 Main contributions and chapter organisation

To the best of our knowledge, there has been no previous work on modelling multivariate images using additive morphological decompositions as tensor structures, which is the subject of this chapter. Our approach is motivated by the desire to discover “interesting” low-dimensional linear projections of high-dimensional images where the spatial information plays an important role. In this chapter, we present an additive scale-space decomposition which incorporates spatial information into the dimensionality reduction stage for multivariate images. In summary, the main contributions of this chapter are as follows.

- A new image decomposition based on mathematical morphology which is more compact and performs better in supervised classification.
- Tensor-PCA based on morphological decomposition producing a workflow where the spatial information is included in the dimensionality reduction step instead of in the classification stage.
- We show in practical examples that our workflow allows to include the spatial information in the dimensionality reduction stage.
- State of the art for classification of HSI in remote sensing based on morphological decomposition.

The chapter is organised as follows. Section 7.2 presents the additive scale-space decomposition with morphological transformations. Section 7.3 introduces tensor modelling of morphological decomposed multivariate images. Section 7.4 proposes a formulation of classification for reduced tensors using support vector machines (SVM) and shows the effectiveness of the modified approach via practical examples with a comparison versus classical approaches. Section 7.5 concludes the chapter.

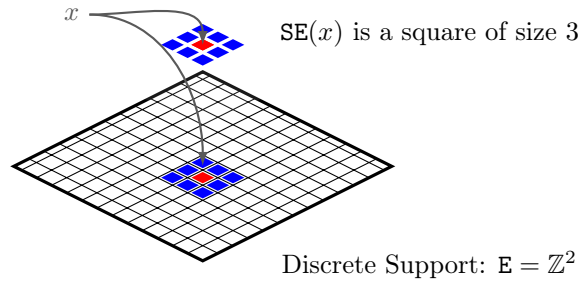


Figure 7.2: Structuring element $SE \subset E$ at $x = (i, j) \in E$. MM operators are non-linear neighbourhood-image transforms associated with the structuring element SE.

7.2 Additive Morphological Decomposition

In this section we focus on mathematical morphology (MM) as a nonlinear image processing methodology composed of a larger family of operators based on the set theory and defined on an abstract structure known as complete lattice of spatial structures [Najman and Talbot \(2010\)](#).

7.2.1 Notation

Let us make precise the terms and notation to be used in the rest of the chapter. Let E be a subset of the discrete space \mathbb{Z}^2 , considered as the support space of the 2D image, and $\mathbb{F} \subseteq \mathbb{R}^d$ be a set of pixels values in dimension d , corresponding to the vector space of values of the image of size $n_1 \times n_2$ and d channels. A *vector-valued image* is represented by the mapping,

$$\mathbf{I} : \begin{cases} E & \rightarrow \mathbb{F} \\ x = (i, j) & \rightarrow \mathbf{x} \end{cases} \quad (7.1)$$

i.e., $\mathbf{I} \in \mathcal{F}(E, \mathbb{F})$ is the set of maps from a point x at the discrete spatial coordinates $(i, j) \in E$ into a vector value $\mathbf{x} \in \mathbb{F} \subseteq \mathbb{R}^d$. Let us assume that the pixel x is represented by a d -dimensional vector $\mathbf{x}(i, j) = [x_1(i, j), x_2(i, j), \dots, x_d(i, j)] \in \mathbb{R}^d$, where \mathbb{R} denotes the set of real numbers in which the pixels spectral response $x_l(i, j)$ at sensor channels $l = 1, \dots, d$. Figure 7.1 shows the notation in two graphical schemes. Additionally, let \mathbf{X} be an $n \times d$ matrix representing d spectral bands for each n pixels in the vector-value image \mathbf{I} . We use the following notations to facilitate presentation: scalars are denoted by lower case letters (a, b, \dots), vectors by bold lower case letters ($\mathbf{a}, \mathbf{b}, \dots$), matrices or images by bold upper-case letters ($\mathbf{X}, \mathbf{Y}, \dots$), and higher-order tensors by calligraphic upper-case letters ($\mathcal{I}, \mathcal{S}, \dots$). The order of tensor $\mathcal{I} \in \mathbb{R}^{n_1 \times n_2 \times \dots \times n_J}$ is J . We use subscripts to illustrate the tensor order, for example \mathcal{I}_{ijkl} is a tensor of order four.

7.2.2 Basic Morphological Transformation

The morphological transformation Φ is an *image to image transformation*, i.e., $\Phi : \mathcal{F}(E, \mathbb{F}) \rightarrow \mathcal{F}(E, \mathbb{F})$. Additionally, it is a *neighbourhood-image transform* [Soille \(2003\)](#), i.e., the output value at a given pixel x is a function of the values of the pixels falling in the neighbourhood induced by the structuring element SE and centred at the considered pixel x as it is illustrated in Figure 7.2. The shape of SE plays the role of the a priori knowledge about the geometry of the interesting and uninteresting spatial structures in the image. In general a transformation $\Phi \in \mathcal{F}(E, \mathbb{F}) \rightarrow \mathcal{F}(E, \mathbb{F})$ is called:

- *extensive* if $\mathbf{I}(x) \leq \Phi(\mathbf{I}(x))$,
- *anti-extensive* if $\Phi(\mathbf{I}(x)) \leq \mathbf{I}(x)$,

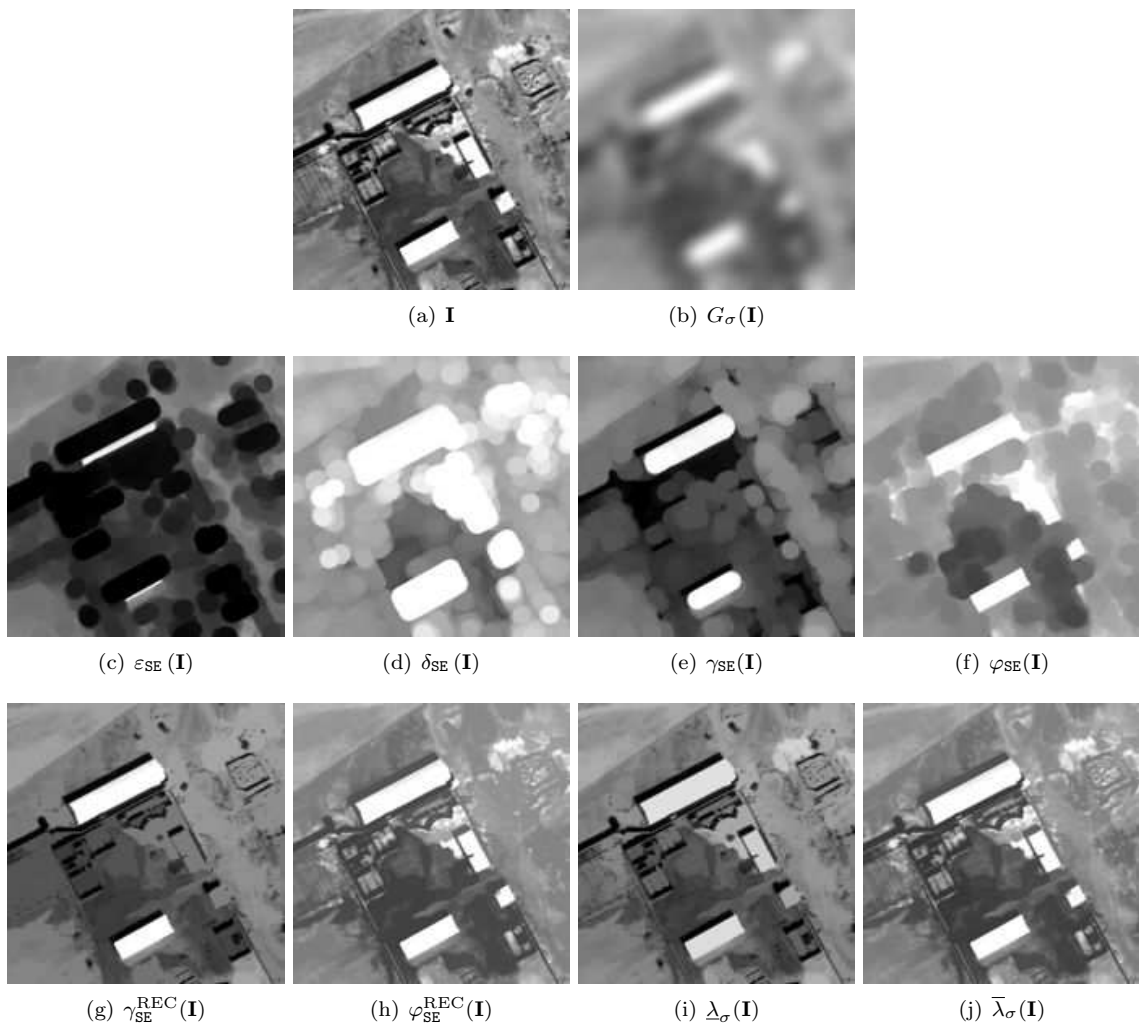


Figure 7.3: Morphological transformations of a scalar (grey level) image. Original image (a) is a 342×342 pixels in 70-cm-resolution satellite image from the panchromatic band of Quickbird.

Table 7.1: Key notations used in the chapter formulation. \mathbf{I} is the original image and \mathbf{M} a marker image. \mathbf{B} is the unitary isotropic structuring element useful in the geodesic operators. \mathbf{SE} is any structuring element. Idempotent means that application the operator twice with the same set of parameters yields the same result. Transformations are illustrated in Fig. 7.3 using a practical example.

Notation	Name	Definition	Idempotent
$G_\sigma(\cdot)$	Gaussian Filter	$G_\sigma(\mathbf{I}) = \mathbf{I} * \mathcal{N}(0, \sigma)$	No
$\varepsilon_{\mathbf{SE}}(\cdot)$	Erosion	$\varepsilon_{\mathbf{SE}}(\mathbf{I})(x) = \{\mathbf{I}(z) : \bigwedge_{y \in \mathbf{SE}(x)} \mathbf{I}(y)\}$	No
$\delta_{\mathbf{SE}}(\cdot)$	Dilation	$\delta_{\mathbf{SE}}(\mathbf{I})(x) = \{\mathbf{I}(z) : \bigvee_{y \in \mathbf{SE}(x)} \mathbf{I}(y)\}$	No
$\gamma_{\mathbf{SE}}(\cdot)$	Opening	$\gamma_{\mathbf{SE}}(\mathbf{I}) = \delta_{\mathbf{SE}}(\varepsilon_{\mathbf{SE}}(\mathbf{I}))$	Yes
$\varphi_{\mathbf{SE}}(\cdot)$	Closing	$\varphi_{\mathbf{SE}}(\mathbf{I}) = \varepsilon_{\mathbf{SE}}(\delta_{\mathbf{SE}}(\mathbf{I}))$	Yes
$\delta_{\mathbf{B}}^i(\cdot, \cdot)$	Geodesic dilation of size i	$\delta_{\mathbf{B}}^i(\mathbf{M}, \mathbf{I}) = \delta_{\mathbf{B}}^1(\delta_{\mathbf{B}}^{i-1}(\mathbf{M}, \mathbf{I}), \mathbf{I})$, with $\delta_{\mathbf{B}}^1(\mathbf{M}, \mathbf{I}) = \delta_{\mathbf{SE}}(\mathbf{M}) \wedge \mathbf{I}$	No
$\varepsilon_{\mathbf{B}}^i(\cdot, \cdot)$	Geodesic erosion of size i	$\varepsilon_{\mathbf{B}}^i(\mathbf{M}, \mathbf{I}) = \varepsilon_{\mathbf{B}}^1(\varepsilon_{\mathbf{B}}^{i-1}(\mathbf{M}, \mathbf{I}), \mathbf{I})$, with $\varepsilon_{\mathbf{B}}^1(\mathbf{M}, \mathbf{I}) = \varepsilon_{\mathbf{SE}}(\mathbf{M}) \vee \mathbf{I}$	No
$\delta_{\mathbf{B}}^\infty(\cdot, \cdot)$	Reconstruction by Dilation	$\delta_{\mathbf{B}}^\infty(\mathbf{M}, \mathbf{I}) = \{\delta_{\mathbf{B}}^i(\mathbf{M}, \mathbf{I}) \mid \delta_{\mathbf{B}}^{i+1}(\mathbf{M}, \mathbf{I}) = \delta_{\mathbf{B}}^i(\mathbf{M}, \mathbf{I})\}$	Yes
$\varepsilon_{\mathbf{B}}^\infty(\cdot, \cdot)$	Reconstruction by Erosion	$\varepsilon_{\mathbf{B}}^\infty(\mathbf{M}, \mathbf{I}) = \{\varepsilon_{\mathbf{B}}^i(\mathbf{M}, \mathbf{I}) \mid \varepsilon_{\mathbf{B}}^{i+1}(\mathbf{M}, \mathbf{I}) = \varepsilon_{\mathbf{B}}^i(\mathbf{M}, \mathbf{I})\}$	Yes
$\gamma_{\mathbf{SE}}^{\text{REC}}(\cdot)$	Opening by reconstruction	$\gamma_{\mathbf{SE}}^{\text{REC}}(\mathbf{I}) = \delta_{\mathbf{SE}}^\infty(\gamma_{\mathbf{SE}}(\mathbf{I}), \mathbf{I})$	Yes
$\varphi_{\mathbf{SE}}^{\text{REC}}(\cdot)$	Closing by reconstruction	$\varphi_{\mathbf{SE}}^{\text{REC}}(\mathbf{I}) = \varepsilon_{\mathbf{SE}}^\infty(\varphi_{\mathbf{SE}}(\mathbf{I}), \mathbf{I})$	Yes
$\lambda_\sigma(\cdot)$	Gaussian Upper-Leveling Meyer (1998)	$\lambda_\sigma(\mathbf{I}) = \delta_{\mathbf{B}}^\infty(G_\sigma(\mathbf{I}) \wedge \mathbf{I}, \mathbf{I})$	No
$\underline{\lambda}_\sigma(\cdot)$	Gaussian Lower-Leveling Meyer (1998)	$\underline{\lambda}_\sigma(\mathbf{I}) = \varepsilon_{\mathbf{B}}^\infty(G_\sigma(\mathbf{I}) \vee \mathbf{I}, \mathbf{I})$	No

- *idempotent* if $\Phi(\Phi(\mathbf{I}(x))) = \Phi(\mathbf{I}(x))$,

for all $x \in \mathbf{E}$ and $\mathbf{I} \in \mathcal{F}(\mathbf{E}, \mathbb{F})$. There are two basic operators in MM named erosion and dilation. The *erosion* of an image \mathbf{I} at pixel $x \in \mathbf{E}$ by the structuring element $\mathbf{SE} \subset \mathbf{E}$ is the transformation given by

$$\varepsilon_{\mathbf{SE}}(\mathbf{I})(x) = \{\mathbf{I}(y) : \mathbf{I}(y) = \bigwedge_{z \in \mathbf{SE}(x)} \mathbf{I}(z)\} \quad (7.2)$$

where \bigwedge is the infimum according to a total ordering in \mathbb{F} and $\mathbf{SE}(x)$ is the structuring element centred at the considered pixel x . The dual operator called *dilation* is the transformation given by

$$\delta_{\mathbf{SE}}(\mathbf{I})(x) = \{\mathbf{I}(y) : \mathbf{I}(y) = \bigvee_{z \in \mathbf{SE}(x)} \mathbf{I}(z)\} \quad (7.3)$$

For binary or grey-scale images, they are simple in the sense that they usually have an intuitive interpretation. Erosion $\varepsilon_{\mathbf{SE}}(\mathbf{I})$ shrinks bright objects, whereas dilation $\delta_{\mathbf{SE}}(\mathbf{I})$ expands bright objects at the boundary. The size effect is controlled by the structuring element \mathbf{SE} . They are not inverses of each other, owing to the non-linear character of the operators, however, they constitute an algebraic-adjunction Serra (1988), Heijmans (1994). The morphological *opening* $\gamma_{\mathbf{SE}}(\cdot)$ is an idempotent transformation defined by composition of erosion and dilation, i.e. $\gamma_{\mathbf{SE}}(\mathbf{I}) = \delta_{\mathbf{SE}}(\varepsilon_{\mathbf{SE}}(\mathbf{I}))$. Duality, the morphological *closing* $\varphi_{\mathbf{SE}}(\cdot)$ is defined as the composition of dilation and erosion i.e. $\varphi_{\mathbf{SE}}(\mathbf{I}) = \varepsilon_{\mathbf{SE}}(\delta_{\mathbf{SE}}(\mathbf{I}))$. Their effect are also intuitive: Closing removes ‘‘holes’’ and thin cavities, and opening removes small object protuberances. Fig. 7.3 shows the basic morphological transformations in a high resolution panchromatic image. Additionally, one of the most interesting properties for $(\gamma_{\mathbf{SE}}(\cdot), \varphi_{\mathbf{SE}}(\cdot))$ is that they forms a *Matheron-semigroup* and they obey the *absorption law* Serra (1982), i.e.

$$\gamma_{\mathbf{SE}_1}(\gamma_{\mathbf{SE}_2}(\mathbf{I})) = \gamma_{\mathbf{SE}_1}(\mathbf{I}) \text{ and } \varphi_{\mathbf{SE}_1}(\varphi_{\mathbf{SE}_2}(\mathbf{I})) = \varphi_{\mathbf{SE}_1}(\mathbf{I}) \quad (7.4)$$

if $\mathbf{SE}_2 \subseteq \mathbf{SE}_1$ in a family of scaled structuring elements. For the case of the family of concentric discrete disks, see Soille (2003) p.325.

7.2.3 Morphological Reconstruction

It is often desirable to remove small objects from the image, while keeping larger objects totally intact. A morphological approach to answer this is the *morphological reconstruction*. For example, in

the case of reconstruction by dilation, a marker image \mathbf{M} is dilated in the usual way, but constrained so as to never grow outside the “control” image \mathbf{I} , called mask image. This operator is iterated until convergence is reached. Similarly, the reconstruction by erosion uses standard erosion and the dual constrain. We use the notation $(\varepsilon_{\mathbf{B}}^{\infty}(\mathbf{M}, \mathbf{I}), \delta_{\mathbf{B}}^{\infty}(\mathbf{M}, \mathbf{I}))$ for the couple erosion and dilation by reconstruction Soille (2003), Vincent (1993). Table 7.1 gives the key notations used and the detailed definitions of morphological transformations required in the following formulation. Additionally, transformations by reconstruction are shown in Fig. 7.3 using a practical example.

7.2.4 Additive Morphological Decomposition

Let $\{\underline{\Phi}^i\}, i = 1 \dots, m$ be a set of m anti-extensive transformations indexed for its scale i , such that:

$$\underline{\Phi}^m(\underline{\Phi}^{m-1}(\mathbf{I})) \leq \dots \leq \underline{\Phi}^2(\underline{\Phi}^1(\mathbf{I})) \leq \underline{\Phi}^1(\mathbf{I}) \leq \mathbf{I} \quad (7.5)$$

Similarly, let $\{\overline{\Phi}^i\}$ be a set of m extensive transformations, where i is associated with the parameter of scale, such that:

$$\mathbf{I} \leq \overline{\Phi}(\mathbf{I}) \leq \overline{\Phi}^2(\overline{\Phi}^1(\mathbf{I})) \leq \dots \leq \overline{\Phi}^m(\overline{\Phi}^{m-1}(\mathbf{I})). \quad (7.6)$$

Let us define the consecutive residuals from (7.5) and (7.6), as follows

$$\mathbf{R}_i^+ = \overline{\Phi}^i(\overline{\Phi}^{i-1}(\mathbf{I})) - \overline{\Phi}^{i-1}(\overline{\Phi}^{i-2}(\mathbf{I})) \geq 0 \quad (7.7)$$

$$\mathbf{R}_i^- = \underline{\Phi}^{i-1}(\underline{\Phi}^{i-2}(\mathbf{I})) - \underline{\Phi}^i(\underline{\Phi}^{i-1}(\mathbf{I})) \geq 0 \quad (7.8)$$

with $\overline{\Phi}^0 = \underline{\Phi}^0 = \mathbf{Id}$, the identity transform. From (7.5) and (7.6) we obtain,

$$\mathbf{I} = \overline{\Phi}^m(\overline{\Phi}^{m-1}(\mathbf{I})) - \sum_{i=1}^m \mathbf{R}_i^+ \quad (7.9)$$

and likewise,

$$\mathbf{I} = \underline{\Phi}^m(\underline{\Phi}^{m-1}(\mathbf{I})) + \sum_{i=1}^m \mathbf{R}_i^- \quad (7.10)$$

combining (7.9) and (7.10) provides us with an additive decomposition of the original image as follows

$$\begin{aligned} \mathbf{I} &= \underbrace{\frac{\overline{\Phi}^m(\overline{\Phi}^{m-1}(\mathbf{I})) + \underline{\Phi}^m(\underline{\Phi}^{m-1}(\mathbf{I}))}{2}}_{\mathbf{S}} + \sum_{i=1}^m \underbrace{\frac{(\mathbf{R}_i^- - \mathbf{R}_i^+)}{2}}_{\mathbf{R}_i} \\ &= \mathbf{S} + \sum_{i=1}^m \mathbf{R}_i = \mathbf{S} + \mathbf{R}. \end{aligned} \quad (7.11)$$

We now need to determine what kind of transformations $(\underline{\Phi}^i, \overline{\Phi}^i)$ should use to have interesting additive decomposition.

1. Firstly, we consider the case of a family of morphological operators by reconstruction indexed by the size of the structuring element, i.e., $(\underline{\Phi}^i, \overline{\Phi}^i) = (\gamma_{\mathbf{SE}_i}^{\infty}, \phi_{\mathbf{SE}_i}^{\infty})$ such that $\mathbf{SE}_i \subseteq \mathbf{SE}_j$ for all $i < j$. In this *additive morphological decomposition* (AMD), the couple $(\mathbf{R}_i^-, \mathbf{R}_i^+)$ is essentially composed by image structures associated with bright and dark objects in the image at different scales. The results for a spectral band of a hyperspectral image are shown in Fig.7.4(a)-(d). In this case, thanks to idempotence and absorption laws of the openings Soille (2003), i.e. $\phi_{\mathbf{SE}_i}^{\infty}(\phi_{\mathbf{SE}_j}^{\infty}) = \phi_{\mathbf{SE}_j}^{\infty}$ if $\mathbf{SE}_i \subseteq \mathbf{SE}_j$, the implementation of AMD does not require the composition of transformations associated with different scales. We remark that AMD has the same residues produced by the *differential morphological profile* (DMP) Benediktsson et al. (2003) but its representation has dimension $(m+1)d$ instead than $2md$, and in addition the AMD includes the term \mathbf{S} associated with the image structure.

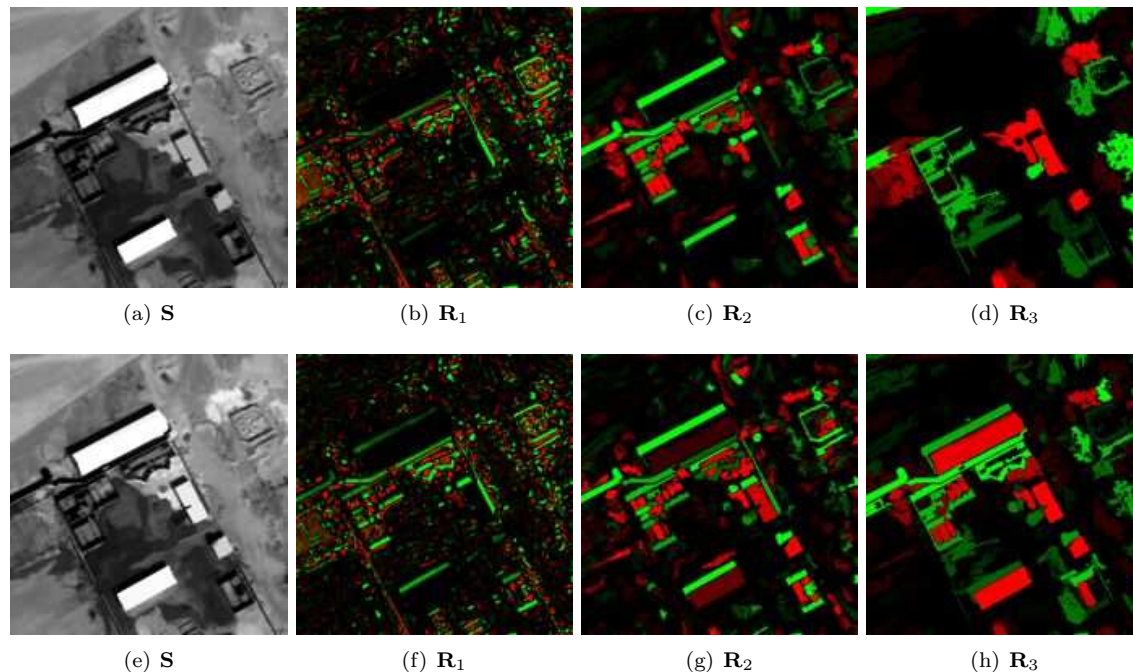


Figure 7.4: Comparison of Additive decomposition for the image shown in Fig. 7.3(a). (a)-(d) Additive Morphological Decomposition (AMD) with SEs disks of diameters equal to 3,7,11. (e)-(h) Additive Decomposition by Gaussian Upper and Lower Leveling (ADL) with standard deviation σ_i equal to 3,7,11. Note that residuals can be negatives(red) or positives(green).

2. Secondly, the additive decomposition (7.11) can be even applied if the transformations do not satisfy the absorption law as in the previous case. That is the case of $(\underline{\Phi}^i, \overline{\Phi}^i) = (\underline{\lambda}_{\sigma_i}(\cdot), \overline{\lambda}_{\sigma_i}(\cdot))$ the pair of *Upper/Lower Leveling* where marker \mathbf{M} is the minimum (maximum) between $G_\sigma(\mathbf{I})$ (the convolution of the original image with a Gaussian kernel with variance σ^2) and the original image \mathbf{I} Meyer (1998). See Table 7.1 to get details of the definition. We use the acronym ADL for *additive decomposition by leveling* to refer to this approach. In ADL, the multiscale effect is controlled by the value σ in the Gaussian kernel associated to the marker. Results for ADL are shown in Fig.7.4(f)-(h) for a practical example. In remote sensing applications, the leveling transformation was advocated in Soille and Pesaresi (2002). Other kind of function can be considered instead of a Gaussian convolution, for instance, subtraction of the original image and a constant as in Meyer (2010).

The decomposition step extracts the most relevant parts from the original image \mathbf{I} , resulting to a cartoon-like image \mathbf{S} , formed by homogeneous regions with sharp boundaries. Expressed in a different way, image \mathbf{S} retains all contrast and boundary information but loses all small scale pattern details. The correspondent residue $\mathbf{R} = \{\mathbf{R}_1, \dots, \mathbf{R}_m\}$, constitutes a hierarchy of multiscale texture components. It should be remarked that the scope of this decomposition is not to find the optimum additive decomposition as done in Buades et al. (2010), Vese and Osher (2003), but it is a simple decomposition scheme where the spatial size of the texture can be interpreted. In the particular case of remote sensing imagery, several morphological decompositions have been proposed as summarised in Table 7.2. In section 7.4, we include experiments of performance of AMD, ADL and DMP in well-known hyperspectral images. Recently, difference of morphological attributes filters have been also introduced by Dalla-Mura et al. (2010, 2011), Ouzounis et al. (2012). The extension of additive morphological decomposition using these filters is straightforward but it is out of the scope of this chapter. At this point, we have introduced an additive decomposition for a multivariate image. The

Table 7.2: Different morphological decomposition considered in m levels.

Acronym	Additive	Trans. ($\underline{\Phi}/\overline{\Phi}$)	Dimension
Differential Morphological Profile (DMP) Benedikts-son et al. (2003)	No	$\gamma_{SE}^{REC}(\cdot)/\varphi_{SE}^{REC}(\cdot)$	$2 \times m \times d$
Morphological Profile by Leveling (MPL) Velasco-Forero and Angulo (2009)	Yes	$\underline{\lambda}_\sigma(\cdot)/\overline{\lambda}_\sigma(\cdot)$	$2 \times m \times d$
Additive Morphological Decomposition (AMD)	Yes	$\gamma_{SE}^{REC}(\cdot)/\varphi_{SE}^{REC}(\cdot)$	$(m + 1) \times d$
Additive Decomposition by Leveling (ADL)	Yes	$\underline{\lambda}_\sigma(\cdot)/\overline{\lambda}_\sigma(\cdot)$	$(m + 1) \times d$

next challenge is to find a way to handle the increase of the dimensionality.

7.3 Tensor Modeling

7.3.1 Introduction

The most popular dimensional reduction approach in HSI is PCA. However, PCA requires a preliminary data arrangement, i.e., the original hyperspectral image \mathbf{I} of size $n_1 \times n_2 \times n_3$ is firstly vectorised into a matrix \mathbf{X} of size $(n_1 n_2) \times n_3$ permitting the use of classic linear algebra approaches, but neglecting spatial rearrangement. The main shortcoming of this method is the assumption of separability between spatial processing and spectral processing. The dimensional reduction approach based on tensor decomposition considers the multivariate image \mathbf{I} as a third order tensor \mathcal{I} [Kolda and Bader \(2009\)](#). This kind of model based on tensor signal processing had been previously applied in HSI [Muti et al. \(2008\)](#) [Bourennane et al. \(2010\)](#). Let us introduce the notation commonly used within tensor analysis literature, followed by the core of dimensional reduction problem and its solution. Let the tensor $\mathcal{I} \in \mathbb{R}^{n_1 \times n_2 \times n_3}$ be an $n_1 \times n_2 \times n_3$ array containing the original information of image \mathbf{I} . Note that $n_3 = d$. Each index in the tensor is called *mode*: the first two are spatial and the third is spectral. Our approach is based on applying multilinear algebra on the whole tensor structure instead of adapting the data tensor to classical matrix-based algebraic techniques by rearrangement.

7.3.2 Tensor Decomposition

A matrix $\mathbf{X} \in \mathbb{R}^{n_1 \times n_2}$ is a two-mode mathematical object that has two associated vector spaces, a row space and a column space. Singular Value Decomposition (SVD) orthogonalises these two spaces and decomposes the matrix as $\mathbf{X} = \mathbf{U}_1 \mathbf{\Sigma} \mathbf{U}_2^T$, where \mathbf{U}_1 and \mathbf{U}_2^T represent orthogonal column space, and $\mathbf{\Sigma}$ is a diagonal singular value matrix. In terms of the i -mode products, this SVD decomposition can be rewritten as $\mathbf{X} = \mathbf{\Sigma} \times_1 \mathbf{U}_1 \times_2 \mathbf{U}_2$, where \times_i is the i -mode product [Lathauwer et al. \(2000\)](#) [Kolda and Bader \(2009\)](#). Extension to a J -order tensor $\mathcal{I} \in \mathbb{R}^{n_1 \times n_2 \times n_3 \times \dots \times n_J}$ was presented by [Lathauwer et al. \(2000\)](#) orthogonalising J spaces and expressing the tensor as the J -mode product of J -orthogonal spaces

$$\mathcal{I} = \mathcal{C} \times_1 \mathbf{U}_1 \times_2 \mathbf{U}_2 \times_3 \dots \times_J \mathbf{U}_J \quad (7.12)$$

Tensor \mathcal{C} , known as the core tensor, is analogous to the diagonal singular value matrix in conventional matrix SVD. It is important to realise, however, that the core tensor has no diagonal structure; rather, \mathcal{C} is in general a full tensor. The core tensor governs the interaction between the mode matrices \mathbf{U}_i , for $i = 1, \dots, J$. Mode matrix \mathbf{U}_i contains the orthonormal vectors spanning the column space of the matrix \mathbf{X}_i that results from the i -mode *flattening* of \mathcal{I} . Flattening, also known as matricization or unfolding, is the process of reordering the elements of an i -mode into a matrix

Kolda and Bader (2009).

This tensor version of singular value decomposition is known as higher-order SVD (HOSVD) from the work of De Lathauwer, De Moor, and Vandewalle [Lathauwer et al. \(2000\)](#), who showed that the HOSVD is a convincing generalisation of the matrix SVD and discussed ways to efficiently compute the leading left singular vectors of \mathbf{X}_i . An excellent compendium about tensor decomposition is presented in [Kolda and Bader \(2009\)](#). The HOSVD is usually performed using Alternative Least Square algorithm used to jointly find i -mode matrices \mathbf{U}_i , but recently other approaches have been introduced [Eldén and Savas \(2009\)](#). In the case of three mode tensors \mathcal{I} , the objective of HOSVD is to select subspaces $\mathbf{U}_1, \mathbf{U}_2$ and \mathbf{U}_3 and the core tensor \mathcal{C} such that the L_2 -norm reconstruction error is minimised [Kolda and Bader \(2009\)](#),

$$\min_{\mathbf{U}_1, \mathbf{U}_2, \mathbf{U}_3, \mathcal{C}} E_1 = \|\mathcal{I} - \mathcal{C} \times_1 \mathbf{U}_1 \times_2 \mathbf{U}_2 \times_3 \mathbf{U}_3\|^2 \quad (7.13)$$

where $\mathbf{U}_1, \mathbf{U}_2, \mathbf{U}_3$ are required to be orthogonal, i.e., $\mathbf{U}_1^T \mathbf{U}_1 = \mathbf{U}_2^T \mathbf{U}_2 = \mathbf{U}_3^T \mathbf{U}_3$. With the orthonormality condition, we can obtain $\mathcal{E} = \mathcal{I} \times_1 \mathbf{U}_1^T \times_2 \mathbf{U}_2^T \times_3 \mathbf{U}_3^T$, and (7.13) can be written as:

$$\begin{aligned} \min_{\mathbf{U}_1, \mathbf{U}_2, \mathbf{U}_3} E_1 &= \|\mathcal{I}\|^2 - \|\mathcal{E}\|^2 \\ \Leftrightarrow \max_{\mathbf{U}_1, \mathbf{U}_2, \mathbf{U}_3} E_2 &= \|\mathcal{E}\|^2 \end{aligned} \quad (7.14)$$

As it was presented by [Huang et al. \(2008\)](#), the equation (7.14) is equivalent to maximize:

$$\begin{aligned} \max_{\mathbf{U}_1, \mathbf{U}_2, \mathbf{U}_3} E_2 &= \text{Trace}(\mathbf{U}_1^T \mathbf{F} \mathbf{U}_1) = \\ \text{Trace}(\mathbf{U}_2^T \mathbf{G} \mathbf{U}_2) &= \text{Trace}(\mathbf{U}_3^T \mathbf{H} \mathbf{U}_3) \end{aligned} \quad (7.15)$$

where:

$$\begin{aligned} \mathbf{F}_{ii'} &= \sum_{ll'} (\mathbf{X}_{(l)} \mathbf{U}_2 \mathbf{U}_2^T \mathbf{X}_{(l')}^T)_{ii'} (\mathbf{U}_3 \mathbf{U}_3^T)_{ll'} \\ \mathbf{G}_{jj'} &= \sum_{ll'} (\mathbf{X}_{(l)} \mathbf{U}_1 \mathbf{U}_1^T \mathbf{X}_{(l')}^T)_{jj'} (\mathbf{U}_3 \mathbf{U}_3^T)_{ll'} \\ \mathbf{H}_{ll'} &= \sum_{ii' jj'} \mathcal{I}_{ijl} \mathcal{I}_{i'j'l'} (\mathbf{U}_1 \mathbf{U}_1^T)_{ii'} (\mathbf{U}_2 \mathbf{U}_2^T)_{jj'} \end{aligned}$$

Since $\mathbf{F}, \mathbf{G}, \mathbf{H}$ are semi-positive definite, $\|\mathcal{E}^2\|$ is monotonically increasing, therefore HOSVD algorithm converges to a local optimum. Thus theoretically, the solutions HOSVD are not unique. That issue was already pointed in [Kolda and Bader \(2009\)](#) and studied in detail for [Luo et al. \(2011\)](#) in real life databases concluding that the convergence depends on the eigenvalue distribution for the matrix \mathbf{F}, \mathbf{G} and \mathbf{H} . However, our analysis of the algorithm convergence in real HSIs has shown that cumulative values in the eigenvalues of \mathbf{F} and \mathbf{G} is a better criterion [Velasco-Forero and Angulo \(2010c\)](#).

7.3.3 Tensor Principal Component Analysis (TPCA)

In high-dimensional images as HSI, it is of great interest to reduce the spectral dimension in order to exceed problems as ‘‘Curse of Dimensionality’’ in distance-based analysis or nonparametric analysis and ‘‘Hughes phenomenon’’ in linear classifiers ([Jiménez et al. \(2007\)](#)). Commonly a pre-processing step consists in performing a PCA to the reduce feature space by considering only the k first components. We present a tensor version for PCA based on [Renard and Bourennane \(2008\)](#). It is a lower rank approximation, where classical PCA is a particular case, if no subspace reduction is performed in the modes associated with rows and columns. We assume that the hyperspectral image \mathcal{I} is a zero-mean tensor in the flattening matrix related to the J -mode, i.e., $\bar{\mathbf{X}}_J = \mathbf{0}$. That is equivalent to subtracting the empirical mean vector from each column of the data matrix \mathbf{X} as in

PCA. In addition, the best lower rank tensor approximation of \mathcal{I} [Lathauwer et al. \(2000\)](#), denoted by $\tilde{\mathcal{I}}$ is:

$$\tilde{\mathcal{I}} = \mathcal{I} \times_1 \mathbf{P}_1 \times_2 \mathbf{P}_2 \times_3 \dots \times_J \mathbf{P}_J \quad (7.16)$$

where $\mathbf{P}_i = \mathbf{U}_i \mathbf{U}_i^T$, and \mathbf{U}_i is found by using expression (7.12). This representation allows to include noise filtering in the sense of SVD filtering [Andrews and Patterson \(1976\)](#) if only the largest eigenvectors are considered per mode. Thus, the tensor-PCA (TPCA) approximation of the image \mathcal{I} with parameters $(s_1, s_2, \dots, s_{J-1}, k)$, $1 \leq s_i \leq n_i, \forall i = 1, \dots, J-1$, is defined as follows:

$$\tilde{\mathcal{I}} = \mathcal{I} \times_1 \tilde{\mathbf{U}}_{s_1} \tilde{\mathbf{U}}_{s_1}^T \times_2 \tilde{\mathbf{U}}_{s_2} \tilde{\mathbf{U}}_{s_2}^T \times_3 \dots \times_J \tilde{\mathbf{U}}_k^T \quad (7.17)$$

where k denotes the dimension in the J -mode, i.e., the number of components in the dimensional reduction. Additionally, s_i is the number of eigenvectors included in the filtering with respect to the i -mode and $\tilde{\mathbf{U}}_{s_i}$ contains the s_i eigenvectors associated with the s_i largest eigenvalues holding of the unfolding matrix \mathbf{X}_i . We define the first k *tensor principal components* with parameters (s_1, \dots, s_{j-1}) of \mathcal{I} as the first k column of the matrix $\tilde{\mathbf{U}}_k^T$ from (7.17). Summarising, for a HSI \mathbf{I} , the tensor principal component analysis with parameters (s_1, s_2, k) is a transformation $\mathcal{F}(\mathbf{E}, \mathbb{R}^d) \rightarrow \mathcal{F}(\mathbf{E}, \mathbb{R}^k)$. The equivalence to the principal component analysis is presented in the next section.

7.3.4 Equivalence with PCA

In the case of a typical hyperspectral image represented as a tensor, \mathcal{I} of size $n_1 \times n_2 \times n_3$, the expression (7.17) is particularised as

$$\tilde{\mathcal{I}} = \mathcal{I} \times_1 \tilde{\mathbf{U}}_{s_1} \tilde{\mathbf{U}}_{s_1}^T \times_2 \tilde{\mathbf{U}}_{s_2} \tilde{\mathbf{U}}_{s_2}^T \times_3 \tilde{\mathbf{U}}_k^T, \quad (7.18)$$

where $\tilde{\mathbf{U}}_1$ and $\tilde{\mathbf{U}}_2$ has the s_1 and s_2 largest eigenvectors associated of the unfolding matrix \mathbf{X}_1 and \mathbf{X}_2 , respectively. Firstly, it is important to remark that if $s_1 = n_1$ and $s_2 = n_2$, $\tilde{\mathbf{U}}_1 \tilde{\mathbf{U}}_1^T = \mathbf{I}_{n_1 \times n_1}$ and $\tilde{\mathbf{U}}_2 \tilde{\mathbf{U}}_2^T = \mathbf{I}_{n_2 \times n_2}$ in that case, expression (7.18) becomes:

$$\tilde{\mathcal{I}} = \mathcal{I} \times_3 \tilde{\mathbf{U}}_k^T,$$

where $\tilde{\mathbf{U}}_k$ contains the k -largest eigenvectors associated of the unfolding matrix \mathbf{X}_3 , i.e., the matrix \mathbf{X} of $(n_1 \times n_2)$ rows and n_3 columns that is the traditional unfolding of \mathcal{I} . Using the assumption that \mathcal{I} is a zero-mean tensor in the third order, the eigenvectors associated to \mathbf{X} are the same as the expression $(\mathbf{X} - \mu)^T (\mathbf{X} - \mu)$ which are the projections calculated by PCA. To illustrate this results in a practical example, we calculate the first five components in both PCA and TPCA. The absolute value of the differences between the squares of projections calculated by PCA and TPCA are illustrated in Fig. 7.5 for a real HSI (Indian Pines). It is easy to see that when the components number in the spatial dimension (s_1, s_2) for TPCA are equal to the image original dimension, the projections calculated by TPCA and PCA become similar. The differences become larger as soon as the spatial dimension reduces. Consequently, by this spatial dimension reduction with $s_1 < n_1$ and $s_2 < n_2$ we obtain through TPCA a spatial smoothing separately in rows and columns of the image, which is not produced in PCA.

7.3.5 Modeling additive morphological decomposition with TPCA

The basic idea of our approach is summarised in Fig. 7.6. For a hyperspectral image \mathcal{I} we find the additive decomposition in m levels, as it was introduced in Section 7.2, i.e. $\mathcal{I} = \mathcal{S} + \mathcal{R}_1 + \dots + \mathcal{R}_m$. We regroup the whole decomposition in a four-order tensor $\mathcal{D} = [\mathcal{S}, \mathcal{R}_1, \dots, \mathcal{R}_m]$. We apply the TPCA with parameters s_1, s_2, k_1, k_2 with $k = k_1 \times k_2$,

$$\tilde{\mathcal{D}} = \mathcal{D} \times_1 \tilde{\mathbf{U}}_{s_1} \tilde{\mathbf{U}}_{s_1}^T \times_2 \tilde{\mathbf{U}}_{s_2} \tilde{\mathbf{U}}_{s_2}^T \times_3 \tilde{\mathbf{U}}_{k_1}^T \times_4 \tilde{\mathbf{U}}_{k_2}^T \quad (7.19)$$

where $\tilde{\mathcal{D}}$ is a tensor of size $n_1 \times n_2 \times k_1 \times k_2$. The parameters s_1 and s_2 are associated with the spatial filtering in the sense of SVD filtering in the rows and columns space, k_1 is the reduction in

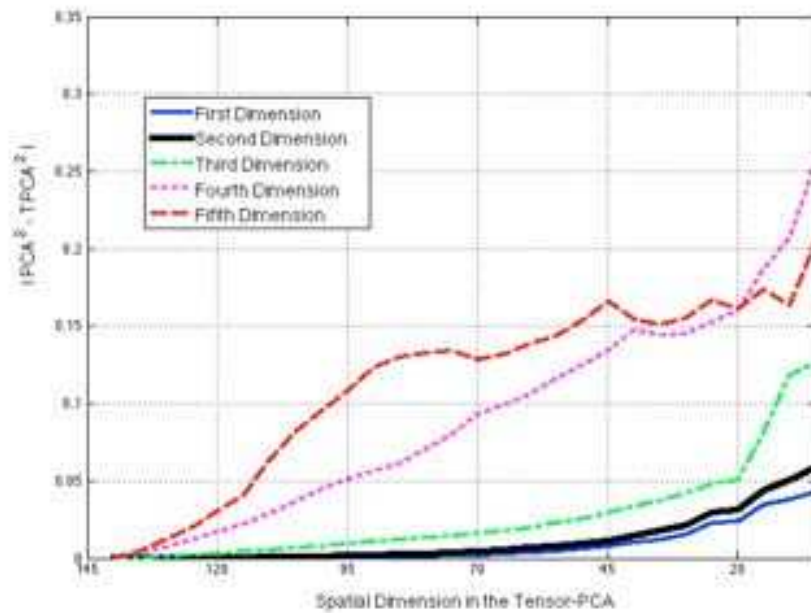


Figure 7.5: Experiment shows clearly that TPCA is equivalent to PCA. Experiments are presented with $s_1 = s_2$ in the interval $[n_1 = n_2, \dots, 1]$, for the Indian Pines hyperspectral image of size 145×145 in 200 bands.

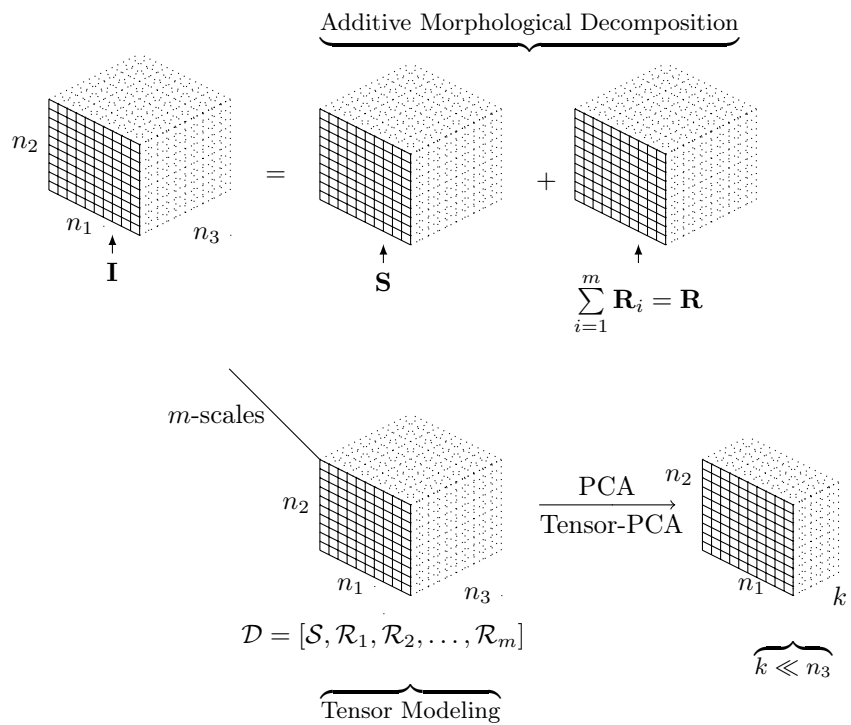


Figure 7.6: Illustration of dimensional reduction stage using additive morphological decomposition.

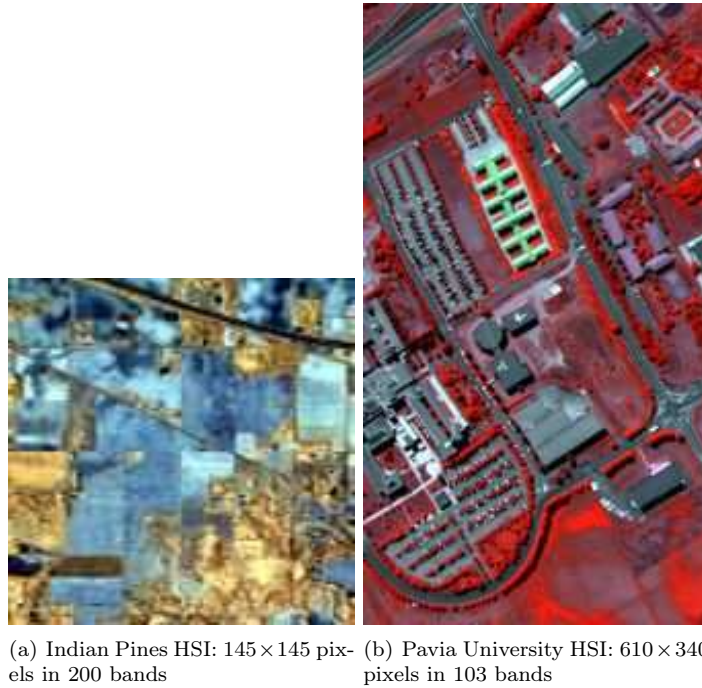


Figure 7.7: False colour composition of the HSI considered in the experiments.

the spectral space and k_2 is corresponding to the scale decomposition. The connection to precedent subsection is established for TPCA in four-order tensors, to traditional PCA in the case of $k_1 = n_1$, $k_2 = n_2$ and no scale decomposition. In summary, the proposed workflow yields a reduced feature space as PCA where the spatial information included in the morphological decomposition is relevant. Additionally, spatial filtering can be included through the tensor decomposition.

7.4 Experiments

In this section, we present the experimental results obtained in our analysis. Firstly, we overview the characteristics of the data used in the experimental setup. After that, several experiments are presented in order to compare the effectiveness of the proposed additive decompositions and tensor dimensional reduction. The application of the introduced approach requires a morphological transformation for vector images. Supervised or unsupervised ordering introduced in the first part of the thesis can be used in this proposed. However, for the sake of simplicity and comparison with the state of the art, we present the results of our approach applying the transformations marginally, i.e. for each channel $i = 1, \dots, d$ independently. For instance, the dilation of the d -variate image \mathbf{I} is given by $\delta_{SE}(\mathbf{I})(\mathbf{x}) = [\delta_{SE}(x_1), \delta_{SE}(x_2), \dots, \delta_{SE}(x_d)]$, where $\mathbf{x} = [x_1, x_2, \dots, x_d]$. And similarly, for all the other operators summarised in Table 7.1.

7.4.1 Data Description and Experimental Setup

In order to further evaluate and compare the proposed algorithm with other state-of-the-art approaches for spatial-spectral classification, we use two real hyperspectral images:

1. Airborne Visible/Infrared imaging spectrometer hyperspectral image (AVIRIS) Indian Pines Scene. The AVIRIS sensor generates 220 bands across the spectral range from 0.2 to 2.4 μm . In the experiments, the number of bands is reduced to 200 by removing 20 water absorption

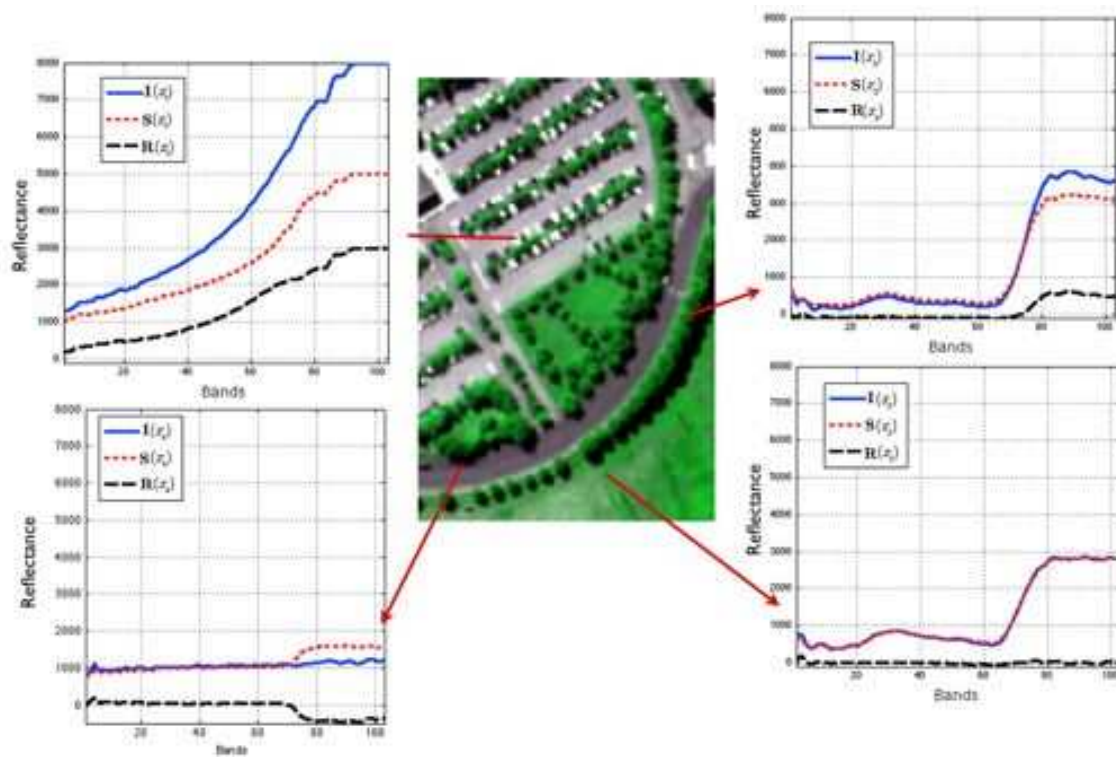


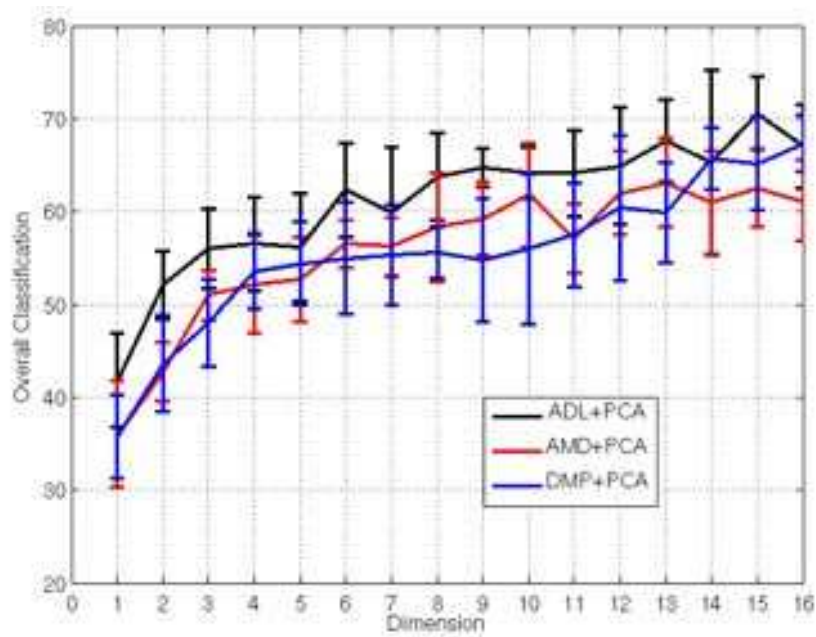
Figure 7.8: AMD using $\{SE_1, SE_2\}$ a disk of diameter 2 and 4 is shown for four pixels in the ROSIS Pavia University HSI. First pixel (Left-Up) is a one-pixel set object. Its residual component (\mathbf{R}) is large in comparison to the structure one \mathbf{S} , i.e., the pixel is very different from its neighbours. Second pixel (Right-Up) is a tree. The residual component is important only in the spectrum associated with vegetation. Third pixel (Left-Down) is a shadow-tree. Residual is negative and significant only in the vegetation section of the spectrum. Fourth pixel (Right-Down) is a pixel in a homogeneous zone, i.e., it has no texture component.

Table 7.3: Classification accuracy for Indian Pines HSI. Only five samples per class are included in the training set.

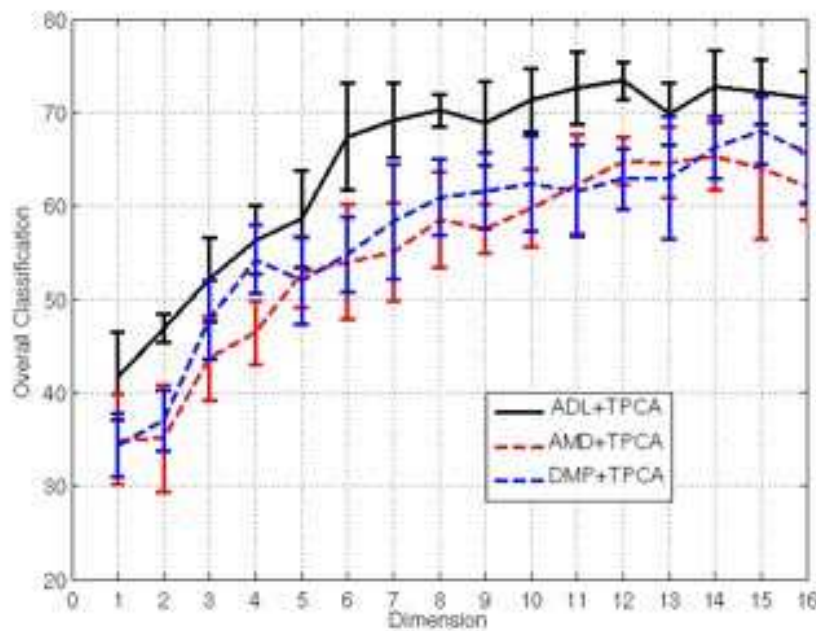
Method	OA %	Kappa statistics (κ)
Spatial Kernel Camps-Valls et al. (2007)		
Spectral +SVM	45.79	0.43
Spectral +Graph	48.96	0.46
Summation + SVM	48.88	0.46
Summation + Graph	52.27	0.49
Cross +SVM	61.75	0.60
Cross+Graph	66.04	0.64
Random Field+Multinomial Logistic Regression Li et al. (2009)		
SS	72.62	N/A
LORSAL	58.10	N/A
Differential Morphological Profile		
DMP + PCA(16)+SVM	67.33	0.62
DMP + TPCA(15)+SVM	68.10	0.63
Additive Morphological Decomposition		
ADL + PCA(15)+SVM	70.57	0.66
ADL + TPCA(12)+SVM	73.39	0.69
AMD + PCA(13)+SVM	63.13	0.57
AMD + TPCA(14)+SVM	65.31	0.60

bands. The image has a spatial resolution of 20 meters per pixel and a spatial dimension of 145×145 pixels. For illustrative purpose, Fig. 7.7(a) shows a false colour composition of the AVIRIS Indian Pines. This image is a classical benchmark to validate the accuracy of HSI analysis algorithms and constitutes a challenging problem due to the significant presence of mixed pixels in all available classes and also because of the unbalanced number of available labeled pixels per class. We follow the experiment proposed in [Camps-Valls et al. \(2007\)](#) to analyse HSI classification in a very difficult situation. From the 16 different land-cover classes available in the original ground-truth, seven were discarded due to an insufficient number of training samples. The finally selected classes with the training sample size in parenthesis were: \hat{O} Corn-no till \hat{O} (1434), \hat{O} Corn-min till \hat{O} (834), \hat{O} Grass/Pasture \hat{O} (497), \hat{O} Grass/Trees \hat{O} (747), \hat{O} Hay-wind-rowed \hat{O} (489), \hat{O} Soybean-no till \hat{O} (968), \hat{O} Soybean-min till \hat{O} (2468), \hat{O} Soybean-clean till \hat{O} (614), and \hat{O} Woods \hat{O} (1294). Summarising, the ground-truth contains nine classes, as seen in Fig. 7.10(a). In the experiment, we test the introduced method in different ill-posed scenarios where only five pixels are used as training samples per class. Our results are compared with those reported by [Camps-Valls et al. \(2007\)](#), [Li et al. \(2009\)](#).

- University of Pavia, is an urban image acquired by Reflective Optics System Imaging Spectrometer (ROSIS). The ROSIS sensor generates 115 spectral bands ranging from 0.43 to 0.86 μm with a band of 4nm and has a spatial resolution of 1.3-meter per pixel. The image consists of 610×340 pixels as shown in Fig. 7.7(b), each having 103 bands with 12 most noisy bands removed. There are nine ground-truth classes of interest, as shown in Fig. 7.12(a). Nine thematic land-cover classes were identified in the university campus: Trees, Asphalt, Bitumen, Gravel, Metal sheets, Shadows, Self-blocking Bricks, Meadows, and Bare soil. For this data set, a total of 3921 and 42776 pixels were available as training and test sets, respectively, as seen in Fig. 7.12(b). Proposed approach results are compared with those obtained from [Landgrebe \(2003\)](#), [Tarabalka et al. \(2010c\)](#), [Li et al. \(2011, 2012\)](#), [Fauvel et al. \(2012\)](#).



(a) Overall accuracy of morphological decompositions as a function of the number of components in PCA.



(b) Overall accuracy of morphological decompositions as a function of the number of component in TPCA.

Figure 7.9: First scenario of classification using Indian Pines. Only five pixels per class are selected for the training set. The results show the average and standard deviation in 25 repetitions.

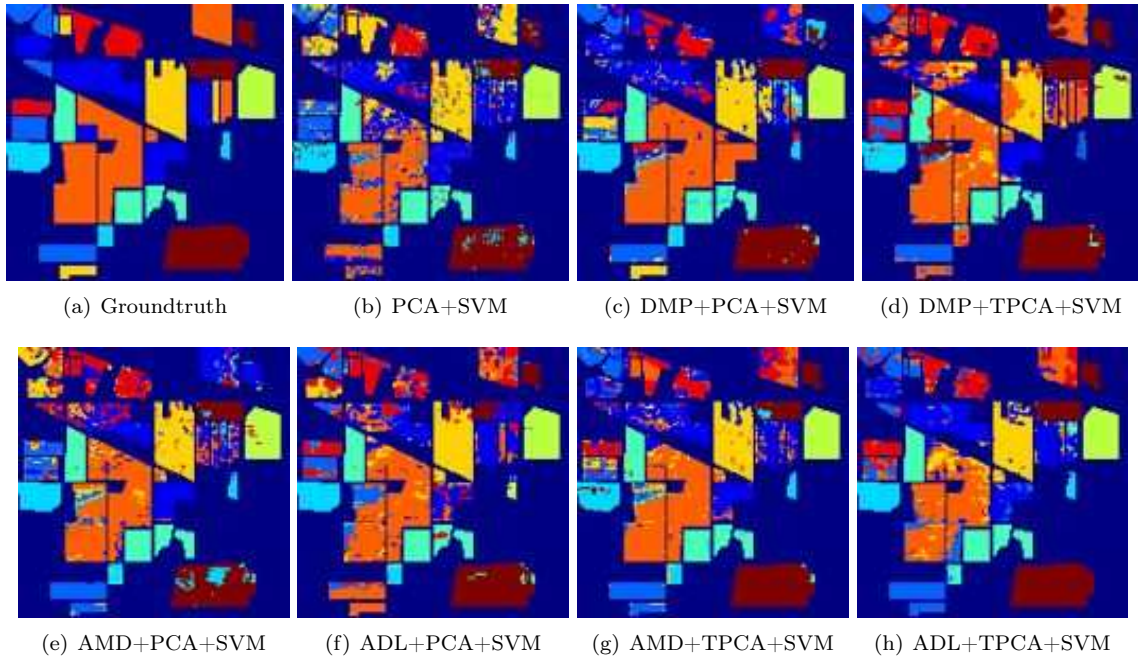


Figure 7.10: Classification maps for the Indian Pines HSI using different approaches. Only five training pixels in nine classes are considered. The classification map is the best result in 25 random repetitions.

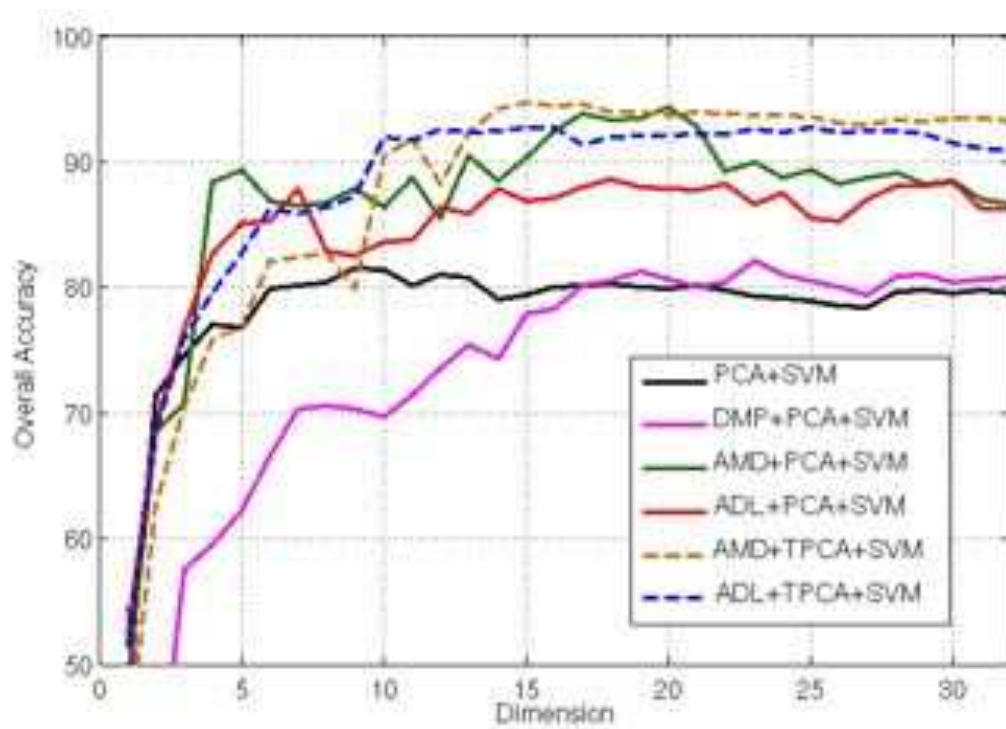


Figure 7.11: Behaviour of the overall accuracy in the Pavia University dataset for different morphological decompositions and dimensional reduction approach.

Table 7.4: Overall and average classification accuracies and κ statistics obtained after comparing the proposed framework with other spatial-spectral classifiers for Pavia University data set. Classification task is performed by SVM.

Method	Overall Accuracy	Average Accuracy	Kappa statistics (κ)
ECHO Landgrebe (2003)	87.58	92.16	.8390
SVMMSF+MV Tarabalka et al. (2010c)	91.08	94.76	.8830
SSK Fauvel et al. (2012)	86.11	91.98	.8235
LORSAL-MLL Li et al. (2011)	85.57	92.54	.8180
MLRsubMLL Li et al. (2012)	94.10	93.45	.9224
PCA+SVM(9)	81.57	87.39	.7662
DMP+PCA+SVM(23)	82.12	83.54	.7675
AMD+PCA+SVM(20)	94.32	94.64	.9253
ADL+PCA+SVM (18)	88.67	91.39	.8508
AMD+TPCA+SVM(15)	94.70	94.51	.9301
ADL+TPCA+SVM(15)	92.72	91.77	.9043

Table 7.5: Overall, average, and individual class accuracies (in percentage) and κ statistic obtained for Pavia University data set. The best results are highlighted in bold typeface. Additive decomposition are compared with others morphological analysis. EMP is the algorithm introduced by [Benediktsson et al. \(2005\)](#) and SSK is the procedure suggested by [Fauvel et al. \(2012\)](#)

Class	SVM	EMP	SSK	PCA(9)	DMP + PCA(23)	AMD + PCA(20)	ADL + PCA(18)	AMD + TPCA(15)	ADL+ TPCA(15)
Asphalt	80.64	93.33	84.36	83.52	88.30	96.56	92.75	93.45	93.30
Meadow	68.47	73.40	78.52	74.89	84.06	94.01	89.72	95.77	94.07
Gravel	73.80	52.45	84.80	70.32	55.03	84.52	88.71	82.80	65.41
Tree	97.49	99.31	96.87	98.07	84.30	98.56	97.91	98.86	98.56
Metal sheet	99.49	99.48	99.88	99.48	99.78	99.48	100	99.48	99.55
Bare soil	94.83	61.90	95.61	82.86	57.49	88.86	59.14	89.72	87.69
Bitumen	91.50	97.67	95.56	90.30	99.02	99.17	96.84	99.02	97.44
Brick	91.88	95.17	95.44	88.78	93.78	98.23	99.13	98.86	98.56
Shadow	97.04	92.29	97.78	98.21	90.07	92.40	98.31	92.61	91.34
Overall	80.13	79.83	86.11	81.57	82.12	94.32	88.67	94.70	92.72
Average	88.33	85.00	91.98	87.39	83.54	94.64	91.39	94.51	91.77
κ	.7519	.7415	.8235	.7662	.7675	.9253	.8508	.9301	.9043

7.4.2 Classification

Support Vector Machine (SVM) have shown promising results in terms of prediction accuracy in HSI [Melgani and Bruzzone \(2004\)](#). A pixel-wise classification was performed using the multi-class one versus one SVM classifier in the correspondent dimension produced by PCA and TPCA in the morphological decompositions considered in Section 7.2. The reduced space is scaled to the range of $[0, 1]$ and SVM is trained with Gaussian kernel, and parameters tuned in the range $\{-1, \dots, 3\}$ for the regularisation parameter and $\{-4, 1\}$ for the Gaussian kernel parameter by using cross-validation. The following measures of accuracy were used: Overall accuracy (OA) is the percentage of correctly classified pixels, average accuracy (AA) is the mean of class-specific accuracies, i.e., the percentage of correctly classified pixels for each class, and kappa coefficient (κ) is the percentage of agreement, i.e., correctly classified pixels, corrected by the number of agreements that would be expected purely by chance. In order to compare the performance of the proposed technique to include the spatial information into a classification task, we have also included results of the previously proposed methods: ECHO spatial classifier [Landgrebe \(2003\)](#), Spatial kernels [Camps-Valls et al. \(2007\)](#), Markov Random Field [Li et al. \(2009\)](#) Bayesian approach to active learning [Li et al. \(2011\)](#), subspace multinomial logistic regression [Li et al. \(2012\)](#) and classification followed by post-processing [Tarabalka et al. \(2010c\)](#). Morphological approaches to analysis HSI are also included [Fauvel et al. \(2012\)](#) and [Benediktsson et al. \(2005\)](#). Additionally, the objective in the experiment is to complete the comparative analysis in feature spaces of different dimension size produced by the proposed additive morphological decomposition and extracted by PCA and TPCA. The parameters in the TPCA (s_1, s_2) have been set to avoid the convergence problem in the tensor decomposition, as it has been suggested in [Velasco-Forero and Angulo \(2010c\)](#).

7.4.3 Results and discussion

Firstly, to illustrate the motivation behind this work and to clarify the concept of additive decomposition for multivariate images, Fig. 7.8 visualises the concept of additive decomposition for four types of pixels in a well-know HSI. Spectra are decomposed accordingly to their relationship in the spatial neighbourhood. Simple interpretations can be done regarding the structure+texture decomposition in the spectrum range (See caption in Fig. 7.8). Secondly, a quantitative comparison is carried out using two real HSI. The Indian Pines experiment shows the importance to incorporate spatial information previously to feature reduction. To reliably evaluate the performance of the proposed method, the results were averaged over 25 different randomly selected training (of size five) for a number of feature yield by PCA and TPCA in the range of $[1, \dots, 16]$. Mean and standard deviation are shown in Fig. 7.9. In the broader range of results, ADL performs better than AMD and DMP, it was applied in different reduced feature dimensions. ADL led to the best classification results, as it can also be seen from Table 7.3. On the other hand, this experiment confirms our intuition that the inclusion of a spatial prior can significantly improve the classification results provided by using only spectral information. Fig. 7.10 shows the thematic classification maps for the pixel wise SVM and the spectral-spatial classification by morphological decomposition after the dimensional reduction step.

Our approach involving morphological information is clearly better than its spectral equivalent. Additionally, our proposal ADL involving tensor reduction has the best performance with more than 73% in overall classification in this very difficult scenario.

In turn, it can also be seen in Fig. 7.11 that the inclusion of the tensor structure provides much higher classification accuracies than those reported for PCA. Pavia University HSI allows us to compare the results of our workflow with spatial-spectral classifiers based on different approaches. From Table 7.4, it can be observed that the proposed additive decompositions (AMD and ADL) obtain good result when compared with other methods. Tensor structure improves the classification accuracy and yields a representation with better separability in lower dimension, for instance, from 20 features for ADL+PCA+SVM (OA-88.67%) to 15 features for ADL+TPC+SVM (OA-92.72%). Table 7.5 gives the class-specific accuracies of the best pixel wise classification in the projected space induced by the correspondent dimensional reduction algorithm. The performances of the proposed additive decomposition are compared with those obtained by other morphological based approaches

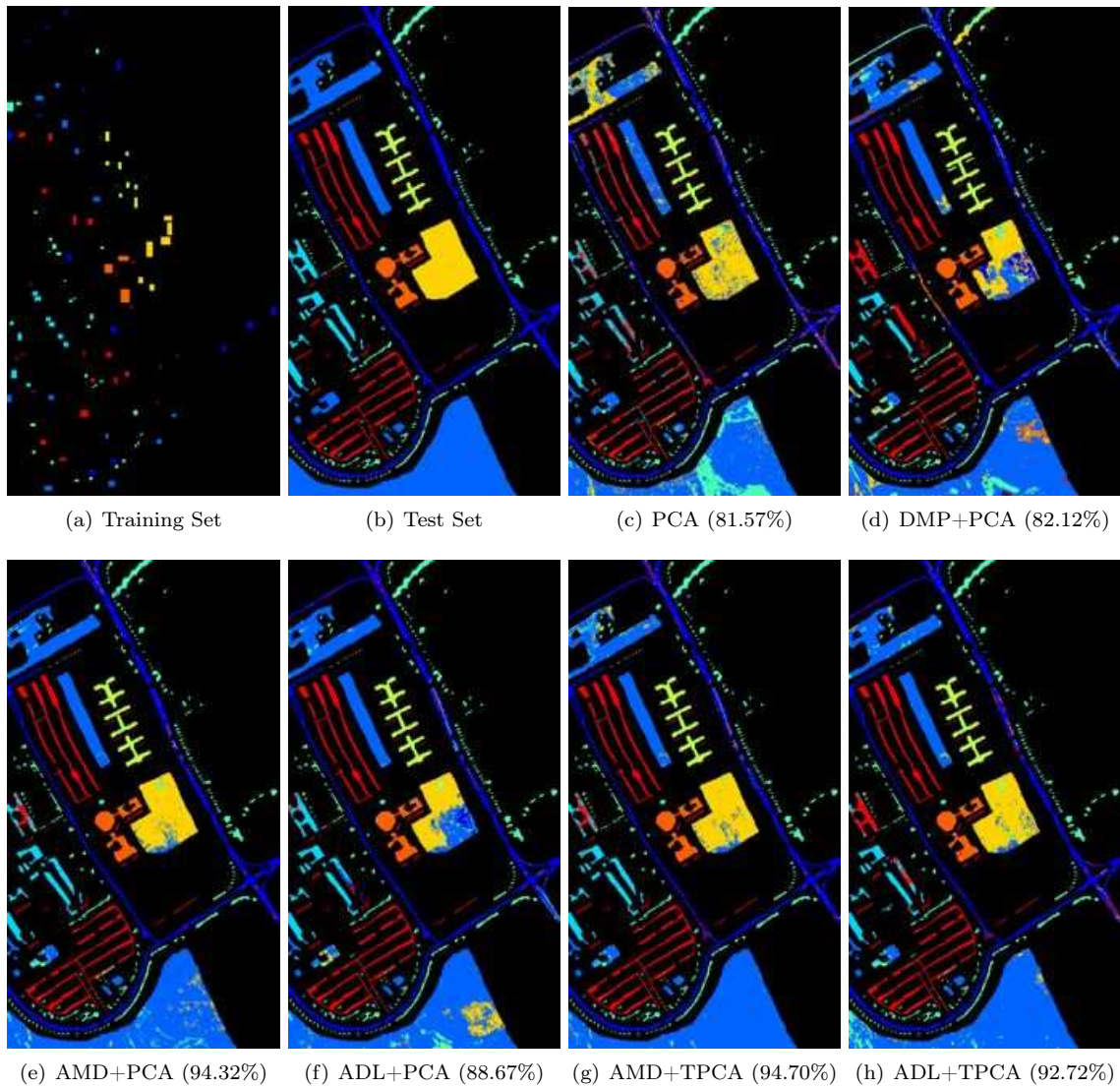


Figure 7.12: Classification maps obtained by the different tested methods for Pavia University data set (Overall accuracies are reported in parentheses)

Benediktsson et al. (2005), Fauvel et al. (2012). The AMD+TPCA yields the best OA and kappa coefficient. Most of the best class-specific accuracies are obtained by AMD with PCA or TPCA. This approach significantly outperforms other classification approaches. For illustrative purposes, the effectiveness of the proposed framework with Pavia University HSI is further shown in Fig. 7.12 and the classification maps obtained are displayed along with their associated OA scores. Fig. 7.12 shows the classification maps of PCA, DMP+PCA, and additive decompositions reduced by PCA and TPCA. As it can be seen, the ADM map contains much more homogeneous spatial structures when compared for instance to the PCA map.

7.5 Conclusions of the chapter

This chapter proposed a framework integrating structural/spatial information in unsupervised dimensionality exploration and feature extraction for multivariate images. Additive morphological decomposition is a nonlinear representation that favourably incorporates the spatial information in dimension reduction approaches. Tensor modelling integrates structural/spatial information, together with the spectral one, in feature extraction causing drastic dimension reductions without detrimental effect to classifier performance. We notice that complex objects are not defined by single level sets and consequently their structures appear in several scales of the decomposition. Results in real hyperspectral images show how the tensor approach incorporates more usefully spatial information in dimensional reduction stage in comparison with its matrix equivalent version.

8

Conditional mathematical morphology for enhancement and impulse noise removal

There are known knowns; there are things we know we know. We also know there are known unknowns; that is to say we know there are some things we do not know. But there are also unknown unknowns – there are things we do not know we don't know.

Donald Rumsfeld

Résumé

Nous considérons dans ce chapitre les deux problèmes suivants : l'amélioration du contraste d'une image et la restauration d'une image «contaminée» par de bruit poivre-et-sel. Un cadre unifié et de faible complexité, basé sur la morphologie mathématique conditionnelle, est introduit. Nous introduisons la notion de morphologie mathématique conditionnelle et ses opérateurs sont utilisés pour définir un critère pour l'opérateur de contraste (Toggle Mapping) basé sur un masque conditionnant. Ce cadre unifié est basé sur la définition d'un masque initial, qui varie selon le type de traitement requis. En comparaison avec de techniques complexes plus avancées, telles que les médianes non locales et la régression à noyau, notre approche a un meilleur comportement dans le cas d'images très bruitées (>75%), menant à une performance relativement stable, même pour de très forts niveaux de bruit (>90%)¹.

8.1 Introduction

Denosing and edge enhancement are probably two of the most studied problems in signal and image processing. Digital signals and images are frequently affected by impulse noise, also known as salt-and-pepper noise, during their acquisition and/or transmission. It is well known that linear filtering techniques fail when the noise is non-additive and are not effective in removing impulse noise [Gonzalez and Woods \(2008\)](#). This has led to the development of nonlinear signal processing techniques. A class of widely used nonlinear digital filters are mathematical morphology filters. In general, mathematical morphology is a nonlinear image processing methodology based on the

¹The content of this chapter is mainly based on the following paper:

- [Velasco-Forero et al. \(2012\)](#), *Conditional mathematical morphology for edge enhancement and salt-and-pepper noise reduction*, submitted.

application of lattice theory to spatial structures. This means that the definition of morphological operators needs a complete lattice structure, i.e., the possibility of defining an ordering relationship between the points to be processed.

On the one hand, image enhancement is used to refine the quality of an image for visualisation purposes, or to provide better input for other automated image processing techniques. Available techniques of image enhancement can be roughly divided into two broad categories: spatial domain methods and frequency domain methods [Gonzalez and Woods \(2008\)](#). The spatial domain methods operate on image pixels directly. Many of these methods are based on grey-level histogram modifications, while others are based on PDEs or morphological versions of *shock filters*. The basic idea behind shock filters is to perform dilations and erosions in order to create a “shock” between influence zones. Dilations are performed around maxima and erosion around minima. Thus, shock filters belong to the class of morphological image enhancement methods. Most of the current shock filters are based either on the original definition of [Kramer and Bruckner \(1975\)](#) or on modifications of Osher and Rudin formulation in terms of partial differential equations (PDEs) [Osher and Rudin \(1990\)](#). Shock filters offer a number of advantages: They create strong discontinuities at image edges, and within a region the filtered signal becomes flat. Since they satisfy a *maximum-minimum principle* stating that the range of the filtered image remains within the range of the original image, and they do not increase the L_1 norms of the derivatives of a signal (total variation), they possess inherent stability properties [Weickert \(2003\)](#). Moreover, in contrast to frequency domain methods based on Fourier or wavelet transforms, over- and undershoots cannot appear [Mallat \(2008\)](#). This makes shock filters attractive for a number of applications where edge sharpening and a piecewise constant segmentation is desired. Several interesting modifications of the original schemes have been proposed, for instance: morphological toggle mappings [Serra and Vincent \(1992\)](#), [Meyer and Serra \(1989\)](#), PDE-based enhancing [Gilboa et al. \(2002\)](#), [Osher and Rudin \(1991\)](#), [Schavemaker et al. \(2000\)](#) as well as coherence-enhancing shock filters [Weickert \(2003\)](#) combining the stability properties of shock filters with the possibility of enhancing flow based on the eigenvalues of the second-moment matrix or structure tensor. All these variants, however, still pursue the original intention of shock filtering, namely *edge enhancement*. In many practical situations, the intensity of pixels within an object vary slowly across the “interior” of objects [Elder and Zucker \(1998\)](#). A good edge enhancement algorithm should alter pixels “close” to the edges and preserve local contrast for interior pixels. However, the image contrast is highly correlated with the gradient magnitude of its edges [Elder and Zucker \(1998\)](#). Thus, some shock filters can cause unpleasant ring or halo effects. This drawback was pointed out by different authors [Meyer and Serra \(1989\)](#), [Gilboa et al. \(2004\)](#). In this chapter a conditional shock filter is formulated. It is robust to halo problems, with convergence in a few number of iterations. This is achieved by generalising the original Kramer formulation with an enhancing flow based on a mask image. We use the name *conditional toggle mapping* to refer to our approach.

On the other hand, there are many methods for the *removal of impulse noise*. Some of the more relevant with respect to the present work are those of vector median filter [Astola et al. \(1990\)](#), vector directional filter [Trahanias and Venetsanopoulos \(1993\)](#), and methods that combine noise detection with noise removal [Hwang and Haddad \(1995\)](#). Each of these studies has several variants and combinations [Chan et al. \(2005\)](#), [Zhang and Karim \(2002\)](#), [Eng and Ma. \(2001\)](#), [Srinivasan and Ebenezer \(2007\)](#). These papers detect possible noisy pixels and replaced by using median value or its variant while leaving uncorrupted pixels unchanged. The main contribution of this chapter is the formulation of an unified framework for enhancement and impulse noise reduction.

The chapter is outlined as follows. Section 8.2 briefly recalls the notion of shock filters and toggle mappings. The proposed conditional toggle mapping is detailed in Section 8.3. It is followed by experimental results in well-known grey and colour images in Section 8.4. Section 8.5 ends the chapter with concluding remarks.

8.2 Brief review

Let us precise the terms and notation to be used in the rest of the chapter. Let \mathbf{E} be a subset of the discrete space \mathbb{Z}^2 , considered as the support space of the image, and $\mathbb{F} \subseteq \mathbb{R}^d$ be a set of pixels values in dimension d , corresponding to the space of values of the image with d channels. A *vector-value image* is represented by the mapping,

$$\mathbf{I} : \begin{cases} \mathbf{E} & \rightarrow & \mathbb{F} \\ x & \rightarrow & \mathbf{x} \end{cases} \quad (8.1)$$

i.e., $\mathbf{I} \in \mathcal{F}(\mathbf{E}, \mathbb{F})$ the set of maps from a pixel $x \in \mathbf{E}$ into a vector value $\mathbf{x} \in \mathbb{F} \subseteq \mathbb{R}^d$. The two basic morphological mappings $\mathcal{F}(\mathbf{E}, \mathbb{F}) \rightarrow \mathcal{F}(\mathbf{E}, \mathbb{F})$ are the *erosion* and *dilation* by a flat (symmetric) structuring element \mathbf{SE} and are given respectively by:

$$\varepsilon_{\mathbf{SE}}(\mathbf{I})(x) = \{\mathbf{I}(z) : \mathbf{I}(z) = \bigwedge_{y \in \mathbf{SE}(x)} \mathbf{I}(y)\} \quad (8.2)$$

and

$$\delta_{\mathbf{SE}}(\mathbf{I})(x) = \{\mathbf{I}(z) : \mathbf{I}(z) = \bigvee_{y \in \mathbf{SE}(x)} \mathbf{I}(y)\} \quad (8.3)$$

where $\mathbf{SE}(x) \in \mathbf{E}$ denote the spatial neighbourhood induced by the structuring element \mathbf{SE} centred at x . These operators require than \mathbb{F} should be a lattice with suitable operators \bigvee and \bigwedge . In the grey-level case ($d = 1$) basic morphological operators (8.2) and (8.3) have an unified definition. However, in multivariate case ($d > 1$) maximum and minimum operators do not have a natural extension. Existing multichannel image processing approaches can be roughly discerned between marginal methods, which act on each channel separately, and vector methods, which analyse pixels as multivariate objects. Specifically, in applying our approach to multichannel images, we use a marginal approach where the conditional toggle mappings are applied to the different channels independently. In any case, methods of extension of mathematical morphology introduced in first part of this thesis can be used for the conditional toggle mapping discussed in this chapter. Consider now, \mathbf{I} is a grey-level image. The first definition of the shock filter may be traced back to 1975 when Kramer and Bruckner have proposed the non-linear transformation for enhancement of digital images as follows,¹

Definition 5. *Kramer and Bruckner (1975)* Given an image \mathbf{I} the shock filter is defined as follows

$$\tau_{\mathbf{SE}}(\mathbf{I}) = \begin{cases} \varepsilon_{\mathbf{SE}}(\mathbf{I}) & \text{if } \Delta_{\mathbf{SE}}(\mathbf{I}) < 0, \\ \delta_{\mathbf{SE}}(\mathbf{I}) & \text{if } \Delta_{\mathbf{SE}}(\mathbf{I}) > 0, \\ \mathbf{I} & \text{otherwise.} \end{cases} \quad (8.4)$$

where $\Delta_{\mathbf{SE}}(\mathbf{I}) = \Delta_{\mathbf{SE}}^{\varepsilon}(\mathbf{I}) - \Delta_{\mathbf{SE}}^{\delta}(\mathbf{I}) = (\mathbf{I} - \varepsilon_{\mathbf{SE}}(\mathbf{I})) - (\delta_{\mathbf{SE}}(\mathbf{I}) - \mathbf{I})$ is the morphological Laplacian of the original image, $\varepsilon_{\mathbf{SE}}(\cdot)$ and $\delta_{\mathbf{SE}}(\cdot)$ are erosion and dilation by using a structuring element \mathbf{SE} .

It is based on the idea of using a dilation process near a local maximum and an erosion process around a local minimum. The decision whether a pixel belongs to the influence zone of a maximum or a minimum is made on the basis of the morphological Laplacian Vliet et al. (1989). If the Laplacian is negative, then the pixel is considered to be in the influence zone of a maximum, while it is regarded to belong to the influence zone of a minimum if the Laplacian is positive. Iterating this procedure produces a sharp discontinuity (shock) at the borderline between two influence zones. Within each zone, a constant segment is created. The method of Kramer and Bruckner has been formulated in a fully discrete way. The term *shock filtering* has been introduced by Osher and Rudin (1991). Shock filtering constitutes an example of a PDE that is difficult to analyse in the continuous setting, while

¹The original formulation includes less or equal in the dilation case. Schavemaker et al. (2000) includes the "otherwise" case to preserve the original signal in a single-slope signal ($\forall x : \Delta_{\mathbf{SE}}^{\varepsilon}(f(x)) = \Delta_{\mathbf{SE}}^{\delta}(f(x))$)

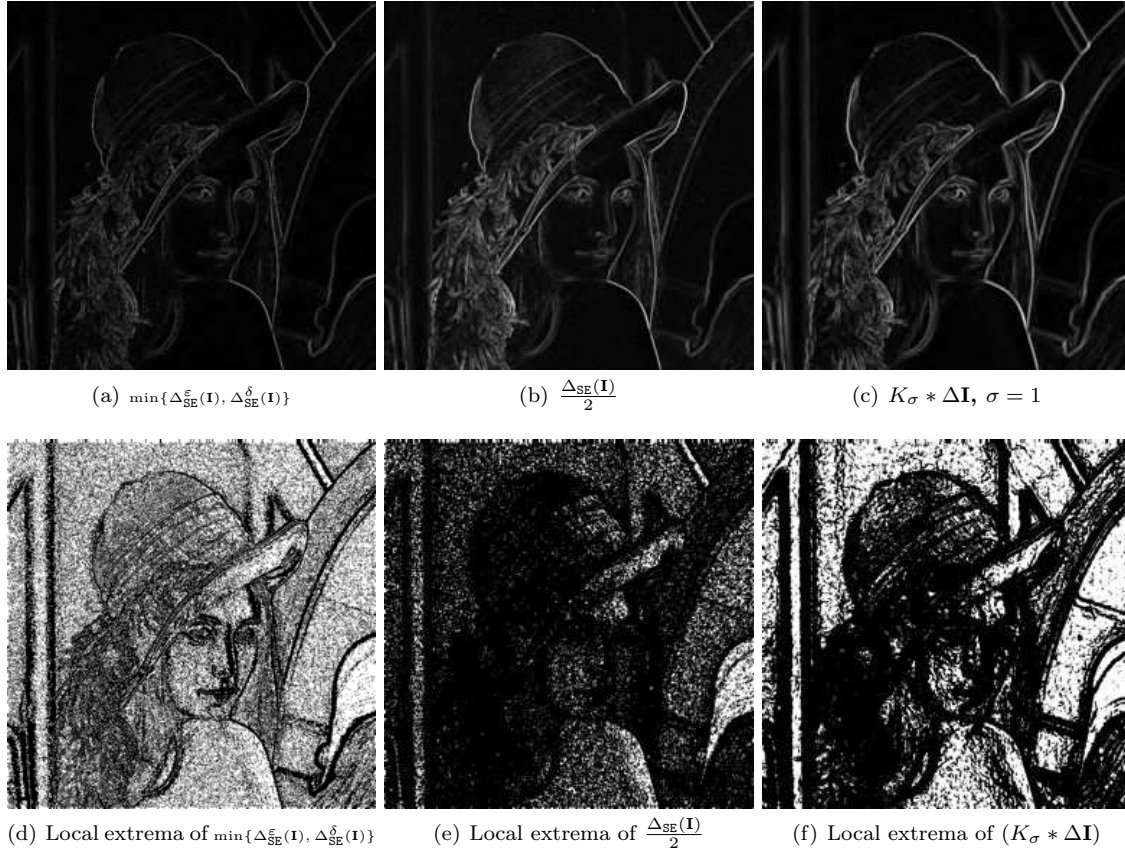


Figure 8.1: (a-c) Gradient definition used in the chapter, and other definitions by [Kramer and Bruckner \(1975\)](#) and [Alvarez and Mazorra \(1994\)](#). SE is a disk of size 1 and $\sigma = 1$. (d-f) Local extrema detector (< 2) by using (a-c).

for a 1-D space discretization in [Welk et al. \(2007\)](#) has been shown that this process is well-posed and satisfies a maximum-minimum principle. An analytic solution of the corresponding dynamical system was even found [Welk et al. \(2007\)](#). Different modifications have been proposed in order to improve the performance of shock filters. Alvarez and Mazorra [Alvarez and Mazorra \(1994\)](#) replaced the Laplacian as edge detector by $K_\sigma * \Delta(\mathbf{I})$, where K_σ is a Gaussian with standard deviation σ , $\Delta\mathbf{I}$ is the gradient of \mathbf{I} , and $*$ denotes convolution. Fig. 8.1 illustrates different edge detector and associated local extrema (pixels considered as local maxima or local minima) according to different definitions.

On the other hand, in the literature of mathematical morphology, a *toggle mapping* is defined for the original image \mathbf{I} and a series of transformations $\Psi = \{\psi_1, \psi_2, \dots, \psi_n\}$ as the transformation based on a *toggling criterion* operating over Ψ , i.e. a decision rule which determines at each point the “best” value among the “candidates” Ψ [Serra \(1988\)](#), [Serra and Vincent \(1992\)](#), [Meyer and Serra \(1989\)](#). A trivial example of a toggle mapping is the threshold operator. The primitives Ψ are the white and black images, and the decision rule involves a simple comparison of \mathbf{I} with a threshold value. The classical shock filter (8.4) is also a particular case of a toggle mapping denominated as *toggle contrast* [Serra \(1989b\)](#). Additionally, the *morphological centre* [Serra \(1988\)](#) defined by the median among the triplet $(\wedge\Psi(\mathbf{I}), \vee\Psi(\mathbf{I}), \mathbf{I})$ is a notion which naturally appears in the self-dual morphological filters [Serra \(1988\)](#). Toggle contrast is usually applied not only once but is iterated, i.e.,

$$\tau_{SE}^\infty(\mathbf{I}) = \{\tau_{SE}^i(\mathbf{I}) | \tau_{SE}^i(\mathbf{I}) = \tau_{SE}(\tau_{SE}^i(\mathbf{I}))\}, \quad (8.5)$$

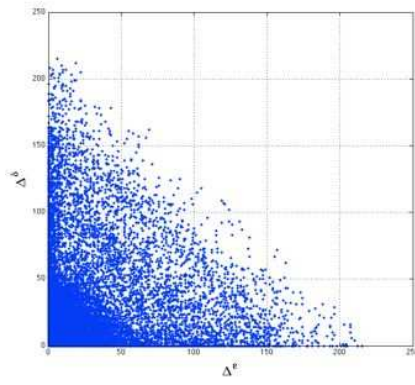
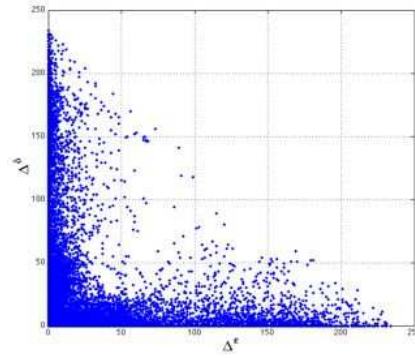
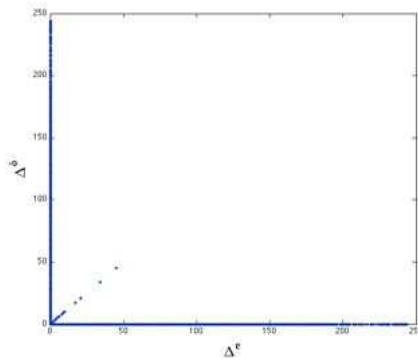
(a) $\Delta_{SE}^\epsilon(\mathbf{I})$ vs $\Delta_{SE}^\delta(\mathbf{I})$ (b) $\Delta_{SE}^\epsilon(\tau_{SE}(\mathbf{I}))$ vs $\Delta_{SE}^\delta(\tau_{SE}(\mathbf{I}))$ (c) $\Delta_{SE}^\epsilon(\tau_{SE}^\infty(\mathbf{I}))$ vs $\Delta_{SE}^\delta(\tau_{SE}^\infty(\mathbf{I}))$ (d) \mathbf{I} (e) Red pixels are local maximum (minimum) according to $\min\{\mathbf{I} - \varepsilon_{SE}(\mathbf{I}), \delta_{SE}(\mathbf{I}) - \mathbf{I}\} = 0$ and blue according to $\mathbf{I} - \varepsilon_{SE}(\mathbf{I}) = \delta_{SE}(\mathbf{I}) - \mathbf{I}$. Green are pixels satisfying both definitions.(f) $\tau_{SE}^\infty(\mathbf{I})$

Figure 8.2: Bi-dimensional representation of the evolution in the classical shock filter (8.4) for the Cameraman grey-scale image in (d).

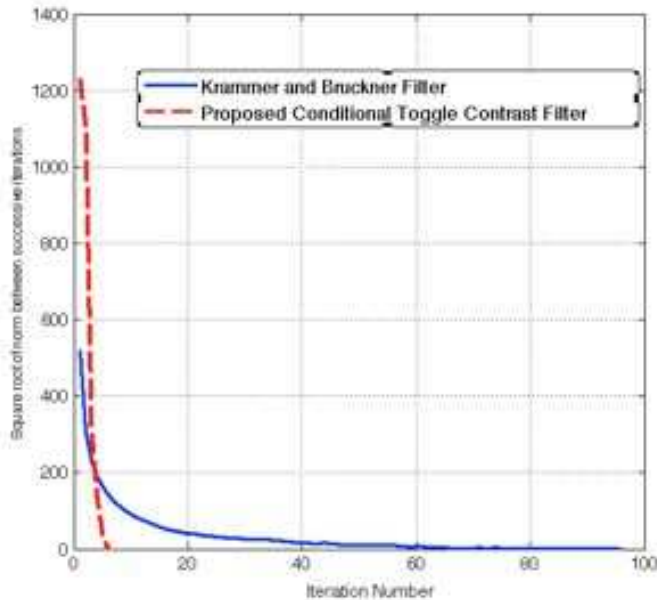


Figure 8.3: Iteration number versus residual between two consecutive iterations of classical $\|\tau_{SE}^{i+1}(\mathbf{I}) - \tau_{SE}^i(\mathbf{I})\|$ and conditional $\|\tilde{\tau}_{SE}^{i+1}(\mathbf{I}, \mathbf{M}) - \tilde{\tau}_{SE}^i(\mathbf{I}, \mathbf{M})\|$ approach in a grey scale image of size 256×256 pixels. The proposed conditional toggle mapping converges in at small number of iterations in comparison with the original one. In terms of processing time, the original toggle mapping takes at least four times than conditional toggle mapping (110 ms in a 2.4 GHz Intel Core 2 Duo with 4 GB 1067 MHz.)

where $\tau_{SE}^0(\mathbf{I}) = \mathbf{I}$ and $\tau_{SE}^1(\mathbf{I})$ is given by (8.4). The iterations of toggle contrast converge to a *fixed point* [Krammer and Bruckner \(1975\)](#) reached after a finite number of iterations. [Heijmans \(1997\)](#) defines self-dual operators based on the morphological center and subsequently self-dual filters. Basically, he considers the important fact that every increasing, self-dual operator can be modified in such a way that the sequence of iterations of a given image is pixelwise monotone (strictly increasing or decreasing in each pixel). This implies on a convergence to a limit operator, thus avoiding oscillation problems typical in non-convergent filters such as median filtering. The convergence is obtained when all the pixels are fixed points, as shown in Fig. 8.2. To illustrate the evolution until convergence, Figs. 8.2(a-b) show the first and second iteration of (8.5) in a bi-dimensional representation of image value gradient by erosion and dilation. When convergence is reached, Fig. 8.2(c), all the pixels are fixed points according to the criterion (8.4). Note the presence of pixels in the line $\Delta_{SE}^\varepsilon(\mathbf{I}) = \Delta_{SE}^\delta(\mathbf{I})$. Classic shock filters have two main drawbacks. First, the halo effect [Meyer and Serra \(1989\)](#), [Gilboa et al. \(2002\)](#) can be produced due to the tie case in the definition. The second problem lies in the large number of iterations until convergence. Convergence curve for the toggle mapping in the case of cameraman image is shown in Fig. 8.3. These two drawback motivated us to define the conditional toggle mapping introduced in the next section.

8.3 Conditional toggle mapping

In this section, we introduce the central idea in our approach: the definition of a *conditional toggle mapping*. Let \mathbf{M} be the characteristic function of a mask, i.e., $\mathbf{M} \in \mathcal{F}(\mathbf{E}, \{0, 1\})$ maps each pixel $x \in \mathbf{E}$ into $\mathbf{M}(x) = \{0, 1\}$. Our approach is based on a neighbourhood associated to a structuring element SE and to the mask \mathbf{M} ,

$$N_{(SE, \mathbf{M})}(x) = \{y \in SE(x) \text{ and } \mathbf{M}(y) = 1\}.$$

That allows us to define the conditional version of the erosion, the morphological mapping $\mathcal{F}(\mathbf{E}, \mathbb{F}) \rightarrow \mathcal{F}(\mathbf{E}, \mathbb{F})$ as follows,

Definition 6. Conditional erosion of an image \mathbf{I} with respect to a binary mask \mathbf{M} is defined by the following expression:

$$\varepsilon_{\text{SE}}(\mathbf{I}, \mathbf{M})(x) = \begin{cases} \bigwedge_{y \in N_{(\text{SE}, \mathbf{M})}(x)} \mathbf{I}(y) & \text{if } \mathbf{M}(x) = 0 \text{ and } N_{(\text{SE}, \mathbf{M})}(x) \neq \emptyset, \\ \mathbf{I}(x) & \text{otherwise,} \end{cases} \quad (8.6)$$

and equivalently for the dilation,

Definition 7. Conditional dilation of an image \mathbf{I} with respect to \mathbf{M} is defined by

$$\delta_{\text{SE}}(\mathbf{I}, \mathbf{M})(x) = \begin{cases} \bigvee_{y \in N_{(\text{SE}, \mathbf{M})}(x)} \mathbf{I}(y) & \text{if } \mathbf{M}(x) = 0 \text{ and } N_{(\text{SE}, \mathbf{M})}(x) \neq \emptyset \\ \mathbf{I}(x) & \text{otherwise.} \end{cases} \quad (8.7)$$

The idea of conditional morphology was firstly presented by [Jochems \(1997\)](#) for binary images. Expression (8.6) and (8.7) are equivalent to the ones introduced in [Jochems \(1997\)](#) for binary images but differs in grey-scale images due to the “otherwise” case. The motivation of this idea is that pixels in the mask are considered as sources in the morphological operation, and they are invariants (See Fig. 8.4 for visual intuition).

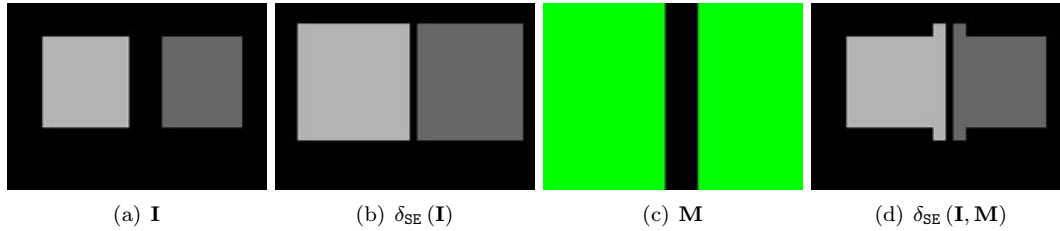


Figure 8.4: Conditional vs Classical Dilation. \mathbf{I} is a grey scale image of 175×245 pixels, SE is a square of size 25. Pixels of the mask are displayed in green. Note that objects in the mask are not dilated.

Algebraic properties of morphological operators have been studied extensively in [Heijmans \(1994, 1997\)](#), [Roerdink \(2009\)](#), [Maragos \(2005\)](#). One of the main ingredients of the theory of the algebraic properties of morphological operator is the definition of adjunction.

Definition 8. [Heijmans \(1994\)](#) Let \mathcal{L}_1 and \mathcal{L}_2 be two complete lattices, ε an operator $\mathcal{L}_1 \rightarrow \mathcal{L}_2$, and δ an operator $\mathcal{L}_2 \rightarrow \mathcal{L}_1$. The pair (ε, δ) is called an adjunction if $\delta(\mathbf{I}) \leq_{\mathcal{L}_1} \mathbf{J} \iff \mathbf{I} \leq_{\mathcal{L}_2} \varepsilon(\mathbf{J})$.

We prove the following equivalence between adjunction and the composition of morphological operators.

Theorem 1. (ε, δ) is an adjunction $\iff \delta$ and ε are both increasing and $\delta(\varepsilon(\mathbf{J})) \leq_{\mathcal{L}_1} \mathbf{J} \quad \forall \mathbf{J} \in \mathcal{L}_1$ and $\mathbf{I} \leq_{\mathcal{L}_2} \varepsilon(\delta(\mathbf{I})) \quad \forall \mathbf{I} \in \mathcal{L}_2$.

Proof. (Only if) Suppose (ε, δ) is an adjunction, so we have

$$\begin{aligned} \delta(\mathbf{I}) \leq_{\mathcal{L}_1} \mathbf{J} &\iff \mathbf{I} \leq_{\mathcal{L}_2} \varepsilon(\mathbf{J}), \text{ so in the particular case of } \delta(\mathbf{I}) \\ \delta(\mathbf{I}) \leq_{\mathcal{L}_1} \delta(\mathbf{I}) &\iff \mathbf{I} \leq_{\mathcal{L}_2} \varepsilon(\delta(\mathbf{I})) \end{aligned}$$

Similarly for the other half

$$\begin{aligned} \delta(\mathbf{I}) \leq_{\mathcal{L}_1} \mathbf{J} &\iff \mathbf{I} \leq_{\mathcal{L}_2} \varepsilon(\mathbf{J}), \text{ so in the particular case of } \varepsilon(\mathbf{J}) \\ \iff \delta(\varepsilon(\mathbf{J})) \leq_{\mathcal{L}_1} \mathbf{J} &\iff \varepsilon(\mathbf{J}) \leq_{\mathcal{L}_2} \varepsilon(\mathbf{J}) \end{aligned}$$

(if) Now assume that $\delta(\varepsilon(\mathbf{J})) \leq_{\mathcal{L}_1} \mathbf{J}$ and $\mathbf{I} \leq_{\mathcal{L}_2} \varepsilon(\delta(\mathbf{I}))$ holds and ε and δ are increasing.

$$\begin{aligned} \text{If } \delta(\mathbf{I}) \leq_{\mathcal{L}_1} \mathbf{J}, \text{ then by increasing assumption,} \\ \Rightarrow \varepsilon(\delta(\mathbf{I})) \leq_{\mathcal{L}_2} \varepsilon(\mathbf{J}), \text{ by hypothesis} \\ \Rightarrow \mathbf{I} \leq_{\mathcal{L}_2} \varepsilon(\mathbf{J}) \end{aligned}$$

Similarly for the other half, if

$$\begin{aligned} \mathbf{I} \leq_{\mathcal{L}_2} \varepsilon(\mathbf{J}), \text{ (increasing)} \\ \Rightarrow \delta(\mathbf{I}) \leq_{\mathcal{L}_1} \delta(\varepsilon(\mathbf{J})), \text{ (hypothesis)} \\ \Rightarrow \delta(\mathbf{I}) \leq_{\mathcal{L}_1} \mathbf{J}. \end{aligned}$$

□

We can now note that the pair $(\varepsilon_{\text{SE}}(\cdot, \mathbf{M}), \delta_{\text{SE}}(\cdot, \mathbf{M}))$ is not an adjunction as it is illustrated in Fig. 8.5. However, we can calculate the algebraic adjunction of the conditional dilation. It is important

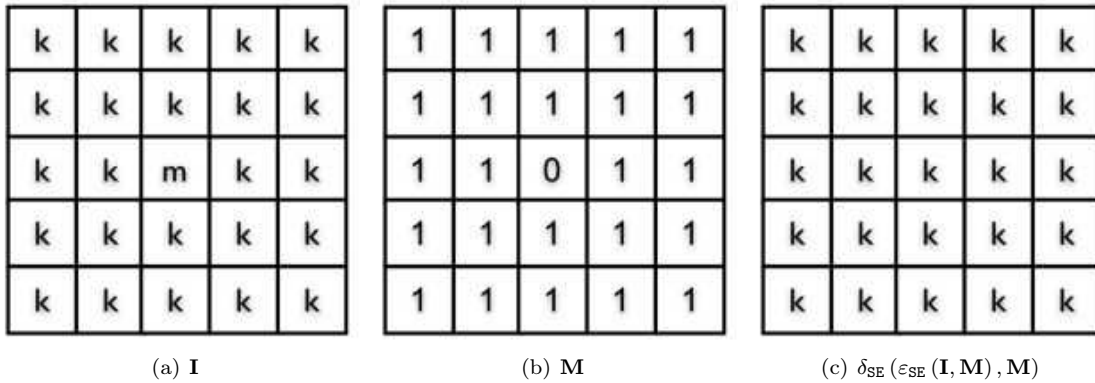


Figure 8.5: Example showing that the pair conditional operators are not an adjunction in algebraic sense. If $k \neq m$, $\delta_{\text{SE}}(\varepsilon_{\text{SE}}(\mathbf{I}, \mathbf{M}), \mathbf{M}) = \varepsilon_{\text{SE}}(\delta_{\text{SE}}(\mathbf{I}, \mathbf{M}), \mathbf{M})$ but not equal to \mathbf{I} , so by Theorem 1, $(\varepsilon_{\text{SE}}(\cdot, \mathbf{M}), \delta_{\text{SE}}(\cdot, \mathbf{M}))$ is not an adjunction. In the example, SE is a square of side three (8-connectivity).

because it produces a link in a unique way between morphological operators, and idempotent filtering can be achieved by composition (opening). Additionally, it guarantees that the composition reduces the information content. This kind of analysis has been carried out in morphological operators applied to images Heijmans and Ronse (1990), graphs Heijmans et al. (1992), pyramids Keshet and Heijmans (2003), and curve evolution Keshet and Heijmans (2003).

Proposition 3. Let $\tilde{\varepsilon}_{\text{SE}}(\mathbf{I}, \mathbf{M})$ be defined by:

$$\tilde{\varepsilon}_{\text{SE}}(\mathbf{I}, \mathbf{M})(x) = \begin{cases} \bigwedge_{y \in N_{(\text{SE}, \mathbf{M}^c)}(x)} \mathbf{I}(y) & \text{if } x \in \mathbf{M}, \text{ and } \exists y \in N_{(\text{SE}, \mathbf{M}^c)}(x), \\ \mathbf{I}(x) & \text{otherwise} \end{cases} \quad (8.8)$$

then the pair $(\tilde{\varepsilon}_{\text{SE}}(\mathbf{I}, \mathbf{M}), \delta_{\text{SE}}(\mathbf{I}, \mathbf{M}))$ is an adjunction.

Proof. For every $\text{SE} \in \mathbf{E}$ and a given $\mathbf{M} \in \mathcal{F}(\mathbf{E}, \{0, 1\})$, the pair $(\tilde{\varepsilon}_{\text{SE}}(\cdot, \mathbf{M}), \delta_{\text{SE}}(\cdot, \mathbf{M}))$ defines an adjunction on $\mathcal{F}(\mathbf{E}, \mathbb{F})$ [Proposition 4.33, Heijmans (1994)]. In other words

$$\delta_{\text{SE}}(\mathbf{I}, \mathbf{M}) \leq \mathbf{J} \iff \mathbf{I} \leq \tilde{\varepsilon}_{\text{SE}}(\mathbf{J}, \mathbf{M})$$

for all $\mathbf{I}, \mathbf{J} \in \mathcal{F}(\mathbf{E}, \mathbb{F})$.

Definition (8.7) is equivalent to

$$\delta_{\text{SE}}(\mathbf{I}, \mathbf{M})(x) = \begin{cases} \mathbf{I}(x) & \text{if } x \in \mathbf{M}, \\ \mathbf{I}(x) & \text{if } \mathbf{M}(x) = 0 \text{ and } \nexists y \in N_{(\text{SE}, \mathbf{M})}(x), \\ \bigvee_{y \in N_{(\text{SE}, \mathbf{M})}(x)} \mathbf{I}(y) & \text{if } \mathbf{M}(x) = 0 \text{ and } \exists y \in N_{(\text{SE}, \mathbf{M})}(x). \end{cases} \quad (8.9)$$

We start analysing the first two cases, i.e., $\mathbf{M}(x) = 0$, and, $x \in \mathbf{M}$ and $\nexists y \in N_{(\text{SE}, \mathbf{M})}(x)$, where the proof is simple: $\delta_{\text{SE}}(\mathbf{I}, \mathbf{M})(x) \leq \mathbf{J}(x) \iff \mathbf{I}(x) \leq \mathbf{J}(x) \leq \tilde{\varepsilon}_{\text{SE}}(\mathbf{J}, \mathbf{M})(x)$ due to $\mathbf{M}(x) = 0$ or $\nexists y \in N_{(\text{SE}, \mathbf{M})}(x)$. To prove in the third case is enough to see that $y \in N_{(\text{SE}, \mathbf{M})}(x) \iff \mathbf{J}(y) \leq \varepsilon_{\text{SE}}(\mathbf{J}, \mathbf{M})$ and following a similar idea that in Roerdink (2009) we have:

$$\begin{aligned} & \delta_{\text{SE}}(\mathbf{I}, \mathbf{M})(x) \leq \mathbf{J}(x) \quad \forall \mathbf{M}(x) = 0 \\ \iff & \bigvee_{y \in N_{(\text{SE}, \mathbf{M})}(x)} \mathbf{I}(y) \leq \mathbf{J}(x) \quad \forall \mathbf{M}(x) = 0 \\ \iff & \mathbf{I}(y) \leq \mathbf{J}(x), \quad \forall \mathbf{M}(x) = 0, \quad y \in N_{(\text{SE}, \mathbf{M})}(x) \\ \\ \iff & \mathbf{I}(y) \leq \mathbf{J}(x), \quad \forall y \in \mathbf{M}, \quad x \in N_{(\text{SE}, \mathbf{M}^c)}(y) \\ \iff & \mathbf{I}(y) \leq \bigwedge_{x \in N_{(\text{SE}, \mathbf{M}^c)}(y)} \mathbf{J}(x), \quad \forall y \in \mathbf{M}, \quad x \in N_{(\text{SE}, \mathbf{M}^c)}(y) \\ \iff & \mathbf{I}(y) \leq \tilde{\varepsilon}_{\text{SE}}(\mathbf{J}, \mathbf{M}^c), \quad \forall y \in \mathbf{M}, \quad x \in N_{(\text{SE}, \mathbf{M}^c)}(y). \end{aligned}$$

□

However, in the practical application considered in this chapter (noise reduction and edge enhancement), the operator $\tilde{\varepsilon}_{\text{SE}}(\cdot, \cdot)$ does not have any interest. Finally, we present a list of properties for the conditional morphological operators defined in (8.6) and (8.7). Let $\varepsilon_{\text{SE}}(\cdot, \cdot)$, $\delta_{\text{SE}}(\cdot, \cdot)$ be the pair of conditional operators. Define $\phi_{\text{SE}}(\mathbf{I}, \mathbf{M}) = \varepsilon_{\text{SE}}(\delta_{\text{SE}}(\mathbf{I}, \mathbf{M}), \mathbf{M})$ and $\gamma_{\text{SE}}(\mathbf{I}, \mathbf{M}) = \delta_{\text{SE}}(\varepsilon_{\text{SE}}(\mathbf{I}, \mathbf{M}), \mathbf{M})$, the following properties hold:

- (a) $\bigwedge_{i=1}^i \varepsilon_{\text{SE}}(\mathbf{I}_i, \mathbf{M}) = \varepsilon_{\text{SE}}\left(\bigwedge_{i=1}^i \mathbf{I}_i, \mathbf{M}\right)$, (distributivity)
- (b) $\bigvee_{i=1}^i \delta_{\text{SE}}(\mathbf{I}_i, \mathbf{M}) = \delta_{\text{SE}}\left(\bigvee_{i=1}^i \mathbf{I}_i, \mathbf{M}\right)$, (distributivity)
- (c) $\mathbf{I} \leq \mathbf{J} \Rightarrow \varepsilon_{\text{SE}}(\mathbf{I}, \mathbf{M}) \leq \varepsilon_{\text{SE}}(\mathbf{J}, \mathbf{M})$, (increasing)
- (d) $\mathbf{I} \leq \mathbf{J} \Rightarrow \delta_{\text{SE}}(\mathbf{I}, \mathbf{M}) \leq \delta_{\text{SE}}(\mathbf{J}, \mathbf{M})$, (increasing)
- (e) $\gamma_{\text{SE}}(\gamma_{\text{SE}}(\mathbf{I}, \mathbf{M}), \mathbf{M}) = \gamma_{\text{SE}}(\mathbf{I}, \mathbf{M})$, (idempotence)
- (f) $\phi_{\text{SE}}(\phi_{\text{SE}}(\mathbf{I}, \mathbf{M}), \mathbf{M}) = \phi_{\text{SE}}(\mathbf{I}, \mathbf{M})$, (idempotence)
- (g) $\varepsilon_{\text{SE}}(\mathbf{I}, \mathbf{M}) \leq \delta_{\text{SE}}(\mathbf{I}, \mathbf{M})$
- (h) $\gamma_{\text{SE}}(\mathbf{I}, \mathbf{M}) \leq \phi_{\text{SE}}(\mathbf{I}, \mathbf{M})$
- (i) $\varepsilon_{\text{SE}}(\mathbf{I}, \mathbf{M}) = \mathbf{t}_{\max} - (\delta_{\text{SE}}(\mathbf{t}_{\max} - \mathbf{I}, \mathbf{M}))$, (duality)
where, $\mathbf{t}_{\max} = \max(\mathbf{I})$.

The demonstration of these properties is straightforward from the definition of conditional operators and is therefore omitted.

The key question in conditional morphology is how to define the mask \mathbf{M} . On the one hand, if the main interest is edge enhancement, \mathbf{M} should have the *local max/minimum* pixels, because they must not be enhanced. This means that the grey value at a local maximum or minimum must not increase or decrease, respectively. For this purpose, we propose to use the notion of transition pixels

Soille and Grazzini (2009),

$$\mathbf{M}_E(x) = \begin{cases} 1 & \text{if } \min(\Delta_{SE}^\varepsilon(x), \Delta_{SE}^\delta(x)) = 0 \\ 0 & \text{otherwise,} \end{cases} \quad (8.10)$$

but other options can be also considered, for instance, the classical edge detector as it is shown in Fig. 8.1, the morphological gradient Soille (2003) or the inverse of geodesic path distance as in Grazzini and Soille (2009). On the other hand, if the purpose is impulse noise removal, \mathbf{M} should have the pixels that are not corrupted by the impulse noise. We propose,

$$\mathbf{M}_N(x) = \begin{cases} 1 & \text{if } \min(\Delta_{SE}^\varepsilon(x), \Delta_{SE}^\delta(x)) > 0 \\ 0 & \text{otherwise.} \end{cases} \quad (8.11)$$

Other impulse detectors have been proposed in Hwang and Haddad (1995), Zhang and Karim (2002) (see also the review Lukac et al. (2005)).

Thus, for the definition of the toggle criterion, we keep the definition $\varepsilon_{SE}(\cdot, \cdot)$, i.e.,

Definition 9. *The conditional toggle criterion based on \mathbf{M} is defined as follows,*

$$\tau_{SE}(\mathbf{I}, \mathbf{M}) = \begin{cases} \varepsilon_{SE}(\mathbf{I}, \mathbf{M}) & \text{if } \delta_{SE}(\mathbf{I}, \mathbf{M}) - \varepsilon_{SE}(\mathbf{I}, \mathbf{M}) < 0, \\ \delta_{SE}(\mathbf{I}, \mathbf{M}) & \text{if } \delta_{SE}(\mathbf{I}, \mathbf{M}) - \varepsilon_{SE}(\mathbf{I}, \mathbf{M}) > 0, \\ \mathbf{I} & \text{otherwise.} \end{cases} \quad (8.12)$$

The motivation behind definition (8.12) is that the mask \mathbf{M} plays the role of a seed indicator, where the pixel values spread through the image \mathbf{I} according to the toggling criterion. Similarly to non-conditional toggle mapping, conditional toggle mapping should be applied iteratively. In this point, the detector matrix \mathbf{M} have to spread their values through the image. Thus, the iterative conditional toggle mapping $\tilde{\tau}_{SE}^i(\mathbf{I}, \mathbf{M})$ based on \mathbf{M} is defined as a mapping from and onto the pair image \mathbf{I} image and the mask \mathbf{M} , i.e. it is a mapping $\mathcal{F}(\mathbf{E}, \mathbb{F}) \times \mathcal{F}(\mathbf{E}, \{0, 1\}) \rightarrow (\mathcal{F}(\mathbf{E}, \mathbb{F}), \mathcal{F}(\mathbf{E}, \{0, 1\}))$ such that

$$\tilde{\tau}_{SE}(\mathbf{I}, \mathbf{M}) = (\tau_{SE}(\mathbf{I}, \mathbf{M}), \delta_{SE}(\mathbf{M})).$$

An iteration should be calculate as

$$\begin{aligned} \tilde{\tau}_{SE}^2(\mathbf{I}, \mathbf{M}) &= \tilde{\tau}_{SE}(\tilde{\tau}_{SE}(\mathbf{I}, \mathbf{M})) \\ &= \tilde{\tau}_{SE}(\tau_{SE}(\mathbf{I}, \mathbf{M}), \delta_{SE}(\mathbf{M})) \\ &= (\tau_{SE}(\tau_{SE}(\mathbf{I}, \mathbf{M}), \delta_{SE}(\mathbf{M})), \delta_{SE}(\delta_{SE}(\mathbf{M}))) \\ &= (\tau_{SE}(\tilde{\tau}_{SE}(\mathbf{I}, \mathbf{M})), \delta_{SE}^2(\mathbf{M})) \end{aligned}$$

Accordingly an iterative version of (8.12), named as *generalised conditional toggle mapping* is defined by iteration until convergence as follows

Definition 10. *The generalised conditional toggle criterion based on \mathbf{M} is defined by,*

$$\tilde{\tau}_{SE}^\infty(\mathbf{I}, \mathbf{M}) = \{\tilde{\tau}_{SE}^i(\mathbf{I}, \mathbf{M}) \mid \tilde{\tau}_{SE}^i(\mathbf{I}, \mathbf{M}) = \tilde{\tau}_{SE}^{i-1}(\mathbf{I}, \mathbf{M})\}, \quad (8.13)$$

where $\tilde{\tau}_{SE}^i(\mathbf{I}, \mathbf{M}) = \tau_{SE}(\tilde{\tau}_{SE}^{i-1}(\mathbf{I}, \mathbf{M}), \delta_{SE}^i(\mathbf{M}))$ and $\tilde{\tau}_{SE}^0(\mathbf{I}, \mathbf{M}) = (\mathbf{I}, \mathbf{M})$.

Proposition 4. *If $i^D \geq \max(\mathbf{D}_{SE}(\mathbf{M}))$ then $\tilde{\tau}_{SE}^{i^D}(\mathbf{I}, \mathbf{M})$ converge, where $\mathbf{D}_{SE}(\mathbf{M})$ is the distance transform of the binary image \mathbf{M} associated with connectivity induced by the structuring element SE .*

Proof. Let $\mathbf{M} : \mathbb{Z}^2 \rightarrow [0, 1]$ be a binary image. The distance transform (DT) is the transformation that generates a map \mathbf{D} whose value in each pixel x is the smallest distance from this pixel to \mathbf{M}^c , i.e.:

$$\mathbf{D}_{SE}(\mathbf{M})(x) = \max\{i \mid \mathbf{M}(x) = \delta_{SE}^i(\mathbf{M}(x))\} \quad (8.14)$$

By definition, $\tilde{\tau}_{SE}^i(\mathbf{I}, \mathbf{M}) = (\tau_{SE}(\tilde{\tau}_{SE}^{i-1}(\mathbf{I}, \mathbf{M})), \delta^i(\mathbf{M}))$. Let $i \geq i^D = \max(\mathbf{D}_{SE}(\mathbf{M}))$ so we have $\delta_{SE}^{i+1}(\mathbf{M}) = \delta_{SE}^i(\mathbf{M}) = \mathbf{1}$, where $\mathbf{1}$ is the indicator image of \mathbb{Z}^2 . Accordingly, by definition of conditional morphology, $\varepsilon_{SE}(\mathbf{I}, \mathbf{1}) = \delta_{SE}(\mathbf{I}, \mathbf{1}) = \tau_{SE}(\mathbf{I}, \mathbf{1}) = \mathbf{I}$. Therefore, $\tilde{\tau}_{SE}^i(\mathbf{I}, \mathbf{M}) = \tilde{\tau}_{SE}^i(\mathbf{I}, \mathbf{1}) = \tilde{\tau}_{SE}^{i+1}(\mathbf{I}, \mathbf{1}) = \tilde{\tau}_{SE}^{i+1}(\mathbf{I}, \mathbf{M})$. Proposition 4 means that expression (8.13) converges in no more iterations than $i^D = \max(\mathbf{D}_{SE}(\mathbf{M}))$, where $\mathbf{D}_{SE}(\mathbf{M})$ is the distance transform of \mathbf{M} with connectivity induced by the structuring element \mathbf{SE} . Fig. 8.3 compares the number of iterations until convergence for the classical shock filter given by expression (8.5) and the proposed one based on conditional mathematical morphology defined by (8.13). \square

The actual implementation relies on matrix representation and classical morphological operators. The pseudocode of the proposed conditional toggle mapping is displayed in Algorithms 2 and 3 respectively. Algorithm 2 is an iteration of the conditional toggle criterion (8.12) by using a binary mask. Algorithm 3 implements generalised conditional toggle mapping described in (8.13). We present simple examples to illustrate the advantages of our approach. Let us consider the one dimensional signal examples given in Figs. 8.6 and 8.7 which illustrate the outperformance of proposed conditional toggle mapping with respect to the traditional shock filter. In the sinusoidal signal, $f(x) = |5 \cos(x)|$ of Fig. 8.6, the behavior of classical and proposed approach are both accurate. However, classical shock filter fails in the ramp case, $f(x) = \min(7, 3|x|)$, as it is illustrated in Fig. 8.7. Proposed conditional enhancement operates without including obnoxious halos.

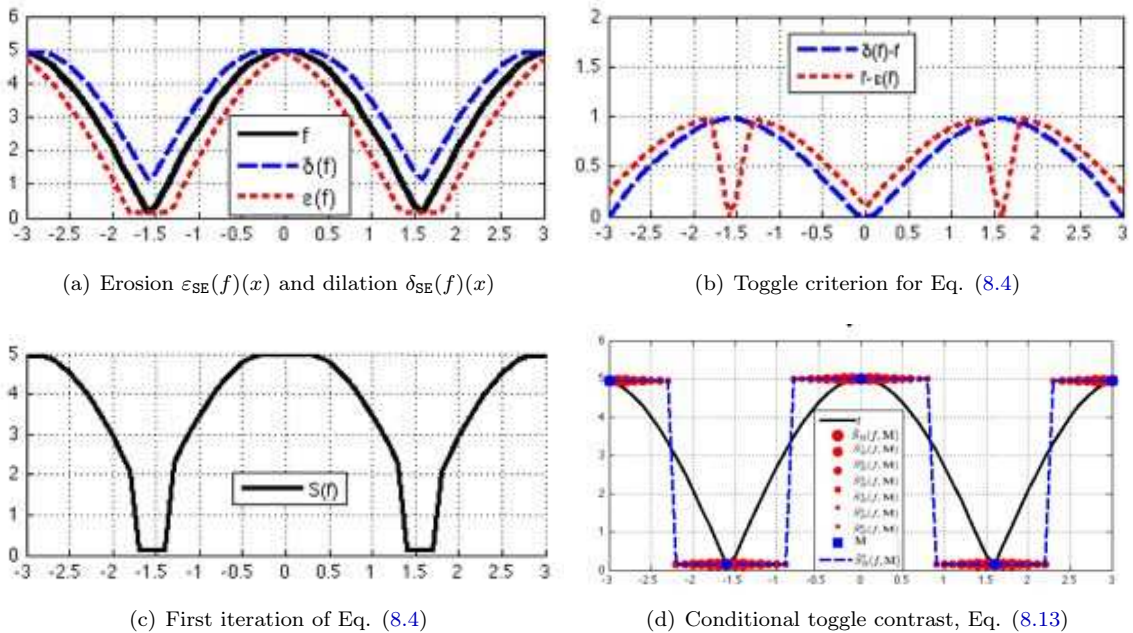


Figure 8.6: The proposed conditional toggle contrast sharpens the signal as well as classical enhancement method. $f(x) = |5 \cos(x)|$ with $x = [-3, 3]$, \mathbf{SE} is a symmetric window of length 0.5. The size of the points in (d) gives the different iteration of the conditional toggle contrast.

For a given image \mathbf{I} , the conditional toggle mapping $\tilde{\tau}_{SE}^\infty(\mathbf{I}, \mathbf{M})$ produces results in accordance with the mask \mathbf{M} . To illustrate the flexibility in the proposed framework to handle noise removal and edge enhancement, we present the obtained mask by (8.10) and (8.11) in free-noise colour images. Fig. 8.8 shows the outputs for conditional toggle mapping by using as mask \mathbf{M} expressions (8.10) and (8.11) in the proposed conditional toggle mapping defined in (8.13). For a free-noise image the mask (8.11) is a kind of image simplification, where local maximum/minimum are preserved and the rest of the pixels have been substituted by using the toggle criterion.

Algorithm 2 Conditional toggle mask (A single iteration).

Require: Original Image (\mathbf{I}), Mask(\mathbf{M}) and Structuring Element \mathbf{SE} . \cdot denotes the pixel-wise multiplication.

```

 $\mathbf{I}_d = \delta_{\mathbf{SE}}(\mathbf{I} \cdot \mathbf{M})$ 
 $\mathbf{A} = \mathbf{I}_d - \mathbf{I}$ 
 $\mathbf{I}_n = \max(\mathbf{I}) - \mathbf{I}$ 
 $\mathbf{I}_e = \delta_{\mathbf{SE}}(\mathbf{I}_n \cdot \mathbf{M})$ 
 $\mathbf{I}_e = \max(\mathbf{I}) - \mathbf{I}_e$ 
 $\mathbf{B} = \mathbf{I} - \mathbf{I}_e$ 
 $\mathbf{k} = \mathit{find}(\mathbf{A} > \mathbf{B})$ 
 $\mathbf{I}_{out}(\mathbf{k}) = \mathbf{I}_e(\mathbf{k})$ 
 $\mathbf{k} = \mathit{find}(\mathbf{A} < \mathbf{B})$ 
 $\mathbf{I}_{out}(\mathbf{k}) = \mathbf{I}_d(\mathbf{k})$ 
 $\mathbf{m} = \mathit{find}(\mathbf{M} == 1)$ 
 $\mathbf{I}_{out}(\mathbf{m}) = \mathbf{I}(\mathbf{m})$ 
 $\mathbf{M} = \delta_{\mathbf{SE}}(\mathbf{M})$ 
return  $[\mathbf{I}_{out}, \mathbf{M}]$ 

```

Algorithm 3 Conditional Toggle Mapping.

Require: Original Image (\mathbf{I}), Mask(\mathbf{M}) and Structuring Element \mathbf{SE} .

```

 $\mathbf{I}_o = \mathbf{I}, i = 0, e = 1;$ 
while  $e > 0$  do
   $i = i + 1$ 
   $[\mathbf{I}_i, \mathbf{M}] = \mathit{ToggleMask}(\mathbf{I}_o, \mathbf{M}, \mathbf{SE})$ 
   $e = \|\mathbf{I}_i - \mathbf{I}_o\|^2$ 
   $\mathbf{I}_o = \mathbf{I}_i$ 
end while
return  $\mathbf{I}_o$ 

```

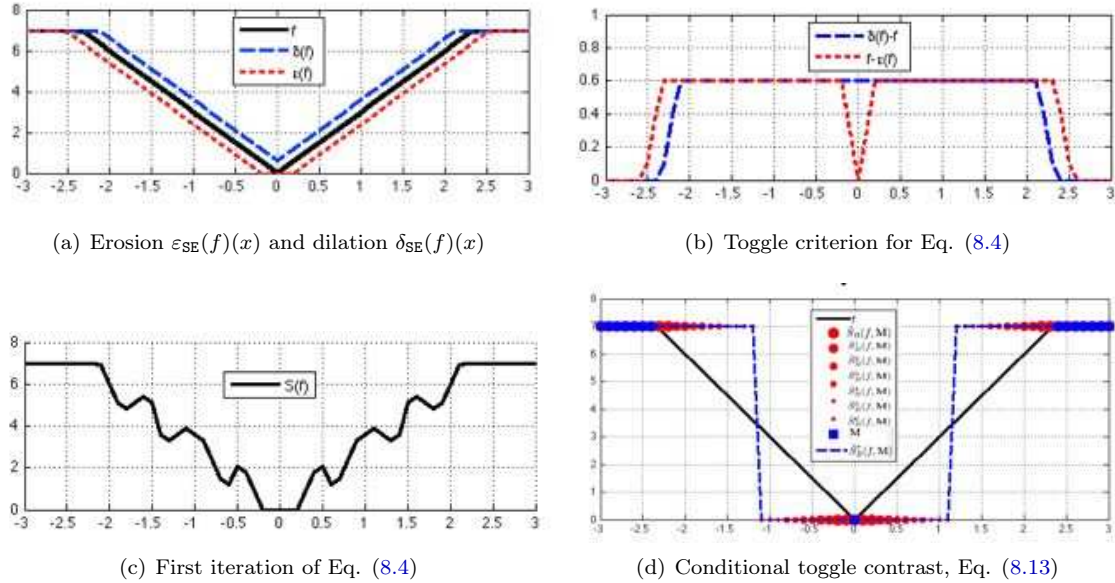


Figure 8.7: The proposed conditional toggle contrast does not produce halos as classical filters in ramp signals, i.e., oscillate signal in (c). $f(x) = \min(7, 3|x|)$ with $x = [-3, 3]$, SE is a symmetric window of length 0.5. The size of the points in (d) gives the different iteration of the conditional toggle contrast.

8.4 Experiments

In order to test the proposed conditional toggle contrast, we conducted experiments in high resolution remote sensing images as well as in classical examples of grey and colour images. Firstly, numerical experiments are carried out to demonstrate the performance of our proposed conditional toggle mapping for noise removal in standard test images (Lena, Goldhill, Cameraman, and Grey-Boat). Additionally, examples in colour images from the Kodak PhotoCD dataset are also included. Secondly, the proposed method is compared in the edge enhancement task. Segmentation after/before are compared according to the number of segmented regions and reconstruction error. Our conditional toggle mapping is parameter-free, which reduces the complexity of searching the optimal configuration of parameter for image restoration. The peak signal-to-noise ration (PSNR) in decibels is used to assess the strength of the filtered image defined as:

$$PSNR = 10 \log_{10} \frac{255^2}{1/N^2 \|\mathbf{I}_{rest} - \mathbf{I}\|^2} \quad (8.15)$$

where \mathbf{I}_{rest} is the restored image by operator given in Eq. (8.13), and N is the number of pixels in the image \mathbf{I} . This is used to measure the quality of an image. In the case of colour images a channel-independent salt-and-pepper noise was simulated according to the following rule [Boncelet \(2000\)](#): the value of pixels was replaced by 0 with probability $\theta/2$ and replaced by 1 with probability $\xi/2$ with $\xi \in [0, 1]$.

8.4.1 Salt & pepper noise reduction

Images are contaminated with salt-and-pepper noise ranging from 20% to 95%, with increment steps of 5%. Results of the proposed conditional toggle mapping by using the mask \mathbf{M}_N are compared with three well-known algorithms: Decision based Filtering [Srinivasan and Ebenezer \(2007\)](#), Progressive Switching Median Filter [Wang and Zhang \(1999\)](#) and Classical Median Filter [Gonzalez and Woods](#)



Figure 8.8: Comparison in free-noisy scenario. Conditional toggle mapping handled with different image processing problem according to the mask \mathbf{M} . Particular cases of $\mathbf{M} = \mathbf{M}_E$ as Eq. (8.10) provide edge enhancement (second column) or $\mathbf{M} = \mathbf{M}_N$ as Eq. (8.11) produce an image simplification (fourth column). Masks are computed marginally and displayed as black pixels.

(2008). The PSNR values resulting from various experiment are shown in Fig.8.9. From these curves, it can be easily observed that the proposed conditional toggle mapping outperforms the other filtering schemes in noise level greater than 50%. We remark that the results reported in Fig. 8.9 are the average of results of 25 repeated experiments. Furthermore, a subjective visual result of the noise reduction is presented in Figs. 8.10-8.11-8.12-8.13-8.14 for different noise densities.

8.4.2 Comparison with the state of the art

Firstly, we compare our approach with two state-of-the-art powerful denoising techniques on the *Set-24* dataset Chan et al. (2005): Non-local means Buades et al. (2005) and Kernel Regression Takeda et al. (2007). The idea in Non-local means Buades et al. (2005), Baudes et al. (2005), is to take advantage of self-similarities in images by comparing local neighbourhoods (patches) across the whole image. To deal with salt-and-pepper noise, the filtered pixel value is estimated as a weighted median of the pixels whose neighbourhoods are the most similar to the neighbourhood of the one to be denoised. Kernel Regression Takeda et al. (2007) is roughly based on the idea of a robust adaptive fitting of the image by using kernel functions. The kernel regression framework provides a rich mechanism for computing point-wise estimates of the regression function with minimal assumptions about global signal or noise models. The filtering result is a weighted mean from this local adaptive regression problem. Some popular existing methods as bilateral filter Tomasi and Manduchi (1998), are special cases of the kernel regression framework Chatterjee and Milanfar (2010). Table 8.1 summarises the results for the experiments. For the latter, we include the average PSNR over the set of images (as done also for the results reported in Motta et al. (2011)). From the quantitative results show that for the heavily noisy data set (salt-and-pepper noise larger than 50%) the proposed approach works better than non-local techniques Baudes et al. (2005)Takeda et al. (2007). However, these approaches work better when the noise level is less than 50%. The authors suppose that this fact may due to two factors. On the one hand, the estimation step in non-local techniques is clearly affect to the lack of information (Noise level greater than 50%). On the other hand, the proposed approach is "myope" in the sense that information considered in spatial neighbours is not greater than the 8-connectivity for a given pixel. However, that allows to deal with noise level higher than 90% as it is shown in Table 8.1.

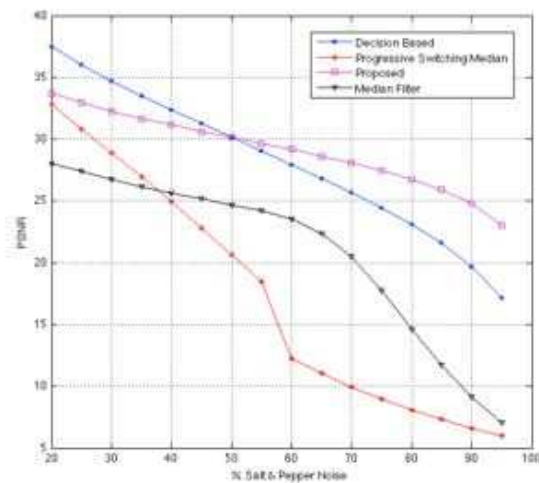
Secondly, we compare our results to those of Chan et al. (2005), Motta et al. (2011). The scheme of Motta et al. (2011) was selected for comparison as it presents, to the best of knowledge, the best published results for salt-and-pepper noise available in the literature. The performance of the proposed approach is significantly lower for the noisy level which have been considered in the published works, namely, iDUDE and regularisation based denoisers. However, our approach has very low complexity (there are not parameters) and it can be implemented using standard dilation and erosion transformations. We remark that both Motta et al. (2011) and Chan et al. (2005) start with a traditional median filter, where the window size is related with noise level of the image. Our approach could be used instead of the traditional median filter to avoid that parameter in the algorithm. Once again, a remarkable point concerning the behaviour the proposed approach is the fact that between 50% and 95% is obtained a difference of less than 5% in PNSR, which proves the stability of the method with respect to the noise level. Finally, the other significant advantage of our approach is the fact that the proposed procedure handles other kind of problems such as image enhancement.

8.4.3 Image enhancement

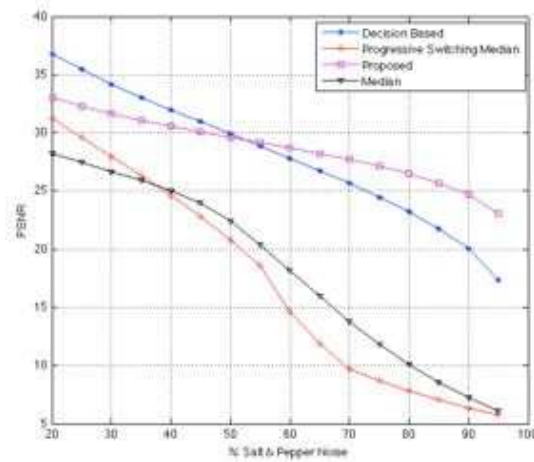
Optical remote sensing imagery has been a paradigm in the last decade. From Landsat 7 launched in 1999 to WorldView-2 in 2009 the spatial resolution has increased considerably from 15m to 0.46m. This led to research on new data-driven segmentation algorithms. Hierarchical region based segmentation approach is a very natural manner since the target has different meanings according to object size, i.e., from tile to building there are an entire range of scales. Recently, constrained connectivity Soille (2008) has emerged as a data-driven approach useful to handle practical problems in remote sensing. However, objects transitions depend on orientation Soille (2011), so it can alter

% Noise	CHN05 Chan et al. (2005)	iDUDE Motta et al. (2011)	NL-Medians Buades et al. (2005)	Kernel-Regression Takeda et al. (2006)	Proposed
30%	34.5	35.1	27.93	28.94	26.81
50%	31.1	31.6	23.56	24.53	25.29
70%	28.1	28.6	22.28	21.29	24.28
75%	27.3	N/A	21.28	20.78	23.92
80%	N/A	N/A	19.90	18.65	23.47
90%	N/A	N/A	14.79	13.60	22.08
95%	N/A	N/A	10.09	9.93	20.69

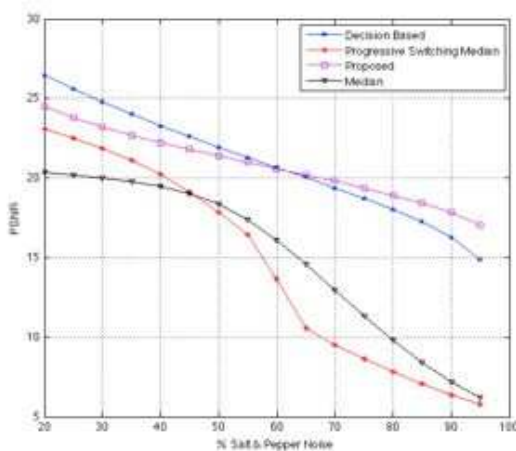
Table 8.1: Comparison with state of the art in salt-and-pepper noise removal. Proposed approach is a parameter-free algorithm.



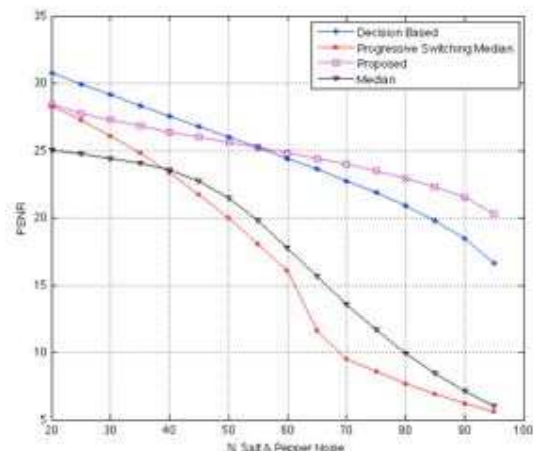
(a) Lena Grey



(b) Lena Color



(c) Baboon Color



(d) Boat Color

Figure 8.9: Experimental results in PSNR for grey and colour Lena, Baboon and Boat at various noise levels for different approaches: Decision based [Srinivasan and Ebenezer \(2007\)](#), Progressive Switching Median Filter [Wang and Zhang \(1999\)](#), and Classical Median Filter [Gonzalez and Woods \(2008\)](#).

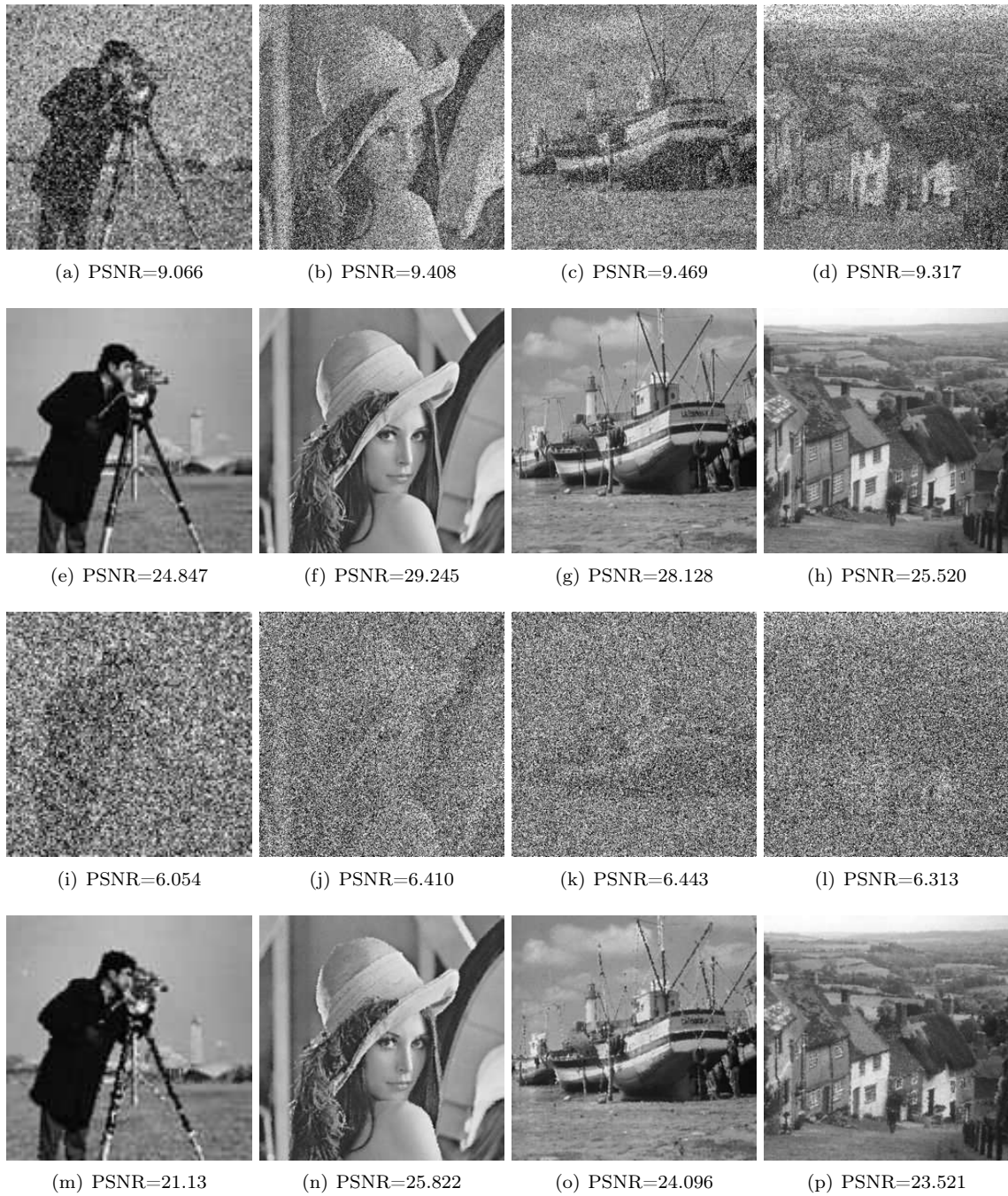


Figure 8.10: Example of noise removal by proposed method. Images contaminated by salt-and-pepper noise. (a)-(d) Noisy images (40%). (e)-(h) Results restored by using the conditional toggle mapping. (i)-(l) Noisy images (80%). (m)-(p) Image restored by the conditional toggle mapping.

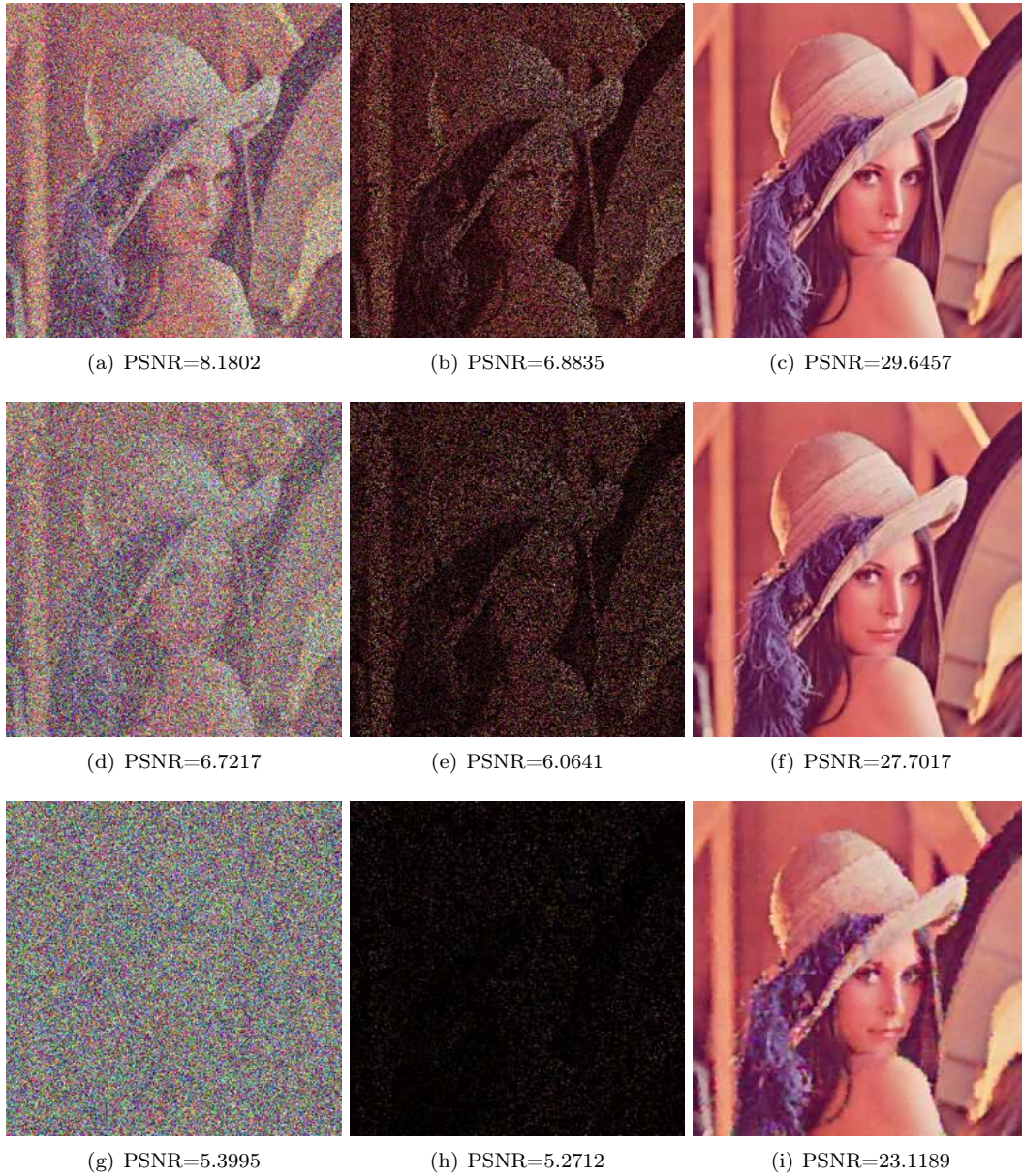


Figure 8.11: Example of noise removal by proposed method. Images contaminated by marginal salt-and-pepper noise. (a)-(c) Experiment (50%). (d)-(f) Experiment (70%). (g)-(i) Experiments (95%).

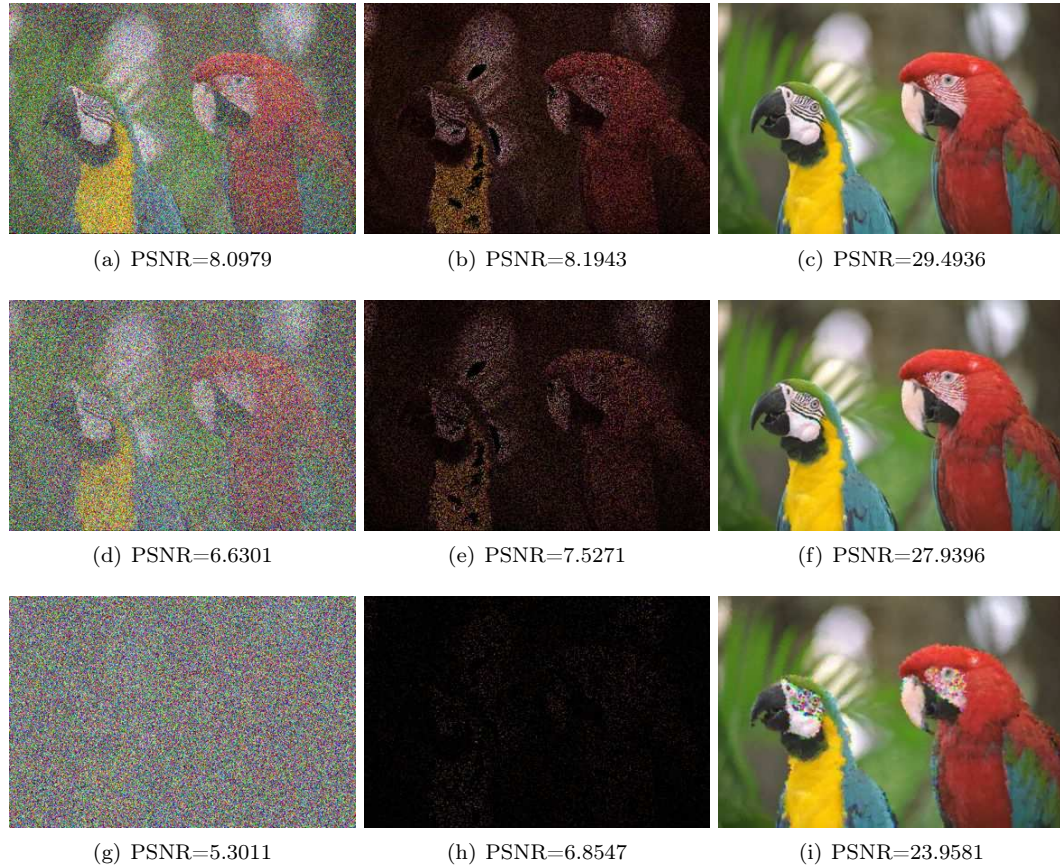


Figure 8.12: Example of noise removal by proposed method.(a)-(c) Experiment (50%). (d)-(f) Experiment (70%). (g)-(i) Experiments (95%). First column shows images contaminated by marginal salt-and-pepper noise, second column includes mask image by using Eq. (8.11) and third column displays the result of the conditional toggle mapping.

segmentation results. A question of considerable practical interest in remote sensing is: How well can image enhancement algorithms avoid unpleasant result in hierarchical image segmentation? Thus, in this section we discuss the results obtained applying the conditional toggle contrast to hierarchical segmentation based on α connectivity from Soille (2008).

α -connectivity

α -connectivity produces nested partitions with successive degree of coarseness by changing the connectivity threshold Soille (2008, 2011). Given two pixels x and $y \in \mathbf{E}$, they are α -connected if there exist a path \mathcal{P} going from x to y such that the dissimilarity (d) between any two successive pixels of this path does not exceed the value α , i.e.,

$$\begin{aligned} \text{CC}_\alpha(x) &= \{x\} \cup \{y | \exists \mathcal{P} \langle x = p_1, p_2, \dots, p_{i-1}, p_i = y \rangle, i > 1, \\ &d(p_i, p_j) \leq \alpha \quad \forall i, j \quad 1 \leq i, j \leq i \} \end{aligned} \quad (8.16)$$

Basically, (8.16) is equivalent to the single linkage clustering method Gower and Ross (1969) considering finite similarities only among horizontal and vertical neighbours (4-neighbours or also known as direct-neighbour Gonzalez and Woods (2008)). Additionally, (8.16) is equivalent to quasi-flat zones in the grey level case with dissimilarity set to absolute difference Meyer (1998). In the sequel, $\text{CC}_\alpha(\mathbf{I})$ denotes the segmentation by (8.16) of the image \mathbf{I} . α -connectivity (8.16) has the drawback

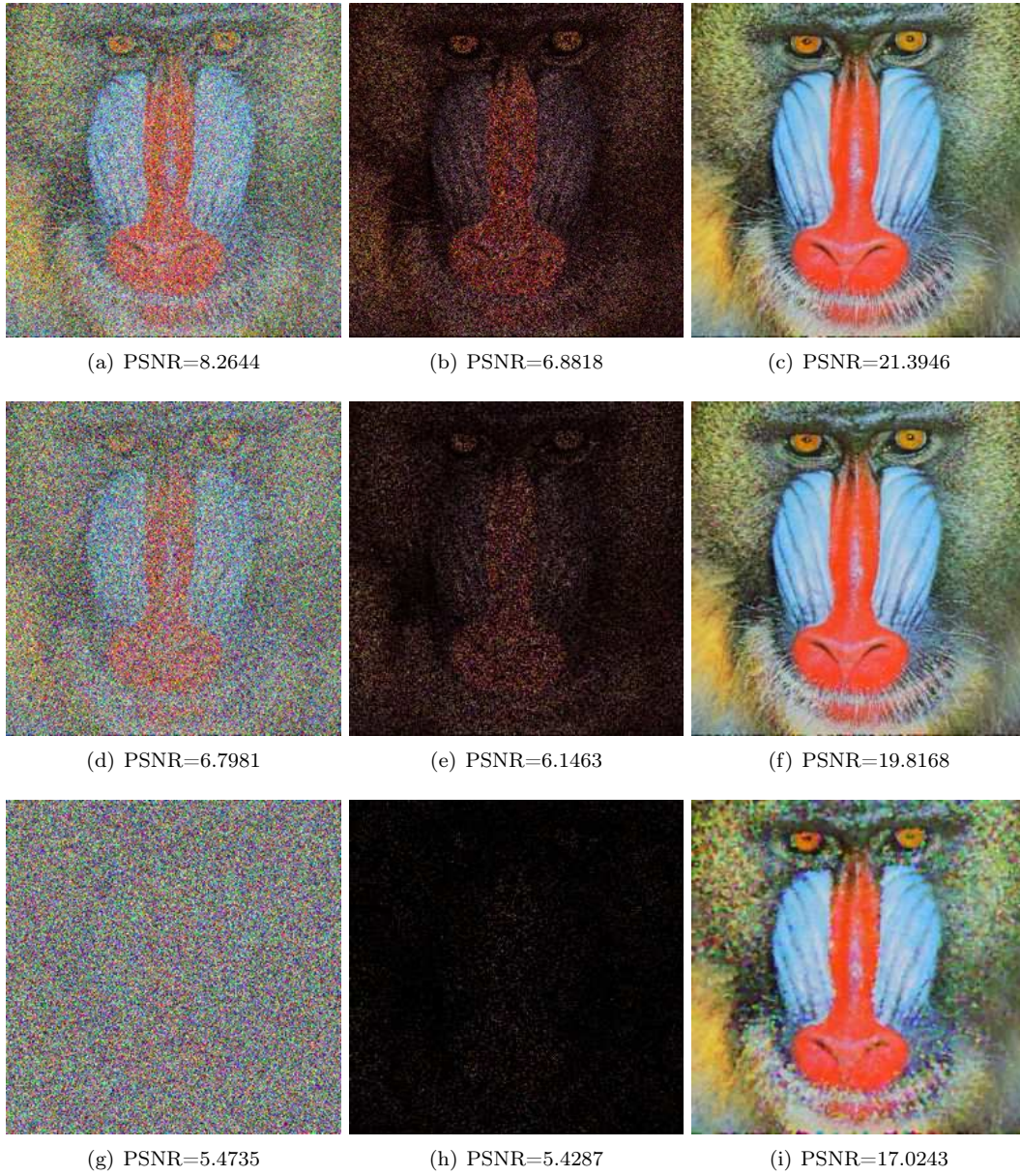


Figure 8.13: Example of noise removal by proposed method. Images contaminated by marginal salt-and-pepper noise. (a)-(c) Experiment (50%). (d)-(f) Experiment (70%). (g)-(i) Experiments (95%).

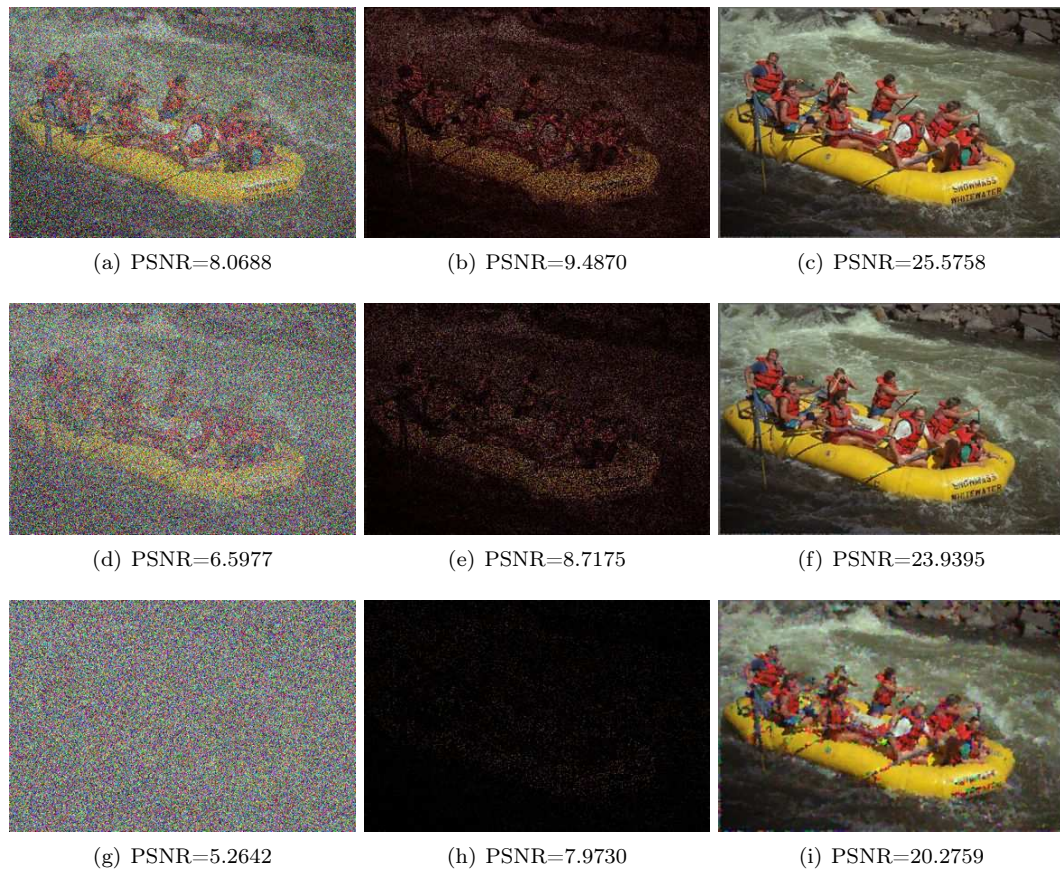


Figure 8.14: Example of noise removal by proposed method. Images contaminated by marginal salt-and-pepper noise. (a)-(c) Experiment (50%). (d)-(f) Experiment (70%). (g)-(i) Experiments (95%).

that if two distinct image objects are separated by one or more transitions going in steps having dissimilarity value than or equal to α , they appear within the same CC_α . Accordingly, we evaluate the performance of conditional toggle mapping as a preprocessing to avoid unpleasant segmentations.

Evaluation

The performance of the conditional toggle enhancement is first qualitatively evaluated through the visual appearance of associated segmentation and their filtered images and Fig. 8.15. Secondly, a quantitative comparison is performed. The mean of $\mathbf{I}(\mathbf{x})$ in each connected component of $CC_\alpha(\mathbf{I})$ is used as restored image and the PSNR (8.15) is calculated for values of $\alpha = [3, 4, \dots, 25]$. Fig. 8.16 shows that segmentation in the conditional toggle mapping provides better PSNR in comparison with segmentation on the original images with equivalent number of connected components. The performance is comparable with classical toggle mapping but our approach is obtained in a few number of iterations as shown Fig. 8.3.

8.5 Conclusions and Perspectives of this chapter

In this chapter, we introduced a new free-parameters unified approach for both edge enhancement and salt-and-pepper noise removal by using conditional mathematical morphology. The unified framework is based on defining a seed mask \mathbf{M} , which is different according to type of processing, and by using condition mathematical morphology operators in an iterative toggle contrast style. The task can be obtained a relative few number of iterations. The proposed filter also shows consistent and stable performance across a wide range of noise densities from 10% to 95%. A remarkable point concerning the behaviour the present approach is the fact that between 50% and 95% is obtained a difference of less than 5 in PNSR, which proves the stability of the method with respect to the noise level. Conditional toggle contrast has the additional advantage of easy of implementation. Specifically, interesting future work includes:

1. Compression based on conditional morphology.
2. Extension to high dimensional images by using vector morphology [Velasco-Forero and Angulo \(2011c,a\)](#) instead of the marginal ordering scheme adopted in this chapter.

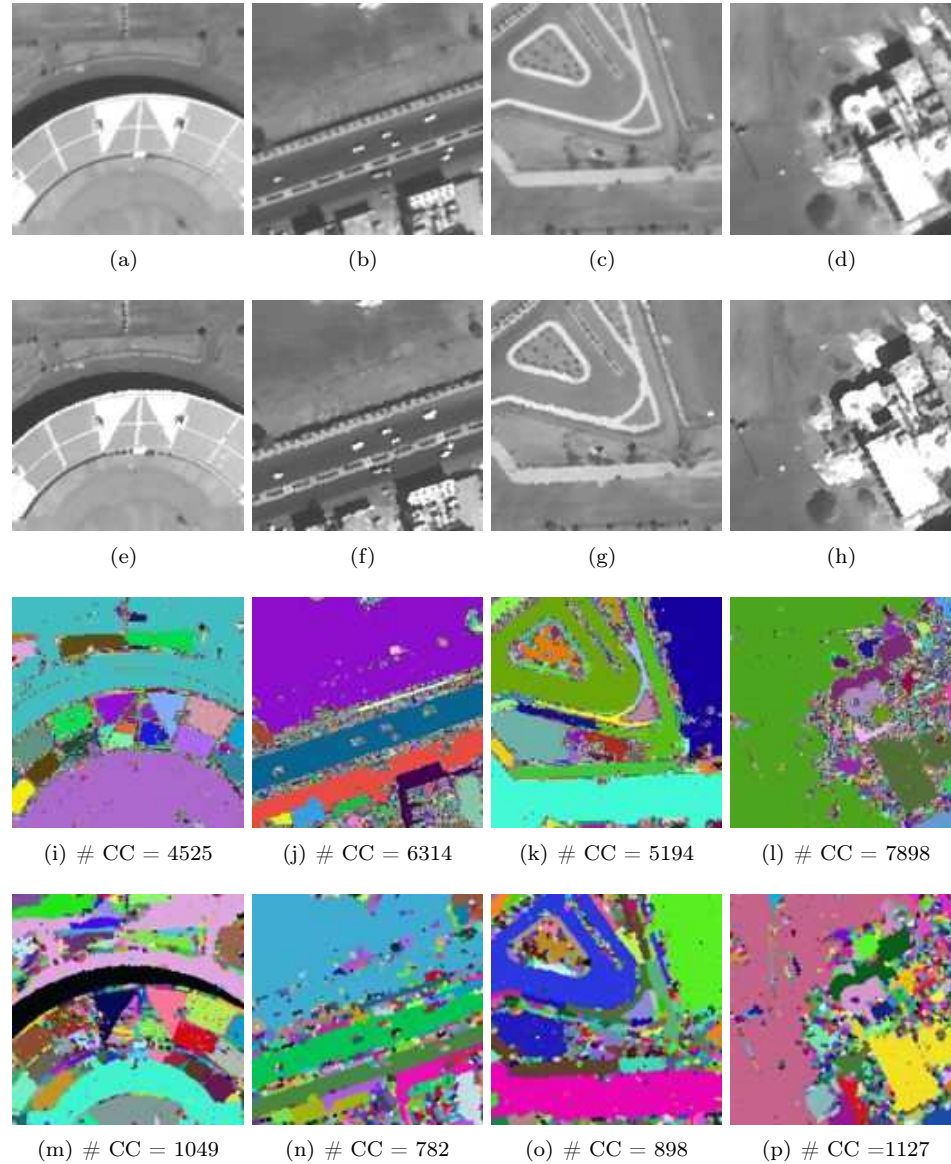
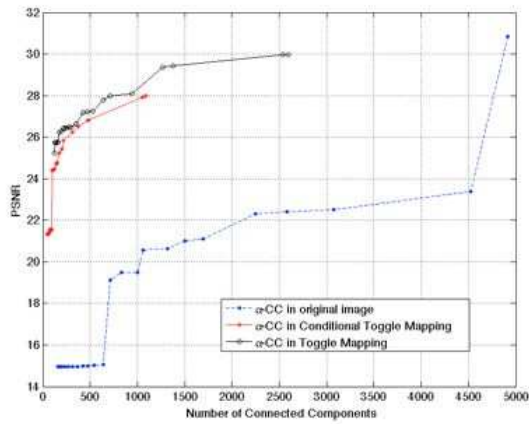
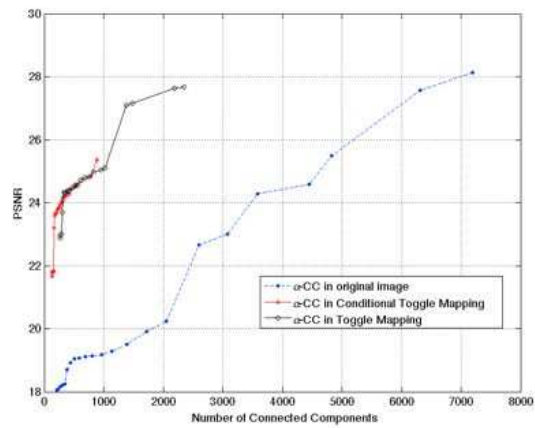


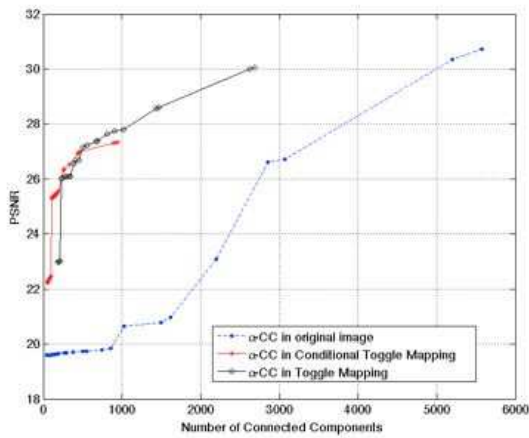
Figure 8.15: (a)-(d) Original Image \mathbf{I} , (e)-(h) Conditional Toggle Mapping $\tilde{\tau}(\mathbf{I}, \mathbf{M})$, (i)-(l) $CC_{\alpha}(\mathbf{I})$ and (m)-(p) $CC_{\alpha}\tilde{\tau}(\mathbf{I}, \mathbf{M})$. The dissimilarity measure is the absolute different and $\alpha = 4$ in all the experiments. The input images were extracted from the WorldView-2 satellite image (European Space Imaging) with spatial resolution of 50 cm. The number of α -connected component is reported in each segmentation.



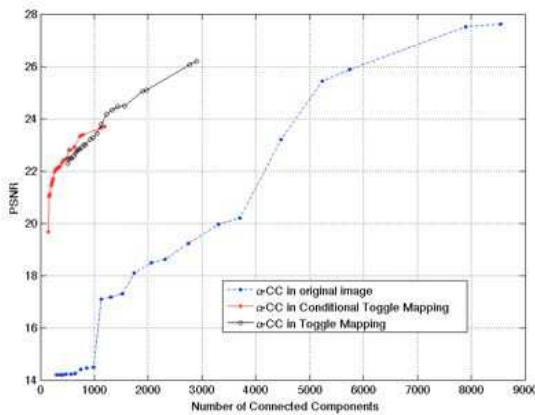
(a) Original image is 8.15(a)



(b) Original image is 8.15(b)



(c) Original image is 8.15(c)



(d) Original image is 8.15(d)

Figure 8.16: PSNR of restored image by using mean per α -connected component in original, toggle mapping and conditional toggle mapping. $\alpha = [3, 4, \dots, 25]$. Proposed conditional toggle mapping can be calculated in a quarter of the computational time of classical one.

9

Towards multivariate Chain-Boolean models for texture simulation

Great things are done by a series of small things brought together. *Vincent Van Gogh*

Résumé

Les premiers pas de la généralisation du modèle Booléen dans le cas d'images multivariées sont présentés dans ce chapitre. Une approche de type treillis complet totalement ordonné, basée sur la généralisation marginale, est formulée. Des exemples obtenus à partir d'images réelles sont présentés.

9.1 Introduction

Multivariate images are now commonly produced in many applications. Some are images in the conventional sense (such as satellite data) while others are not (secondary ion mass spectroscopy, Raman spectroscopy, SIMS). The growth in the acquisition dimension can be observed in different scientific areas and this new category of images is referred to as hyperspectral or ultraspectral images [Chang \(2003\)](#). In these images, an almost arbitrary number of variables is associated with each pixel that represent, for instance, different spectral bands or different imaging parameters or modalities. Therefore, these images can no longer be interpreted as gray-value or color images, and new approaches are needed for their modeling and their analysis.

In various practical applications, the characterization of texture is an important issue to study the physical objects acquired in the image. A germ-grain model may provide a good description for a very irregular pattern observed in microscopy materials science, biology and analysis of images [Molchanov \(2005, 1997\)](#). Perhaps the best known model is the Boolean model [Matheron \(1975\)](#) generating a configuration of independent randomly placed particles. In the binary case, a Boolean model is formed by placing random balls centered at the points of a Poisson process and taking the union of these balls. The model was later extended to numerical Boolean function by [Serra \(1989a\)](#). The natural generalization of the Boolean model for multivariate images consists in replacing the union by the maximum in a marginal approach [Jeulin and Jeulin \(1981\)](#), [Jeulin \(1991, 1992a\)](#), i.e., band-wise extension which is stable under the maximum of marginal bands. This indeed yields worthwhile procedures but fails to take into account the *geometric features* often inherent in multivariate data. In this chapter, we are concerned with the analysis of overlapping events in multivariate images. To approach this problem, we introduce a generation of Boolean model for multidimensional images in a

chain representation, i.e. including total ordering representation. The proposed model formalizes the configuration of independent randomly placed events with multivariate independent information. In particular, we consider the vector ordering computed from images using statistical depth functions, introduced in Chapter 6.

9.2 Chain compact capacity

A random closed set is a random element whose values are closed subsets of a basic setting space. They can be interpreted as imprecise observations of random variables which assign to each element of the underlying probability space a set instead of a single value. We will consider random closed sets, that is, random maps whose values are closed subsets of a topological space \mathbf{E} . The family of all closed subsets of \mathbf{E} will be denoted by $\mathbf{F}_{\mathbf{E}}$ which can in turn be topologised by the so-called Hit-or-Miss topology (or Fell topology). Random closed set can then be seen as random elements with values in \mathbf{F} and classical probability theory can be applied. Thus, one is more interested in events from the Borel- σ -algebra $\mathcal{B}(\mathbf{E})$, than from $\mathcal{B}(\mathbf{F}_{\mathbf{E}})$ and non-additive set functions (Choquet capacity) are introduced to measure if a random closed set hits or misses a certain set from $\mathcal{B}(\mathbf{E})$. The link between these two interpretations is given by the so-called Choquet-Matheron-Kendall Theorem, which states a one-to-one correspondence between probability distributions on $\mathcal{B}(\mathbf{F}_{\mathbf{E}})$ and a certain class of non-additive functions, called capacity functionals, on $\mathcal{B}(\mathbf{E})$. In the context of multivariate image processing, object of interest are spatial structures (two or three dimensional arrays of pixels) with a vector information pixel-wise. These kind of structures can be considered as maps from \mathbf{E} to \mathcal{L} , where \mathcal{L} is a chain: a total ordered set of pixels according to \leq . In this section, we introduce the concept that allows us to generalise the idea of random sets to vector images. Let us fix a complete probability space $(\Omega, \mathbf{F}, \mathbf{P})$, where Ω is a sample space, \mathbf{F} the set of events, and \mathbf{P} a measure of probability of events, which will be used to define random elements in $\mathcal{L}^{\mathbf{E}}$. Additionally, we denote \mathbf{F} the family of closed subsets of $\mathcal{L}^{\mathbf{E}}$.

Definition 11. For any $K \subseteq \mathbf{E}$ and $r \in \mathcal{L}$, the cylinder of base K and level r is the function $C_{K,r}$ defined by

$$\forall x \in \mathbf{E}, C_{(K,r)} = \begin{cases} r & \text{if } x \in K, \\ \perp & \text{if } x \notin K. \end{cases}$$

Now, we would like to generalize the concept of a random closed set including a cylinder with a given lattice value. Thus,

Definition 12. A cylinder of base K and level $k_{\mathcal{L}}$, $C_{(K,k_{\mathcal{L}})} \in \mathcal{L}^{\mathbf{E}}$ is a compact chain-set if $K \subset \mathbf{E}$ is a compact set and $k_{\mathcal{L}} \in \mathcal{L}$.

Definition 13. A map $C_{(X,x_{\mathcal{L}})} : \Omega \mapsto \mathbf{F}$ is called a random closed chain-set if, for every compact chain-set $(K, k_{\mathcal{L}}) \in \mathcal{L}^{\mathbf{E}}$,

$$\{\omega \in \Omega : X \cap K \neq \emptyset, \perp_{\mathcal{L}} <_{\mathcal{L}} k_{\mathcal{L}} \leq_{\mathcal{L}} x_{\mathcal{L}}\} \in \mathbf{F}, \quad (9.1)$$

or equivalently,

$$\{\omega \in \Omega : \omega \in X \cap K, \perp_{\mathcal{L}} <_{\mathcal{L}} k_{\mathcal{L}}(\omega) \leq_{\mathcal{L}} x_{\mathcal{L}}(\omega)\} \in \mathbf{F}. \quad (9.2)$$

Definition (13) simply means that observing $C_{(X,x_{\mathcal{L}})}$ one can always say if $C_{(X,x_{\mathcal{L}})}$ hits or misses any given compact chain-set $(K, k_{\mathcal{L}})$. The following definition is fundamental for the rest of this study.

Definition 14. The functional $\mathbf{T}_{X,x_{\mathcal{L}}}(\cdot, \cdot) : \mathcal{L}^{\mathbf{E}} \mapsto [0, 1]$ given by

$$\begin{aligned} \mathbf{T}_{C_{(X,x_{\mathcal{L}})}}(C_{(K,k_{\mathcal{L}})}) &= \mathbf{P}\{\omega \in \Omega : \omega \in X \cap K, \perp_{\mathcal{L}} <_{\mathcal{L}} k_{\mathcal{L}}(\omega) \leq_{\mathcal{L}} x_{\mathcal{L}}(\omega)\} \\ &= \mathbf{P}\{X \cap K \neq \emptyset, \perp_{\mathcal{L}} <_{\mathcal{L}} k_{\mathcal{L}} \leq_{\mathcal{L}} x_{\mathcal{L}}\} \end{aligned} \quad (9.3)$$

is said to be the capacity chain functional of $C_{(X,x_{\mathcal{L}})}$. For simplicity, we write $\mathbf{T}(C_{(K,k_{\mathcal{L}})})$ instead of $\mathbf{T}_{C_{(X,x_{\mathcal{L}})}}(C_{(K,k_{\mathcal{L}})})$ where no ambiguity occurs.

We can consider in particular the simplest case which show the compatibility of our framework with the classical Boolean model.

Proposition 5. (*Capacity chain functional of simple random sets*).

1. If $C_{(x, x_{\mathcal{L}})} = (\xi, \top_{\mathcal{L}})$ is a random singleton with chain value equal to the maximum of \mathcal{L} , and $(\mathbb{K}, k_{\mathcal{L}})$ is a non-trivial compact chain-set then

$$\mathbf{T}_{(\xi, \top_{\mathcal{L}})}(C_{(\mathbb{K}, k_{\mathcal{L}})}) = \mathbf{P}\{\xi \cap \mathbb{K} \neq \emptyset\} = \mathbf{P}\{\xi \in \mathbb{K}\}, \quad (9.4)$$

so that the capacity chain functional is the probability distribution of ξ .

2. If $C_{(x, x_{\mathcal{L}})} = (\mathbb{X}, \top_{\mathcal{L}})$ is a random closed chain-set with chain value equal to the maximum of \mathcal{L} , and $(\mathbb{K}, k_{\mathcal{L}})$ is a non-trivial compact chain-set then

$$\mathbf{T}_{(\mathbb{X}, \top_{\mathcal{L}})}(C_{(\mathbb{K}, k_{\mathcal{L}})}) = \mathbf{P}\{\mathbb{X} \cap \mathbb{K} \neq \emptyset\} = \mathbf{T}_{\mathbb{X}}(\mathbb{K}), \quad (9.5)$$

so that the capacity chain functional is the classical Choquet capacity functional.

It follows immediately from Definition (14) that:

- $\mathbf{T}_{C_{(x, x_{\mathcal{L}})}}(C_{\emptyset, r_{\mathcal{L}}}) = 0$, for all $r_{\mathcal{L}} \in \mathcal{L}$,
- $\mathbf{T}_{C_{(x, x_{\mathcal{L}})}}(C_{\mathbb{K}, \perp_{\mathcal{L}}}) = 0$, for all $\mathbb{K} \in \mathcal{K}$,
- $0 \leq \mathbf{T}_{C_{(x, x_{\mathcal{L}})}}(C_{(\mathbb{K}, k_{\mathcal{L}})}) \leq 1$, for all $\mathbb{K} \in \mathcal{K}, k_{\mathcal{L}} \in \mathcal{L}$.

It is easy to see that the capacity chain functional is monotone in \mathbf{E} , i.e., $\mathbf{T}(\mathbb{K}_1, r_{\mathcal{L}}) \leq \mathbf{T}(\mathbb{K}_2, r_{\mathcal{L}})$ if $\mathbb{K}_1 \subseteq \mathbb{K}_2, \forall r_{\mathcal{L}} \in \mathcal{L}$, and it is monotone in \mathcal{L} for chain value not greater than $x_{\mathcal{L}}$, i.e., $\mathbf{T}(\mathbb{K}, r_1) \leq \mathbf{T}(\mathbb{K}, r_2)$ if $r_1 \leq_{\mathcal{L}} r_2 \leq_{\mathcal{L}} x_{\mathcal{L}}, \forall r_1, r_2 \in \mathcal{L}$, and accordingly monotone in $\mathcal{L}^{\mathbf{E}}$ for all $r_1, r_2 \leq_{\mathcal{L}} x_{\mathcal{L}} \in \mathcal{L}$. In contrast to the notion of measure, the capacity chain functional $\mathbf{T}(\cdot, \cdot)$ is not additive, but only subadditive in \mathcal{K} , i.e., for $\mathbb{K}_1, \mathbb{K}_2 \in \mathcal{K}$

$$\mathbf{T}(\mathbb{K}_1 \cup \mathbb{K}_2, r) \leq \mathbf{T}(\mathbb{K}_1, r) + \mathbf{T}(\mathbb{K}_2, r) \quad (9.6)$$

and also in \mathcal{L} , i.e., for $r_1, r_2 \in \mathcal{L}$

$$\mathbf{T}(\mathbb{K}, r_1 \vee r_2) = \max\{\mathbf{T}(\mathbb{K}, r_1), \mathbf{T}(\mathbb{K}, r_2)\} \leq \mathbf{T}(\mathbb{K}, r_1) + \mathbf{T}(\mathbb{K}, r_2) \quad (9.7)$$

Therefore,

$$\mathbf{T}(\mathbb{K}_1 \cup \mathbb{K}_2, r_1 \vee r_2) \leq \mathbf{T}(\mathbb{K}_1, r_1) + \mathbf{T}(\mathbb{K}_1, r_2) + \mathbf{T}(\mathbb{K}_2, r_1) + \mathbf{T}(\mathbb{K}_2, r_2) \quad (9.8)$$

The advantages of the representation introduced by Definition (14) is the fact that $\mathbf{T}(\mathbb{K}, r)$ can be calculated by simple transformations. Thus, it is often desirable to represent the capacity by using morphological transformations [Matheron \(1975\)](#).

Definition 15. A transformation $\mathcal{L}^{\mathbf{E}} \mapsto \mathcal{L}^{\mathbf{E}}$, called the dilation in the chain representation, denoted by δ , is defined as

$$\delta_{(C_{(\mathbb{K}, k_{\mathcal{L}})})}(\mathbb{X}, x_{\mathcal{L}})(x) = \begin{cases} \bigvee_{y \in \mathbb{K}_x, k_{\mathcal{L}}(y) \leq x_{\mathcal{L}}(y)} x_{\mathcal{L}}(y) & \text{if } x \in \delta_{\mathbb{K}}(\mathbb{X}), \\ \perp_{\mathcal{L}} & \text{otherwise.} \end{cases} \quad (9.9)$$

From (9.9) and Definition (14), the capacity can be expressed as follows

Proposition 6. (*Capacity chain functional using dilation*)

1. $\mathbf{T}_{C_{(x, x_{\mathcal{L}})}}(C_{(\mathbb{K}, k_{\mathcal{L}})}) = \mathbf{P}\{\delta_{(C_{(\mathbb{K}, k_{\mathcal{L}})})}(\mathbb{X}, x_{\mathcal{L}}) \geq_{\mathcal{L}} \perp_{\mathcal{L}}\}$,
2. $\mathbf{P}\{\delta_{(C_{(\mathbb{K}, k_{\mathcal{L}})})}(\mathbb{X}, \top_{\mathcal{L}}) >_{\mathcal{L}} \perp_{\mathcal{L}}\} = \mathbf{P}\{\mathbb{X} \cap \mathbb{K} \neq \emptyset\} = \mathbf{T}_{\mathbb{X}}(\mathbb{K})$
3. $\mathbf{P}\{\delta_{(C_{(\mathbb{K}, k_{\mathcal{L}})})}(\mathbb{X}, x_{\mathcal{L}}) >_{\mathcal{L}} \perp_{\mathcal{L}}\} = \mathbf{T}_{(\mathbb{X}, \top_{\mathcal{L}})}(C_{(\mathbb{K}, k_{\mathcal{L}})})$

We now wish to look at a simpler representation of Definition (14) for particular cases. We follow Jeulin (1992b,a) to get a level-set representation of the capacity chain functional. We define two auxiliary functions as

$$A_{C(x,x_{\mathcal{L}})}(z_{\mathcal{L}}) = \begin{cases} x_{\mathcal{L}}(x), & \text{if } x \in \mathbf{X}, x_{\mathcal{L}}(x) \geq z_{\mathcal{L}}, \\ \perp_{\mathcal{L}} & \text{otherwise.} \end{cases} \quad (9.10)$$

and

$$B_{C(k,k_{\mathcal{L}})}(z_{\mathcal{L}}) = \begin{cases} k_{\mathcal{L}}(x), & \text{if } x \in \mathbf{K}, \perp_{\mathcal{L}} < k_{\mathcal{L}}(x) \leq z_{\mathcal{L}}, \\ \perp_{\mathcal{L}} & \text{otherwise.} \end{cases} \quad (9.11)$$

It is straightforward to see that:

$$\mathbf{T}_{C(x,x_{\mathcal{L}})}(C(k,k_{\mathcal{L}})) = \mathbf{P}\{\delta_{(C(k,k_{\mathcal{L}}))}(\mathbf{X}, k_{\mathcal{L}}) >_{\mathcal{L}} \perp_{\mathcal{L}}\} = \mathbf{P}\left\{\bigcup_{z_{\mathcal{L}} \in \mathcal{L}} \delta_{B(\tilde{K}, k_{\mathcal{L}})}(z_{\mathcal{L}})(A_{C(x,x_{\mathcal{L}})}(z_{\mathcal{L}})) >_{\mathcal{L}} \perp_{\mathcal{L}}\right\} \quad (9.12)$$

Assume that $k_{\mathcal{L}}(x) = k_{\mathcal{L}}, \forall x \in \mathbf{K}$, i.e., "flat compact" constant-value. Thus, (9.12) becomes:

$$\begin{aligned} &= \mathbf{P}\left\{\bigcup_{z_{\mathcal{L}} \in \mathcal{L}} \delta_{(\tilde{K}, k_{\mathcal{L}})}(A_{C(x,x_{\mathcal{L}})}(z_{\mathcal{L}})) >_{\mathcal{L}} \perp_{\mathcal{L}}\right\} \\ &= \mathbf{P}\left\{\bigcup_{z_{\mathcal{L}} \geq_{\mathcal{L}} k_{\mathcal{L}}} \delta_{\tilde{K}}(x_{\mathcal{L}} \geq z_{\mathcal{L}})\right\} \end{aligned}$$

where \tilde{K} is the transposed compact set in \mathbf{E} . That is the probability of the dilation of the upper level set in the lattice higher that the chain value in the compact \mathbf{K} .

9.3 From Boolean Random Model to Chain Boolean Random Models

The aim of this section is to explain how can be generated a realisation of function $\mathcal{L}^{\mathbf{E}}$ which fits the Chain Boolean Random Model.

9.3.1 Notation

A point process M is a form of stochastic or random process. It may be thought of as a set of random points in a space, with a certain probability defined over the same space. We remark that a realisation of M comprises the number $k \geq 0 \in \mathbb{N}$ and the locations $M_k = \{x_1, \dots, x_k\}$, where $x_i \in \mathbf{E} \forall i$. In general we can broadly distinguish two kinds of point process, spatial homogeneous and inhomogeneous. We assume that M is spatial homogeneous, i.e. stationary. That is to say that the distribution of the shifted point $M + z$ is the same for all $z \in \mathbf{E}$. We denote Ξ the *primary grains* assumed to be non-empty convex subset of \mathbf{E} . The intuitive idea behind this is that the points M_k are the "germs" and the compact sets $\Xi(M_k) = \{\Xi_1, \dots, \Xi_k\}$ are the "grains". Germ-grain models of this form are a rather flexible class of random closed sets. An important special case is the *Boolean model*, where the germ form a homogeneous *Poisson process*. We refer to Molchanov (1997), Lantuéjoul (2002) for a detailed introduction into the subject.

9.3.2 Binary Boolean Random Model

For binary images, the vector space is simply $\mathcal{L} = \{0, 1\}$, and a realisation of the Boolean model denoted by $\mathcal{B}(\Xi(M))$ falls into the following stages:

1. An homogeneous Poisson process with intensity λ is generated. We denote it as $M_{\lambda} = \{x_1, \dots, x_k\}$, where $k \sim \text{Poisson}(\lambda)$.

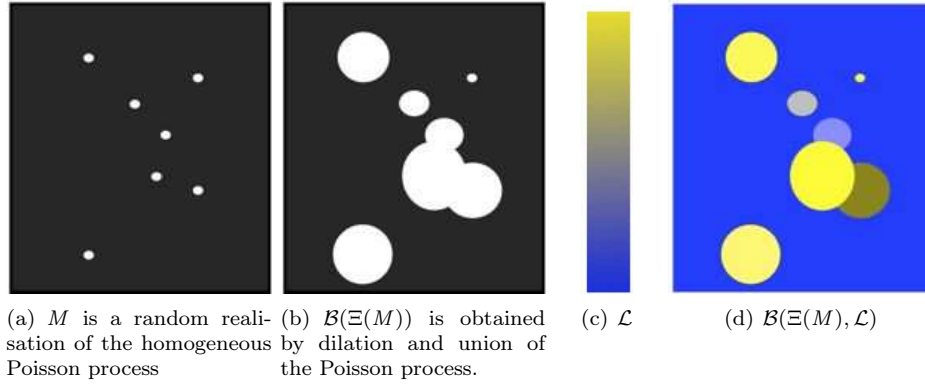


Figure 9.1: Example of Binary Boolean Random image and Chain Boolean Random multivariate image. For illustration, the same $\Xi(M)$ is used in both simulations. We notice that \mathcal{L} is a color lattice from blue ($\perp_{\mathcal{L}}$) to yellow ($\top_{\mathcal{L}}$).

2. Second, the set of germs $\Xi(M_k)$ is determined. For example, $\Xi(M_k) = \mathbf{B}_{r_k}$ denoting balls of radius r_k centered at point x_k . The germs $\Xi(M_k)$ follow a particular distribution. For instance the radius of balls can follow an uniform distribution.
3. Finally, the Boolean model is produced by:

$$\mathcal{B}(\Xi(M)) := \bigcup \delta_{\Xi(M_i)}(x_i) \quad (9.13)$$

where $\delta_{\mathbf{SE}}(x)$ denote the dilation (Minkowski addition) by a structuring element \mathbf{SE} centered at x . Note the $\mathcal{B}(\Xi(M))$ is an binary image, i.e. $\mathcal{B}(\Xi(M)) \in \mathcal{F}(\mathbf{E}, \{0, 1\})$.

9.3.3 Chain Boolean Random Model

The aim of this section is to generate a multivariate image from $(M, \Xi(M), \mathcal{L})$, where M is a point process, $\Xi(M)$ is a set of germs associated to the given point process M , \mathcal{L} is a lattice. The idea of Germ-grain model is based on the notion that the an image can be characterised by using an approximation of independent discrete objects of different sizes. To generate a new version according to this characterisation, a random disposition of these discrete objects have to be implanted and the application of an occlusion criterion in the interception of objects give us the final result. In our setting, the idea "implantation" implies the definition of a background, i.e., the part of the image that serves as a setting to the implanted objects. We denote $\perp_{\mathcal{L}}$ the minimum of the lattice \mathcal{L} . Thus, a Chain Boolean Random Model based on a lattice \mathcal{L} , the point process M and the primary grains Ξ is denoted by $\mathcal{B}(\Xi(M), \mathcal{L})$ and it can be generated in the following stages:

1. An homogeneous Poisson process with intensity λ is generated. We denote it as $M_\lambda = \{x_1, \dots, x_k\}$, where $k \sim \text{Poisson}(\lambda)$.
2. Second, the set of germs $\Xi(M_k)$ is determined. For example, $\Xi(M_k) = \mathbf{B}_{r_k}$ denoting balls of radius r_k .
3. Third, a random sample of size k , $\{x_{\mathcal{L}}^1, \dots, x_{\mathcal{L}}^k\}$ is drawn from \mathcal{L} and implanted at M_λ over an homogeneous background with vector value equal to $\perp_{\mathcal{L}}$.
4. Finally, the Boolean model is produced by:

$$\mathcal{B}(\Xi(M), \mathcal{L}) := \bigvee_{i=1}^k \delta_{(\Xi(M_k), x_{\mathcal{L}}^k)}(\mathbf{X}, \top_{\mathcal{L}}) \quad (9.14)$$

where $\delta_{\mathbf{SE}}(\cdot)$ denote the dilation in the lattice formulation. Note the $\mathcal{B}(\Xi(M), \mathcal{L})$ is by construction an image with values from \mathcal{L} , i.e., $\mathcal{B}(\Xi(M), \mathcal{L}) \in \mathcal{L}^{\mathbf{E}}$. In Fig. 9.1 is given an example of simulation of a lattice Boolean Random color image.

9.3.4 Properties

In the framework of the theory of random sets, these structures and their models are fully characterised by a functional called Choquet capacity. By the Choquet theorem [15], the distribution of the grain Ξ_0 with M a stationary Poisson process, is determined by the correspondent capacity functional:

$$\mathbf{T}_{\Xi_0}(\mathbf{K}) = \mathbf{P}\{\Xi_0 \cap \mathbf{K} \neq \emptyset\}, \quad (9.15)$$

where \mathbf{K} runs through the family of all compact sets. The capacity functional of the Boolean Model $\mathcal{B}(\Xi_0)$ is defined analogously. It can be evaluated as Molchanov (1997) [p.21] :

$$\mathbf{T}_{\mathcal{B}(\Xi_0)}(\mathbf{K}) = \mathbf{P}\{\mathcal{B}(\Xi_0) \cap \mathbf{K} \neq \emptyset\} = 1 - \exp\{-\mathbf{E}(\delta_{\mathbf{K}}(\Xi_0))\} \quad (9.16)$$

where \mathbf{E} is the expected value operator, and in the stationary case, we obtain the simplified expression:

$$\mathbf{T}_{\mathcal{B}(\Xi_0)}(\mathbf{K}) = \mathbf{P}\{\mathcal{B}(\Xi_0) \cap \mathbf{K} \neq \emptyset\} = 1 - \exp\{-\lambda \mu_{\mathbf{E}}(\delta_{\mathbf{K}}(\Xi_0))\} \quad (9.17)$$

where $\mu_{\mathbf{E}}$ is the Lebesgue measure of \mathbf{E} , i.e., (Area in 2D images, Volume in 3D images).

Now we assume that the chain value $k_{\mathcal{L}}$ are drawn i.i.d. with distribution $\mathfrak{F}_{\mathcal{L}}$, the capacity chain functional $\mathbf{T}_{\mathcal{B}(\Xi_0, \mathcal{L})}(\mathbf{K})$ is given by

$$\mathbf{T}_{\mathcal{B}(\Xi_0, \mathcal{L})}(\mathbf{K}) = \mathbf{P}\{\mathcal{B}(\Xi_0) \cap \mathbf{K} \neq \emptyset, \perp_{\mathcal{L}} <_{\mathcal{L}} k_{\mathcal{L}} \leq_{\mathcal{L}} x_{\mathcal{L}}\} \quad (9.18)$$

$$= (1 - \exp\{-\lambda \mu_{\mathbf{E}}(\delta_{\mathbf{K}}(\Xi_0))\}) \mathbf{P}_{\mathfrak{F}_{\mathcal{L}}}\{\perp_{\mathcal{L}} <_{\mathcal{L}} k_{\mathcal{L}} \leq_{\mathcal{L}} x_{\mathcal{L}}\} \quad (9.19)$$

Proposition 7. Any random Boolean function $\mathcal{B}(\Xi_0, \mathcal{L})$ from \mathbf{E} into \mathcal{L} is infinitely divisible under $\bigvee_{\mathcal{L}}$; i.e. for each integer k , it can be written as:

$$\mathcal{B} = \bigvee_{\mathcal{L}} \{\mathcal{B}_i, i \in [1 \dots, k]\}, \quad (9.20)$$

in which \mathcal{B}_i are k equivalent independent Boolean random function.

9.3.5 h -ordering and h -adjunctions

The formalism introduced in the previous section requires the notion of a well-ordered set or lattice.

As it was presented in Chapter 3, from a h -ordering, we can define a h -adjunction. Summarising, to define morphological operator in a vector space \mathbb{R}^d , a surjective mapping h is required. It is illustrated in (9.21)

$$\begin{array}{ccc} \mathcal{F}(\mathbf{E}, \mathbb{R}^d) & \xrightarrow{h} & \mathcal{L}^{\mathbf{E}} \\ & & \varepsilon \downarrow \delta \\ \mathcal{F}(\mathbf{E}, \mathbb{R}^d) & \xleftarrow{h^{-1}} & \mathcal{L}^{\mathbf{E}} \end{array} \quad (9.21)$$

For practical application, the lattice \mathcal{L} should be obtained from examples of images. Let us consider the example illustrated in Fig. 9.2: starting from a multivariate image $\mathbf{I} \in \mathcal{F}(\mathbf{E}, \mathbb{R}^d)$, in this case a colour image (i.e., $d = 3$), the first step to deal with it involves to obtain a mapping from the vector space of values \mathbb{R}^d to a complete lattice \mathcal{L} , which introduces an ordering structure compatible with mathematical morphology operators, such as dilation, and with Chain Boolean Random Models.

In particular, for this study, we focus on an ordering mapping which is intrinsically associated to the image \mathbf{I} based on the h -ordering introduced in Chapter 6. Different types of h -ordering have been proposed in the literature. However, it is convenient and natural to orient to a "centre", which can be defined in a variety of ways. This leads naturally to the use the center-outward ordering of points and description in term of *nested contours*.

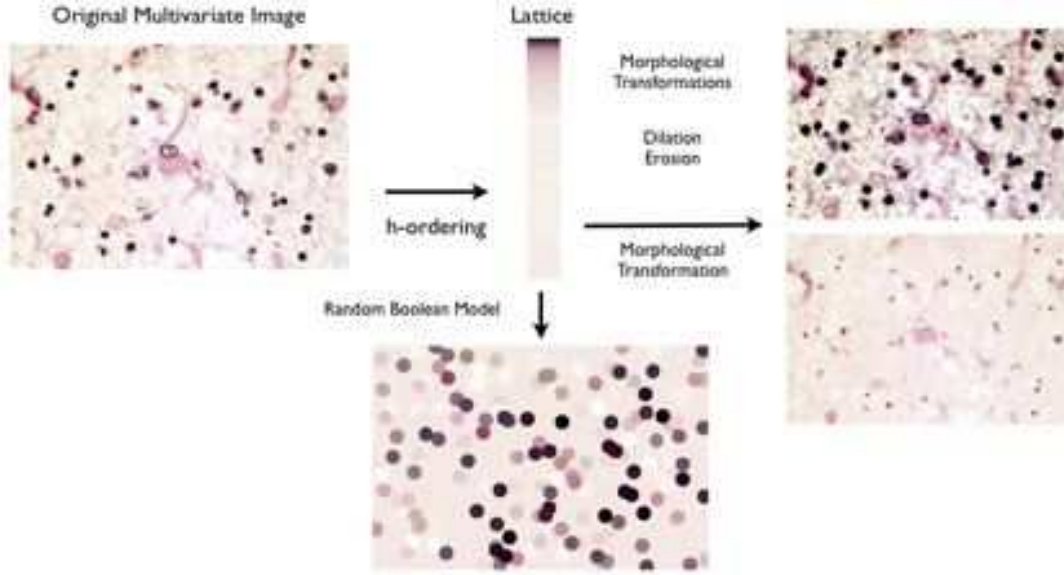


Figure 9.2: The Chain representation of a multivariate image allows the applications of non-linear filtering and random Boolean model theory.

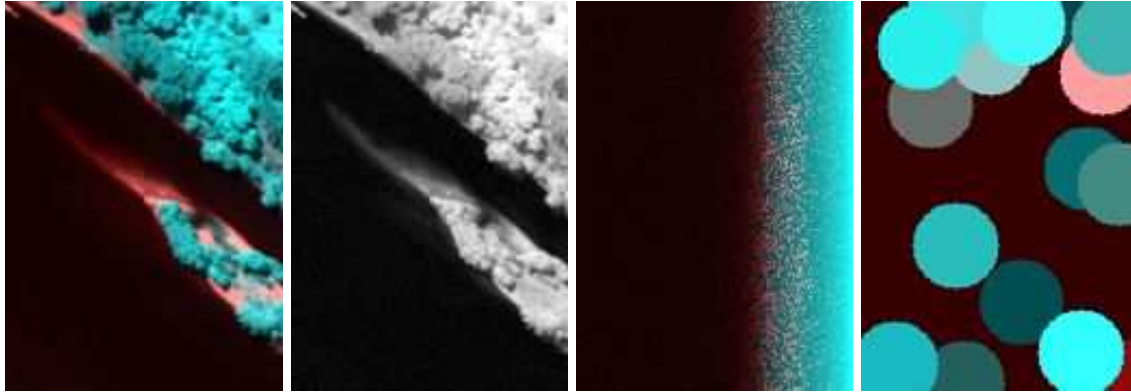
9.4 Experiments

The aim of this section is to provide some initial experiments of multivariate Boolean Random image simulation. We are considering in ongoing research a more systematic study on the issue of image characterising and simulation using the models introduced in this chapter.

Let us consider the first example given in Fig. 9.3(a). This example shows a hyperspectral image with 201 rows, 143 columns in 102 bands. The value of the projection depth function is shown in Fig. 9.3(b), and the associated intrinsic ordering is obtained in Fig. 9.3(c). Now, working on the lattice \mathcal{L}_I induced by this ordering, it is possible to simulate a hyperspectral Boolean image. From the projection depth function, we can, on the one hand, obtain the background value (which correspond to the bottom on the lattice, $\perp_{\mathcal{L}}$) and, on the other hand, the distribution of values of \mathcal{L} , i.e., the histogram of the chain value. The notion of lattice volume fraction $\hat{f}_{\mathcal{L}}$ can be introduced as the fraction lattice of points of the image which are greater than the background in the order induced by the random projection depth. Accordingly, the size distribution of the image associated to the lattice \mathcal{L} , which is obtained by means of a granulometry based on openings with disks as structuring element of increasing size, allows us to estimate the typical size of the image objects: \hat{r} . They are important parameters to simulate multivariate textures according to our model, because from them, we can estimate the intensity $\hat{\lambda}$ of the homogeneous Poisson processing by using Matheron (1975):

$$\begin{aligned} \hat{f}_{\mathcal{L}} &= 1 - \exp(-\hat{\lambda}\pi\hat{r}^2) \\ \iff \hat{\lambda} &= \frac{\ln(1 - \hat{f}_{\mathcal{L}})}{-\pi\hat{r}^2} \end{aligned}$$

We observe that the original (Fig.9.3(a)) and the simulated images have the same spectra (Fig.9.3(d)) but of course the "texture" of the original one does not fit the Boolean model and consequently the simulation is not realistic. On the other hand, even if both images underlay the some lattice, the distribution of the spectral space is not the same. The second and third examples given in Fig.9.4 and 9.5 correspond to natural multivariate images which are more appropriate to be considered under the Boolean paradigm. We have used the same procedure in both cases. Starting from the initial image, the intrinsic ordering associated to the projection depth function is obtained. The germs are generated according to an homogeneous Poisson process with intensity estimated from $\hat{f}_{\mathcal{L}}$ and \hat{r} . The next step consist in generating a lattice Boolean random image $\mathcal{B}(\Xi, \mathcal{L})$, where the primary grain Ξ



(a) Original image is a Hy- (b) Projection Depth Func- (c) Lattice (\mathcal{L}_I) by using (d) Simulation of a Boolean
 perspectral image \mathbf{I} . False tion associated to \mathbf{I} Projection Depth Ordering model in \mathcal{L}_I .
 colour in the bands corre- from Chapter 5.
 spondent to $\{50, 90, 100\}$

Figure 9.3: Example of simulation for a hyperspectral image

is a disk of size \hat{r} . The random values in the disks are drawn from \mathcal{L} following the distribution of the image.

The extension of the classical Boolean model presented in this Chapter discusses the basic ingredients of the model, however more research work is necessary to consolidate the theoretical basis of the approach. Despite that, we believe that the examples are useful to illustrate the interest of the procedure.

9.5 Conclusions of this chapter

We have introduced in this chapter the first milestone towards a theoretical framework for lattice Boolean Random Model. The interest of such a stochastic geometry models is the characterization and simulation of multivariate images, and in particular the analysis and simulation of multi/hyperspectral texture images. We have discussed the basic ingredients of the model, however more research work is necessary to consolidate the theoretical basis of the approach.

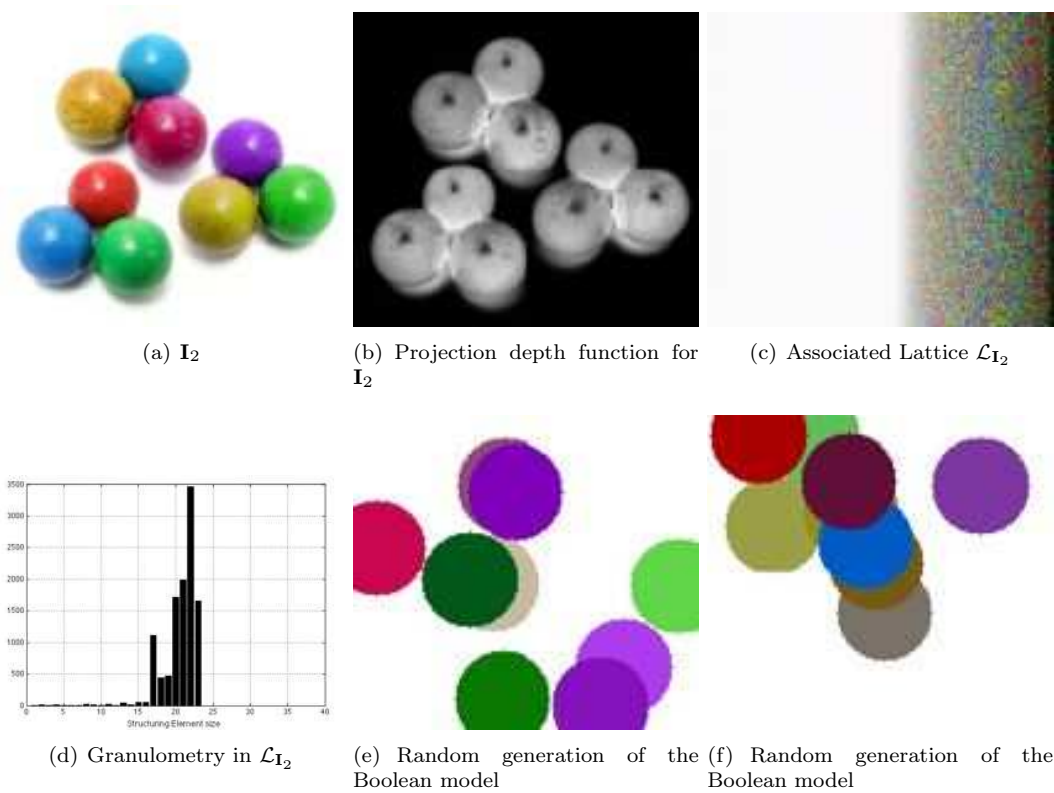


Figure 9.4: Summary of proposed steps to generate random realization of a Boolean model in the lattice induced by the random projection depth function.

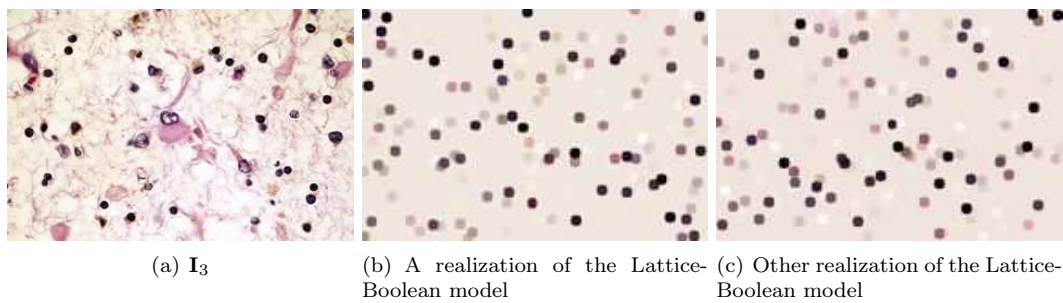


Figure 9.5: Realisations of the proposed algorithm of Multivariate Boolean model in the lattice induced for the projection depth function

10

Conclusion and Perspectives

Résumé

Dans ce chapitre, les contributions plus importantes de cette thèse sont rappelées. Quelques remarques finales sont accompagnées de perspectives concernant de possibles travaux futurs.

10.1 Conclusion

We studied multivariate ordering and its relationship with mathematical morphology to analyse multi/hyperspectral images as well as connections between techniques of dimensionality reduction, tensor structures and supervised classification of remote sensing imagery. The main idea and contribution of this thesis is to demonstrate that the study of the multivariate statistics and machine learning techniques such as supervised learning and distances based on random projections is closely related to the idea of ordering in high-dimensional spaces with applications to nonlinear image processing, i.e. mathematical morphology for multivariate images.

The work presented in this dissertation addressed the problem of modelling multivariate images in a partially ordered set through techniques based on mathematical morphology. The main contributions of our work include the following points:

- The introduction of new notions as supervised ordering, background/foreground decomposition, order based on random projections, additive morphological decomposition, and conditional toggle mapping transformation and showed that they are closely related to the morphological analysis of multivariate images.
- The idea of supervised ordering allows us to generalise, in a natural way, classical morphological operators. In particular a multivariate version of the hit-and-miss transformation, which is applied in the template matching problem from high resolution remote sensing images.
- We bring a theoretical idea from the literature of multivariate statistics (the elliptically contoured distribution), to prove that for data following this class of probability distributions, the ordering based on random projections is equivalent to the classical Mahalanobis distance. Additionally, our formulation allow us to include robust estimators to build a multivariate ordering with natural interpretation in many real-life images.
- We introduced a new free-parameters unified approach for both edge enhancement and salt-and-pepper noise removal by using conditional mathematical morphology. The unified frame-

work is based on defining a seed mask, which is different according to type of processing, and by using condition mathematical morphology operators in an iterative toggle contrast style. The proposed filter also shows consistent and stable performance across a wide range of noise densities from 10% to 95%. A remarkable point concerning the behaviour of the present approach is the fact that between 50% and 95% is obtained a difference of less than 5 in PNSR, which proves the stability of the method with respect to the noise level.

- Inspired by the necessity of including spatial information in dimensionality reduction techniques, we proposed the additive morphological decomposition (AMD). A spatial/spectral dimensional reduction technique with a really good performance in classification task have been proposed by interacting AMD with a tensor version of classical principal component analysis. Practical examples achieved in supervised classification show that the proposed additive morphological decomposition outperforms traditional decompositions in remote sensing scenarios. Additionally, the morphological additive decomposition is more compact, in the sense of dimension size, than classical decompositions.
- We introduced the first milestone towards a theoretical framework for lattice Boolean Random Model. The interest of such a stochastic geometry model is the characterization and simulation of multivariate images, and in particular the analysis and simulation of multi/hyperspectral texture images.

For all of these approaches, there are a variety of open theoretical and algorithmic questions, that are included in the next section.

10.2 Suggestions for Future Works

Here, we discuss some questions and suggestions for future works on mathematical morphology in multivariate images.

Chapter 1:

- The orders proposed in this thesis are image adaptive, so a natural question is how can we define a measure of agreement between an order and a image?.
- Degree of conformity, i.e., a measure of conformity of a given set to its ordering principle. Thus, sets that share the same ordering principle may differ in their degree of conformity, i.e., an order can be more adequate to a given image than to another.
- Degree of complexity; it should measure the amount of distinctions resulting from the application of an ordering principle to a set, i.e., in the context of multivariate morphology, it should answer the question "Does the order allow us to extract the important objects of the image?"

Chapter 4

- Multiscale Ordering: One can define a multi-scale representation of a multivariate image. So, it is important to know what kind of ordering can be calculated in the reduced image to get an order that is invariant to the sampling size in the representation.
- Semi-supervised Ordering: Machine Learning approaches allow the generation of classification function from labeled and unlabeled data at the same time. These types of approaches are named "semi-supervised". What properties of type of learning approaches can be feasible for multivariate ordering?
- Can the ordering be learned from some images and then be applied to others from the same scene? For instance, the analysis of a video sequence by morphological operators.

Chapter 5

- The main question in the multivariate version of the hit-and-miss transform is how to find automatically the best value of threshold parameter ϵ .

Chapter 6

- Does Proposition 6 stating that the random projection depth is equivalent to the Mahalanobis distance ($k \rightarrow \infty$) hold for a more general family of probability distribution?
- Can we apply the same idea of random projections to manifold structures (graph, shapes, etc) or to data with missing information ?

Chapter 7

- To understand the advantage of the additive decomposition, it is important to know the statistical properties and their relationship with classical estimators (mean, median, etc).
- Tensor decomposition is not invariant to rotations of the scene. So, an important question is how to get invariant decompositions, for instance, in a polar representation of the original image.

Chapter 8

- The conditional toggle mapping allows us to solve simple in-painting problems. Thus, image compression or super-resolution can be performed by using the same approach.
- Ideally, non-flat and local adaptive morphology have to be used to improve the performance of the proposed algorithms to filter salt-and-pepper noise.
- An adequate multivariate extension have to be considered. For instance, the order based on random projection can be performed before the mask detection stage.

Chapter 9

- Ideally, if we are interested to generate random version of a given multivariate image, our model should capture the structure (granulometry) and texture of objects of interest. So, the real challenge in such generalisation of Multivariate Boolean Models would be developing methods for deducing structure plus texture information about the original image based on, for instance, random projections.

List of Symbols

Symbol	Meaning
\mathbf{I}	Original image.
d	Dimension of the vector space.
n	Number of pixels.
x	A pixel in the original image.
\times	A coordinate in the original image.
\mathbf{E}	Spatial space of points.
\mathbb{F}	Domain of vector values.
\mathbf{SE}	Structuring Element.
$\tilde{\mathbf{SE}}$	Transpose of the structuring element.
\mathbf{B}	Ball centered at x .
t_{max}	Maximum value for a grey value image.
\mathbf{X}	Matrix version of the original image \mathbf{I} .
$\delta_{\mathbf{SE}}(\cdot), \varepsilon_{\mathbf{SE}}(\cdot)$	Dilation, Erosion operator.
$\gamma_{\mathbf{SE}}(\cdot), \varphi_{\mathbf{SE}}(\cdot)$	Opening, Closing operator.
τ	Toggle mapping operator.
$\delta_{\mathbf{B}}^{\infty}(\mathbf{M}, \mathbf{I})$	dilation by reconstruction from the \mathbf{M} to \mathbf{I}
$\Lambda(\mathbf{I})$	Leveling
$\bar{\lambda}_{\sigma}(\mathbf{I})$	Upper Leveling
$\underline{\lambda}_{\sigma}(\mathbf{I})$	Lower Leveling
T	Training set.
B, F	Background, Foreground set.
b, f, p	A pixel in the background, foreground or path.
\mathbf{M}	Mask or Marker image.
\mathbf{K}	A kernel matrix.
\mathbf{D}	Distance matrix.
$\Delta_{\mathbf{SE}}^{\varepsilon}(\mathbf{I}), \Delta_{\mathbf{SE}}^{\delta}(\mathbf{I})$	Gradient by Erosion, Gradient by Dilation.
$\Delta_{\mathbf{SE}}(\mathbf{I})$	Morphological Gradient.
$\varepsilon_{\mathbf{SE}}(\mathbf{I}, \mathbf{M}), \delta_{\mathbf{SE}}(\mathbf{I}, \mathbf{M})$	Conditional Erosion, Conditional Dilation.
$\tau_{\mathbf{SE}}(\mathbf{I}, \mathbf{M})$	Conditional Toggle Mapping.
$N_{(\mathbf{SE}, \mathbf{M})}(\mathbf{I})$	Conditional Neighborhood.
$\tilde{\varepsilon}_{\mathbf{SE}}(\mathbf{I}, \mathbf{M})$	Algebraic Adjunction of Conditional Dilation.
\mathcal{L}	A lattice
\perp, \top	Minimum, maximum in the lattice.
r	Element in the lattice.
\mathbf{R}	A set.
r	A element in the set.
$DP(\mathbf{x}; \mathbf{I})$	Depth function for a vector \mathbf{x} based on an image \mathbf{I} .
$h_{D(\cdot; \mathbf{I})}$	h -ordering for a given image \mathbf{I} based on a the depth function.
$h_{\{B, F\}}$	h -supervised ordering based on the sets $\{B, F\}$.
$\delta_{\mathbf{SE}, h}(\cdot)$	Dilation by the h ordering.
med	Median.
mad	Median absolute difference.
CC	Connected component.
\mathbf{K}	Compact set in the space support.
M	Point Process
Ξ	Primary grain
$\mathbf{T}(\mathbf{K})$	Choquet capacity of \mathbf{K}

Bibliography

- Al-Otum, H. M. (2003). Morphological operators for color image processing based on mahalanobis distance. *Optical Engineering*, 42(9):2595–2606.
- Alvarez, L. and Mazorra, L. (1994). Signal and image restoration using shock filters and anisotropic diffusion. *SIAM Journal of Numerical Analysis*, 31:590–605.
- Andrews, H. and Patterson, C. L. (1976). Singular value decompositions and digital image processing. *IEEE Trans. Acoust., Speech, Signal Processing*, 24(1):26–53.
- Angulo, J. (2007). Morphological colour operators in totally ordered lattices based on distances: Application to image filtering, enhancement and analysis. *Computer Vision and Image Understanding*, 107(1-2):56–73.
- Angulo, J. and Jeulin, D. (2007). Stochastic watershed segmentation. In *Mathematical Morphology and its Applications to Image and Signal Processing*, page 265–276.
- Angulo, J. and Serra, J. (2003). Color segmentation by ordered mergings. In *Proc. IEEE Int’l Conf. Image Processing*, pages 125–128.
- Aptoula, E. and Lefèvre, S. (2007). A comparative study on multivariate mathematical morphology. *Pattern Recognition*, 40(11):2914–2929.
- Aptoula, E. and Lefèvre, S. (2008). On lexicographical ordering in multivariate mathematical morphology. *Pattern Recognition Letters*, 29:109–118.
- Aptoula, E. and Lefèvre, S. (2009). On the morphological processing of hue. *Image Vision Comput.*, 27(9):1394–1401.
- Astola, J., Haavisto, P., and Neuvo, Y. (1990). Vector median filters. *Proceedings IEEE*, 78:678–689.
- Barbin, D., Elmasry, G., Sun, D., and P.Allen (2011). Near-infrared hyperspectral imaging for grading and classification of pork. *Meat Science*, 90(1):259–268.
- Barnett, V. (1976). The ordering of multivariate data (with discussion). *Journal of the Royal Stat. Soc. Series A*, 139(3):318–354.
- Baudes, A., Coll, B., and Morel, J. (2005). A review of image denoising algorithms, with a new one. *Multiscale Modeling and Simulation*, 4(2):490–530.
- Belkin, M. and Niyogi, P. (2002). Laplacian eigenmaps for dimensionality reduction and data representation. *Neural Comp.*, 15:1373–1396.
- Bellman, R. (1957). *Dynamic Programming*. Princeton University Press.
- Benediktsson, J., Palmason, J., and Sveinsson, J. (2005). Classification of hyperspectral data from urban areas based on extended morphological profiles. *IEEE Transaction on Geoscience and Remote Sensing*, 43(3):480–491.
- Benediktsson, J., Pesaresi, M., and Arnason, K. (2003). Classification and feature extraction for remote sensing images from urban areas based on morphological transformations. *IEEE Transaction on Geoscience and Remote Sensing*, 41(9):1940–1949.

- Bertrand, G. (2005). On topological watersheds. *Journal of Mathematical Imaging and Vision*, 22((2-3)):217–230.
- Beucher, S. and Lantuejoul, C. (1979). Use of Watersheds in Contour Detection. In *International Workshop on Image Processing: Real-time Edge and Motion Detection/Estimation, Rennes, France*.
- Beucher, S. and Meyer, F. (1993). The morphological approach to segmentation: the watershed transformation. *Mathematical morphology in image processing. Optical Engineering*, 34:433–481.
- Bolton, J. and Gader, P. (2009). Random set framework for context-based classification with hyperspectral imagery. *IEEE Transaction on Geoscience and Remote Sensing*, 47:3810–3821.
- Boncelet, C. (2000). Image noise models. In Bovik, A. C., editor, *Handbook of image and video processing*, pages 325–335. New York: Academic.
- Bourennane, S., Fossati, C., and Cailly, A. (2010). Improvement of classification for hyperspectral images based on tensor modeling. *Geoscience and Remote Sensing Letters, IEEE*, 7(4):801–805.
- Boyd, S. and Vandenberghe, L. (2004). *Convex Optimization*. Cambridge University Press.
- Brekke, C. and Solberg, A. H. (2005). Oil spill detection by satellite remote sensing. *Remote Sensing of Environment*, 95(1):1–13.
- Bruzzone, L. and Carlin, L. (2006). A multilevel context-based system for classification of very high spatial resolution images. *IEEE Transaction on Geoscience and Remote Sensing*, 44(9):2587–2600.
- Buades, A., Coll, B., and Morel, J. M. (2005). A review of image denoising algorithms, with a new one. *Multiscale Modeling Simulation*, 4:490–530.
- Buades, A., Le, T., Morel, J., and Vese, L. (2010). Fast cartoon + texture image filters. *IEEE Transaction on Image Processing*, 19(18):1978–1986.
- Camps-Valls, G., Bandos, T., and Zhou, D. (2007). Semi-supervised graph-based hyperspectral image classification. *IEEE Transaction on Geoscience and Remote Sensing*, 53(10):3044–3054.
- Camps-Valls, G. and Bruzzone, L. (2005). Kernel-based methods for hyperspectral image classification. *IEEE Transaction on Geoscience and Remote Sensing*, 43(6):1351–1362.
- Caselles, V. and Morel, J. M. (1999). Topographic maps and local contrast changes in natural images. *International Journal of Computer Vision*, 33(1):5–27.
- Cayley, A. (1859). On Contour and Slope Lines. *The Philosophical magazine*, 18:264–168.
- Chakrabarti, A. and Zickler, T. (2011). Statistics of Real-World Hyperspectral Images. In *Proc. IEEE Conf. on Computer Vision and Pattern Recognition (CVPR)*, pages 193–200.
- Chan, R., Chung-Wa, H., and Nikolova, M. (2005). Salt-and-pepper noise removal by median-type noise detectors and detail-preserving regularization. *IEEE Transaction on Image Processing*, 14(10):1479–1485.
- Chang, C.-I. (2003). *Hyperspectral Imaging: Techniques for Spectral Detection and Classification*. Plenum Publishing Co.
- Chanussot, J., Crawford, M. M., and Kuo, B.-C. (2010). Foreword to the special issue on hyperspectral image and signal processing. *IEEE Transaction on Geoscience and Remote Sensing*, 48(11):3871–3876.
- Chanussot, J. and Lambert, P. (2000). Extending mathematical morphology to color image processing. In *International Conference on Color in Graphics and Image Processing*, pages 158–163.

- Chatterjee, P. and Milanfar, P. (2010). Is denoising dead? *IEEE Transaction on Image Processing*, 19(4):895–911.
- Chen, C.-M., Hepner, G., and Forster, R. (2003). Fusion of hyperspectral and radar data using the ihs transformation to enhance urban surface features. *ISPRS Journal of Photogrammetry and Remote Sensing*, 58(1-2):19–30. Algorithms and Techniques for Multi-Source Data Fusion in Urban Areas.
- Clark, M. L., Roberts, D. A., and Clark, D. B. (2005). Hyperspectral discrimination of tropical rain forest tree species at leaf to crown scales. *Remote Sensing of Environment*, 96(3-4):375–398.
- Clarkson, K. (1994). An algorithm for approximate closest point queries. In *Proceedings of the Tenth Annual ACM Symposium on Computational Geometry*, pages 160–164.
- Coupric, C., Grady, L., Najman, L., and Talbot, H. (2011). Power watershed: A unifying graph-based optimization framework. *IEEE Transaction on Pattern Analysis and Machine Intelligence*, 33(7):1384–1399.
- Cousty, J., Bertrand, G., Najman, L., and Couprie, M. (2009). Watershed cuts: Minimum spanning forests and the drop of water principle. *IEEE Transaction on Pattern Analysis and Machine Intelligence*, 31(8):1362–1374.
- Cousty, J., Bertrand, G., Najman, L., and Couprie, M. (2010). Watershed cuts: Thinnings, shortest path forests, and topological watersheds. *IEEE Transaction on Pattern Analysis and Machine Intelligence*, 32(5):925–939.
- Cristianini, N. and Shawe-Taylor, J. (2000). *An Introduction to support vector machines and other kernel based learning methods*. Cambridge University Press.
- Cuesta-Albertos, J. and Nietos-Reyes, A. (2008). The random tukey depth. *Computational Statistics and Data Analysis*, 52(11):4979–4988.
- Cuevas, A., Febrero, M., and Fraiman, R. (2007). Robust estimation and classification for functional data via projection-based depth notions. *Computational Statistics*, 22(3):481–496.
- Cui, X., Lin, L., and Yang, G. (2008). An extended projection data depth and its application to discrimination. *Communication in Statistics - Theory and Methods*, 37(14):2276–2290.
- Dalla-Mura, M., Benediktsson, J., and Bruzzone, L. (2011). Self-dual attribute profiles for the analysis of remote sensing images. In *Mathematical Morphology and Its Applications to Image and Signal Processing*, volume 6671 of *Lecture Notes in Computer Science*, pages 320–330. Springer Berlin / Heidelberg.
- Dalla-Mura, M., Benediktsson, J., Waske, B., and Bruzzone, L. (2010). Morphological attribute profiles for the analysis of very high resolution images. *IEEE Transaction on Geoscience and Remote Sensing*, 48(10):3747–3762.
- Donoho, D. and Gasko, M. (1992). Breakdown properties of location estimates based on halfspace depth and projected outlyingness. *The Annals of Statistics*, 20(4):1803–1827.
- Duarte-Carvajalino, J., Sapiro, G., Velez-Reyes, M., and Castillo, P. E. (2008). Multiscale representation and segmentation of hyperspectral imagery using geometric partial differential equations and algebraic multigrid methods. *IEEE Transaction on Geoscience and Remote Sensing*, 46(8):2418–2434.
- Dundar, M., Theiler, J., and Perkins, S. (2006). Incorporating spatial contiguity into the design of a support vector machine classifier. In *Geoscience and Remote Sensing Symposium, 2006. IGARSS 2006. IEEE International Conference on*, pages 364–367.

- Eldén, L. and Savas, B. (2009). A newton-grassmann method for computing the best multi-linear rank- (r_1, r_2, r_3) approximation of a tensor. *SIAM J. Matrix Anal. Appl.*, 31:248–271.
- Elder, J. and Zucker, S. (1998). Local scale control for edge detection and blur estimation. *IEEE Transaction on Pattern Analysis and Machine Intelligence*, 20(7):699–716.
- Eng, H. and Ma., K. (2001). Noise adaptive soft-switching median filter. *IEEE Transaction on Image Processing*, 10(2):242–251.
- Fang, K.-T., Kotz, S., and Ng, K. W. (1990). *Symmetric multivariate and related distributions*. Number 36 in Monographs on statistics and applied probability. Chapman Hall, London.
- Fauvel, M., Benediktsson, J., Chanussot, J., and Sveinsson, J. (2008). Spectral and spatial classification of hyperspectral data using svms and morphological profiles. *IEEE Transaction on Geoscience and Remote Sensing*, 46(11):3804–3814.
- Fauvel, M., Chanussot, J., and Benediktsson, J. (2012). A spatial-spectral kernel-based approach for the classification of remote-sensing image. *Pattern Recognition*, 45:381–392.
- Garcia, A., Vachier, C., and Vallée, J. (2008). Multivariate mathematical morphology and bayesian classifier application to colour and medical images. In Astola, J. T., Egiazarian, K. O., and Dougherty, E. R., editors, *Image Processing: Algorithms and Systems VI*, volume 6812, page 681203. SPIE.
- Gauch, J. (1999). Image segmentation and analysis via multiscale gradient watershed hierarchies. *IEEE Transaction on Image Processing*, 8(1):69–79.
- Gendrin, A., Mangold, N., Bibring, J., Langevin, Y., Gondet, B., Poulet, F., Bonello, G., Quantin, C., Mustard, J., Arvidson, R., et al. (2005). Sulfates in Martian Layered Terrains: The OMEGA/Mars Express View.
- Ghahramani, Z. and Hinton, G. E. (1997). The EM algorithm for mixtures of factor analyzers. Technical report, Department of Computer Science, University of Toronto.
- Gilboa, G., Sochen, N., and Zeevi, Y. (2004). Image enhancement and denoising by complex diffusion processes. *IEEE Transaction on Pattern Analysis and Machine Intelligence*, 25(8):1020–1034.
- Gilboa, G., Sochen, N. A., and Zeevi, Y. Y. (2002). Regularized shock filters and complex diffusion. In *Proceeding of the 7th European Conference on Computer Vision-Part I, ECCV '02*, pages 399–413, London, UK. Springer-Verlag.
- Gonzalez, R. and Woods, R. (2008). *Digital image processing*. Prentice Hall.
- Goutsias, J. and Heijmans, H. J. A. M. (2000). *Mathematical Morphology*. IOS.
- Goutsias, J., Heijmans, H. J. A. M., and K.Sivakumar (1995). Morphological operators for image sequences. *Computer Vision and Image Understanding*, 62(3):326–346.
- Gower, J. and Ross, G. (1969). Minimum spanning trees and single linkage cluster analysis. *Applied Statistics*, 18(1):54–64.
- Grana, M., Villaverde, I., Maldonado, J., and Hernandez, C. (2009). Two lattice computing approaches for the unsupervised segmentation of hyperspectral images. *Neurocomputing*, 72:2111–2120.
- Grazzini, J. and Soille, P. (2009). Edge-preserving smoothing using a similarity measure in adaptive geodesic neighborhoods. *Pattern Recognition*, 42:2306–2316.
- Green, A., Berman, M., Switzer, P., and Craig, M. (1988). A transformation for ordering multi-spectral data in terms of image quality with implications for noise removal. *IEEE Transaction on Geoscience and Remote Sensing*, 26(1):65–74.

- Guichard, F. and Morel, J. (2002). Mathematical morphology almost everywhere. In *Proc. of the ISMM'02*, pages 293–303.
- Haboudane, D. (2004). Hyperspectral vegetation indices and novel algorithms for predicting green lai of crop canopies: Modeling and validation in the context of precision agriculture. *Remote Sensing of Environment*, 90(3):337–352.
- Hampel, F., Ronchetti, E., Rousseeuw, P., and Stahel, W. (1986). *Robust Statistics*. John Wiley and Sons.
- Harsanyi, J. C., i Chang, C., and Member, S. (1994). Hyperspectral image classification and dimensionality reduction: an orthogonal subspace projection approach. *IEEE Transaction on Geoscience and Remote Sensing*, 32:779–785.
- Heijmans, H. J. A. M. (1994). *Morphological Image Operators*, volume 10. Academic Press.
- Heijmans, H. J. A. M. (1995). Mathematical morphology: A modern approach in image processing based on algebra and geometry. *SIAM Review*, 37(1):1–36.
- Heijmans, H. J. A. M. (1997). Composing morphological filters. *IEEE Transaction on Image Processing*, 10(8):713–723.
- Heijmans, H. J. A. M., Nacken, P., Toet, A., and Vincent, L. (1992). Graph morphology. *Journal of Visual Communication and Image Representation*, 3:24–38.
- Heijmans, H. J. A. M. and Ronse, C. (1990). The algebraic basis of mathematical morphology. i. dilations and erosions. *Comput. Vision Graph. Image Process.*, 50:245–295.
- Huang, H., Ding, C., Luo, D., and Li, T. (2008). Simultaneous tensor subspace selection and clustering: the equivalence of high order svd and k-means clustering. *KDD '08: Proceeding of the 14th ACM SIGKDD international conference on Knowledge discovery and data mining*, 200:327–335.
- Hwang, H. and Haddad, R. A. (1995). Adaptive median filters: new algorithms and results. *IEEE Transaction on Image Processing*, 4:499–502.
- Jackson, Q. and Landgrebe, D. (2002). Adaptive bayesian contextual classification based on markov random fields. *IEEE Transaction on Geoscience and Remote Sensing*, 40(11):2454–2463.
- Jeulin, D. (1991). *Modèles Morphologiques de Structures Aléatoires et de Changement d’Echelle*. Thèse de doctorat ès sciences physiques, University of Caen.
- Jeulin, D. (1992a). Multivariate random image models. *Acta Stereologica*, (11):59–66.
- Jeulin, D. (1992b). Random image models for microstructures analysis and simulation. *Scanning Microscopy Supplement*, 6:121–128.
- Jeulin, D. and Jeulin, P. (1981). Synthesis of rough surfaces by random morphological models. *Stereol. Jugosl.*, 3(1):239–246.
- Jiménez, L., Arzuaga, E., and Vélez, M. (2007). Unsupervised linear feature-extraction methods and their effects in the classification of high-dimensional data. *IEEE Transaction on Geoscience and Remote Sensing*, 45(2):469–483.
- Jochems, T. (1997). *Morphologie Mathématique Appliquée au Contrôle Industriel de Pièces Coulées*. PhD thesis, Ecole National Supérieure des Mines de Paris.
- Johnson, R. and Wichern, D. (2007). *Applied Multivariate Statistics Analysis, 6rd edition*. London: Prentice-Hall International Inc.
- Jolliffe, I. T. (1986). *Principal Component Analysis*. Springer-Verlag.

- Kambhatla, N. and Leen, T. (1997). Dimension reduction by local principal component analysis. *Neural Comp.*, 9(7):1493–1516.
- Keshava, N. and Mustard, J. (2002). Spectral unmixing. *Signal Processing Magazine, IEEE*, 19(1):44–57.
- Keshet, R. and Heijmans, H. J. A. M. (2003). Adjunctions in pyramids, curve evolution and scale-spaces. *Int. J. Comput. Vision*, 52:139–151.
- Kiely, A. and Klimesh, M. (2009). Exploiting calibration-induced artifacts in lossless compression of hyperspectral imagery. *IEEE Transaction on Geoscience and Remote Sensing*, 47(8):2672–2678.
- Kolda, T. and Bader, B. (2009). Tensor decompositions and applications. *SIAM Review*, 51(3):455–500.
- Koppen, M. (2000). The curse of dimensionality. In *5th Online World Conference on Soft Computing in Industrial Applications (WSC5)*.
- Kramer, H. P. and Bruckner, J. B. (1975). Iterations of a non-linear transformation for enhancement of digital images. *Pattern Recognition*, 7(1-2):53–58.
- Kruse, F. A., Boardman, J. W., and Huntington, J. F. D. A. J. (2003). Comparison of airborne hyperspectral data and eo-1 hyperion for mineral mapping. *IEEE Transaction on Geoscience and Remote Sensing*, 41(6):1388–1400 ST – Comparison of airborne hyperspectr.
- Landgrebe, D. (2002). Hyperspectral image data analysis as a high dimensional signal processing problem. *Special issue of the IEEE Signal Processing Magazine*, 19(1):17–28.
- Landgrebe, D. (2003). *Signal Theory Methods in Multispectral Remote Sensing*. John Wiley and Sons.
- Lantuéjoul, C. (1978). *La squelettisation et son application aux mesures topologiques des mosaques polycristallines*. PhD thesis, Ecole des Mines.
- Lantuéjoul, C. (2002). *Geostatistical simulation: Models and algorithms*. Springer-Verlag.
- Lathauwer, L., Moor, B., and J.Vandewalle (2000). A multilinear singular value decomposition. *SIAM Journal Matrix Anal. Appl.*, 21(4):1253–1278.
- Lezoray, O., Charrier, C., and Elmoataz, A. (2009). Learning complete lattices for manifold mathematical morphology. In *Proc. of the ISMM'09*, pages 1–4.
- Lezoray, O., Elmoataz, A., and Meurie, C. (2007). Mathematical morphology in any color space. In *Proc. of ICIAPW '07*, pages 183–187.
- Li, J., Bioucas-Dias, J. M., and Plaza, A. (2009). Semi-supervised hyperspectral image classification based on markov random field and sparse multinomial logistic regression. *Proceeding of IGARSS*, 1:1–4.
- Li, J., Bioucas-Dias, J. M., and Plaza, A. (2011). Hyperspectral image segmentation using a new bayesian approach with active learning. *IEEE Transaction on Geoscience and Remote Sensing*, 49(10):3947–3960.
- Li, J., Bioucas-Dias, J. M., and Plaza, A. (2012). Spectral-spatial hyperspectral image segmentation using subspace multinomial logistic regression and markov random fields. *IEEE Transaction on Geoscience and Remote Sensing*, 50(3):809–823.
- Liu, R. (1990). On a notion of data depth based on random simplices. *Annals of Statistics*, 18:405–414.

- Lorand, R. (2000). *Aesthetic order: a philosophy of order, beauty and art*. Routledge studies in twentieth century philosophy. Routledge.
- Lukac, R., Smolka, B., Martin, K., Plataniotis, K., and Venetsanopoulos, A. (2005). Vector filtering for color imaging. *Signal Processing Magazine, IEEE*, 22(1):74–86.
- Lunga, D. and Ersoy, O. (2011). Unsupervised classification of hyperspectral images on spherical manifolds. In *ICDM*, pages 134–146.
- Luo, D., Ding, C. H. Q., and Huang, H. (2011). Are tensor decomposition solutions unique? on the global convergence hosvd and parafac algorithms. In *PAKDD (1)*, pages 148–159.
- Mallat, S. (2008). *A wavelet tour of signal processing, third edition: The sparse way*. Academic Press, 3rd edition.
- Manolakis, D., Marden, D., and Shaw, G. A. (2003). Hyperspectral image processing for automatic target detection applications. *Lincoln Laboratory Journal*, 14(1):79–116.
- Manolakis, D., Siracusa, C., and Shaw, G. (2001). Hyperspectral subpixel target detection using the linear mixing model. *IEEE Transaction on Geoscience and Remote Sensing*, 39(7):1392–1409.
- Maragos, P. (2005). Lattice image processing: A unification of morphological and fuzzy algebraic systems. *J. Math. Imaging Vis.*, 22:333–353.
- Martin-Herrero, J. (2007). Anisotropic diffusion in the hypercube. *IEEE Transaction on Geoscience and Remote Sensing*, 45(5):1386–1398.
- Matheron, G. (1969). *Le krigeage universel*. Ecole des Mines de Paris.
- Matheron, G. (1975). *Random Sets and Integral Geometry*. John Wiley.
- Matheron, G. (1997). *Les Nivellements*. Centre de Morphologie Mathématique.
- Maxwell, J. C. (1870). On hills and dales. *The Philosophical magazine*, 40:421–424.
- Melgani, F. and Bruzzone, L. (2004). Classification of hyperspectral remote sensing images with support vector machines. *IEEE Transaction on Geoscience and Remote Sensing*, 42(8):1778–1790.
- Meyer, F. (1998). The levelings. In *Proc. of the ISMM'98*, pages 199–206, Norwell, MA, USA. Kluwer Academic Publishers.
- Meyer, F. (2001). An overview of morphological segmentation. *International Journal of Pattern Recognition and Artificial Intelligence*, 15(7):1089–1118.
- Meyer, F. (2010). Leveling and flat zone morphology. In *International Conference on Pattern Recognition*, pages 1570–1574.
- Meyer, F. (2012). The steepest watershed: from graphs to images. Preprint: arXiv:1204.2134v1.
- Meyer, F. and Beucher, S. (1990). Morphological segmentation. *Journal of Visual Communication and Image Representation*, 1(1):21–46.
- Meyer, F. and Serra, J. (1989). Contrasts and activity lattice. *Signal Processing*, 16:303–317.
- Molchanov, I. (1997). *Statistics of the Boolean Models for Practitioners and Mathematicians*. Wiley.
- Molchanov, I. (2005). *Theory of Random Sets*. Springer-Verlag.
- Motta, G., Ordentlich, E., Ramírez, I., Seroussi, G., and Weinberger, M. J. (2011). The idude framework for grayscale image denoising. *IEEE Transaction on Image Processing*, 20(1):1–21.

- Muti, D., Bourennane, S., and Marot, J. (2008). Lower-rank tensor approximation and multiway filtering. *SIAM J. Matrix Analysis Applications*, 30(3):1172–1204.
- Naegel, B., Passat, N., and Ronse, C. (2007). Grey-level hit-or-miss transforms - Part I: Unified theory. *Pattern Recognition*, 40(2):635–647.
- Najman, L. (2011). On the equivalence between hierarchical segmentations and ultrametric watersheds. *J. Math. Imaging Vis.*, 40(3):231–247.
- Najman, L. and Schmitt, M. (1994). Watershed of a Continuous Function. *Signal Processing*, 38:99–112. Special issue on Mathematical Morphology.
- Najman, L. and Talbot, H. (2010). *Mathematical morphology: from theory to applications*. ISTE-Wiley.
- Nguyen, T. M. and Wu, Q. J. (2011). Dirichlet gaussian mixture model: Application to image segmentation. *Image Vision Computing*, 29:818–828.
- Noyel, G., Angulo, J., and Jeulin, D. (2007). Morphological segmentation of hyperspectral images. *Image Analysis and Stereology*, 26(3):101–109.
- Osher, S. and Rudin, L. (1990). Feature-oriented image enhancement using shock filters. *SIAM Journal on Numerical Analysis*, 27:919–940.
- Osher, S. and Rudin, L. (1991). Shocks and other nonlinear filtering applied to image processing. In *Society of Photo-Optical Instrumentation Engineers (SPIE) Conference Series*, volume 1567, pages 414–431.
- Ouzounis, G., Pesaresi, M., and Soille, P. (2012). Differential area profiles: Decomposition properties and efficient computation. *IEEE Transaction on Pattern Analysis and Machine Intelligence*, 34(8):1533–1548.
- Palmason, J. A., Benediktsson, J. A., Sveinsson, J. R., and Chanussot, J. (2005). Classification of hyperspectral data from urban areas using morphological preprocessing and independent component analysis. In *Geoscience and Remote Sensing Symposium, 2005. IGARSS '05. Proceedings. 2005 IEEE International*, volume 1, pages 1–4.
- Perona, P. and Malik, J. (1990). Scale-space and edge detection using anisotropic diffusion. *IEEE Transactions on Pattern Analysis and Machine Intelligence*, 12:629–639.
- Pesaresi, M. and Benediktsson, J. (2001). A new approach for the morphological segmentation of high-resolution satellite imagery. *IEEE Transaction on Geoscience and Remote Sensing*, 39(2):309–320.
- Peyré, G. (2009). Manifold models for signals and images. *Computer Vision and Image Understanding*, 113(2):249–260.
- Pizarro, L., Mrázek, P., Didas, S., Grewenig, S., and Weickert, J. (2010). Generalised nonlocal image smoothing. *International Journal of Computer Vision*, 90:62–87.
- Plaza, A., Benediktsson, J. A., Boardman, J., Brazile, J., Bruzzone, L., Camps-Valls, G., Chanussot, J., Fauvel, M., Gamba, P., Gualtieri, A., Tilton, J., and Triani, G. (2009). Recent advances in techniques for hyperspectral image processing. *Remote Sensing Environment*, 113(1):110–122.
- Plaza, A., Martinez, P., Perez, R., and Plaza, J. (2004). A new approach to mixed pixel classification of hyperspectral imagery based on extended morphological profiles. *Pattern Recognition*, 37(6):1097–1116.
- Qin, A. and Clausi, D. A. (2010). Multivariate image segmentation using semantic region growing with adaptive edge penalty. *IEEE Transaction on Image Processing*, 19:2157–2170.

- Rasmussen, C. E. and Williams, C. K. I. (2006). *Gaussian Processes for Machine Learning*. MIT Press.
- Regazzoni, C. and Teschioni, A. (1997). A new approach to vector median filtering based on space filling curves. *IEEE Transaction on Image Processing*, 6(7):1025–1037.
- Renard, N. and Bourennane, S. (2008). Improvement of target detection methods by multiway filtering. *IEEE Transaction on Geoscience and Remote Sensing*, 46(8):2407–2417.
- Rodionova, O. Y., Houmoller, L. P., Pomerantsev, A. L., Geladi, P., Burger, J., Dorofeyev, V. L., and Arzamastsev, A. P. (2005). Nir spectrometry for counterfeit drug detection: A feasibility study. *Analytica Chimica Acta*, 549(1-2):151 – 158.
- Roerdink, J. and Meijster, A. (2000). The watershed transform: Definitions, algorithms and parallelization strategies. *Fundamenta Informaticae*, 41:187–228.
- Roerdink, J. B. T. M. (2009). Adaptivity and group invariance in mathematical morphology. In *International Conference of Image Processing*, pages 2253–2256. IEEE.
- Ronse, C. (1990a). Order-configuration functions: mathematical characterizations and applications to digital signal and image processing. *Information Sciences*, 50(3):275–327.
- Ronse, C. (1990b). Why mathematical morphology needs complete lattices. *Signal Processing*, 21(2):129–154.
- Ronse, C. (1996). A lattice-theoretical morphological view on template extraction in images. *Journal of Visual Communication and Image Representation*, 7(3):273 – 295.
- Ronse, C. (2006). Flat morphology on power lattices. *Journal of Mathematical Imaging and Vision*, 26:185–216.
- Schavemaker, J., Reinders, M. J. T., Gerbrands, J. J., and Backer, E. (2000). Image sharpening by morphological filtering. *Pattern Recognition*, 33(6):997–1012.
- Schetzen, M. (1980). *The Volterra and Wiener Theories of Nonlinear Systems*. John Wiley.
- Scholkopf, B., Smola, A., and Muller, K. (1998). Nonlinear component analysis as a kernel eigenvalue problem. *Neural Comp.*, 10(5):1299–1319.
- Schultz, R. A., Nielsen, T., Zavaleta, J. R., Ruch, R., Wyatt, R., and Garner, H. R. (2001). Hyper-spectral imaging: a novel approach for microscopic analysis. *Cytometry*, 43(4):239–247.
- Serra, J. (1982). *Image Analysis and Mathematical Morphology*. Academic Press, Inc., Orlando, FL, USA.
- Serra, J. (1988). *Image Analysis and Mathematical Morphology, Vol. 2: Theoretical Advances*. Academic Press.
- Serra, J. (1989a). Boolean random functions. *Journal of Microscopy*, 156(1):41–63.
- Serra, J. (1989b). Toggle mappings. In *From Pixels to Features*, pages 61–72, North Holland, Amsterdam. Simon, Ed.
- Serra, J. (2009). The “false colour” problem. In *Proc. of the ISMM’09*, pages 13–23, Berlin, Heidelberg. Springer-Verlag.
- Serra, J. and Vincent, L. (1992). An overview of morphological filtering. *Circuits, Systems and Signal Processing*, 11(1):47–108.
- Shih, F. and Mitchell, O. (1989). Threshold decomposition of gray-scale morphology into binary morphology. *IEEE Transaction on Pattern Analysis and Machine Intelligence*, 11:31–42.

- Sim, D., Kwon, O., and Park, R. (1999). Object matching algorithms using robust hausdorff distance measures. *IEEE Transaction on Image Processing*, 8(3):425–429.
- Soille, P. (2002). On morphological operators based on rank filters. *Pattern Recognition*, 35(2):527–535.
- Soille, P. (2003). *Morphological Image Analysis*. Springer-Verlag.
- Soille, P. (2008). Constrained connectivity for hierarchical image partitioning and simplification. *IEEE Transaction on Pattern Analysis and Machine Intelligence*, 30(7):1132–1145.
- Soille, P. (2011). Preventing chaining through transitions while favouring it within homogeneous regions. In *Mathematical Morphology and Its Applications to Image and Signal Processing*, volume 6671 of *Lecture Notes in Computer Science*, pages 96–107. Springer Berlin / Heidelberg.
- Soille, P. and Grazzini, J. (2009). Constrained connectivity and transition regions. In *Proc. of the ISMM'09*, pages 59–69, Berlin, Heidelberg. Springer-Verlag.
- Soille, P. and Pesaresi, M. (2002). Advances in mathematical morphology applied to geoscience and remote sensing. *IEEE Transaction on Geoscience and Remote Sensing*, 40(9):2042–2055.
- Srinivasan, K. and Ebenezer, D. (2007). A new fast and efficient decision-based algorithm for removal of high density impulse noises. *IEEE Signal Processing Letters*, 14(3):189–192.
- Sun, D. (2010). *Hyperspectral Imaging for Food Quality Analysis and Control*. Academic Press. Elsevier Science & Technology.
- Tadjudin, S. and Landgrebe, D. (1998). Classification of High Dimensional Data with Limited Training samples. Technical report, School of Electrical Engineering, Purdue University.
- Takeda, H., Farsiu, S., and Milanfar, P. (2006). Robust kernel regression for restoration and reconstruction of images from sparse, noisy data. In *Proc. Int. Conf. Image Processing (ICIP)*, pages 1257–1260.
- Takeda, H., Farsiu, S., and Milanfar, P. (2007). Kernel regression for image processing and reconstruction. *IEEE Transaction on Image Processing*, 16(2):349–366.
- Tarabalka, Y., Benediktsson, J. A., Chanussot, J., and Tilton, J. C. (2010a). Multiple spectral-spatial classification approach for hyperspectral data. *IEEE Transaction on Geoscience and Remote Sensing*, 48(11):4122–4132.
- Tarabalka, Y., Chanussot, J., and Benediktsson, J. (2010b). Segmentation and classification of hyperspectral images using watershed transform. *Pattern Recognition*, 43(7):2367–2379.
- Tarabalka, Y., Fauvel, M., Chanussot, J., and Benediktsson, J. (2010c). Svm- and mrf-based method for accurate classification of hyperspectral images. *IEEE Geosci. Remote Sens. Lett.*, 7(4):736–740.
- Tenenbaum, J., Silva, V., and Langford, J. (2000). A global geometric framework for nonlinear dimensionality reduction. *Science*, 290(5500):2319–2323.
- Tomasi, C. and Manduchi, R. (1998). Bilateral filtering for gray and color images. In *Computer Vision, 1998. Sixth International Conference on*, pages 839–846.
- Trahanias, P. and Venetsanopoulos, A. (1993). Vector directional filters - a new class of multichannel image processing filters. *IEEE Transaction on Image Processing*, 2(4):528–534.
- Tukey, J. (1975). Mathematics and picturing data. *Proceeding of the International Congress on Mathematics*, 2:523–531.
- Vapnik, V. and Lerner, A. (1963). Pattern recognition using generalized portrait method. *Automation and Remote Control*, 24:774–780.

- Vardi, Y. and Zhang, C. (2000). The multivariate l_1 median and associated data depth. *Proceeding of the Nacional Academy of Sciences*, 97(4):1423–1436.
- Velasco-Forero, S. and Angulo, J. (2009). Morphological scale-space for hyperspectral images and dimensionality exploration using tensor modeling. *First IEEE Workshop on Hyperspectral Image and Signal Processing: Emerging Remote Sensing (WHISPERS 2009)*, 08.
- Velasco-Forero, S. and Angulo, J. (2010a). Hit-or-miss transform in multivariate images. In *Advanced Concepts for Intelligent Vision Systems*, volume 6474 of *Lecture Notes in Computer Science*, pages 452–462. Springer-Verlag.
- Velasco-Forero, S. and Angulo, J. (2010b). Morphological processing of hyperspectral images using kriging-based supervised ordering. In *IEEE - International Conference of Image Processing*.
- Velasco-Forero, S. and Angulo, J. (2010c). Parameters selection of morphological scale-space decomposition for hyperspectral images using tensor modeling. In *Proceeding of the SPIE: 7695*", volume 7695, page 76951B (12pp).
- Velasco-Forero, S. and Angulo, J. (2011a). Mathematical morphology for vector images using statistical depth. In *Mathematical Morphology and Its Applications to Image and Signal Processing*, volume 6671 of *Lecture Notes in Computer Science*, pages 355–366. Springer Berlin / Heidelberg.
- Velasco-Forero, S. and Angulo, J. (2011b). Multiclass ordering for filtering and classification of hyperspectral images. In *Hyperspectral Image and Signal Processing: Evolution in Remote Sensing (WHISPERS), 2011 3rd Workshop on*, pages 1–4.
- Velasco-Forero, S. and Angulo, J. (2011c). Supervised ordering in \mathbb{R}^p : Application to morphological processing of hyperspectral images. *IEEE Transaction on Image Processing*, 20(11):3301–3308.
- Velasco-Forero, S. and Angulo, J. (2012). Random projection depth for multivariate mathematical morphology. *Journal of Selected Topics in Signal Processing*, 6(7):753–763.
- Velasco-Forero, S. and Angulo, J. (2013). Classification of hyperspectral images by tensor modeling and additive morphological decomposition. *Pattern Recognition*, 46(2):566–577.
- Velasco-Forero, S. and Manian, V. (2009). Improving hyperspectral image classification using spatial preprocessing. *IEEE Transaction on Geoscience and Remote Sensing Letters*, 6:297–301.
- Velasco-Forero, S., Soille, P., and Angulo, J. (2012). Conditional mathematical morphology for edge enhancement and salt-and-pepper noise reduction. *submitted*.
- Vese, L. and Osher, S. (2003). Modeling textures with total variation minimization and oscillating patterns in image processing. *Journal of Scientific Computing*, 19(1):553–572.
- Vincent, L. (1993). Morphological grayscale reconstruction in image analysis: Applications and efficient algorithms. *IEEE Transaction on Image Processing*, 2:176–201.
- Vincent, L. and Soille, P. (1991). Watersheds in Digital Spaces: An Efficient Algorithm Based on Immersion Simulations. *IEEE Transaction on Pattern Analysis and Machine Intelligence*, 13(6):583–598.
- Vliet, L. V., Young, I., and Beckers, G. (1989). A nonlinear laplace operator as edge detector in noisy images. *Computer Vision, Graphics, and Image Processing*, 45(2):167–195.
- Wang, Y., Niu, R., and Yu, X. (2010). Anisotropic diffusion for hyperspectral imagery enhancement. *Sensors Journal, IEEE*, 10(3):469–477.
- Wang, Z. and Zhang, D. (1999). Progressive switching median filter for the removal of impulse noise from highly corrupted images. *IEEE Trans. Circuits and Systems II: Analog and Digital Signal Processing*, 46(1):78–80.

- Weber, J. and Lefevre, S. (2008). A multivariate Hit-or-Miss transform for conjoint spatial and spectral template matching. In *Image and Signal Processing*, volume 5099 of *Lectures Notes in Computer Science*, pages 226–235. Springer-Verlag.
- Weickert, J. (2003). Coherence-enhancing shock filters. In *Lecture Notes in Computer Science*, pages 1–8. Springer-Verlag.
- Welk, M., Weickert, J., and Galc, I. (2007). Theoretical foundations for spatially discrete 1-d shock filtering. *Journal Image Vision Computing*, 25:455–463.
- Wendt, P., Coyle, E., and Gallaher, N. (1986). Stack filters. *IEEE Trans. Acoustics, Speech and Signal Processing*, 34:898–911.
- Wright, J., Ma, Y., Mairal, J., Sapiro, G., Huang, T. S., and Yan, S. (2010). Sparse Representation for Computer Vision and Pattern Recognition. *Proceedings of the IEEE*, 98(6):1031–1044.
- Zhang, Q., Wang, H., Plemmons, R. J., and Pauca, V. P. (2008). Tensor methods for hyperspectral data analysis: a space object material identification study. *Journal of the Optical Society of America A*, 25(12):3001–3012.
- Zhang, S. and Karim, M. (2002). A new impulse detector for switching median filters. *IEEE Signal Processing Letters*, 9(11):360–363.
- Zhu, Z., Tang, M., and Lu, H. (2004). A new robust circular gabor based object matching by using weighted hausdorff distance. *Pattern Recognition Letters*, 25(4):515–523.
- Zuo, Y. (2003). Projection-based depth function and associated medians. *Annals of Statistics*, 31(5):1460–1490.
- Zuo, Y. (2006). Multidimensional trimming based on projection depth. *Annals of Statistics*, 34(5):2211–2251.
- Zuo, Y. and Serfling, R. (2000). General notions of statistical depth function. *Annals of Statistics*, 28(2):461–482.

Contributions en morphologie mathématique pour l'analyse d'images multivariées

Résumé : Cette thèse contribue au domaine de la morphologie mathématique et illustre comment les statistiques multivariées et les techniques d'apprentissage numérique peuvent être exploitées pour concevoir un ordre dans l'espace des vecteurs et pour inclure les résultats d'opérateurs morphologiques au processus d'analyse d'images multivariées. En particulier, nous utilisons l'apprentissage supervisé, les projections aléatoires, les représentations tensorielles et les transformations conditionnelles pour concevoir de nouveaux types d'ordres multivariés et de nouveaux filtres morphologiques pour les images multi/hyperspectrales. Nos contributions clés incluent les points suivants :

- Exploration et analyse d'ordre supervisé, basé sur les méthodes à noyaux.
- Proposition d'un ordre non supervisé, basé sur la fonction de profondeur statistique calculée par projections aléatoires. Nous commençons par explorer les propriétés nécessaires à une image pour assurer que l'ordre ainsi que les opérateurs morphologiques associés, puissent être interprétés de manière similaire au cas d'images en niveaux de gris. Cela nous amènera à la notion de décomposition en arrière plan / premier plan. De plus, les propriétés d'invariance sont analysées et la convergence théorique est démontrée.
- Analyse de l'ordre supervisé dans les problèmes d'appariement par forme de référence, qui correspond à l'extension de l'opérateur tout-ou-rien aux images multivariées grâce à l'utilisation de l'ordre supervisé.
- Discussion sur différentes stratégies pour la décomposition morphologique d'images. Notamment, la décomposition morphologique additive est introduite comme alternative pour l'analyse d'images de télédétection, en particulier pour les tâches de réduction de dimension et de classification supervisée d'images hyperspectrales.
- Proposition d'un cadre unifié basé sur des opérateurs morphologiques, pour l'amélioration de contraste et pour le filtrage du bruit poivre-et-sel.
- Introduction d'un nouveau cadre de modèles Booléens multivariés par l'utilisation d'une formulation en treillis complets. Cette contribution théorique est utile pour la caractérisation et la simulation de textures multivariées.

Mots clés : Morphologie mathématique, Télédétection, Projections aléatoires, Structure tensorielle, Traitement d'images.

Topics in Mathematical Morphology to Multivariate Image Analysis

Abstract: This thesis contributes to the field of mathematical morphology and illustrates how multivariate statistics and machine learning techniques can be exploited to design vector ordering and to include results of morphological operators in the pipeline of multivariate image analysis. In particular, we make use of supervised learning, random projections, tensor representations and conditional transformations to design new kinds of multivariate ordering, and morphological filters for color and multi/hyperspectral images. Our key contributions include the following points:

- Exploration and analysis of supervised ordering based on kernel methods.
- Proposition of an unsupervised ordering based on statistical depth function computed by random projections. We begin by exploring the properties that an image requires to ensure that the ordering and the associated morphological operators can be interpreted in a similar way than in the case of grey scale images. This will lead us to the notion of background/foreground decomposition. Additionally, invariance properties are analyzed and theoretical convergence is showed.
- Analysis of supervised ordering in morphological template matching problems, which corresponds to the extension of hit-or-miss operator to multivariate image by using supervised ordering.
- Discussion of various strategies for morphological image decomposition, specifically, the additive morphological decomposition is introduced as an alternative for the analysis of remote sensing multivariate images, in particular for the task of dimensionality reduction and supervised classification of hyperspectral remote sensing images.
- Proposition of an unified framework based on morphological operators for contrast enhancement and salt-and-pepper denoising.
- Introduces a new framework of multivariate Boolean models using a complete lattice formulation. This theoretical contribution is useful for characterizing and simulation of multivariate textures.

Keywords: Mathematical Morphology, Remote Sensing, Random Projections, Tensor Structure, Image Processing.

